Halide Segregation in Mixed-Halide Perovskites

Alexander James Knight
University College
University of Oxford

A thesis submitted for the degree of
Doctor of Philosophy
Hilary 2021

For Mum and Dad,
thank you for everything.

Acknowledgements

While the acknowledgement section of any thesis may seem a little insignificant and inconsequential when compared to the bulk of work that immediately follows it, I cannot help but feel that if I were to thank the people listed below as they deserve, the emphasis of this thesis would be flipped: no longer on my conducted research, but on them instead.

Firstly, **Prof. Laura Herz** has been a wonderful supervisor, and I cannot overstate my gratitude for her mentorship. I have learnt so much and grown as a researcher because of her. In addition, **Prof. Michael Johnston** has provided significant advice and opportunities for me over the years, for which I thank him deeply.

The members of the Herz-Johnston group have been eternally welcoming and gracious, and I genuinely believe I couldn't have found a better research group anywhere in the world. Unfortunately I cannot list every happy memory I have shared with them, I can only simply thank Leonardo Buizza, James Ball, Elisabeth Duijnstee, Karim Elmestekawy, Juliane Gong, Vincent Lim, Kilian Lohmann, Laura Martínez Maestro, Rebecca Milot, Silvia Motti, Robert Oliver, Elizabeth Parrott, Kun Peng, Waqaas Rehman, Mathias Rothmann, Sabrina Sterzl, Michael Trimpl, Alex Ulatowski, Chelsea Xia, and Qimu Yuan.

I would particularly like to thank **Adam Wright**, **Jay Patel**, and **Juliane Borchert** for directly helping me with experimental research, tutoring me, and experiencing the highs and lows of experimental physics with me. I would also like to thank the members of my office – **Djamshid Damry**, **Hannah Eggimann**, **Kimberley Savill**, and **Timothy Crothers** – for those extremely important non-academic aspects of office life, occasionally distracting me, and – rather more frequently – allowing me to distract them.

Finally, my family. **Mum** and **Dad** have always encouraged me and taken an interest in whatever I do, but they have also allowed me the space to learn and grow. I love you both greatly, and I hope you are proud of this thesis, it is dedicated to you. **Emily**, thank you for being an incredible sister who is always ready to support or humble me, as required. **Gabi**, I love you dearly, thank you for being who you are.

Abstract

Metal halide perovskites have garnered a great deal of interest over the last few years due to their impressive – and rapidly increasing – performance as materials for solar cells. In particular, mixed-halide perovskites are essential for use in all-perovskite or perovskite-silicon tandem solar cells due to their tunable bandgap. However, one major obstacle to their use is the compositional instability some mixed-halide perovskites experience under illumination or charge-carrier injection, during which the perovskite material demixes into regions of differing halide content. Such segregation of halide ions adversely affects the electronic properties of the material and severely limits the prospects of mixed-halide perovskite technology. While, empirically, the crystallinity, stoichiometry, and optoelectronic properties of the perovskite – alongside other factors – are known to influence the halide segregation dynamics, the underlying mechanisms are still poorly understood. The work of this thesis elucidates many issues regarding the halide segregation phenomenon, and helps to explain the fundamental dynamics at the heart of this instability problem.

The dependence of the halide segregation mechanism on the atmospheric environment surrounding the perovskite is investigated, revealing that encapsulation of the films with a thick layer of poly(methyl methacrylate) allows the segregation dynamics to be fully reversible and repeatable. From measurements of photon efficacy on halide ion separation, electronic trap states are revealed to play a pivotal role in the segregation mechanism. A predictive, empirical model is created to quantify this relationship, and is shown to match results in the literature.

An investigation is conducted on full mixed-halide perovskite photovoltaic devices to study the impact of electric fields on both the dynamics of halide segregation and other mobile ionic behaviours. Three distinct defect species are identified in the perovskite, and their influence on the perovskite material is determined. Additionally, charge-carrier extraction from low-bandgap regions of perovskite suggests the existence of charge-carrier percolation pathways through grain boundaries.

Finally, simultaneous, in situ X-ray diffraction and photoluminescence measurements are made utilising a home-built setup, and are used to study the role of stoichiometry on halide segregation in two different perovskite compositions. Fast ionic pathways – proposed to exist at grain boundaries – are found to strongly impact the ionic movement associated with halide segregation, resulting in extremely different compositional evolutions in high- and low-stability materials.

Contents

List of Publications

A. J. Knight, A. D. Wright, J. B. Patel, D. P. McMeekin, H. J. Snaith, M. B. Johnston, and L. M. Herz. Electronic Traps and Phase Segregation in Lead Mixed-Halide Perovskite. *ACS Energy Letters* **2019**, *4* (1), 75-84.

A. J. Knight, J. B. Patel, H. J. Snaith, M. B. Johnston, and L. M. Herz. Trap States, Electric Fields, and Phase Segregation in Mixed-Halide Perovskite Photovoltaic Devices. *Advanced Energy Materials* **2020**, *10* (9), 1903488.

A. J. Knight and L. M. Herz. Preventing Phase Segregation in Mixed-Halide Perovskites: A Perspective. *Energy & Environmental Science* **2020**, *13* (7), 2024-2046.

A. J. Knight, J. Borchert, R. D. J. Oliver, J. B. Patel, P. G. Radaelli, H. J. Snaith, M. B. Johnston, and L. M. Herz. Halide Segregation in Mixed-Halide Perovskites: Influence of A-Site Cations. *ACS Energy Letters* **2021**, *6* (2), 799-808.

List of Abbreviations

C-C . . . . . Charge-carrier

EQE . . . . . External quantum efficiency

FA . . . . . Formamidinium ion, $CH(NH_2)_2^+$

FACs . . . . . Formamidinium-caesium

FTMR . . . . Fraction of trap-mediated recombination

FTO . . . . . Fluorine doped tin oxide

FWHM . . . . Full width at half maximum

LED . . . . . Light-emitting diode

MA . . . . . Methylammonium ion, $CH_3NH_3^+$

MHP . . . . . Metal halide perovskite

n . . . . . The excited charge-carrier density

PEDOT:PSS . Poly(3,4-ethylenedioxythiophene) polystyrene sulfonate

PL . . . . . Photoluminescence

PLQY . . . . . Photoluminescence quantum yield

PMMA . . . . Poly(methyl methacrylate)

PTAA . . . . . Poly[bis(4-phenyl)(2,4,6-trimethylphenyl)amine]

PV . . . . . Photovoltaic

SEM . . . . . Scanning electron microscope

SRH . . . . . Shockley-Read-Hall (recombination)

SPAD . . . . . Single-photon avalanche diode

SPO . . . . . Stabilised power output

TCSPC . . . . Time-correlated single photon counting

XRD . . . . . X-ray diffraction

1 Introduction

The acquisition and effective utilisation of energy sources have always been prime concerns of any human civilisation. From the discovery of fire, through the industrial revolution, and on to the advent of non-fossil fuel based power, the development of energy sources is intimately and deeply tied to the development of human civilisation itself. Unfortunately, the use of energy sources throughout human history has not been without consequence [1, 2]. Fossil fuels – coal, gas and oil – have, due to their relative abundance and ease of use, dominated as energy sources over the last 100 years [3], but emit harmful pollutants such as CO_2 that are having a devastating and lasting impact on the earth's climate [1, 2]. As a result there has recently been increasing interest in developing non-polluting, sustainable energy sources. While the laws of thermodynamics ensure that no energy source can ever be considered perfectly sustainable for all time, power sources that derive immediately or nearly immediately from the sun, such as solar, wind and hydropower, are considered to have a lifetime long enough – around 5 billion years – to be considered "sustainable". Additionally, and perhaps more importantly, generating power from the sun results in a lower emission of greenhouse gases than the utilisation of fossil fuels. As a result, sustainable energy sources represent – almost by

definition – a long-term solution to mankind's energy needs, although certain hurdles must first be overcome in order to make such energy sources viable on large scales.

In the remarkably short timescale of around a decade perovskite solar cells have progressed from an interesting academic curiosity, to a genuine competitor to the more established technologies of other solar cell materials [4, 5]. As discussed more in Chapter 2, perovskite materials combine a large number of excellent or ideal optoelectronic properties with cheap and relatively low-energy manufacturing methods [4–6]. The record certified efficiency for single-layer perovskite research solar cells is now 25.5% [7], higher than that of polycrystalline silicon solar cells (23.3% [7]), and comparable to that of single-crystal silicon solar cells (26.1% [7]). Importantly, the facile manufacture of perovskite materials means that they could be utilised alongside silicon technology to form a 'tandem' solar cell [8–10]. By incorporating perovskite layers into silicon solar cells, the overall efficiency of the solar cell could be cheaply increased by a few percentage points, and perovskite as a technology may be able to piggy-back off the success and infrastructure of silicon photovoltaic technology [10].

Unfortunately there are still several major hurdles for the commercialisation of perovskite photovoltaic materials, one of the most major being the general instability of such perovskites when exposed to oxygen [11–13], humidity [14–16], or even light [17]. The work in this thesis studies a particular light-induced instability problem known as 'halide segregation' [17], which can affect perovskite materials that contain multiple halide ion species in their structure, a group that notably includes perovskites used in the highest efficiency perovskite-silicon solar cells [8, 9]. Halide segregation appears to be a problem intrinsic to these afflicted perovskite materials, and only requires incident illumination to proceed, making it both difficult to suppress in perovskite solar cells, and an interesting phenomenon to study [17–19]. Halide segregation reduces the power

conversion efficiency of perovskite solar cells [20–23], thereby making it a pertinent problem to solve for perovskite solar cells to become commercially viable.

In this thesis, a comprehensive examination of the underlying dependencies, driving factors, and mechanisms of the halide segregation phenomenon is conducted from various experimental angles. By understanding the fundamental aspects of the segregation mechanism, the work in this thesis highlights a pathway to the future manufacture of light-stable mixed-halide perovskite materials. In Chapter 2, brief introductions to semiconductor charge-carrier dynamics, photovoltaic devices, and perovskite materials in general are followed by an in-depth review of the literature on halide segregation in mixed-halide perovskite materials. In particular, three factors are determined to have a strong influence on the halide segregation dynamics in mixed-halide perovskites, which are: the stoichiometry of the perovskite and in particular the choice of the singly charged cation in the perovskite structure, the crystallinity of the perovskite, and the trap state density within the perovskite material. Several further factors are evaluated and discussed in detail.

Chapter 3 describes the experimental theory and methods utilised in this thesis. Photoluminescence techniques were heavily relied upon to perform the work presented in this thesis, as they are extremely sensitive to the movement of the halide ions in the perovskite material that occurs during the halide segregation process. In addition, X-ray diffraction measurements, absorption spectroscopy, and photovoltaic device characterisation techniques were utilised to grant a broader experimental picture of the halide segregation dynamics, and the respective theory and experimental setups are detailed in Chapter 3.

The experimental work of this thesis begins in Chapter 4 with a fundamental examination of the halide segregation mechanism in methylammonium-based, mixed-halide perovskite thin films. In order to investigate how environmental factors may

affect experimental results, and to establish conditions under which repeatable results may be obtained, Chapter 4 begins by studying the influence of different atmospheric conditions on the behaviour of halide segregation in methylammonium-based, mixed-halide perovskite thin films. The behaviour of the photoluminescence emitted from the mixed-halide perovskite is observed to change markedly according to the atmosphere the material is held under, indicating both atmospherically-dependent halide segregation dynamics and additional atmospheric effects as observed in other, single-halide perovskite materials [24–32]. The influence of the atmosphere is found to be suppressed when the perovskite thin film is coated with a thick layer of poly(methyl methacrylate) and held under vacuum, which is an experimental setup utilised whenever possible throughout the experimental work presented in this thesis to eliminate atmospheric influences on the halide segregation dynamics. Chapter 4 continues with an investigation into the role of the photogenerated charge-carrier density on the halide segregation dynamics, in order to uncover the underlying link between excited charge carriers and halide ion movement. Charge carriers that recombine through trap states are concluded to be responsible for the halide segregation mechanism, and a corresponding empirical model is generated to explain observations of halide segregation under other conditions.

Following on from the fundamental investigation of perovskite thin films conducted in Chapter 4, Chapter 5 studies the interactions between electric fields, halide segregation, and mobile ion defects in working perovskite solar cells, and the resulting influence on charge-carrier extraction. To do so, full, methylammonium-based, mixed-halide perovskite photovoltaic devices are studied using photoluminescence techniques, and external electric fields are applied across the electrical contacts of the devices. Three defects and/or mobile ion species are identified in the perovskite material due to their differing behaviours under applied electric fields, and each is observed to affect the behaviour of the photovoltaic device in different ways. First, charged methylammonium ions in the perovskite lattice

are shown to move slowly through the perovskite material in response to an electric field, and detrimentally affect the radiative efficiency of the perovskite material. Second, in a continuation of the work of Chapter 4, charge-neutral crystal lattice distortions are proposed to trap photoexcited charge carriers and contribute to the halide segregation mechanism. Third, charged, highly mobile halide vacancies and/or interstitials are shown to move rapidly in response to an electric field and electrically screen the bulk perovskite. Furthermore, while halide segregation is found to detrimentally affect the current extracted from a perovskite solar cell, current is still extracted from the low-bandgap regions of perovskite that form during halide segregation, suggesting a network of percolation pathways that are proposed to exist along the grain boundaries of the perovskite material. Finally, a Sankey (flow) diagram is presented to summarise the work of Chapters 4 and 5 on the charge-carrier dynamics within a perovskite material experiencing halide segregation.

Having completed an extensive exploration of the charge-carrier dynamics in mixed-halide perovskites experiencing halide segregation in Chapters 4 and 5, Chapter 6 moves on to explore the role of perovskite composition in both the halide segregation mechanism and general ionic behaviour in mixed-halide perovskites. Two different compositions of perovskite are investigated (one methylammonium-based, one mixed formamidinium/caesium-based) which are known to have vastly differing stabilities against the halide segregation phenomenon [18]. Additionally, a home-built experimental setup allows for time-resolved, in situ photoluminescence and X-ray diffraction measurements to be conducted simultaneously. This setup allows for the measurement and comparison of changes to both the optoelectronic and compositional properties of the perovskite materials during the halide segregation process. It is found that halide segregation occurs through different ionic pathways in different perovskite materials. In methylammonium-based perovskites the presence of fast ionic pathways allows the halide segregation mechanism to initially occur rapidly in small, localised regions of perovskite, before these segregated

regions grow and engulf the remaining bulk material. In formamidinium/caesium-based perovskites the lack of such ionic pathways results in a more stable perovskite material, however over long time periods halide segregation occurs throughout the bulk material simultaneously, possibly via a 2-step mechanism that first involves the segregation of the formamidinium and caesium cations. The observations of these two different halide segregation pathways for the two different perovskite materials help to explain their difference in stability, and the role of crystallinity and ionic behaviour on the halide segregation mechanism.

Finally, Chapter 7 concludes and reviews the work of this thesis, compiling the results of previous chapters to present a fuller picture of the halide segregation mechanism.

2

Background and Fundamentals

Contents

Metal-halide perovskite (MHPs) have experienced a great deal of research interest over the last decade due to the unusual coupling of their high quality optoelectronic properties and the facile fabrication techniques required to make them [4–6]. As a result of both their ideal properties and an intense research drive, the efficiencies of photovoltaic perovskite devices are now over 25% [7], and the commercial prospects of perovskite technologies in solar cell [33] – and light emitting diode (LED) [34, 35] – applications are increasingly significant. A key factor of optoelectronic perovskite materials is the amount of ionic freedom and movement accommodated by the perovskite crystal [36], which is at least partly responsible for many important properties of perovskite technologies. For example, the ease by which perovskite photovoltaic devices are manufactured can be attributed to the low energetic barriers for ion movement allowing for solution-processing, low temperature (∼100 °C) fabrication methods to be used [37, 38]. Furthermore, the high quality of such solution-processed devices is often ascribed to the ionic freedom in the material allowing for a degree of 'self-healing' – an ability of the perovskite to correct imperfections in the material or recover from degradation simply through random ionic movement [39–42]. Additionally, the ionic disorder accommodated by metal-halide perovskites allows for multiple species of ions to occupy similar lattice sites in the perovskite structure, generating a huge compositional space for researchers to explore and allowing for high-precision stoichiometric engineering [5, 43]. However, the ionic freedom allowed within MHPs is a double-edged sword, as it leads to low-barrier degradation routes in the perovskite material, resulting in the greatest weakness of MHPs – their instability when exposed to oxygen [11–13], humidity [14–16], or light [17]. While direct engineering of the perovskite material [18, 44, 45] and encapsulation techniques [46, 47] can improve the lifetime of MHP photovoltaic devices, a major hurdle for this technology is the stringent requirements demanded of a commercial solar cell that must

last at least 20-25 years in a variety of outdoor conditions with minimal maintenance. A particularly puzzling and intrinsic instability problem known as "halide segregation" occurs in certain perovskite compositions under sufficient illumination intensities [17, 18], and represents the main focus of this thesis. The commercial prospects of MHPs are intimately connected with the halide segregation problem, making an understanding of the underlying mechanisms and the finding of corresponding solutions of utmost importance.

This chapter begins in Section 2.1 with an overview of the fundamental charge-carrier dynamics present in materials, such as MHPs, that are well described by semiconductor physics. This overview is followed by a brief discussion of the working principles of photovoltaic devices in Section 2.2. Section 2.3 focuses on the basic structural and optoelectronic properties of MHPs in particular, with emphasis placed on topics of importance to the halide segregation problem. A much more detailed discussion is dedicated in Section 2.4 to explaining the literature results on halide segregation in MHPs, as this is the main focus of this thesis. The work in Section 2.4 was originally published as a perspective paper (Ref. [18]), and as a result examines the halide segregation process in great detail.

2.1 Charge-Carrier Generation and Recombination

In general, the charge-carrier dynamics in a semiconductor are governed by five processes: stimulated absorption, stimulated emission, spontaneous emission, Shockley-Read-Hall recombination and Auger recombination [48]. The first process, stimulated absorption [48, 49], occurs when the material absorbs a photon by promoting a valence band electron to the conduction band. As a result of energy conservation, the incoming photon must have an energy higher than that of the bandgap to ensure the promoted electron can reach an unfilled energy state. Stimulated absorption is responsible for the generation of free charge carriers in a perovskite material under illumination, whereas the remaining

charge carrier processes are concerned with the demotion of free electrons back to the valence band. Stimulated and spontaneous emission [48, 49], two such demotion processes, release the excess energy of the recombining charge carriers through the release of a photon. Stimulated emission requires an above-gap photon to initiate the demotion and light-emission process, whereas spontaneous emission occurs spontaneously. These two processes encapsulate the possible ways in which an excited electron may recombine with a hole while emitting an above-bandgap photon, i.e. they represent the possible radiative recombination processes. Stimulated absorption, stimulated emission and spontaneous emission are all intrinsic to a semiconducting material as they depend on the band structure and the nature of the incident illumination, and as such they are permanent mechanisms within any semiconductor under light. It can be shown that under strong illumination, the rate of radiative recombination processes in an intrinsic semiconductor scales with n^2, the charge carrier density squared [48]. As a very basic argument, the probability of an excited electron transitioning to a valence band energy state will be proportional to the density of excited electrons available for the transition, multiplied by the density of available energy states to transition into. The proportionally constant in this case corresponds to the quantum mechanical transition probability, among other factors. Due to the fact the perovskite samples investigated in this thesis are – as a first approximation – intrinsic semiconductors, the density of available valence band states is equal to the number of excited, conduction band electrons, hence the overall n^2 dependence of the transition rate.

Shockley-Read-Hall (SRH) recombination, or trap mediated recombination, is a recombination process involving a localised trap state [48, 50, 51]. Depending on the nature of the trap state situated in the bandgap, either an electron is caught and localised on the trap, before recombining with a free hole, or a hole is caught before recombining with a free electron. The excess energy of the charge carriers is typically carried away in

lattice vibrations (phonons) making this process non-radiative, although it is possible for below-gap photons to carry away the additional energy. Because this process is intimately linked with the nature, energy, and density of the trap states within the semiconducting material, it is possible to alter the rate of SRH recombination through control of the material quality [48, 50, 51]. Under the assumptions of an intrinsic semiconductor under intense illumination, it can be shown that the rate of SRH recombination is proportional to n [48, 50, 51]. As an extremely simple argument, the rate of capture of either charge carrier type by a trap state should be proportional to the density of the relative charge carrier – both equal to n – times the density of available trap states. The de-trapping process, from similar logic, is then proportional to the density of filled traps times the density of opposing charge carriers – also equal to n. Assuming a high enough trap state density means that both these steps in the SRH process are controlled by n, and thus overall the recombination process scales with n.

Finally, Auger recombination processes constitute interactions between three charge carriers that result in the annihilation of an electron and a hole, with the excess energy and momentum absorbed by the third free charge carrier and potentially used in the emission of phonons [48]. The excitation of the third charge carrier results in either an electron high in the conduction band, or a hole low in the valence band. As a result of the high number of free charge carriers required, Auger processes generally become dominant at high illumination intensities, or when other recombination processes are limited such as in an extremely pure semiconductor with an indirect bandgap [48]. As no photons are emitted, Auger processes contribute to non-radiative recombination in semiconductors, and due to the band-to-band nature of the process, Auger recombination is intrinsic to the semiconducting material and not directly dependent on the quality of the material. As a similar argument to the one for radiative and SRH recombination

above, Auger recombination concerns the interaction of three free charge carriers and so scales with n^3 [48].

Combining all three dependencies for the processes above, the following rate equation is arrived at:

$$\frac{\mathrm{d}n}{\mathrm{d}t} = G(t) - k_1 n - k_2 n^2 - k_3 n^3 \tag{2.1}$$

Here n is the charge carrier density, t is time, $G(t)$ is the generation rate of photoexcited charge carriers, and k_1, k_2 and k_3 are the first-, second- and third-order recombination rate constants respectively. $k_1 n$ represents SRH recombination and so is highly dependent on film properties such as the density of trap states, whereas $k_2 n^2$ and $k_3 n^3$ represent radiative and Auger recombination respectively and hence depend mostly on intrinsic material properties such as the band structure. $G(t)$ represents the rate of stimulated absorption, which is dependent on the illumination source, and so it is modeled differently depending on the exact nature of the experiment. Two common illumination methods are discussed below: continuous wave illumination where the sample is irradiated with a continuous stream of incident photons; and pulsed illumination where the sample is irradiated with short, repeated, concentrated pulses of light. The focus of the following sections is on calculating the fraction of charge carriers that recombine through trap states under both these types of illuminations, as this is important for the work of Chapter 4.

2.1.1 Charge-Carrier Trapping Fractions Under Continuous Wave Illumination

Under continuous wave illumination, charge carriers are constantly photoexcited and constantly recombine, with the stimulated emission process incorporated into Equation 2.1 as a constant generation rate, $G(t) = G$. The generation rate is calculated from: $G = \frac{P}{VE}$, where P is the illumination power, V is the volume of photoexcited perovskite, and E is the photon energy of the illumination. This constant form of G assumes a uniform

charge-carrier density throughout the film, which should be valid in the perovskite samples studied in this thesis given the rapid spreading out of photoexcited charge carriers due to diffusion and photon recycling processes [52]. The inclusion of G, alongside setting $\frac{dn}{dt} = 0$ to calculate for the steady-state dynamics, results in the following equation:

$$k_3 n^3 + k_2 n^2 + k_1 n - \frac{P}{VE} = 0 \tag{2.2}$$

In order to use this equation, the recombination constants, k_1, k_2, and k_3, must be known from measurement or literature values, the volume of the photoexcited perovskite must be known and can be estimated by multiplying the illumination spot size with the perovskite film thickness (given that the film thickness is much greater than the absorption depth of the material), and the illumination parameters P and E must be known. Utilising the known values of these parameters, Equation 2.2 can be solved numerically to estimate the fraction of all generated charge carriers that recombine non-radiatively, $\frac{k_1 n}{G}$, in the perovskite film.

2.1.2 Charge-Carrier Trapping Fractions Under Pulsed Illumination

Under pulsed laser illumination, charge carriers are photoexcited in a short amount of time by a light pulse and recombine in the period of darkness before the subsequent light pulse arrives. Assuming all the generation from a pulse happens instantaneously – valid for a small pulse width – the time period of stimulated absorption is negligible, and $G(t)$ is set to 0 in Equation 2.1 in order to describe the charge-carrier dynamics in the respite period before the next pulse:

$$\frac{dn}{dt} = -k_1 n - k_2 n^2 - k_3 n^3 \tag{2.3}$$

Here, as before, n is the charge carrier density, t is time, and k_1, k_2 and k_3 are the first-, second- and third-order recombination constants respectively. The initial density

of charge carriers, n_0, is calculated from the number of photons in the incident light pulses, which assumes perfect absorption, and that there are no excited charge carriers remaining from the previous light pulse. This second assumption is generally very good, unless an extremely high pulse fluence or repetition rate is used, in which case charge carriers may survive across multiple measurements, a process that causes "wrap-around". $n(t)$ can then be solved for numerically, and the rate of change of the charge-carrier density from monomolecular decay processes is then $k_1 n(t)$. This charge-carrier decay rate is then integrated over the time between light pulses to produce the number of charge carriers that decay through trap mediated channels per unit volume per pulse, $\int k_1 n(t) \mathrm{d}t$. This quantity then divided by the photoexcited charge carriers per unit volume per pulse, n_0, produces the fraction of charge carriers that recombine through trap states averaged over one pulse, $\frac{\int k_1 n(t) \mathrm{d}t}{n_0}$.

2.2 Photovoltaic Devices

As a future application of MHPs will be in commercial solar cells, it is important to investigate the influence and dynamics of halide segregation in working photovoltaic devices. Such an investigation is conducted in Chapter 5 on mixed-halide perovskite n-i-p solar cells, and the relevant principles of photovoltaic device operation are briefly outlined in this section.

In the operation of all photovoltaic devices, excited electrons and holes must be separated and extracted into an external electrical circuit [48]. While the separation of these charge carriers can in principle be achieved by several means, a common practical method is to utilise materials of differing Fermi level. In an n-i-p solar cell, an intrinsic, "i" material – with a Fermi level in the middle of its bandgap – is sandwiched between an "n" material – with a high Fermi level – and a "p" material – with a low Fermi level. The different Fermi levels in the three layers results in a changing landscape

of charge-carrier densities within the device. Correspondingly, the n-layer has a high population of electrons in the conduction band, the p-layer has a high population of holes in the valence band, and the i-layer only has a small, thermally activated population in both bands. When the three – initially electrically-neutral – layers are brought into contact, electrons from the n-layer are able to traverse the i-layer and recombine with holes from the p-layer, resulting in a build-up of positive charge in the n-layer, and negative charge in the p-layer. This charge build-up generates an electric field across the i-layer – known as the built-in electric field – and is integral to separating the different charge carriers in the device and thereby generating a current under illumination.

The result of the charge carrier transfer between the n- and p-layers – and the generation of the built-in electric field – is that the Fermi level across the entire device becomes constant, and the system reaches equilibrium. This equilibrium can be altered by either illuminating the solar cell and thereby influencing the charge-carrier densities, or by applying an external voltage across the device and thereby influencing the energy landscape experienced by the charge carriers. In both scenarios (or in the combination of both scenarios), the key processes to consider in the operation of the photovoltaic device are charge-carrier diffusion and charge-carrier drift, both of which generate current in the device [48].

The diffusion current results from majority charge carriers diffusing along their concentration profiles against the built-in electric field. The strength of the built-in electric field, and any additional, applied electric fields across the device, therefore strongly influences this diffusion current, and the diffusion current can therefore be controlled by applying an external bias across the photovoltaic device. The diffusion current, following the concentration of positive, free charge carriers in the device, runs from the p- to n-layers.

The drift current results from the thermally-excited population of minority charge carriers being swept by the built-in potential field into the n- and p-layers. The drift

current is mostly independent of the strength of the built-in and external electric fields, as under ideal conditions most of the minority charge-carriers will be swept in the direction of the overall field, regardless of its magnitude. Instead, the predominant contribution to the drift current is the density of minority charge carriers in the material, which is itself – under equilibrium – determined by the Fermi level and temperature of the device. The drift current therefore is strongly influenced by any incident illumination upon the device, which increases the populations of free charge carriers in the conduction and valence bands of the i-layer. The drift current follows the built-in electric field and runs from the n- to the p-layer – the opposite direction to the diffusion current.

Under darkness and with no external bias applied, the n-i-p photovoltaic device is at equilibrium, and so no net current flows. Under these circumstances the drift and diffusion currents cancel out. If an applied bias opposes the built-in potential formed by the n- and p-layers (the applied bias is referred to as a *forward* bias under these circumstances), then the barrier against the diffusion current is somewhat (or totally) cancelled out, and a larger diffusion current flows from the p- to the n-layer. This behaviour of the current density extracted from the photovoltaic device under darkness – J_{Dark} – under an applied bias – V – is characterised (under very idealised assumptions) by the ideal diode equation:

$$J_{\text{Dark}}(V) = J_0(e^{\frac{qV}{k_B T}} - 1) \tag{2.4}$$

where q is the electronic charge, k_B is Boltzmann's constant, T is temperature, and J_0 is known as the dark saturation constant and is characteristic of the photovoltaic device. The exponential form of Equation 2.4 indicates that a small forward voltage – positive V – results in a large current [48].

As mentioned above, the effect of illumination upon the photovoltaic device is, to a first approximation, primarily upon the drift current. The additional free charge carriers generated by the illumination are swept by the total electric field across the device and

generate a current. Under extremely idealised conditions, this additional current is only dependent on the direction of the total electric field across the photovoltaic device, and is therefore independent of V (for small values of V). This photoexcited current density – known as the short-circuit current density, J_{SC} – is by convention taken as positive and runs in the opposite direction to J_{Dark}. As such, the total extracted current density from the photovoltaic device under illumination and voltage is:

$$J(V) = J_{SC} - J_{\text{Dark}} = J_{SC} - J_0(e^{\frac{qV}{k_B T}} - 1) \tag{2.5}$$

Using Equation 2.5, a simple understanding of the response of a solar cell under illumination to an external voltage, V, can be obtained. Under short-circuit conditions there is no external voltage across the device, resulting in that $V = 0\,\text{V}$, and $J = J_{SC}$ (hence the reason the J_{SC} is referred to as the 'short-circuit current density'). As the load across the device is increased from short-circuit, the extracted current density drops. At a given point, the load across the device is sufficient to prevent any current from being extracted – the diffusion current has increased to the point of cancelling out the drift current. This external voltage is known as the open circuit voltage, as it is the voltage which is generated between the contacts of the photovoltaic device by the photocurrent when an open circuit (i.e. no circuit) is connected externally. The open circuit voltage is, under ideal conditions, only slightly less than the built-in voltage generated in the solar cell by the n- and p-layers [48].

The power extracted from an illuminated solar cell is equal to the extracted current multiplied by the load across the cell, and so is equal to zero under both short-circuit (zero load) and open-circuit (zero current) conditions. Between these two load conditions, both the extracted current from and the load across the solar cell are positive, and so useful power can be extracted. The point of maximal power extraction is known as the 'maximum power point', and is highly dependent on many of the material and device properties of the solar cell [48].

2.3 Metal-Halide Perovskites

2.3.1 Structure and Stoichiometry

While the term "perovskite" originally referred to a particular calcium titanium oxide mineral – $CaTiO_3$ – it is now often used in reference to any material with a similar, ABX_3 structure. The cubic perovskite crystal system is shown in Figure 2.1, with other common perovskite phases displaying orthorhombic and tetragonal crystal systems [53] depending on the perovskite composition and temperature. Whether or not a perovskite structure is formed is dependent on the radii of the constituent elements, a factor described by the Goldschmidt tolerance factor:

$$\text{Goldschmidt tolerance factor, } t = \frac{R_A + R_X}{\sqrt{2}(R_B + R_X)} \tag{2.6}$$

where R_A, R_B, and R_X refer to the radii of the A-, B-, and X-site components, respectively, of the perovskite material in a solid-sphere approximation. A Goldschmidt tolerance factor of $t = 1$ would indicate that the solid-sphere ions would stack perfectly into a cubic perovskite structure, and in reality a cubic perovskite structure is generally observed for materials with $0.9 \leq t \leq 1$ [54, 55]. As t increases or decreases outside of this range, lower-symmetry perovskite structures and eventually lower-dimensional perovskites [56, 57] or entirely non-perovskite structures are formed.

For photovoltaic and light-emitting applications, the choice of the A, B, and X components of the perovskite structure is somewhat limited, but still gives rise to a wide range of materials with differing properties. Importantly, MHPs are typically able to accommodate large amounts of disorder in their structure, allowing for multiple ionic species to occupy similar lattice sites in the perovskite crystal, and enabling a huge amount of stoichiometric engineering and adjustment [5, 43]. For the A-site cation, methylammonium molecular ions (MA^+, $CH_3NH_3^+$), formamidinium molecular ions (FA^+, $CH(NH_2)_2^+$), caesium ions (Cs^+), or a mixture thereof are typically used in perovskite solar

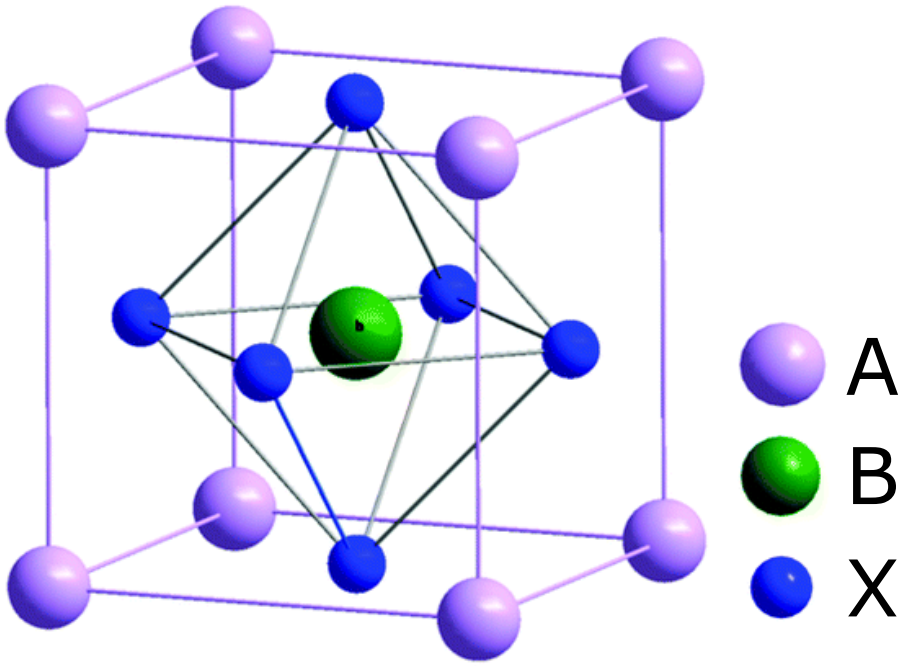

Figure 2.1: Unit cell of a cubic perovskite structure. The stoichiometric formula for a perovskite is ABX_3, where A is a cation with a 1+ charge, B is a cation with a 2+ charge, and X is an anion with a 1− charge. Adapted from Ref. [58] with permission from The Royal Society of Chemistry.

cells and LEDs [5, 34], although additional ions like rubidium (Rb^+) are also sometimes added [9, 21]. For the B-site cation, lead ions (Pb^{2+}) are by far the most commonly used, with tin ions (Sn^{2+}) or a lead-tin mix also sometimes incorporated into a perovskite structure [59]. The X-site anion typically consists of bromide ions (Br^-), iodide ions (I^-), or chloride ions (Cl^-), with various mixtures of the halide ions also commonly utilised [60]. Because the B-site cation is typically a metal ion, and the X-site anion is typically a halide ion, perovskite materials for photovoltaic or light-emitting applications are usually referred to as metal-halide perovskites (MHPs). The choice of ions incorporated into the perovskite structure has a strong influence on the structural, optoelectronic and stability properties of the resulting material [5, 43], and so investigating and exploring different perovskite compositions has been an integral part of perovskite photovoltaic research.

2.3.2 Optoelectronic Properties

Despite the common incorporation of an organic component into the perovskite crystal (MA^+ and/or FA^+ molecular ions), the charge-carrier dynamics in MHPs are well described by semiconductor band theory [61]. MHPs are generally reported to possess a direct bandgap [61], resulting in high measured absorption coefficients across the visible range. A high absorption coefficient is ideal for photovoltaic applications, as it allows for perovskite absorbing layers to be very thin – ∼500 nm thick – reducing the distance photoexcited charge carriers need to travel in order to exit the perovskite material into the associated electrical circuit, and helping to keep manufacturing costs low. The conduction and valence band energy states primarily form from the electronic orbitals of the B-site and X-site components of the perovskite structure, respectively [62], with the orbitals of the A-site component contributing to energy states away from the band edge [62]. As a result, the bandgap of the perovskite material can be controlled relatively easily and continuously by varying the composition of the B-site [63, 64] and X-site [17, 65] components. Furthermore, while the A-site cation does not directly influence energy states at the band edge, it does influence the perovskite structure, which itself is a factor in the formation of the energy levels within the perovskite [43, 62, 66]. Through stoichiometric engineering and other methods, perovskites with bandgaps ranging from ∼1.2 eV [63, 64, 67] to ∼3.0 eV [68–70] have been reported in the literature. Given that the maximum efficiency of a photovoltaic device is dependent on the bandgap of the absorbing layer(s), and the emission wavelength of an LED is dictated by the bandgap of the emitting layer, the existence of a method of continuous control over the bandgap of a perovskite material makes MHPs extremely viable for a huge range of optoelectronic applications. These applications include: single absorbing layer photovoltaic devices [7] (for which the ideal bandgap is around 1.1-1.4 eV [71]); double layer (tandem), perovskite-perovskite photovoltaic devices [72–76] (for which the ideal bandgaps of the two composite layers

are ∼0.9-1.2 eV and ∼1.6-1.8 eV [71]); an absorbing layer in perovskite-silicon tandem solar cells [8, 9] (for which the ideal perovskite bandgap is ∼1.7 eV [77]); and LEDs with emission almost anywhere in the visible range [34, 68–70, 78–82] (the visible range corresponds to energies of around 1.7 eV to 3.3 eV).

Alongside a direct, tunable bandgap, perovskites also possess remarkably good charge-carrier transport properties [61, 83], especially considering the solution-processing techniques used in their manufacture. While the ionic freedom and low energetic barriers for ionic movement generate a large number of defects within the perovskite crystal, the high quality of measured charge-carrier transport properties [83] – and the high reported perovskite solar cell power conversion efficiencies [7] – suggest that the trap states generated by these crystal defects are somewhat benign. The general nature of these trap states, and how they relate to the charge-carrier dynamics in the perovskite material, is somewhat debated, with some reports suggesting that the electronic charge associated with any interstitial ion or ionic vacancy defects will likely cancel with the charge of the trapped charge carrier, screening the filled trap state from any additional charge carriers and thus leading to a low rate of non-radiative recombination [84]. Other reports suggest that most trap states are generated close to the conduction and valence bands, and not often deep within the bandgap where they would significantly contribute to non-radiative losses [85]. Regardless of the exact reason, the benignity of the trap states within perovskite materials results in exceptional charge-carrier diffusion lengths, which are often reported to be greater than 1 µm [83, 86, 87]. These large charge-carrier diffusion lengths, coupled with the thinness of perovskite absorbing layers (∼500 nm), results in the facile charge-carrier transport to the electron and hole extraction layers in a photovoltaic device architecture, and thus highly efficient perovskite-based solar cells [7].

Figures 2.2 and 2.3 present example data from the literature on $MAPbI_3$, a perovskite material that exemplifies the points made so far in this section on the general properties

of perovskites. Figure 2.2 presents the band structure of $MAPbI_3$ calculated from density functional theory [88], highlighting the direct bandgap of the material at the centre of the Brillouin zone (the Γ point). This direct bandgap results in a very strong absorption onset in $MAPbI_3$, with example absorption coefficient data for this material presented in Figure 2.3 over a range of temperatures [89]. At low temperatures, Figure 2.3 shows that $MAPbI_3$ exhibits a strong absorption feature just below the band edge resulting from excitons (bound electron-hole states), with the absorption feature centred around 1.6-1.65 eV depending on the temperature of the perovskite. At higher temperatures this exciton absorption peak is suppressed, as the increased thermal energy of the perovskite allows for photogenerated excitons to easily dissociated into free electrons and holes. Also visible in Figure 2.3 is a sharp transition of the absorption data at around 160 K, due to a phase transition of the $MAPbI_3$ perovskite from an orthorhombic to tetragonal structure [53, 89].

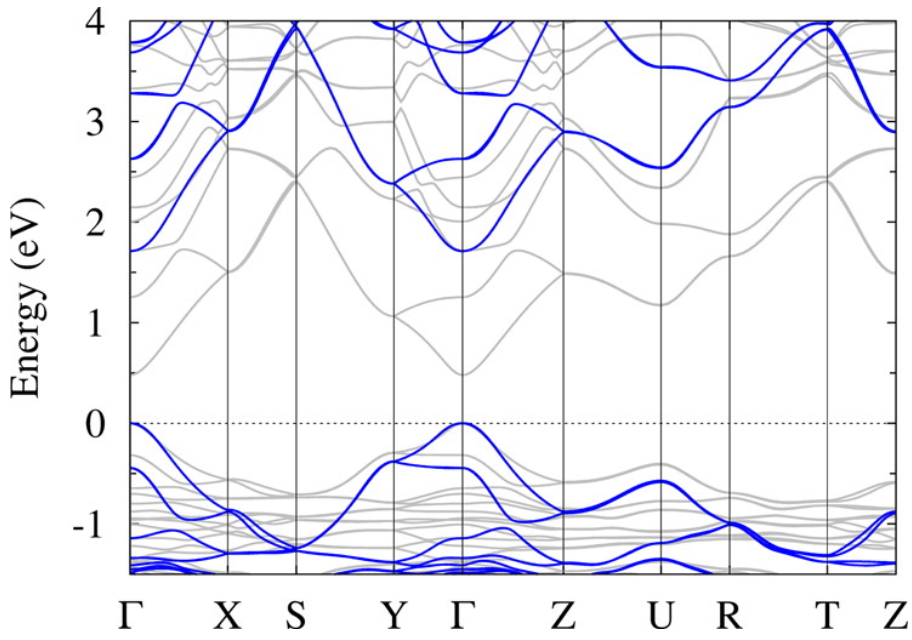

Figure 2.2: Theoretically-predicted band structure of $MAPbI_3$ obtained from density functional theory incorporating spin-orbit coupling effects (grey) and additionally including a self-consistent correction as reported in [90] (blue), for various high-symmetry positions of the perovskite unit cell. Reprinted with permission from Ref. [88]. Copyright 2015, American Chemical Society.

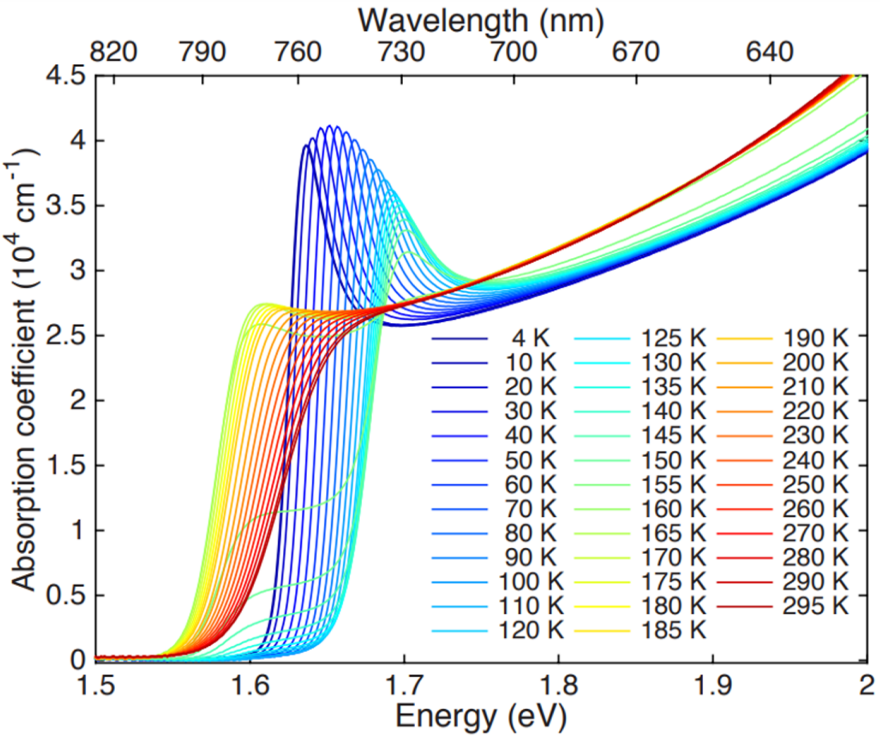

Figure 2.3: Absorption coefficient of $MAPbI_3$ taken at a range of temperatures from 4-295 K. A strong absorption onset is observed around 1.6 eV, depending on the temperature of the perovskite, and a sudden change in the absorption of the perovskite is caused by a phase transition from orthorhombic to tetragonal structures at ∼160 K [53, 89]. Reproduced with permission from Ref. [89] under a Creative Commons Attribution 4.0 International License.

2.4 Halide Segregation

Work presented in this section was initially published as Ref. [18] – reproduced by permission of The Royal Society of Chemistry.

2.4.1 Introduction

The biggest challenge currently facing the commercialisation of perovskite-based devices is the instability of the perovskite itself [47, 91], especially when continuously exposed to oxygen [11–13], humidity [14–16], or light [17]. Specifically for mixed-halide perovskites, a peculiar process referred to as "halide segregation" [17] has been found to be a major source of instability. Here, exposure to above-bandgap illumination or charge-carrier injection results in a loss of phase-stability and the separation of halide ions of different

type, causing the formation of inclusions of lower and higher bandgap perovskite with a different halide composition to the remaining well-mixed perovskite phase [17]. The formation of a spatially inhomogeneous bandgap under illumination or current injection seriously limits the prospects of mixed-halide perovskites for tandem solar cell and tunable LED applications. Fortunately, several reports in the literature have elucidated methods by which halide segregation may be mitigated in mixed-halide perovskite materials, and it is the focus of this chapter to review and summarise these approaches and what they reveal about the halide segregation mechanism.

While X-ray diffraction (XRD) [17, 92] and absorption measurements [93–97] often suggest that only a small fraction of the perovskite actually participates in halide segregation under illumination (estimates go as low as ∼1% [22]), photoluminescence (PL) measurements [17] and the performance of photovoltaic devices [20–23] are disproportionately affected. Such exacerbation of deleterious effects results from the funnelling and concentration of charge carriers into the phase-segregated regions of perovskite which exhibit a lower bandgap than the rest of the material. The PL emitted from the halide-segregated material therefore typically displays a strong redshift and increased intensity, making halide segregation easily detectable through PL even for a low concentration of afflicted regions [17]. Most puzzling, however, is that the segregation of halide ions does not persist once the perovskite is shielded from the illumination, with the material eventually returning to its pre-illumination state under darkness [17]. It is now widely thought that excited charge carriers drive the segregation process, given that halide segregation has been observed in perovskite materials subjected to charge-carrier injection even in the absence of light [20, 21, 78–80]. It is further believed that entropic mixing drives the recovery to the pristine state upon the removal of the excitation source [96, 98]. However, despite the large amount of research into the halide segregation phenomenon,

many facets of the process are still debated in the literature and many questions remain as to the underlying fundamental mechanisms that drive the process.

In this section, the discussion is principally based on the empirical evidence reported in the literature on how both internal properties of the perovskite and external conditions affect the extent to which segregation of the halide ions is induced. This empirical evidence is primarily evaluated here in regards to its potential of preventing halide segregation in commercial, mixed-halide perovskite solar cells, as this is the ultimate goal of research into the halide segregation mechanism. The theoretical explanations presented so far in the literature are numerous, varied, and largely inconsistent with each other, indicating significant scope for future work in this area. As such, theoretical explanations are presented appropriately in this section to supplement the empirical evidence being discussed, but the focus of the discussion remains on experimental data reported in the literature. In particular, three easily implemented methods with strong impact on the stability of the material against halide segregation are highlighted, which are: changing the stoichiometry of the A-site cation in the perovskite structure, improving the perovskite crystallinity, and reducing the trap state density within the perovskite. To a lesser extent, a reduction in the density of halide vacancies in the perovskite structure has also been shown to mitigate halide segregation. Other methods that have proven promising, but require further research, are identified as: changing the stoichiometry of the B-site cation, altering the incident illumination, and changing the perovskite temperature. Alterations in the perovskite crystallographic structure could also theoretically help to mitigate halide segregation but are difficult to achieve practically without affecting other properties of the perovskite material. Structuring of the perovskite into relatively insulated, nanocrystalline domains does appear to mitigate halide segregation under certain conditions, but also reduces the optoelectronic performance of devices made from such perovskite materials. Unfortunately, achieving the necessary balance between

suppressing ion migration and maintaining good electronic conductivity appears to be extremely difficult in such nanocrystalline materials. Utilising a Br/Cl ionic mixture on the X-sites of the perovskite structure and changing the atmospheric environment of the perovskite are concluded to be insignificant and/or impractical methods to mitigate halide segregation. Overall, the breadth of these investigations highlights the impressive quantity and potential of factors available to mitigate halide segregation and indicates the future scope of research to be done in this area. It is concluded that in order for halide segregation to be completely prevented in working photovoltaic devices and LEDs, a combination of stoichiometric engineering, crystallinity control, and trap state passivation will have to be implemented, which conveniently comprise a set of factors already being investigated in the pursuit of high device efficiencies.

2.4.2 Stoichiometric Engineering

This review into the literature on halide segregation commences by exploring how stoichiometric tailoring within the ABX_3 structure affects the propensity of a metal halide perovskite towards halide segregation on the X-sites. In this context, it is important to consider that any changes to the constituents of the A-, B- and X-sites may also affect the optoelectronic properties of the resulting perovskite material, which limits the extent to which ingredients may be independently tuned to limit halide segregation. In particular, the composition of the ions on the B- and X-sites in the perovskite structure directly influence the electronic energy states in the conduction and valence bands, respectively [43, 62, 99], and so altering these components tunes the bandgap energy. Changing the A-component does not directly affect the electronic energy states at the band edge, but can have an indirect influence on the bandgap energy by altering the degree of octahedral distortions or inducing other structural changes [62].

In the following, changes in the A-cation, metal B-cation and halide X-anion are discussed in turn in regards to affecting the phase-stability of the material against halide segregation. In order to establish a reference point, findings for particular compositions are generally compared against those for the archetypal perovskite $MAPb(Br_xI_{(1-x)})_3$ ($MA = CH_3NH_3^+$) which has been examined repeatedly in halide segregation studies and is observed to segregate for halide ratios $0.2 < x < 1$ [17, 95, 100–105]. Because most early reports on perovskite solar cells were based on methylammonium-lead perovskites [106–109], studies of bandgap tunability across the UV, visible, and near IR also initially centred around $MAPb(Br_xCl_{(1-x)})_3$ [68, 110, 111] and $MAPb(Br_xI_{(1-x)})_3$ [17, 65, 112, 113]. Here, the latter Br/I perovskite is of particular interest, as it offers bandgaps near 1.7 eV, the target for efficient two-terminal tandem solar cells with silicon [77, 114]. Below, the stability of $MAPb(Br_xI_{(1-x)})_3$ is compared against that of other metal halide perovskites with various ions or ionic mixtures incorporated onto the A-, B- and X-sites, and stoichiometric engineering is highlighted as a method to mitigate halide segregation in a perovskite material.

2.4.2.1 A-site Cation Variation

Other than methylammonium (MA, $CH_3NH_3^+$), the A-site cations typically implemented in metal halide perovskites for photovoltaic devices and LEDs are formamidinium (FA, $CH(NH_2)_2^+$), and caesium (Cs^+). Halide segregation has been observed in metal halide perovskite materials for a wide range of different ions and ionic mixtures incorporated onto the A-sites of the perovskite structure [9, 17, 102, 115–118]. However, different perovskite compositions require different timescales and excited charge-carrier densities for the effects of halide segregation to emerge, and thus represent materials of different phase-stability. In particular, FA/Cs and FA/MA/Cs metal halide perovskites are observed to be significantly more resistant against halide segregation than other perovskites, e.g.

those with only MA on the A-cation sites. Below the phase-stability of perovskites is discussed as the composition of the A-site cation increases in complexity from neat MA, FA or Cs through to triple- and quadruple-cation perovskites.

While $MAPb(Br_xI_{(1-x)})_3$ has been found to segregate for bromide contents $0.2 < x < 1$ [17, 95, 100–105], its neat FA and Cs counterparts exhibit comparable halide segregation only within the narrower approximate compositional ranges $0.55 < x < 0.9$ [17, 115] and $0.4 < x < 1$ [79, 96, 116, 119], respectively, thus presenting slightly improved stability ranges. Significant halide segregation has also been reported for perovskites with a mixture of MA and Cs incorporated into the perovskite lattice, specifically for compositions $Cs_{0.6}MA_{0.4}Pb(Br_xI_{(1-x)})_3$ $(0.4 < x < 0.8)$ [102] and $Cs_{0.1}MA_{0.9}Pb(Br_{0.4}I_{0.6})_3$ [20]. However Bischak *et al.* reported that the effects of halide segregation diminished in their $MAPb(Br_{0.86}I_{0.14})_3$ perovskite microcrystals when an MA-to-Cs cation exchange reaction was utilised to change the stoichiometry of the microcrystals to $Cs_{0.39}MA_{0.61}Pb(Br_{0.85}I_{0.15})_3$, suggesting that some MA/Cs perovskite materials could potentially be more phase-stable than their equivalent MA-only compositions [120].

Considerable success for mitigating halide segregation was demonstrated early on by McMeekin *et al.*, who showed that for certain mixtures of FA/Cs, the material stability against halide segregation was much enhanced compared to that of the equivalent FA-only lead halide perovskites, across the entire bromide to iodide compositional range [66]. Rehman *et al.* followed on from this work by investigating the photo-stability of FA/Cs perovskites as the ratio of FA to Cs is altered, and concluded that a 20% Cs fraction on the A-cation site is close to ideal for minimal halide segregation; see Figure 2.4 [117]. Braly *et al.* showed that while FA/Cs perovskites are much more stable against halide segregation than their MA or MA/Cs counterparts, and could withstand 1 sun intensity illumination with no detectable halide segregation, a PL redshift was still observed in the emission from their $Cs_{0.17}FA_{0.83}Pb(Br_{0.34}I_{0.66})_3$ films when exposed to high illumination intensities (∼32

sun) [20]. Sutter-Fella *et al.* observed halide segregation in their $Cs_{0.17}FA_{0.83}Pb(Br_xI_{(1-x)})_3$ films under 50 mW cm^{-2} (∼0.5 sun) illumination for compositions x=0.5 and x=0.6, but not for x <0.5, a smaller compositional region of instability than that of $MAPb(Br_xI_{(1-x)})_3$ [121]. Similarly, Zhou *et al.* reported on $Cs_{0.17}FA_{0.83}Pb(Br_xI_{(1-x)})_3$ films that were observed to be photostable over the course of minutes under 150 mW cm^{-2} (∼1.5 sun) illumination for composition x=0.27, but underwent halide segregation for compositions x=0.4, 0.5, and 0.6 under similar conditions [122].

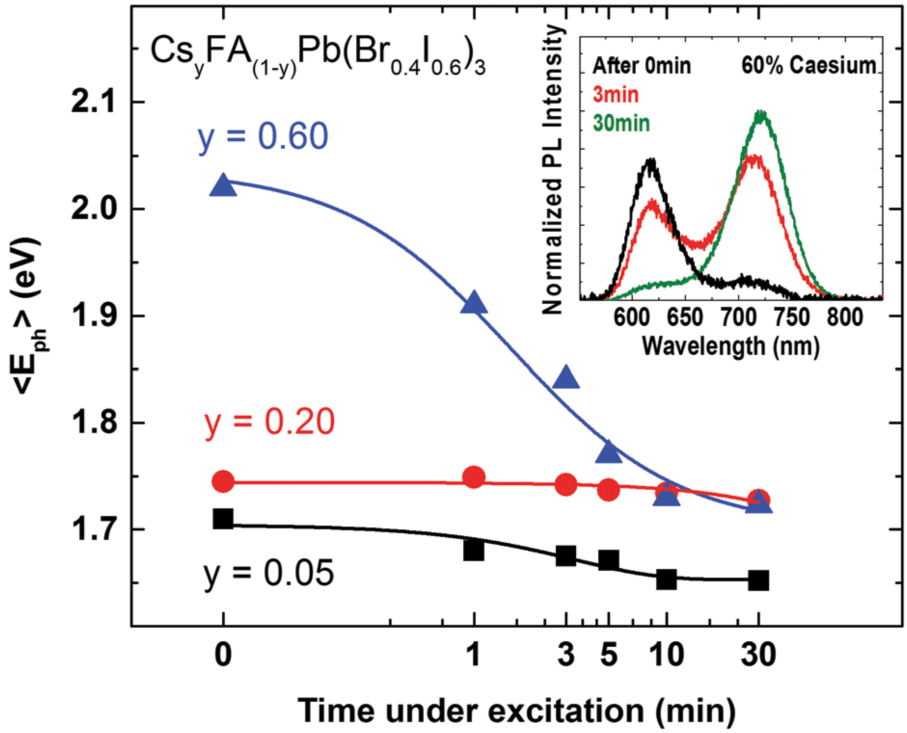

Figure 2.4: Work by Rehman *et al.* highlighting how changes of the FA/Cs ratio on the A-cation sites of a lead halide perovskite affects the rate of halide segregation under illumination [117]. The main figure plots the average PL photon energy $<E_{ph}>$ over time for $Cs_yFA_{(1-y)}Pb(Br_{0.4}I_{0.6})_3$ perovskite films with y=0.05, y=0.2, and y=0.6 under 100 mW cm^{-2} (∼1 sun), 400 nm illumination. For 20% Cs little energetic shift is observed, suggesting negligible halide segregation. The inset shows the spectral evolution of the PL emitted by the y=0.6 sample. Ref. [117] – Published by The Royal Society of Chemistry.

Triple-cation perovskites, with a mixture of Cs, MA, and FA incorporated onto the A-sites of the perovskite structure, have proven to be the most promising to date in terms of stability against halide segregation. While halide segregation is still observed in these triple-cation materials, the timescales and photon doses required to cause significant halide

ion redistribution are often much greater than those needed to cause equivalent segregation in single- or double-cation perovskites [118, 123, 124]. In particular, Andaji-Garmaroudi *et al.* noted that the segregation process in their $(Cs_{0.06}MA_{0.15}FA_{0.79})Pb(Br_xI_{(1-x)})_3$ perovskite films took 30 min to approach equilibrium, and a photon dose three orders of magnitude higher than that required to segregate typical $MAPb(Br_xI_{(1-x)})_3$ films [118]. Duong *et al.* investigated the nature of halide segregation in quadruple-cation, $Rb_{0.05}(Cs_{0.1}MA_{0.15}FA_{0.75})_{0.95}Pb(Br_{0.33}I_{0.67})_3$ perovskite films, in which the characteristic redshift of PL was observed over the course of 12 h under 2 sun illumination [21], again suggesting a significant improvement in photo-stability over typical $MAPb(Br_xI_{(1-x)})_3$ films which may segregate over the course of seconds to minutes under illumination intensities of 1 sun or lower [17].

While engineering the composition of the A-site cation in the mixed-halide perovskite crystal presents perhaps the most promising method in which to completely prevent, or at least slow the progression of, halide segregation in working perovskite solar cells and LEDs, the reason for the changes in photo-stability is still a matter of debate. One explanation proposed is that the composition of the A-site cation is strongly linked to the crystallinity and quality of the resulting perovskite film [20, 66, 117, 125], and therefore the choice of A-site cation has a large influence on a number of factors that could possibly be integral to halide segregation (perovskite crystallite size, trap state density, grain boundaries, halide vacancies, etc., as discussed further below). For example, by investigating $MA_yFA_{(1-y)}Pb(Br_{0.4}I_{0.6})_3$ perovskite films as the ratio of MA to FA was tuned, Xie *et al.* were able to correlate the composition of the A-site cation with both the crystallinity of the resulting film and with the photostability of the perovskite against halide segregation [125]. Alternatively, Bischak *et al.* have suggested that polaronic interactions (interactions between excited charge carriers and the ionic perovskite lattice) are both the driving factor behind halide segregation, and are affected by the composition

of the A-site cation in the perovskite crystal [104, 120]. A detailed investigation of the links between A-site cation composition and phase-stability is conducted in Chapter 6, where it is concluded that the halide ion pathways within and the crystallinity of the perovskite are strongly affected by its stoichiometry, which then determine the corresponding halide segregation dynamics. Regardless of the underlying cause, given the observed strong influence of the A-site cation on the photostability of the perovskite, engineering the perovskite stoichiometry is clearly an important tool for eliminating halide segregation from metal halide perovskite materials.

2.4.2.2 B-site Cation Variation

While lead-based perovskites are the most commonly investigated metal halide perovskites for optoelectronic applications, variants incorporating tin onto the B-sites have also been explored. Tin-based perovskites are of interest since tin has a lower toxicity than lead, and mixed tin-lead iodide perovskites offer bandgap tunability in the near-IR spectral range [59, 63, 64, 73, 76, 126–133]. With regards to halide segregation, partially replacing lead with tin in the perovskite structure has been reported to have a beneficial effect on the stability of the material, however the amount of research on the subject is unfortunately still limited. Yang *et al.* reported that a photovoltaic device incorporating $MAPb_{0.75}Sn_{0.25}(Br_xI_{(1-x)})_3$ exhibited, in comparison with an $MAPb(Br_{0.4}I_{0.6})_3$ device, much less change in measured photocurrents, transient absorption spectra, and XRD patterns [133] over tens of minutes under 1 sun illumination. The stability of the 25% tin composition was attributed to reduced levels of halide segregation resulting from the different properties of the tin-halide as compared to the lead-halide bond. Unfortunately, because the PL quantum efficiency of the tin-based device was too low a PL spectrum could not be acquired over an illumination period of 90 min under 1 sun, and it was therefore impossible to confirm the extent to which halide segregation had actually taken

place in the tin-containing films from PL measurements. In another study, Li *et al.* were able to acquire PL from their $CsPb_{0.75}Sn_{0.25}(Br_{0.67}I_{0.33})_3$ perovskite (25% tin) films and observed no redshift in the emitted PL when the sample was held under illumination (at an unspecified intensity) for 15 min, suggesting phase stability against halide segregation [134]. Under similar conditions, a small peak was observed to emerge below the bandgap energy in the PL spectrum emitted from the $CsPb(Br_{0.67}I_{0.33})_3$ lead-only perovskite counterpart, suggesting that the replacement of lead with 25% tin had improved the photostability of the perovskite, in agreement with the conclusions of Yang *et al.* [134].

While incipient studies suggest that tin incorporation has a beneficial effect on the stability of a perovskite material against halide segregation [133, 134], it is noted that other studies have reported difficulties in forming tin-based perovskite samples with good crystallinity [135–138], at least for certain lead-tin compositions. Given that crystallinity has a large impact on the stability of a perovskite material against halide segregation (see Section 2.4.3.1 below), it is likely that the effects of tin incorporation on halide segregation are more multi-faceted than existing reports suggest. Thus it is recommended that further research should be performed on the topic of halide segregation in tin-based perovskite materials before definite conclusions are drawn on the subject.

Overall, while additional studies on the effect of B-metal substitution on halide segregation would be highly useful, incipient investigations suggest that partially replacing lead with tin has a beneficial effect. The stability considerations of hybrid lead-tin perovskites are especially important for perovskite-perovskite tandem solar cell applications, where the wide tunability of lead-tin, iodide-bromide perovskite systems allows for the stacking of multiple layers with carefully tuned bandgaps to yield matched photocurrents in double- or triple-junction cells [72–74, 76].

2.4.2.3 X-site Anion Variation

As already mentioned above, the halide composition on the X-sites of metal halide perovskites has a strong impact on their propensity towards halide segregation, with compositions in the central range (i.e. around 50% iodide : 50% bromide) being particularly prone to segregation, and majority-iodide perovskites generally reported as more stable than majority-bromide [17, 116]. Therefore, one obvious method by which halide segregation may be prevented is to push the halide ratio into a stable region of the compositional space, which unfortunately limits the range of bandgaps achievable. However, Bush *et al.* demonstrated that by carefully tuning both the ratio of Cs to FA on the A-site cation sites and the Br to I ratio on the X-site cation sites, many compositions of perovskite could be fabricated with a given target bandgap, but with differing stability properties [99]. In particular, devices with perovskite compositions of $Cs_{0.25}FA_{0.75}Pb(Br_{0.2}I_{0.8})_3$ and $Cs_{0.4}FA_{0.6}Pb(Br_{0.3}I_{0.7})_3$ were fabricated with bandgaps measured at 1.68 eV and 1.75 eV respectively, and were found to be stable against halide segregation when illuminated for 10 min under 10 sun illumination intensity. In contrast, perovskite films with similar bandgaps but higher bromide contents were found to be unstable under 10 min of 0.1 sun illumination. Such careful tuning highlights the key role that stoichiometric engineering will play in controlling the photostability of mixed-halide perovskite photovoltaic devices and LEDs [99].

While mixed bromide-iodide perovskites offer particularly attractive bandgaps for tandem solar cell applications, combining chloride and bromide has been shown to tune the bandgap (alongside quantum confinement effects in nanocrystals) in the UV-visible region of 400-570 nm, making these materials suitable for blue-green LEDs [68–70, 78, 80]. However, some conflicting reports still exist in the literature as to the extent of halide segregation in bromide-chloride lead perovskites. Sadhanala *et al.* reported on an $MAPb(Br_{0.4}Cl_{0.6})_3$ perovskite material with stable PL emission under white light

illumination of 1 sun intensity for 10 min, suggesting that minimal halide segregation had occurred [68]. However, multiple alternative studies have instead reported apparent halide segregation for similar bromide/chloride perovskites, such as $MAPb(Br_{0.5}Cl_{0.5})_3$ [104, 139], and $CsPb(Br_xCl_{(1-x)})_3$ for the range $0.3 < x < 0.83$ [69, 78, 80, 140–143], suggesting that the halide segregation mechanism is not limited to mixed bromide-iodide systems, but can be found in bromide-chloride systems as well.

2.4.2.4 Conclusions on Stoichiometric Effects

In conclusion, engineering the A-site cations in the perovskite structure seems to be a powerful method for mitigating halide segregation. Triple A-cation perovskites, with Cs, MA, and FA incorporated into the perovskite structure, are observed to be particularly stable [118, 123, 124], as are quadruple A-cation perovskites which additionally include Rb ions [9]. Altering the composition of the B-site ions from Pb to a $Pb_{0.75}Sn_{0.25}$ mixture has also shown a promising increase in photostability [133, 134], however further research is required to fully explore the possibility of photostable lead-tin perovskites, and the compositional lead-tin range over which this may apply. Finally, replacing all iodide at the X-anion sites with chloride does not appear to significantly improve the stability of the perovskite against halide segregation [68, 69, 78, 80, 139–143]. Careful tuning of the overall stoichiometric space therefore emerges as a powerful tool towards suppression of halide segregation for a given target bandgap.

2.4.3 Crystallinity Control

2.4.3.1 Increased Crystallinity

There is a compelling body of literature evidence that metal halide perovskite films with better crystallinity (i.e. films with a larger average crystal grain size) are more stable against halide segregation [20, 103, 117, 122, 125]. Analysis of comparable perovskite films made via slightly different processing methods has revealed a clear impact of crystalline

quality on the propensity of the material to commence halide segregation under illumination. In one such study, Hu *et al.* showed that deposition of $MAPb(Br_{0.27}I_{0.73})_3$ perovskite films on a non-wetting, poly[bis(4-phenyl)(2,4,6-trimethylphenyl)amine] (PTAA) surface yielded larger grain size and improved photostability than those of films deposited on a poly(3,4-ethylenedioxythiophene) polystyrene sulfonate (PEDOT:PSS) surface [103]. Depositing a thicker perovskite layer on PTAA, on the other hand, reduced the beneficial effect of the non-wetting surface, resulting in the growth of smaller perovskite crystal grains, which again led to faster halide segregation [103]. In another study, Braly *et al.* examined photovoltaic devices incorporating $FA_{0.83}Cs_{0.17}Pb(Br_{0.34}I_{0.66})_3$ and found that a perovskite annealing step of 165 °C for 50 min resulted in much improved crystallinity and photostability as compared to an annealing step of 75 °C for 10 min [20]. Zhou *et al.* demonstrated that the addition of small amounts of $(CsI)_{0.17}(FAI)_{0.83}[Pb(SCN)_2{+}3FAI]_{(1-1.5x)}[Pb(SCN)_2{+}3FABr]_{1.5x}$ to their $Cs_{0.17}FA_{0.83}Pb(Br_xI_{(1-x)})_3$ perovskite precursor solution prior to spincoating resulted in larger crystal grains and improved photostability of the resulting perovskite films [122]. However, Zhou *et al.* also proposed that the additive passivated trap states and altered the nature of the grain boundaries in the perovskite films, leaving unclear whether the larger perovskite crystal grains themselves resulted in the improved photostability [122]. Rehman *et al.* investigated correlations between crystallinity and photostability in $Cs_yFA_{(1-y)}Pb(Br_{0.4}I_{0.6})_3$ perovskite films as a function of caesium content, y, for the range between 0 and 0.6. This study clearly demonstrated that good material crystallinity (indicated by the width of X-ray diffraction peaks and the charge-carrier mobilities and lifetimes) led to improved photostability against halide segregation [117]. The evidence in the literature therefore either directly or indirectly points to perovskite film crystallinity being a critical factor in controlling and preventing halide segregation.

The exact reason why a larger grain size is correlated with greater photostability of mixed-halide perovskites is still a matter of debate. However, films with larger crystal grains necessarily have a lower grain boundary density, and several groups have reported low-bandgap domains forming during halide segregation to be clustered around grain boundaries, e.g. in $MAPb(Br_xI_{(1-x)})_3$ [104, 144] and $CsPb(Br_xI_{(1-x)})_3$ [119] perovskite films. In particular, Tang *et al.* [144] and Li *et al.* [119] only observed halide segregation to occur at the grain boundaries of $MAPb(Br_{0.3}I_{0.7})_3$ and $CsPb(Br_{0.67}I_{0.33})_3$ films, respectively, while PL spectra taken from the grain centres were stable, suggesting that grain surfaces are integral for the halide segregation mechanism – see Figure 2.5. These findings show that an improvement in the crystallinity of a perovskite film reduces the density of grain boundaries, which may in turn offer fewer nucleation points for the formation of halide-segregated regions, or reduce the efficacy of the segregation mechanism. There are several reasons why grain boundaries may induce halide segregation in mixed-halide perovskites. First, ionic motion has been reported to be particularly fast along grain boundaries in single-halide [145–148] and multi-halide [149] perovskites, which may suggest that halide segregation is particularly effective at grain boundaries because of the increased mobility of the halide ions in these regions. Second, trap state density has also been correlated with halide segregation [119, 144, 150–152], as discussed in more detail in Section 2.4.4 below. Therefore, while the exact nature of trap states located at grain boundaries is still being debated [84, 85], grain boundaries in the perovskite film may associate with halide segregation by simply being locations that contain a high density of traps. Finally, grain boundaries may be areas that relieve lattice strain caused by the ion redistribution inherent in the halide segregation process, thereby reducing the energetic barrier to the segregation of the halide ions [117, 121]. Through this mechanism, perovskite films with better crystallinity and lower grain boundary density would be less accommodating to halide segregation and would therefore be more stable.

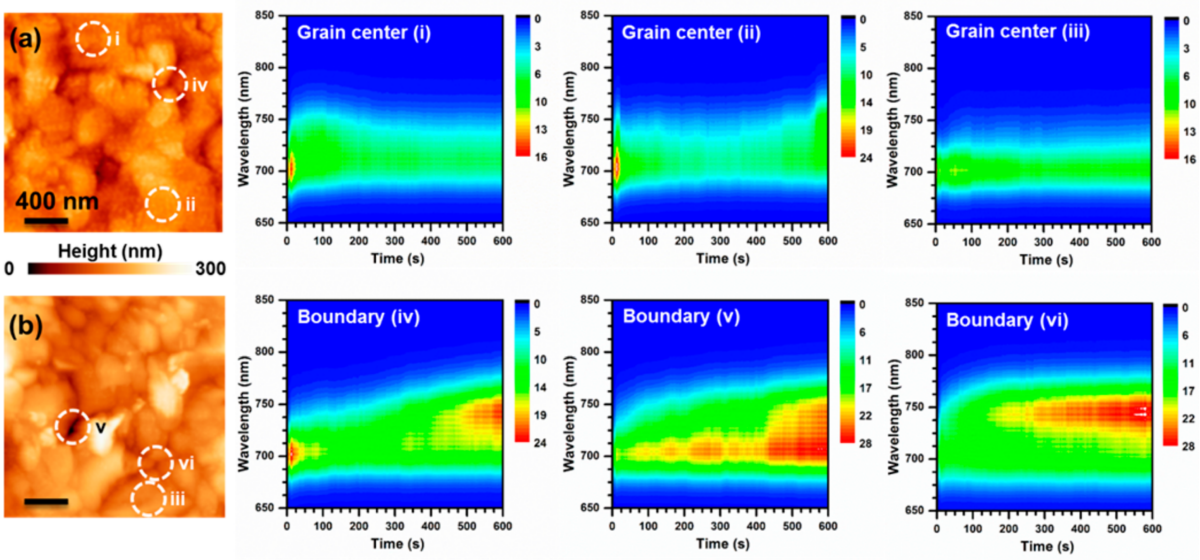

Figure 2.5: Work by Tang *et al.* highlighting how stability against halide segregation differs between the grain centres and boundaries of an $MAPb(Br_{0.3}I_{0.7})_3$ perovskite thin film [144]. (a) and (b): Topography of the film, with regions of interest circled as grain centres (regions i-iii) or grain boundaries (iv-vi). Plotted is the emitted PL from each region while individually illuminated under 500 000 mW cm^{-2} (∼5000 sun), 636 nm illumination for 10 min. Only the PL emitted from the grain boundaries shows signs that halide segregation is occurring, through the emergence of redshifted features. Reprinted with permission from Ref. [144]. Copyright 2018, American Chemical Society.

From the above considerations, it would at first appear that single crystals of mixed-halide perovskite represent ideal environments in which to study how grain boundaries (or the lack thereof) affects halide segregation. However, it is important to note that single crystals have surfaces that have been reported to be highly defective [153] and that techniques used to study halide segregation are often extremely surface-sensitive. It is therefore perhaps not surprising that literature reports on halide segregation in perovskite microplatelets and macro-sized single crystals are largely inconsistent. While it is generally agreed upon that halide segregation can occur in both $MAPb(Br_xI_{(1-x)})_3$ [17, 120, 154, 155] and $CsPb(Br_xI_{(1-x)})_3$ [152] mixed-halide perovskite microplatelets (single crystals with dimensions of the order of micrometres to tens of micrometres), there is disagreement on the locations where segregation occurs. While some reports have suggested that under illumination, iodide-rich perovskite domains form almost exclusively

at the microplatelet surfaces [155], others conclude conversely that the iodide-rich domains can form anywhere within the microplatelet crystals [120, 154]. For truly macro-sized single crystals, there are still only a few reports on the occurrence of halide segregation, and these are, unfortunately, also somewhat contradictory. Tang *et al.* presented PL spectra taken from millimetre-sized $MAPb(Br_{0.3}I_{0.7})_3$ single crystals that showed no signs of an emission shift over the course of minutes under 100 mW cm^{-2} (∼1 sun) illumination [144], suggesting the absence of halide segregation. Conversely, Byun *et al.* observed significant halide segregation in their millimetre-sized, bromide-rich, $MAPb(Br_xI_{(1-x)})_3$ perovskite single crystals over tens of minutes, albeit under a significant illumination intensity of 50 000 mW cm^{-2} (∼500 sun) [156]. In general, it is therefore difficult for solid conclusions to be drawn from the literature on the extent to which halide segregation is suppressed in perovskite single crystals, and it is noted that there remains significant scope for further research to be carried out on this subject.

In summary, literature reports highlight the crystallinity of the perovskite as a key parameter for the mitigation of halide segregation, with an increasing body of evidence suggesting that grain boundaries are important, or even integral, to triggering segregation [119, 123, 144, 155]. However, major questions remain as to the mechanism linking grain boundaries to halide segregation. Possible explanations are that grain boundaries represent regions of high ionic mobility [145–149], that the lattice strain induced by the segregation of halide ions can be relieved at grain boundaries [117, 121], and that grain boundaries represent regions of high trap density, which is itself linked to halide segregation [119, 144, 150–152, 157] (see Section 2.4.4 below). Regardless of the underlying mechanism, the management of grain boundaries through the crystallinity of perovskite thin films represents a critical control factor over halide segregation for device manufacturers.

2.4.3.2 Nanocrystalline Films

Interestingly, a number of research studies have suggested that the photostability of mixed-halide perovskite films composed of nanocrystals is much improved compared to that of standard bulk polycrystalline materials [96, 102, 158, 159]. Such apparent suppression of halide segregation in nanocrystalline materials is surprising at first, given that the previous sections detailed how a propensity for halide segregation normally correlates with low levels of crystallinity. However, the Kuno group proposed that the reduction of halide segregation in nanocrystal films derives from the suppression of charge-carrier diffusion [96]. Restricting the spatial freedom of excited charge carriers makes it less likely for them to channel into the forming low bandgap regions of the perovskite, where they may stabilise such regions or increase their size [96] – see Figure 2.6. Such a mechanism is thus specific to the nature of films made directly from solution pre-cursors which contain small perovskite nanocrystals. For this preparation method, nanocrystals are usually decorated with surface ligands that confer solubility and passivate surface states. Upon casting of a nanocrystalline film, surface ligands initially remain, unless a ligand exchange reaction is successfully carried out and/or the film is sintered leading to the fusion of nanocrystals into a nanoporous but relatively continuous perovskite solid [160–164]. Nanocrystalline perovskite films may therefore differ substantially by the extent to which insulating material between individual crystals limits both the movement of ions and excited charge carriers [165]. The restriction of ionic and charge-carrier movement in nanocrystalline films is in contrast to normal polycrystalline perovskite films in which grain boundaries typically do not obstruct carrier motion significantly. Therefore, the degree to which halide segregation in such nanocrystalline films can be suppressed may also vary widely depending on film treatments following the casting from nanocrystal solutions [96, 158].

In particular, it is noted that nanocrystalline films fabricated with suppressed halide segregation in mind, and therefore hindered charge-carrier migration between perovskite

domains, may not be ideal for optoelectronic device applications whose efficiency relies on excellent long-range charge-carrier transport across the film. Perovskite nanocrystalline films are commonly utilised for LED applications [34, 68–70, 78–82], whose emission colour can be easily tuned either through the nanocrystal size, or the chemical composition of the perovskite [34, 68–70, 78–82], and some nanocrystalline films have also been utilised in photovoltaic devices [161, 162]. While some level of insulation between adjacent nanocrystals in thin films leads to stability improvements and better quantum confinement control over the emitted PL wavelength, sufficiently long range charge-carrier transport is still essential. Therefore, the below examination of the literature concludes that while limiting the spatial freedom of excited charge carriers in mixed-halide perovskite materials does indeed inhibit halide segregation in thin nanocrystal films, this strategy cannot by design be applied to high performance perovskite optoelectronic devices.

To elucidate the reasons for the reported [96, 102, 158, 159] suppression of halide segregation in nanocrystal films, the Kuno group suggested the concomitant reduction in charge-carrier diffusion lengths as the cause [96, 166], given that the accumulation of photoexcited charge carriers in low-gap regions has been blamed for perpetuating halide segregation [20, 21, 104, 120]. In this study, Draguta *et al.* fabricated separate $CsPb(Br_{0.5}I_{0.5})_3$ thin bulk polycrystalline films and nanocrystal films (nanocrystal dimensions ∼10 nm), with the bulk polycrystalline films displaying signs of halide segregation when held under 60 mW cm^{-2} (∼0.6 sun) and the nanocrystal films remaining stable unless held under extremely high excitation intensities (∼500 W cm^{-2}, 5,000 sun), see Figure 2.6 [96]. Similarly, Wang *et al.* observed stable PL from their nanocrystal guest-host composite films – comprised of ∼7.5 nm sized $CsPb(Br_xI_{(1-x)})_3$ perovskite nanocrystals dispersed in a $Cs_4Pb(Br_xI_{(1-x)})_6$ non-perovskite matrix – across the entire Br–I range when held under 300 mW cm^{-2} (∼3 sun) for several hours [159]. Xiao *et al.* compared $Cs_{0.6}MA_{0.4}Pb(Br_xI_{(1-x)})_3$ films created with and without the incorporation of *n*-butylammonium, an organic ligand that

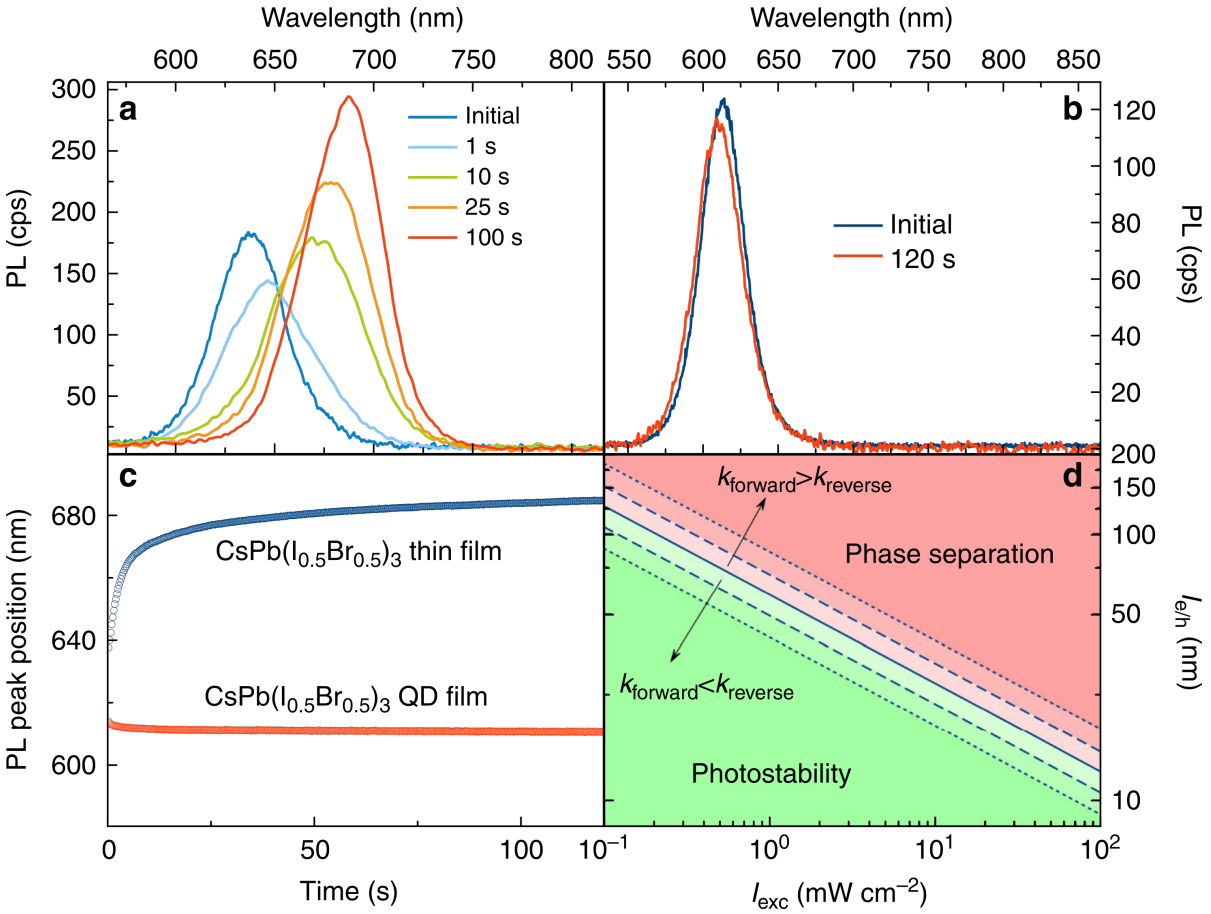

Figure 2.6: Data presented by Draguta *et al.* showing the stability of films made from perovskite nanocrystal solutions versus that for standard polycrystalline thin perovskite films [96]. (a) and (b): Evolution of the PL emitted from both a $CsPb(Br_{0.5}I_{0.5})_3$ perovskite thin film (a) and a nanocrystal film (b) under 60 mW cm^{-2} (∼0.6 sun), 405 nm illumination. (c): The tracked PL peak position from (a) and (b), highlighting that only the bulk thin film experienced a PL redshift and halide segregation. (d): Theoretically predicted phase diagram of the photostability of $MAPb(Br_xI_{(1-x)})_3$ perovskites as a function of illumination intensity (I_{exc}) and excited charge-carrier diffusion length ($l_{e/h}$). Reprinted from Ref. [96]. Copyright 2017, Nature Publishing Group.

occupied the grain surfaces of the perovskite and limited the diffusion of halide ions and charge carriers between the small (dimensions ∼10 nm) crystal grains inside the film [102]. Xiao *et al.* found that while bulk polycrystalline $Cs_{0.6}MA_{0.4}Pb(Br_xI_{(1-x)})_3$ films showed signs of halide segregation under 1 sun illumination over 20 min for $0.4 < x < 0.8$, films whose grain size was limited by BA incorporation remained stable for 8 h under 1 sun illumination across the entire compositional range [102].

The above work demonstrates that separating a perovskite film into nano-scale, highly

insulated domains increases the stability of the material against halide segregation under illumination. However, a further survey of the literature suggests that such films are impractical to use in optoelectronic devices because they offer insufficient long-range charge-carrier transport between the domains. Efficient LEDs based on nanocrystalline mixed-halide perovskite films indeed appear not to share the phase-stability of films formed of small, completely insulated perovskite domains. Reports on $CsPb(Br_xCl_{(1-x)})_3$ [78, 80, 140–142] and $CsPb(Br_xI_{(1-x)})_3$ [78, 79] nanocrystalline perovskite films optimised for LED applications have demonstrated the clear presence of halide segregation under various illumination and/or current injection conditions. In such LED nanocrystalline films a redshift of the electroluminescence or PL emission spectrum is observed to occur over the course of seconds [79] to tens of minutes [78–80] depending on the excitation conditions and perovskite chemical composition. Similarly, a number of reports show that sintering phase-stable mixed-halide nanocrystal perovskite films – thereby increasing the size of and interconnecting crystalline domains – reduces the phase stability and allows halide segregation to proceed [96, 158]. Thus only severe electronic isolation appears sufficient to suppress halide segregation in mixed-halide nanocrystal films.

In conclusion, while insulated, nanocrystalline perovskite domains are stabilised against halide segregation by the inhibition of charge-carrier and ionic motion, such lack of long-range transport would render optoelectronic devices inefficient. Careful balancing may potentially create nanocrystalline films that somewhat mitigate halide segregation while just about retaining the long-range charge-carrier transport properties required for optoelectronic devices. However this may be too challenging a method by which to produce mixed-halide perovskite materials with long-term phase stability for efficient optoelectronic devices.

2.4.4 Charge-Carrier Extraction and Injection and Trap State Passivation

There is now widespread consensus in the literature that excited charge carriers – generated either from photoabsorption or current injection – are the driving factor behind the halide segregation mechanism [20, 21, 78–80]. Halide segregation may therefore be controlled by manipulating the charge-carrier density within the perovskite, e.g. by altering charge-carrier extraction or injection, or the recombination dynamics. For example, Duong *et al.* showed that increasing the rate of charge-carrier extraction from photovoltaic devices based on quadruple-cation $Rb_{0.05}(Cs_{0.1}MA_{0.15}FA_{0.75})_{0.95}Pb(Br_{0.33}I_{0.67})_3$ perovskite significantly reduced the amount of halide segregation observed [9]. Perovskite solar cells may therefore be more stable under working conditions, when significant current extraction takes place, than would be expected from simple photoluminescence measurements on corresponding perovskite films in the absence of charge-extraction layers.

Several studies have linked trap-mediated recombination of excited charge carriers with halide segregation, highlighting trap passivation as a viable method to mitigate halide segregation [123, 151, 152, 167–169]. A myriad of different passivating agents have been linked to the reduction or prevention of halide segregation, including: trioctylphosphine oxide [151], potassium iodide [123], potassium bromide [169], polymethyl methacrylate (PMMA) [152], triiodide (I_3^-) molecules (minor effects) [167], and benzylamine molecules (minor effects) [168]. However, it is noted that the incorporation of a trap passivation agent into a perovskite film often also alters other material properties, such as the nature of grain boundaries and the ion migration channels, which are themselves linked to halide segregation. Abdi-Jalebi *et al.* showed that the changes in $(Cs_{0.06}MA_{0.15}FA_{0.79})Pb(Br_xI_{(1-x)})_3$ perovskite films resulting from halide segregation over 30 min under 60 mW cm^{-2} ($\sim$0.6 sun) illumination were almost entirely prevented for all halide ratios by the addition of potassium iodide to the perovskite precursor solution prior to the deposition of the

films; see Figure 2.7 [123]. The added potassium iodide was assumed to provide an excess of iodide that passivated trap states resulting from halide vacancies and reduced the halide ion mobility. The potassium ions were shown to accumulate at the grain surfaces of the perovskite, passivating more trap states and limiting halide ion movement in these regions [123]. In general, passivating agents represent a powerful method to control halide segregation in perovskite materials, capable of reducing halide segregation on more than one front, e.g. by passivating trap states and also potentially altering ion migration pathways and mobilities. The disadvantages of using such passivating agents mostly stem from the challenges in finding suitable agents, and incorporating the agent into the perovskite film via an appropriate processing method. Additionally, many additives produce side effects that can harm the perovskite material properties – such as charge-carrier transport across grain boundaries – resulting in a sweet spot in the concentration of the additive that must be found in order to optimise the overall optoelectronic performance of the perovskite [123]. The discovery and fine-tuning of effective additives for the mitigation of halide segregation is therefore a direct, but complex, target for the production of stable mixed-halide perovskite solar cells and LEDs.

Several reports have suggested that the link between trap passivation and halide segregation stems from charge carriers caught in localised trap states or at grain boundaries driving the halide segregation mechanism [119, 144, 150–152, 157]. The role of charge-carrier recombination in the halide segregation mechanism is investigated in detail in Chapter 4.

In conclusion, phase segregation in mixed-halide perovskites can clearly be manipulated through a tuning of charge-carrier recombination, extraction and injection rates. Control over the charge-carrier dynamics in a perovskite material is therefore a useful tool for mitigating halide segregation that must likely be implemented in the creation of phase-stable mixed-halide perovskite solar cells.

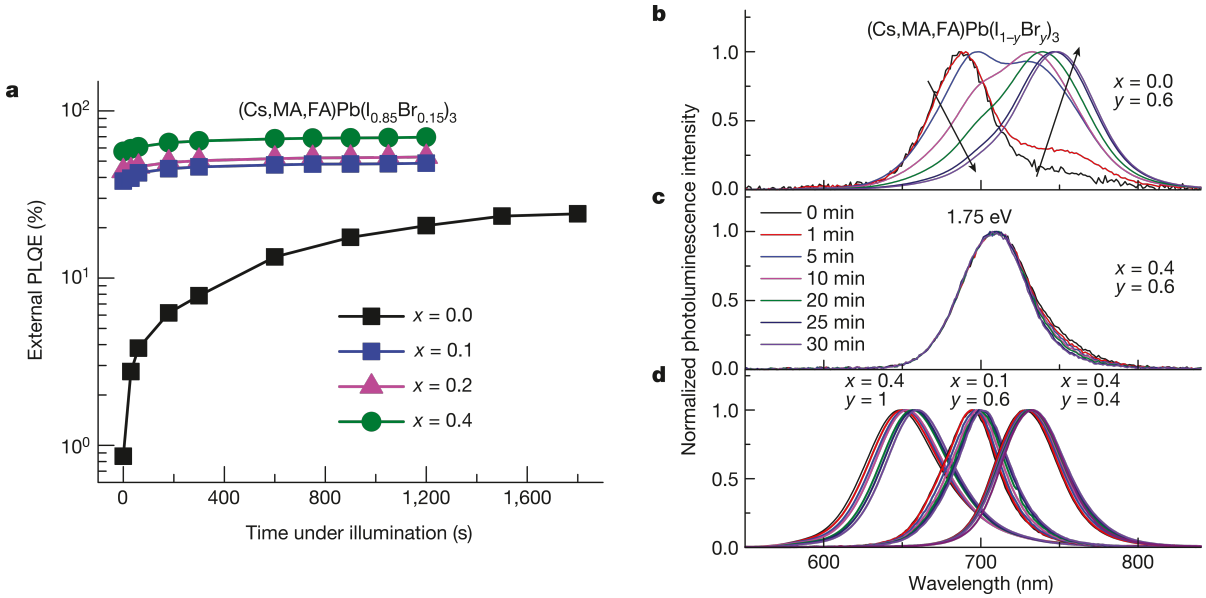

Figure 2.7: Data presented by Abdi-Jalebi *et al.* highlighting the effects of a potassium iodide passivating agent on the photostability of $(Cs_{0.06}MA_{0.15}FA_{0.79})Pb(Br_yI_{(1-y)})_3$ perovskite films [123]. (a): External PL quantum efficiency over time under illumination (60 mW cm^{-2}, ~0.6 sun, 532 nm) for 4 perovskite films with different ratios of potassium iodide to A-site cations (x) added to the perovskite precursor solutions. The external PL quantum efficiency increases in perovskite films undergoing halide segregation due to the funnelling and concentration of excited charge carriers in the forming regions of low-bandgap perovskite. (b): PL spectra observed over 30 min for a $(Cs_{0.06}MA_{0.15}FA_{0.79})Pb(Br_{0.6}I_{0.4})_3$ film with no passivating agent (x=0) under the same illumination conditions as in (a). (c) and (d): PL spectra over 30 min for perovskite films with varying halide content (y=0.6 (c), y=1, 0.6, 0.4 (d)) and varying amounts of passivating agent added (x=0.4 (c), x=0.4, 0.1, 0.4 (d)) under the same illumination conditions as in (a). Reprinted by permission from Springer Nature: Nature Ref. [123], 2018.

2.4.5 Atmospheric Effects

Environmental conditions such as changes in humidity or immersion of the perovskite into different gases are expected to affect the halide segregation mechanisms in mixed-halide perovskites, for a range of reasons. First, environmental conditions have previously been shown to alter the nature and distribution of trap states in metal halide perovskites [11, 24–29, 31, 32, 150]. Second, Brenes *et al.* suggested that halide vacancy sites may be filled by superoxide molecules (O_2^-) formed from the reaction between oxygen and excited electrons [24], which may interfere with the halide ion migration pathways in the perovskite structure [166]. Given the discussion in the previous section, which links trap state passivation to halide segregation, one would therefore expect the atmospheric

environment to have an indirect impact on the extent of phase segregation.

There is indeed ample evidence in the literature for atmospheric effects on halide segregation, however most of it is inconsistent, which could derive from differences in material morphology, composition or experimental conditions between studies. Citing the trap-passivating and vacancy-filling nature of oxygen as the cause, Fan *et al.* reported greater stability against halide segregation – and even recovery from halide segregation while still under illumination – for $MAPb(Br_xI_{(1-x)})_3$ films immersed in a pure oxygen atmosphere, in contrast to a nitrogen-based atmosphere [170]. Conversely, Ruf *et al.* observed significantly more halide segregation in $(Cs_{0.05}MA_{0.16}FA_{0.79})Pb(Br_{0.17}I_{0.83})_3$ perovskite photovoltaic devices under ∼1 sun illumination and an applied AC bias (sinusoidal, amplitude 0.5 V, frequency 990 Hz) when the samples were held under an 80% relative humidity, oxygen environment as compared to air or nitrogen environments with a similar relative humidity level [124]. Other studies have not necessarily agreed on the effect of oxygen on halide segregation, reporting only minor changes in the speed of halide segregation in perovskite samples held under ambient air as compared to inert nitrogen [150] or helium [118] atmospheres. Therefore, the effect of an oxygen atmosphere on halide segregation is still debatable.

With regards to water vapour, Ruf *et al.* observed faster segregation rates in their $(Cs_{0.05}MA_{0.16}FA_{0.79})Pb(Br_{0.17}I_{0.83})_3$ perovskite photovoltaic devices under illumination (∼1 sun) and an AC bias (sinusoidal, amplitude 0.5 V, frequency 990 Hz) when the devices were exposed to air with 80% relative humidity as opposed to air with 23% relative humidity [124]. Howard *et al.* observed a redshift of the PL emission from $Cs_yFA_{(1-y)}Pb(Br_{0.38}I_{0.62})_3$ films when the perovskite was held under a humid air environment [171]. The redshift was observed to increase with the relative humidity level, and recovered when the relative humidity was reduced. The PL measurements were made with minimal light-soaking (0.015 s at 6000 mW cm^{-2}, ∼60 sun) on timescales significantly shorter than

the several seconds to minutes typically required for halide segregation to take place, and so Howard *et al.* suggest that the PL emission redshifts were caused by humidity-induced halide segregation [171]. However further work must be done to determine if the observed PL peak shifts were indeed the result of halide ion movement, or some reversible, humidity-caused chemical or structural changes to the perovskite, as have been observed elsewhere [172, 173].

In summary, the effects of the atmospheric content on halide segregation in mixed-halide perovskites are generally reported to be minor [118, 144, 150], although the conclusions of some reports suggest more significant effects that warrant further research [124, 170, 171]. It is noted that the somewhat incongruous nature of the literature regarding atmospheric effects on halide segregation may stem from several different effects. One problem is that the property of the perovskite being monitored as a measure of halide segregation (usually the emitted PL from the perovskite) is often not only affected by halide segregation itself, but also independently influenced by the environmental atmosphere [150]. In addition, subtle differences in material morphology and crystallinity may result in an inconsistency of results between groups, particularly if the atmospheric effects are subtle, or dependent on the defect density originally present. In Chapter 4, a study on the effects of the surrounding atmospheric environment on the halide segregation dynamics in mixed-halide perovskite films is performed, which helps to clarify the reasons for the inconsistency of the literature. In conclusion, some further work will be required before the direct influence of atmosphere on halide segregation can be fully understood. However, given that commercial perovskite photovoltaic devices and LEDs will likely be encapsulated and held in air, whether or not halide segregation can be mitigated by holding the perovskite material under an exotic atmosphere may not be of the utmost relevance for this technology.

2.4.6 Management of Halide Ion Vacancies

Preparation of mixed-halide perovskites with a stoichiometric excess of halide ions is another well-explored method for the prevention of halide segregation. [95, 123, 166, 167, 169]. Here, the aim is a reduction in the density of halide vacancies in the material in order to suppress the mobility of halide ions that the segregation process relies on. Halide ion movement in perovskite materials is thought to occur predominantly through a nearest-neighbour hopping mechanism via vacant corresponding lattice sites in the perovskite crystal [36, 93, 95, 166]. Therefore, vacant halide lattice sites are integral for both halide mobility and the halide segregation mechanism, and altering the nature and density of halide ion vacancies in the perovskite is a potential method of improving perovskite photostability.

Experimentally, this approach has found good success, albeit sometimes at the expense of degrading other material properties. Both Barker *et al.* [95] and Ruth *et al.* [166] explored the link between halide ion vacancies and halide segregation and observed that a reduction in halide vacancies suppressed the extent of halide segregation. However, if the halide ion density was taken too far away from the stoichiometric ideal, the material properties of the perovskite were frequently found to suffer. Barker *et al.* prepared nominally $MAPb(Br_{0.6}I_{0.4})_3$ films with a 1:5 ratio of lead to halide ions (thus providing a halide ion excess), which they compared with films made from a more stoichiometric 1:3 ratio of lead to halide ions [95]. The films created with a halide excess showed improved stability under $\sim$20 mW cm^{-2} ($\sim$0.2 sun) illumination compared to the stoichiometric films, according to measurements of PL and photothermal deflection spectra. However, the incorporation of excess halide was also found to turn the material more bromide-rich because of the preferential binding of lead to bromide (as compared to iodide) [125, 174], leading to blueshifts in the PL emission peak and absorption edge [95]. Ruth *et al.* found that the speed at which halide segregation occurred in $MAPb(Br_{0.4}I_{0.6})_{(3-y)}$

films increased as the halide content was reduced from excess ($y < 0$) to deficiency ($y > 0$). However, it is noted that the bandgap and crystallinity of their samples were also both significantly affected by the halide content, meaning that changes in crystallinity may also have influenced halide segregation rates (see Section 2.4.3.1 above) [166]. Ruth *et al.* also performed Monte-Carlo simulations of the halide segregation process in modelled $MAPb(Br_{0.5}I_{0.5})_{(3-y)}$ systems with varying levels of halide ion deficiencies, y. The results of the Monte-Carlo simulations were found to match qualitatively with the experimental work, with faster modelled segregation rates correlated with higher halide ion vacancy densities [166].

Based on these first studies set by Barker *et al.* and Ruth *et al.*, others have explored excess halide incorporation directly for perovskite photovoltaic and LED applications, with a good deal of success [123, 167, 169]. As mentioned above in Section 2.4.4, Abdi-Jalebi *et al.* [123] and Yang *et al.* [169] incorporated similar potassium iodide and potassium bromide passivating agents into $(Cs_{0.06}MA_{0.15}FA_{0.79})Pb(Br_xI_{(1-x)})_3$ polycrystalline films and $CsPb(Br_xI_{(1-x)})_3$ nanocrystalline films, respectively. Both reported that significant improvements in the stability of the perovskite material against halide segregation occurred as the excess halide ions reduced the number of halide vacancies. However, trap and surface passivation by the potassium ions accompanied these changes, which unfortunately makes it difficult to evaluate the true effect of the halide ion excess. Importantly, there appeared to be no significant detrimental effect on the perovskite material from the inclusion of excess halides in the precursor solutions. Interestingly, Balakrishna *et al.* observed only minor stability improvements against halide segregation in $MAPb(Br_{0.5}I_{0.5})_3$ perovskite when an I_3^- additive was added to the precursor solutions [167], indicating that while a halide excess alone will improve the stability of a perovskite material to halide segregation, it is unlikely to eliminate halide segregation completely.

In summary, a reduction in halide vacancies has been suggested theoretically [166] and shown experimentally [93, 95, 123, 166, 167, 169] to reduce the rate of halide segregation in mixed-halide perovskites. The main caveat to note is that other properties of the perovskite material are often also inadvertently altered by incorporation of excess halide in the precursor solutions, which can be either beneficial [123] or detrimental [95] for optoelectronic applications. Finally, it is noted that the given formation energy of defect states in perovskite materials will always result in a finite population of halide vacancies at room temperature. Therefore, basic thermodynamic considerations dictate that vacancy-mediated halide ion transport can never be completely eliminated through the incorporation of excess halide ions. In addition, halide ion motion can, to a certain extent, progress even in the absence of halide vacancies. Overall, it is concluded that while a reduction in halide vacancy density will lower halide segregation in mixed-halide perovskites, it is unlikely to yield completely phase-stable materials unless used in tandem with some of the other approaches discussed in this chapter.

2.4.7 Regulating Illumination

The illumination falling upon a solar cell may vary dramatically depending on the location of the solar cell on the globe, the solar cell architecture, and external factors such as implementation in a solar concentrator design [175] or tracking arrangements. Therefore, it is important to consider how properties of the illumination may affect and mitigate halide segregation in mixed-halide perovskites. It should be noted that because LEDs are operated under charge-carrier injection, rather than under illumination, information presented in this section is not applicable for perovskite materials designed for light-emitting applications.

As one would expect, several groups have observed that an increase in illumination intensity results in faster halide segregation in mixed-halide perovskites [17, 94, 96, 97, 101,

150, 151, 166]. Given that excited charge carriers are thought to be responsible for halide segregation [20, 21], a higher illumination intensity photogenerates more excited charge carriers within the perovskite material per second, leading to faster halide segregation. However, it is noted that the observed changes may not necessarily be linear in light intensity, given that the efficiency with which absorbed photons induce halide segregation may also change with illumination intensity – a concept explored in Chapter 4. For example, it has been observed that a certain threshold charge-carrier density exists which must be crossed before halide segregation may commence [96, 97, 115, 166, 176]. Therefore, while generally a higher illumination intensity leads to a greater degree of halide segregation in a given time frame [17, 94, 96, 97, 101, 150, 151, 166], the exact relationship between the two parameters is complex.

As mentioned above, several studies have reported halide segregation to be suppressed for illumination below an extremely low, material-dependent threshold intensity [96, 97, 115, 166, 176]. Slotcavage *et al.* showed that an original mixed-halide perovskite PL emission peak remained dominant for $MAPb(Br_{0.4}I_{0.6})_3$ films under $0.5\,mW\,cm^{-2}$ ($\sim$0.005 sun) illumination for 3 h, indicating suppression of halide segregation [176]. Additionally, Draguta *et al.* observed no segregation for $MAPb(Br_{0.5}I_{0.5})_3$ films when the illumination was kept below a $0.04\,mW\,cm^{-2}$ ($\sim$0.0004 sun) intensity threshold [96]. Interestingly, Elmelund *et al.* found that the highest threshold illumination intensity for which halide segregation in $MAPb(Br_{0.5}I_{0.5})_3$ films remained suppressed increased linearly with increasing sample temperature (this result is discussed further in Section 2.4.8) [97]. These observations may be explained by considering the counteracting effects of halide segregation under illumination and the entropic diffusion of ions against the formed concentration gradients [96, 97, 144]. The point of maximum halide segregation will occur when these two dynamics are balanced. As the strength of the halide segregation dynamic is reduced with decreasing illumination intensity, below a certain low threshold intensity

the stabilisation point between ion segregation and mixing is reached before significant segregation has occurred. For photostable perovskite solar cells, it is therefore essential that the threshold illumination intensity for which halide segregation becomes insignificant over $\sim$ 12 h is identical to or greater than AM1.5 solar illumination conditions.

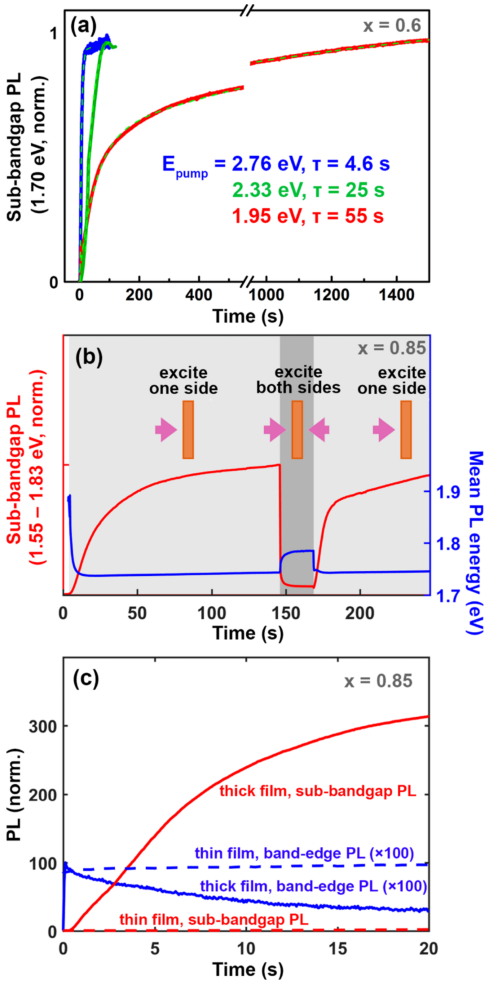

Figure 2.8: Data presented by Barker *et al.* suggesting a link between the illumination profile within a perovskite thin film and the amount of halide segregation induced in the material [95]. (a): The emergence of sub-bandgap PL from an $MAPb(Br_{0.6}I_{0.4})_3$ film under illumination at different photon energies (E_{pump}) and intensities, but similar photon flux. (b): Changes in the sub-bandgap PL (associated with iodide enriched domains) and average PL energy emitted from an $MAPb(Br_{0.6}I_{0.4})_3$ film under either one- or two- (one incident on each side of the film) beam illumination of 100 mW cm^{-2} ($\sim$1 sun) intensity, 405 nm wavelength each. (c): Changes in the PL intensities emitted from thick (280 nm) and thin (70 nm) $MAPb(Br_{0.85}I_{0.15})_3$ perovskite films under the same, one-sided illumination as in (b). Reprinted with permission from Ref. [95], https://pubs.acs.org/doi/10.1021/acsenergylett.7b00282. Further permissions related to the material excerpted should be directed to the ACS.

In addition, halide segregation may potentially be affected by the light absorption

profile and the resulting profile of the photoexcited charge-carrier density through a thin film. Barker *et al.* investigated $MAPb(Br_{0.6}I_{0.4})_3$ and $MAPb(Br_{0.85}I_{0.15})_3$ films [95], reporting three key observations that together suggest that the nature of a non-uniform charge-carrier generation profile – resulting from more charge carriers being generated at the illumination side of the film than at the back side – is a primary driver of halide segregation. First, the wavelength of the illumination was found to influence the speed at which halide segregation took place, with a wavelength of 635 nm inducing much slower segregation than 532 nm wavelength photons whose energy was further above the band edge, see Figure 2.8a [95]. Since the optical density of a semiconducting material is lower for photon energies close to the bandgap, these observations suggest that a more uniform internal light profile and photoexcited charge-carrier density profile through the films will lead to less halide segregation. Second, Barker *et al.* reported that the changes observed in the PL dynamics as halide segregation progressed were somewhat reversed if the perovskite film was illuminated from both sides (despite the fact that this doubled the overall illumination intensity), again leading to more uniform illumination throughout the film, see Figure 2.8b [95]. Finally, halide segregation was found to progress more slowly in thin perovskite films (thickness 70 nm as compared to 280 nm) [95], see Figure 2.8c, which again sustain flatter initial charge-carrier density profiles, although it was also noted that the crystallinity was likely to be different between the films. As a caveat, it is noted that charge-carrier redistribution across film profiles of typically several hundred nanometres is relatively fast, leading to flattening of the distribution on the time scale of ∼nanoseconds [52, 177]. Therefore, in order for the charge-carrier generation profile through a perovskite film to have an influence on the resulting charge-carrier dynamics, the trapping rate in the material must be equally fast and/or the trap states in the perovskite must be unevenly distributed throughout the film. Both of these explanatory scenarios are possible, but they are unlikely to apply to all perovskite compositions that

have been observed to undergo halide segregation, meaning that further experiments are needed to probe the universality of this scenario. However, if the internal light profile within the perovskite is more generally confirmed to have an important influence on the phase-stability of the material, then it may be possible to manufacture photostable perovskite solar cells by utilising a back-reflecting cell design and carefully controlling the device layer thicknesses and absorption properties [178] to mitigate halide segregation.

2.4.8 Temperature Control

Temperature is another potential parameter offering mitigation of halide segregation in mixed-halide perovskites, whose influence is important to explore because of the elevated operating temperatures of solar cells and LEDs. Fortunately, temperature can also to a certain extent be controlled e.g. by passive cooling, and through substrate and overall module design. Temperature is thought to have two major influences on the halide segregation mechanism. Firstly, it has been shown that the halide segregation mechanism is governed by an Arrhenius relation in the temperature range ∼151 to 375 K [17, 95, 97, 104], see Figure 2.9 for data on a portion of this range [97]. Given that halide segregation relies on ion migration, it is understandable that the temperature of the perovskite system is positively correlated with the speed of the segregation dynamics. Secondly, in the case of mixed-halide perovskites, entropy is thought to be the driving mechanism for the mixing of the halide ions. Since the entropic contribution to the free energy of a thermodynamic system is partially determined by its temperature, theoretical calculations suggest that raising the temperature of the perovskite increases the affinity of the halide ions for mixing, and therefore increases the photostability of the material [98, 104]. The disparity between these two effects of temperature on halide segregation – the first suggesting that halide segregation happens faster at higher temperature, the

second proposing that the perovskite material is more phase-stable at higher temperature – is an interesting dichotomy that has yet to be fully explored by the research community.

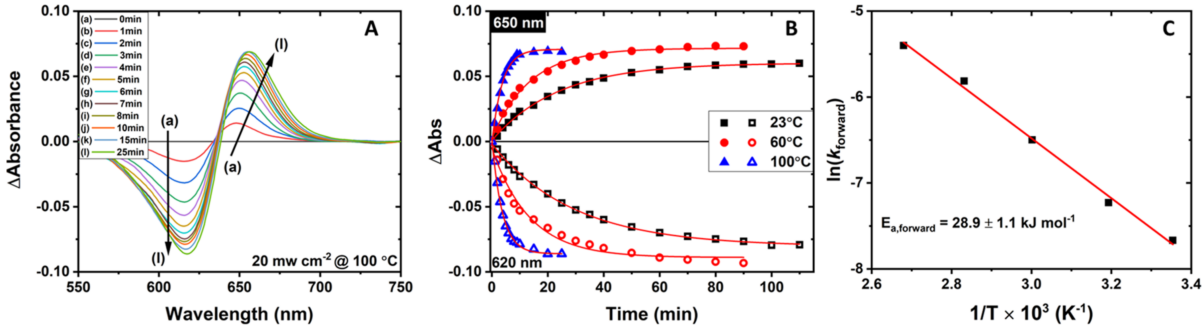

Figure 2.9: Work of Elmelund *et al.* tracking the speed of halide segregation in $MAPb(Br_{0.5}I_{0.5})_3$ perovskite films at different temperatures [97]. The films were illuminated with a white light source at 20 mW cm^{-2} (∼0.2 sun) intensity. (a): Changes in the absorption spectra of an illuminated sample over time as compared to the pre-illumination measurement of absorption. The temperature of the sample was 100 °C. (b): Growth of the sub-bandgap absorption (measured at 650 nm, solid symbols) and shrinkage of the above-bandgap absorption (measured at 620 nm, open symbols) over time for perovskite samples at 23, 60, and 100 °C (black squares, red circles and blue triangles respectively). (c): Plot of the natural log of the rate constant associated with halide segregation versus the inverse temperature of the perovskite material, with the linear trend highlighting an Arrhenius relation. The rate constant associated with halide segregation was obtained from mono-exponential fits to the data in (b). Reprinted with permission from Ref. [97]. Copyright 2019, American Chemical Society.

While there is plenty of experimental evidence for ion migration and segregation occurring faster at higher temperatures [17, 95, 97, 104], the second aspect mentioned above – i.e. an increased entropy at higher temperatures resulting in more stable perovskite materials – has been observed relatively rarely. Experimental work by Elmelund *et al.* showed that the threshold highest illumination intensity that could be applied to $MAPb(Br_{0.5}I_{0.5})_3$ without inducing significant halide segregation increased with temperature [97]. These observations suggest that the photostability of the perovskite may indeed increase with temperature, in qualitative agreement with theoretical studies [98, 104]. Additionally, Wang *et al.* characterised the effects of temperature on the photoinduced changes in slightly unconventional samples consisting of $CsPb(Br_xI_{(1-x)})_3$ perovskite nanocrystals embedded in a $Cs_4Pb(Br_xI_{(1-x)})_6$ endotaxial matrix [159]. In PL spectra taken after several hours of high intensity, 440 000 mW cm^{-2} (∼4400 sun)

illumination, Wang *et al.* observed that, depending on the exact sample composition, a low-energy emission peak emerged and/or separated from the main emission peak at low temperatures, but the films remained photostable at higher temperatures. The authors attributed these observations to lower photostability at lower temperature [159], however, it is noted that other studies have reported similar changes in the PL emitted from single-halide perovskites at low temperatures that are unrelated to halide segregation [179, 180]. Finally, by probing the halide segregation dynamics in near-photostable $MAPb(Br_xI_{(1-x)})_3$ (bromide fraction, x, around 0.2) at a low illumination intensity ($1.5\,mW\,cm^{-2}$, ~0.015 sun), Nandi *et al.* observed halide segregation within a composition-dependent temperature window, and observed photostability over 4 h at higher and lower temperatures under otherwise identical conditions [101]. The work of Nandi *et al.* highlights the interesting interaction between entropic forces and ionic motion at different temperatures, and invites further investigations into how these effects may be utilised to stabilise perovskite optoelectronic devices.

In summary, while there are some experimental studies reporting increased photostability of mixed-halide perovskites at elevated temperatures [97, 101, 159], most appear to find the opposite effect [17, 95, 97, 104]. Exploring the conditions under which either of these scenarios dominate would be greatly beneficial for understanding how temperature may be used to mitigate halide segregation in mixed-halide perovskites. Illumination intensity may well play a crucial role in delineating different regimes here. While the culmination of faster ionic movement and increased entropic factors at higher temperatures result in perovskite materials that are harder to segregate in the low illumination intensity regime (~$0.01\,mW\,cm^{-2}$, 0.0001 sun according to Elmelund *et al.* [97]), it may well lead to faster halide segregation under intense illumination regimes. Direct verification of how ion motion and entropic forces interact in hybrid metal halide perovskites at different temperatures would be a fruitful avenue for further research.

Given that the temperature of LEDs and photovoltaic devices can be controlled via a number of different methods, such research could directly lead to practical means of reducing halide segregation in perovskite optoelectronic devices.

2.4.9 Crystal Structure Engineering

Incipient studies have indicated that the underlying crystal structure of the mixed-halide perovskite may play a role in the halide segregation dynamics. Such links would be fortunate, given that the perovskite structure is relatively easily tuned, for example through changes in A-cation that may influence octahedral tilting. As noted by others [92, 96, 166], the highest bromide fraction x that produces photostable $MAPb(Br_xI_{(1-x)})_3$ films, x=0.2, also denotes the highest fraction for which the perovskite remains tetragonal, with a transition to a cubic structure and ample halide segregation observed as x passes above the threshold of 0.2 [17, 65]. Ruth *et al.* performed computational Monte-Carlo simulations of halide segregation in both cubic and tetragonal perovskite materials to explore how crystal structure may affect the photostability of $MAPb(Br_{0.5}I_{0.5})_3$ perovskites [166]. In a cubic structure, the nearest-neighbour hops available for a halide ion are all symmetrically identical, whereas in a tetragonal structure there are two distinct hop pathways, with distinct energetic barriers. Ruth *et al.* found that the halide segregation rate was sensitive to the difference in the energetic barriers of the two distinct migration pathways in the tetragonal perovskite structure, and so halide segregation could occur at a different rate in tetragonal perovskite structures (where there is some difference in the energetic barriers) compared to cubic perovskite structures (where there is symmetrically no difference in the energetic barriers) [166]. However, the exact difference in segregation rate between tetragonal and cubic structures – or even in which structure halide segregation would occur faster – was not determined, and Ruth *et al.* concluded that halide segregation would likely proceed in both tetragonal and cubic perovskites [166]. However, this

work could possibly explain the observation that halide segregation does not occur in $MAPb(Br_xI_{(1-x)})_3$ perovskites when x <0.2, when the perovskite is in a tetragonal phase.

While $MAPb(Br_xI_{(1-x)})_3$ perovskites have a clear transition from tetragonal to cubic crystal structures around x=0.2 [17, 65], the structure of $FAPb(Br_xI_{(1-x)})_3$ perovskites across the x compositional range is a matter of some discussions [115, 181–183]. Furthermore, some reports suggest an amorphous structural region for $FAPb(Br_xI_{(1-x)})_3$ within the approximate composition range $0.3 < x < 0.5$ [115, 181]. The lack of a clear structural transition in FA-based, mixed-halide perovskites complicates any efforts to correlate crystal structure with stability against halide segregation stability in these materials.

A significant study researching the link between crystal structure and halide segregation was recently conducted by Beal *et al.* [184]. An examination of the XRD patterns of $Cs_yFA_{(1-y)}Pb(Br_xI_{(1-x)})_3$ perovskite materials as the bromide and caesium content (x and y, respectively) was tuned allowed the mapping of a phase diagram for the perovskite material, from a cubic structure at x ~50% and low y, to a cubic-tetragonal mixed phase at low x and y ~50%. These compositions were then determined to be either stable or unstable towards halide segregation through measurements of PL spectra under ~110 mW cm^{-2} (~1.1 sun) illumination for 10 min, and examinations of potential redshifts over time. While perovskites of cubic structure were consistently observed to exhibit halide segregation, cubic-tetragonal perovskites showed both stable and unstable behaviour, leading to the conclusion that the crystal structure is a somewhat unreliable indicator of phase-stability in mixed-halide perovskites [184]. It is also noted that, as mentioned in Section 2.4.2.1 above, tuning the A-site cation may also influence the photostability of perovskite films by changing the crystallinity of the perovskite, making it difficult to determine whether trends observed by Beal *et al.* resulted solely from changes in the crystal structure. Overall, the crystal structure is concluded to be at best a secondary consideration for phase-stability of perovskites, and in any case may prove too

difficult to alter without changing other critical properties of the perovskite material, such as its bandgap, in particular if compositional changes beyond the A-cation are involved.

2.4.10 Summary

In this chapter a wide range of means by which halide segregation can be mitigated in mixed-halide perovskites has been critically evaluated. Applied in combination, such approaches may ultimately yield materials with sufficient photostability for a given application, enabling colour-tunable perovskite semiconductors for applications such as tandem solar cells and light-emitting diodes and displays. The findings of this chapter are summarised below with key strategies grouped by their effectiveness for suppressing halide segregation.

Amongst the most promising tools by which to suppress halide segregation significantly are the judicious choice of ions populating the A-cation site, improvements in material crystallinity, and a reduction in trap density. The modification of the A-site cation in the ABX_3 structure from solely MA, FA or Cs species to a mixture of either FA/Cs or MA/FA/Cs currently presents the most substantial and easily implemented method of increasing the photostability of a lead mixed-halide perovskite with minimal effect on its bandgap [20, 66, 117, 118, 122, 123]. An alternative, highly promising method for limiting halide segregation is an improvement in the crystallinity of the perovskite, i.e. creating films with a larger average grain size [20, 103, 117, 122, 125], which may affect properties at the grain boundaries such as trap density, strain, or ion migration channels [104, 119, 144]. In addition, passivation of electronic trap states through the use of various additives has also been shown to be successful at mitigating halide segregation [123, 151, 152, 167, 168], with potassium iodide being particularly effective [123].

Moderate success has also been reported for the incorporation of excess halide ions into the mixed-halide perovskite, which has been shown to reduce the density of halide

vacancies and suppress halide segregation to a certain extent [95, 123, 166, 167]. However, moving the perovskite stoichiometry too far from its ideal will negatively impact on the perovskite material quality [95, 166]; therefore, the incorporation of excess halide ions must be carefully tuned. In addition, basic thermodynamic arguments dictate that halide vacancies can never be completely eliminated from a perovskite structure, meaning that inclusion of excess halide ions is a technique best used in tandem with other methods aimed at preventing halide segregation.

Other factors explored to enhance the photostability of mixed-halide perovskites have been found to be less promising or impractical to implement. Utilising a bromide/chloride ionic mixture in the perovskite structure realises bandgaps suitable for blue-green LEDs, but these mixed-halide perovskite compositions appear to be similarly unstable towards halide segregation as bromide/iodide perovskite compositions [69, 78, 80, 139]. While the adoption of nanocrystalline materials has been shown to limit the effects of halide segregation through the suppression of charge-carrier diffusion lengths [96, 158, 159, 166], this technique is impractical to implement in optoelectronic devices where efficient charge-carrier transport is key to high performance [160–162]. Whether or not the composition of the surrounding atmosphere alters the speed at which halide segregation takes place is still a matter of debate [118, 124, 144, 150, 170, 171], but it is noted that tuning such exposure is again an impractical idea, given that oxygen- or humidity-rich atmospheres will also eventually degrade the perovskite material [11–13, 15, 16, 91], and devices may ultimately operate under encapsulation. Despite a significant recent study [184], the influence of crystal structure still needs further experimental exploration to assess its significance for the photostability of mixed-halide perovskites. Theoretical predictions have suggested that structure could impact on the ion migration pathways in the perovskite [92, 166], however tuning crystal structure without impacting on important parameters such as electronic bandgaps and material crystallinity may prove difficult.

Finally, as a perspective on the future research avenues in the field of mixed-halide perovskites, it is noted that some methods for mitigating halide segregation require substantial further research, but could prove potentially promising. Partially replacing lead with tin on the B-site cation has shown some promising initial results [133, 134], however, further work is required to elucidate more fully the role of tin on the mixed-halide perovskite photostability. The type of illumination upon the perovskite has been shown to affect the halide segregation dynamics [17, 94–97, 101, 115, 150, 151, 166, 176, 185], and while the nature of solar illumination is an external parameter, the overall photovoltaic device architecture determines the light profile within the perovskite film and could therefore influence halide segregation [95]. The temperature of the mixed-halide perovskite film is another factor affecting halide segregation in mixed-halide films, although the precise trade-off between entropic mixing and ionic diffusion still requires further research. That said, temperature control could to some extent be utilised to mitigate halide segregation in a mixed-halide perovskite solar cell or LED though passive cooling systems [17, 95, 97, 98, 101, 104, 159]. Additional topics for further investigation centre on the role of grain boundaries and interfaces on the halide segregation mechanism. Material crystallinity can clearly affect halide segregation, however there is still no real consensus on the exact mechanism by which grain boundaries influence the halide segregation mechanism. Some studies have also started to investigate the role of surfaces in halide segregation [151, 152], however interface engineering has yet to be fully explored, and could have a large impact on halide segregation due to the strong links between interfaces and crystallinity, trap states, ion migration and charge-carrier extraction [186, 187]. Such investigations are particularly important because the interfaces between the perovskite and charge-extraction layers can vary significantly depending on the device architecture used. Finally, it is noted that 2D perovskites have proven to be generally more stable (especially against moisture) than 3D perovskites,

and ion motion has also been shown to be somewhat limited in a 2D perovskite structure [188, 189]. Therefore, it would be interesting to contrast the stability of 2D layered perovskites against halide segregation with that of their 3D (bulk) counterparts, but little research has so far been done on this topic.

Overall, through a combination of the above factors, halide segregation will likely be mitigated in working perovskite solar cells and LEDs to the extent required for stable operation. Fortuitously, the most promising approaches for reducing halide segregation significantly (i.e. high crystallinity, low trap state density, efficient charge-carrier extraction) are also factors that yield high performance devices, making rapid progress highly likely. Mixed-halide perovskites therefore remain extremely promising candidates for the demanding applications of tandem solar cells and tunable light-emitting diodes.

3

Experimental Theory and Methods

Contents

This chapter details the myriad of experimental techniques presented elsewhere

in this thesis, both from theoretical and practical perspectives. Particular emphasis is placed on the optoelectronic theory and measurement techniques that are heavily relied on in Chapters 4, 5, and 6

3.1 Sample Fabrication

3.1.1 $MAPb(Br_xI_{(1-x)})_3$ Thin Films

The fabrication of $MAPb(Br_xI_{(1-x)})_3$ thin films as detailed in this section was performed by J. B. Patel, Department of Physics, University of Oxford.

Due to the progress made in the fabrication of high-quality $MAPb(Br_xI_{(1-x)})_3$ thin films, different fabrication recipes were used for the samples discussed in Chapter 4 and Chapter 6. Both recipes are detailed below.

3.1.1.1 Thin Film Samples Used in Chapter 4

Substrate cleaning:

z-cut quartz was first cleaned using Hellmanex, acetone and isopropanol, then with oxygen plasma for 10 min.

$MAPb(Br_{0.5}I_{0.5})_3$ perovskite layer preparation:

The $MAPb(Br_{0.5}I_{0.5})_3$ perovskite was prepared using an adaptation of the procedure proposed by F. Huang *et al.* [190]. The perovskite films were prepared by dissolving the precursor salts in anhydrous N,N-dimethylformamide (DMF) and dimethyl sulfoxide (DMSO) mixture (4:1 volume ratio) to obtain a stoichiometric solution with the desired $MAPb(Br_{0.5}I_{0.5})_3$ composition. The precursor solution was prepared using the following precursor salts: methylammonium iodide (MAI) (dyesol), methylammonium bromide (MABr) (dyesol), lead iodide (PbI_2) (99%, Sigma-Aldrich), lead bromide ($PbBr_2$) (98%, Alfa Aesar). The perovskite precursor solution was spin coated from a 1.0 M solution at 4000 rpm for 30 s. N_2 gas was used to quench the growth of the perovskite. The gas

flow was applied 15 s after the start of the spin coating, and sustained for 10 s. The perovskite films were immediately placed on a preheated hot plate set to 100 °C and annealed in a N_2 atmosphere for 20 min.

Poly(methyl methacrylate) (PMMA) layer preparation:

PMMA (Sigma Aldrich, average M_W 97 000 g mol^{-1}) was dissolved in chlorobenzene with a concentration of 150 mg mL^{-1}. The solution was spin coated at 2000 rpm for 45 s on top of the perovskite films.

Final sample preparation:

The back of the quartz substrate was cleaned with isopropanol to ensure no residue at the back of the sample would interfere with measurements.

3.1.1.2 Thin Film Samples Used in Chapter 6

Substrate Cleaning:

Substrates were made of z-cut quartz (area 1.3 cm^2) were cleaned by subsequent sonication in Decon90 (1 vol% in deionised water), deionised water, acetone (Sigma Aldrich) and isopropanol (Sigma Aldrich) for 10 min each. The substrates were then dried using an N_2-gas gun before being transferred into an N_2 filled glovebox prior to deposition of the perovskite layer.

$MAPb(Br_{0.5}I_{0.5})_3$ perovskite layer preparation:

$MAPb(Br_{0.5}I_{0.5})_3$ thin film samples were prepared using the acetonitrile route as reported previously [191]. In summary, the precursor salts (methylammonium iodide, MAI, GreatCell Solar; methylammonium bromide, MABr, GreatCell Solar; lead iodide, PbI_2, TCI; lead bromide, $PbBr_2$, >98%, Alfa-Aesar) were weighed stoichiometrically and dissolved in acetonitrile (Sigma Aldrich) to give a 0.5 M solution as described by Noel *et al.* [191].

The perovskite films were fabricated using the following spincoating recipe: 70 µl of precursor solution was deposited dynamically onto the quartz substrate spinning at

2000 rpm. The films were then annealed for 30 min at 100 °C.

PMMA layer:

PMMA (poly(methyl methacrylate), Sigma Aldrich, mean molar weight 97 000 g mol^{-1}) was dissolved in chlorobenzene (Sigma Aldrich) at 150 mg ml^{-1}. To form the PMMA film, 40 µl of solution was deposited dynamically onto the perovskite film at 2000 rpm, for 25 s. The films were then annealed at 100 °C for 1 min to drive off any residual solvent.

3.1.2 $MAPb(Br_{0.5}I_{0.5})_3$ and $MAPbI_3$ Photovoltaic Devices

The fabrication of $MAPb(Br_{0.5}I_{0.5})_3$ and $MAPbI_3$ photovoltaic devices as detailed in this section was performed by J. B. Patel, Department of Physics, University of Oxford.

Substrate cleaning:

Fluorine-doped tin oxide (FTO) glass substrates (Tec 15, Pilkington) were washed using Hellamanex, acetone, isopropanol and ethanol. Thereafter, the FTO substrates were placed in the oxygen plasma asher for 10 min.

SnO_2 layer:

SnO_2 was prepared as reported previously [192]. In brief, $SnCl_4{\cdot}5H_2O$ in isopropyl alcohol (0.05 M) was spincoated onto clean FTO substrates at 3000 rpm and then annealed at 180 °C for 1 h. The substrates were then placed in a chemical bath consisting of $SnCl_2{\cdot}2H_2O$ (108 mg), 3-Mercaptopropionic acid (10 µl), deionised water (40 ml), Urea (500 mg) and 37% HCl (500 µl). The chemical bath containing the substrates were placed in an oven for 3 h at 70 °C. Afterwards, the films were washed with deionised water and annealed for 1 h at 180 °C.

Perovskite thin-films:

$MAPb(Br_{0.5}I_{0.5})_3$ thin films were prepared using the acetonitrile route as reported previously [191]. In brief, MAI, MABr, PbI_2 and $PbBr_2$ were weighed out and dissolved in acetonitrile to give a 0.5 M solution as described by Noel *et al.* [191]. The solution

was then spincoated onto the substrate in a nitrogen filled glovebox at 2000 rpm. The films were then annealed for 1 h at 100 °C.

$MAPbI_3$ thin films were prepared similarly to the $MAPb(Br_{0.5}I_{0.5})_3$ thin films, except that a 1 M solution of MAI and PbI_2 in acetonitrile was made to ensure that the films were of the same thickness as the $MAPb(Br_{0.5}I_{0.5})_3$ films.

Spiro-OMeTAD layer:

73 mg of 2,2',7,7'-Tetrakis[N,N-di(4-methoxyphenyl)amino]-9,9'-spirobifluorene (spiro-OMeTAD) was dissolved in 1 ml of chlorobenzene. Thereafter 38 µl of lithium bis(trifluoromethanesulfonyl)imide solution (170 mg ml^{-1} in 1-butanol) and 21 µl of 4-tert-butylpyridine was added to the 1 ml solution of spiro-OMeTAD. The final solution was then spincoated in a nitrogen filled glovebox at 2000 rpm for 45 s. The resulting films were left to oxidise in a desiccator for 24 h.

Gold electrode:

Gold electrodes were deposited at 1×10^{-6} mbar in a thermal evaporator. The thickness of the electrodes was ∼100 nm.

PMMA layer for thin-film samples:

PMMA (Sigma Aldrich, average M_W 97 000 g mol^{-1}) was dissolved in chlorobenzene with a concentration of 150 mg mL^{-1}. The solution was spin coated at 2000 rpm for 45 s on top of the perovskite films.

3.1.3 $FA_{0.83}Cs_{0.17}Pb(Br_xI_{(1-x)})_3$ Thin Films

The fabrication of $FA_{0.83}Cs_{0.17}Pb(Br_xI_{(1-x)})_3$ thin films as detailed in this section was performed by R. D. J. Oliver, Department of Physics, University of Oxford.

Substrate cleaning:

Substrates made of z-cut quartz (area 1.3 cm^2) were cleaned by subsequent sonication in Decon90 (1 vol% in deionised water), deionised water, acetone (Sigma Aldrich) and

isopropanol (Sigma Aldrich) for 5 min each. The substrates were then dried using an N_2 gun before being transferred into an N_2 filled glovebox prior to deposition of the perovskite layer.

$FA_{0.83}Cs_{0.17}Pb(Br_xI_{(1-x)})_3$ perovskite layer preparation:

$FA_{0.83}Cs_{0.17}Pb(Br_xI_{(1-x)})_3$ thin film samples were fabricated in line with a previous report [193], with slight modification to account for the different substrate area and different bromide fractions. In summary, the precursors salts (formamidinium iodide, FAI, GreatCell Solar; caesium iodide, CsI, 99.99%, Alfa-Aesar; lead iodide, PbI_2, 99.999%, Alfa-Aesar; lead bromide, $PbBr_2$, >98%, Alfa-Aesar) were weighed stoichiometrically in an N_2 filled glove box. The precursor salts were dissolved in a 4:1 ratio by volume of N,N-dimethylformamide (DMF, Sigma Aldrich) to dimethyl sulfoxide (DMSO, Sigma Aldrich), to a concentration of 1.3 M. The solution was stirred overnight before deposition. To allow a conversion between perovskite emission energy and perovskite bromide content – see Section 3.4.2 – two solutions of $FA_{0.83}Cs_{0.17}PbI_3$ and $FA_{0.83}Cs_{0.17}PbBr_3$ were prepared and mixed in appropriate ratios to span the compositional range from $x = 0$ to $x = 1$. For all other photoluminescence (PL) and X-ray diffraction (XRD) measurements – those presented in Chapter 6 – the $FA_{0.83}Cs_{0.17}Pb(Br_{0.4}I_{0.6})_3$ perovskite precursor solution was prepared directly.

The perovskite films were fabricated using the following spincoating recipe: 50 µl of precursor solution was deposited dynamically onto the quartz substrate spinning at 1000 rpm. After 5 s, the substrate accelerated at 800 rpm s^{-1}, until it reached a final spin speed of 5000 rpm where it remained for 30 s. An antisolvent quench using 50 µl of Anisole (Sigma Aldrich) was performed 5 s before the end of this step. The films were then annealed at 100 °C for 30 min.

PMMA layer:

PMMA (poly(methyl methacrylate), Sigma Aldrich, mean molar weight 97 000 g mol^{-1}) was dissolved in chlorobenzene (Sigma Aldrich) at 150 mg ml^{-1}. To form the PMMA film, 40 µl of solution was deposited dynamically onto the perovskite film at 2000 rpm, for 25 s. The films were then annealed at 100 °C for 1 min to drive off any residual solvent.

Final sample preparation:

After deposition of the PMMA layer, the $FA_{0.83}Cs_{0.17}Pb(Br_{0.4}I_{0.6})_3$ thin film samples were annealed at 100 °C for 30 min.

3.2 Photoluminescence

Photoluminescence (PL) contains a wealth of information about the electronic energy states experienced by the excited charge-carriers within the emitting material. As such, PL measurements are ideal tools for examining the changing energy landscape within mixed-halide perovskites experiencing the halide segregation phenomenon, and PL techniques are heavily utilised throughout the work presented in this thesis. PL emission from a material can be described as a three-stage process. First, a photon incident on the material is absorbed and generates an electron-hole pair through stimulated absorption. Second, these photoexcited charge carriers then experience the electronic energy states available in the material, and may go through several process such as thermalisation or capture by trap states. Third, an electron-hole pair recombines through the spontaneous emission process, and thereby emits a photon with a wavelength dictated by the difference in energy levels of the recombining charge carriers. The distribution of PL photon wavelengths emitted from the material, and the temporal distribution of PL photon emission times, can then reveal information about the behaviour of the charge carriers within the material between the photoexcitation and recombination events. Therefore, the emitted PL photons are often differentiated either by their wavelength (or energy), or by the time at which they were detected. The first case (differentiating by wavelength

or energy) has the benefits of being a relatively simple measurement technique, and can reveal basic information about the electronic energy states surrounding the band edges in a semiconducting material. This PL measurement technique was used to collect a large amount of the data presented throughout this thesis, and is discussed in Section 3.2.1. The second case (differentiating the PL photons by detection time) is slightly more complicated, and can be achieved through a technique known as time-correlated single photon counting (TCSPC), which is detailed below in Section 3.2.2.

3.2.1 Steady-State PL Measurements

Steady-state PL measurements are a fundamental spectroscopy tool, and are often used to investigate the basic optoelectronic properties of a semiconducting material. In particular for the work presented in this thesis, steady-state PL measurements are very sensitive to the bandgap of a material, and so are commonly used to track the low-bandgap regions of perovskite that form during the halide segregation process [17]. Steady-state PL refers to the measurement of the photons emitted from a photoexcited sample that is in equilibrium with an illumination source, such as a continuous-wave laser. A steady-state PL measurement setup therefore consists of an illumination source to photoexcite the sample, and collection optics to collect the PL emitted from the measurement sample. In the setup used to collect the steady-state PL data presented in this thesis, a 400 nm wavelength diode laser (Picoharp, LDH-D-C-405M), operated under continuous wave conditions was used as an illumination source. The intensity of the incoming laser illumination was coarsely controlled with suitable neutral-density filters along the incoming beam path, and finely controlled by adjusting the settings of the laser driver. Apertures and lenses along the beam path were used to control the beam spot size and shape. An achromatic doublet was used to collimate the PL from the sample, which is emitted over a wide range of angles. A linear polariser was

then used to avoid the effects of Wood's anomaly from the diffraction grating later in the beam path, and a filter was used to remove any laser scatter from the PL signal. The collimated PL was then focused onto the entrance slit of a grating spectrometer (Princeton Instruments, SP-2558), which then internally re-collimated the light onto a diffraction grating. The diffraction grating split the light spatially according to its wavelength, and the separated light was then focused onto an intensified charge-coupled device (iCCD) camera for detection. The iCCD camera has a 2-dimensional detection face, one dimension of which was aligned with the spectral separation of the measured PL. The position of the PL signal upon the iCCD camera detection face could then be used to determine the wavelength of the PL, and the associated photon energy.

iCCD cameras are ideal for PL measurements due to their high sensitivity to incoming photons, which is due to the image intensifier tube component of the iCCD [194]. In short, the image intensifier tube is comprised of three components, which together multiple the number of incoming photons into a larger number of output photons, allowing for easier detection of low PL signals. The first component is a photocathode, which releases a photoelectron when struck by an incident photon. The released electron is then accelerated by an electric field into and through the microchannel plate – the second component of the intensifier tube. The microchannel plate consists of narrow hexagonal tubes ($\sim$10 µm across), one of which the accelerated electron travels through. After being accelerated to high enough speeds, the original photoelectron has enough kinetic energy to excite more electrons from the tube walls of the microchannel plate, which themselves are accelerated by the electric field and can repeat the same process. Eventually the generated cloud of electrons strike a phosphor screen, causing a large number of photons – more than those associated with the original PL signal – to be emitted. The emitted photons are then coupled into a charge-coupled device (CCD) array, which accumulates charge according to the number of incident photons. Finally, the charge attributed to each bin in the CCD

array is read off as a voltage and converted into an image, which contains both spatial and intensity data regarding the original incident PL signal [194, 195].

3.2.2 Time-Correlated Single Photon Counting

As mentioned above, TCSPC is a technique used to gain temporal information about the PL emitted from a given material, and is used in Chapters 4 and 5 to uncover information about the charge-carrier dynamics in mixed-halide perovskite materials. In TCSPC measurements, a short pulse of illumination is used to photoexcite charge carriers in the measurement sample, before those charge carriers recombine and emit photons with a time-dependent distribution, typically over the course of nanoseconds to microseconds [196]. For the TCSPC measurements presented in this thesis, illumination was provided by a 400 nm wavelength diode laser (Picoharp, LDH-D-C-405M) operated under pulsed conditions, and the collection of the emitted PL photons was done as described in Section 3.2.1. An adjustable mirror within the grating spectrometer (Princeton Instruments, SP-2558) was used to direct the measured PL onto a single-photon avalanche diode (SPAD) (PDM series from MPD) for TCSPC measurements, as opposed to the iCCD camera used for stead-state PL measurements. Signal timing in the TCSPC setup was controlled by a PicoHarp 300 TCSPC Event Timer.

Measuring the temporal distribution of PL emitted from a sample after a short burst of incident illumination is difficult because photon detectors are often unable to register photon events for a short time immediately following a previously registered photon event. This “dead” time commonly associated with the detector and electronics of the system can last up to several tens of nanoseconds, and so if multiple photons spread over a few nanoseconds are incident on the detection apparatus, only the ones with the earliest arrival times are likely to be registered. The over-emphasis of photons with early arrival times is an effect known as “pile-up”, and makes it impossible to accurately

measure the temporal distribution of photons emitted from a sample on a nanosecond timescale when using a single illuminating laser pulse. Instead, the accumulation of data occurs over multiple laser pulses, and the incoming PL signal is attenuated such that only one photon is likely to be detected from each pulse, preventing a second incoming photon from going unrecorded during the detection process of the previous photon. For example, a typical TCSPC setup will run with about a 1% chance of detecting an emitted PL photon from any given pulse, making the probability of missing a second emitting photon from any given pulse around 0.01%. Photons from many illumination pulses can then be binned according to their arrival time at the detector, allowing for the creation of a histogram of arrival times that reflects the emission time of the photons from the photoexcited material, and which is therefore a measure of the underlying charge-carrier dynamics within the material [196].

Purposely receiving small amounts of signal in order to minimise error means that highly sensitive detection equipment – often alongside long accumulation times – is required to perform TCSPC measurements. In the setup used to measure the TCSPC data presented in this thesis, a single-photon avalanche diode (SPAD) was used to detect the PL signal. A SPAD consists of a p-n diode capable of absorbing incident photons and generating free charge carriers, with a large voltage held across the diode to accelerate any photoexcited free charge carriers. The accelerated charge carriers are given enough kinetic energy to excite further free charge carriers within the diode, which are themselves also accelerated, causing an avalanche of current to be generated from a single photon-absorption event. In this manner, a SPAD is highly sensitive to even single incident photons, allowing for the low-signal conditions required for TCSPC measurements to be met [196].

3.2.2.1 Fitting to TCSPC Data

This section outlines the specific data analysis techniques used on the TCSPC data discussed in Chapter 4. As discussed in Section 2.1, the rate of radiative recombination in semiconductors under certain film and illumination conditions is approximately equal to $k_2 n(t)^2$, where k_2 is the bimolecular recombination constant, n is the photoexcited charge-carrier density, and t is time. TCSPC measurements record photons emitted from the photoexcited sample, making TCSPC sensitive only to radiative recombination and so to $k_2 n(t)^2$. Accordingly, in order to extract values for k_1 and k_2, a functional form for $k_2 n(t)^2$ is required to fit to the TCSPC data. Given that TCSPC measurements occur under pulsed laser conditions, the discussion in Section 2.1.2 explains that the charge-carrier dynamics are governed by Equation 2.3. Rather than extract values for k_1 and k_2 simultaneously, it is desirable to first use a fitting method that is sensitive to k_1 only. At low charge-carrier densities, such as at low excitation fluence or at times long after the pulse arrival, the dominant term in Equation 2.3 is $k_1 n$, and so the charge-carrier dynamics are well approximated by:

$$\frac{\mathrm{d}n}{\mathrm{d}t} = -k_1 n \tag{3.1}$$

Solving Equation 3.1 for $n(t)$ results in the following equation for $k_2 n(t)^2$:

$$\text{PL Intensity} \propto k_2 n(t)^2 = k_2 n_0^2 e^{-2k_1 t} \tag{3.2}$$

Here n_0 is the charge carrier density initially generated by the laser pulse, and the other symbols have been otherwise stated. Taking the natural logarithm of Equation 3.2 results in:

$$\ln\left(\frac{(k_2 n(t)^2)}{(k_2 n_0^2)}\right) = -2k_1 t \tag{3.3}$$

Thus, at low charge-carrier densities, the gradient of TCSPC data plotted on a log-lin scale is related only to the monomolecular decay rate constant, k_1. Measuring the gradient

of the logarithm of TCSPC data taken with a low excitation fluence, or only extracting the value of the gradient at long times in the data plot, therefore allows for the extraction of the value of $-2k_1$, and therefore the value of k_1.

In order to extract the value for k_2 from TCSPC data, it is necessary to consider the regime in which the charge-carrier density is high enough to induce a significant amount of radiative recombination. It is assumed, however, that the charge-carrier densities reached under the typical illumination intensities used in TCSPC measurements ($< 1800\,\mathrm{W\,m^{-2}}$ in the work presented in this thesis) do not significantly excite the higher-order Auger recombination processes. As a result of this assumption, the dynamics of the recombination processes are described by the following rate equation:

$$\frac{\mathrm{d}n}{\mathrm{d}t} = -k_1 n - k_2 n^2 \tag{3.4}$$

This equation can be solved analytically to find:

$$n(t) = \frac{k_1 n_0 e^{-k_1 t}}{k_1 + k_2 n_0 (1 - e^{-k_1 t})} \tag{3.5}$$

And so:

$$k_2 n(t)^2 = \frac{k_2 k_1^2 n_0^2 e^{-2k_1 t}}{(k_1 + k_2 n_0 (1 - e^{-k_1 t}))^2} \tag{3.6}$$

In theory, n_0 can be calculated from knowledge of the illumination pulse fluence and volume, and the absorption parameters of the measured sample. Equation 3.6, multiplied by a constant to take into account the imperfect outcoupling of photons emitted from radiative recombination to the measurement apparatus, and utilising the previously fitted value for k_1, can then be fitted to acquired TCSPC data to extract values for k_2. In the work presented in Chapter 4, it is unclear how the flux of photons incident on the measured sample relates to the charge-carrier density within the sample, due to the funnelling of charge carriers within the perovskite material experiencing halide segregation. Therefore in Chapter 4 values for both k_2 and n_0 were extracted from fits of the data to Equation 3.6.

3.3 X-Ray Diffraction

3.3.1 Theory

X-ray diffraction (XRD) measurements are extremely versatile and can uncover a wealth of structural information about crystalline and polycrystalline materials, making them ubiquitous throughout many branches of condensed matter physics. Accordingly, XRD measurements have been used to varying degrees in the study of mixed-halide perovskites and the halide segregation process [17, 92, 121]. In Chapter 6, XRD and PL techniques are used in tandem to correlate structural and optoelectronic properties of mixed-halide perovskites during illumination, and during the movement of halide ions associated with halide segregation. This section briefly introduces the main principles of XRD measurements.

As with any experiment that involves the scattering of a beam of incoming particles, energy and momentum conservation laws are key to XRD experiments [197]. Typically XRD experiments involve the measurement of elastically scattered X-rays off a crystalline structure, resulting in the conservation of energy across the incoming and outgoing X-ray waves. The conservation of energy in this case means that the wavevector of the incoming X-ray beam ($\vec{k}$) remains equal in magnitude to the wavevector of the scattered, measured beam ($\vec{k'}$), i.e.:

$$\left|\vec{k}\right| = \left|\vec{k'}\right| \tag{3.7}$$

The fundamental periodicity of a crystalline lattice means that scattering events occurring within such an environment must conserve crystal momentum, rather than actual momentum (the actual momentum of the system is conserved by changes to the momentum of the crystal lattice itself). The conservation of crystal momentum means that the difference in the wavevectors of the incoming and outgoing X-ray waves must be equal

to a reciprocal lattice vector, $\vec{G}$:

$$\vec{k}' - \vec{k} = \vec{G} \tag{3.8}$$

Within the two constraints of energy and crystal momentum conservation, only certain X-ray scattering events are allowed. In fact, it can be seen geometrically that for every reciprocal lattice vector, $\vec{G}$, there exists only one incoming angle at which X-ray photons can enter the crystal structure and be scattered, and only one corresponding outgoing angle they can be scattered to. Figure 3.1 highlights that these incoming and outgoing angles of a scattered X-ray beam are, in fact, equal, and depend on the reciprocal lattice vector, $\vec{G}$. Each reciprocal lattice vector corresponds to a single family of planes in the corresponding real-space crystalline structure. Therefore, measurements of the allowed scattering angles for X-rays incident on a crystalline material reveal information about the type and nature of the lattice planes within said material [197].

A common parameter investigated in XRD measurements – and in particular in Chapter 6 – is the distance between lattice planes in a crystalline material. The reciprocal lattice vector, $\vec{G}$, associated with a set of similar lattice planes satisfies the following relation:

$$\left|\vec{G}\right| = \frac{2\pi}{d} \tag{3.9}$$

where d is the distance between adjacent lattice planes in the set of planes associated with $\vec{G}$. Using the above relation between $\vec{G}$ and d, the relation between the wavevector of a photon and its wavelength ($\left|\vec{k}\right| = \frac{2\pi}{\lambda}$), the equations for the conservation of energy (Equation 3.7) and crystal momentum (Equation 3.8), and the geometric relations between $\vec{G}$, $\vec{k}$ and $\vec{k}'$ highlighted in Figure 3.1 allows for the following derivation:

$$\begin{aligned}
\vec{G} \cdot (\vec{k}' - \vec{k}) &= \vec{G} \cdot \vec{G} \\
\frac{2\pi}{d}\frac{2\pi}{\lambda}(\sin\theta - -\sin\theta) &= \left(\frac{2\pi}{d}\right)^2 \\
2d\sin\theta &= \lambda
\end{aligned}$$

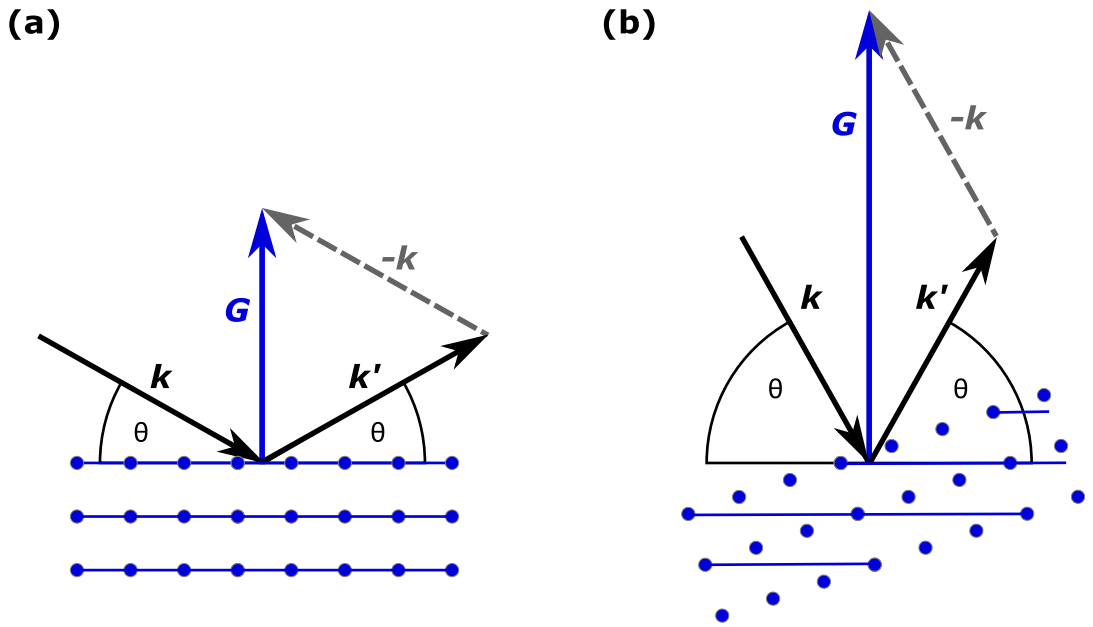

Figure 3.1: Diagrams showing incident and outgoing X-ray beams when scattered off a crystalline structure, and highlighting the geometric nature of the situation. For an elastic scattering event to occur in a crystalline structure, the difference in wavevectors of the incoming and outgoing X-ray beams ($\vec{k}' - \vec{k}$) must equal a reciprocal lattice vector, ($\vec{G}$), and the lengths of the incoming and outgoing X-ray beam wavevectors must be equal ($\left|\vec{k}\right| = \left|\vec{k}'\right|$). Given these conditions, the diagrams in (a) and (b) highlight the only available scattering geometry for a smaller and larger value of $\vec{G}$, respectively. The direction and magnitude of $\vec{G}$ is shown in (a) and (b) to depend on the nature and spacing of the associated lattice planes in the crystal, although the diagrams are not to scale.

With the final line above corresponding to the Bragg condition. Using the relation $2d\sin\theta = \lambda$, experiments can be conducted where λ is known, and θ is varied. When a sharp peak in the amplitude of the scattered X-rays is measured, the Bragg condition is assumed to be fulfilled, and so the lattice spacing d can be deduced by the value of θ the peak corresponds to. More generally, by measuring the θ – or, more commonly, the total angle of beam deflection, 2θ – position of multiple scattered X-ray peaks, information regarding the existence and spacings of multiple sets of lattice planes in a crystalline structure can be obtained. Using such information, detailed knowledge about the structure of the crystalline material can be deduced [197].

3.3.2 Crystallite Size Estimation

The fracturing of a crystalline material into smaller crystalline domains results in the broadening of the recorded XRD peaks from the material [198]. As a result, the size of the crystalline domains within the measured material can be estimated from the width of the recorded XRD peaks according to the Scherrer equation [198]:

$$D = \frac{K\lambda}{\beta \cos\theta} \tag{3.10}$$

where D is the size estimate of the crystalline domains, K is a dimensionless shape factor that is assumed to be equal to 1 for the purposes of the basic crystalline size estimates presented in this thesis, λ is the wavelength of the incident X-rays used for the XRD measurement, β is the full width at half maximum (FWHM) of the investigated XRD peak when measured in radians, and θ is the Bragg angle of the investigated peak. Equation 3.10 allows an estimate of the crystalline domain size within a sample to be made from measurements of a corresponding XRD peak. It is noted that this XRD peak analysis is only perfectly valid if the material is compositionally homogeneous, which is not expected to be true for materials experiencing halide segregation, and for such materials this analysis is expected to only give an estimate of the lower bound to the crystalline domain size of the material. In addition, other factors not accounted for by a basic use of Equation 3.10 – such as the true from of K – may introduce further errors into this analysis. It is emphasised that the crystallite size analysis performed in Chapter 6 according to Equation 3.10 is only meant to highlight the relationship between XRD peak broadening and crystallite size breakdown, rather than to provide accurate estimates of the crystalline domain sizes within the perovskite films.

3.3.3 Basic XRD Measurements

The basic XRD measurements presented in Chapter 6 were made using either a Rigaku Smartlab X-ray diffractometer, or a PANalytical X'Pert powder X-ray diffractometer, and

in both cases were taken from diffraction angle 10° to 50° 2θ, with differing scan speeds of $0.02\,^{\circ}\,s^{-1}$ and $0.01\,^{\circ}\,s^{-1}$, respectively, for the two diffractometers. For both diffractometers the Cu-$K_{\alpha 1}$ line was used as incident radiation, and in order to correct against sample tilt, a relevant z-cut quartz peak in the data was used as a reference and fixed to 2θ =16.43°.

3.4 Simultaneous PL and XRD Measurements

3.4.1 Measurement Overview

Much of the data presented in Chapter 6 were taken utilising a home-built insert to an X-ray diffractometer, allowing concurrent, in situ, PL and XRD measurements to be made while illuminating the investigated sample. The experimental setup consisted of a small setup of optical equipment – displayed in Figure 3.2 – integrated within a Rigaku SmartLab X-ray diffractometer. The illumination source used for the PL measurements was an LDH-D-C-470 fibre-coupled laser, with an emission wavelength of ∼470 nm. Optical fibres were used to feed the incident illumination from the laser source into the Rigaku SmartLab diffractometer, whereupon the laser light was launched into free space and onto the sample. A lens was used to control the laser beam illumination area and intensity. The PL emitted from the sample was collected and coupled into another optical fibre, before being led out of the Rigaku SmartLab and into an Ocean Optics USB2000 spectrometer.

The XRD measurements were taken via the Rigaku SmartLab diffractometer that contained the optical insert, with a HyPix-3000 2D X-ray detector, utilising a Bragg-Brentano reflection geometry. The Cu-$K_{\alpha 1}$ line was used as incident radiation. The 2-dimensional detection face of the X-ray detector allowed measurements to be made over a range of 2θ values without moving the X-ray source, the sample, or the detector. Utilising this static experimental setup, XRD measurements could be taken at a sufficiently fast rate to gain time-resolved information about the halide segregation process. It is noted that, because of the flat measurement face of the X-ray detector, only a small area of the

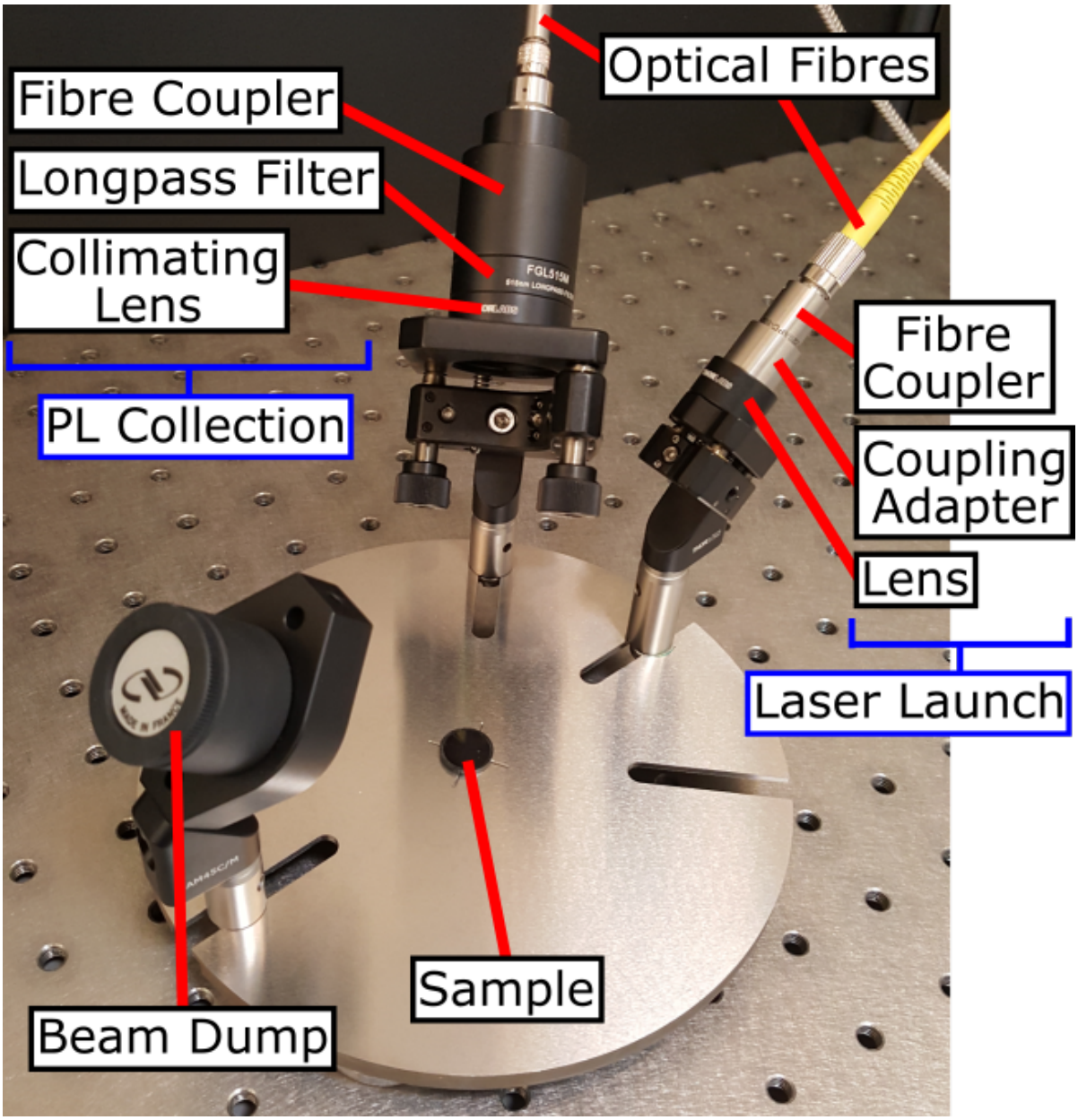

Figure 3.2: Photograph of the optical equipment used to both provide illumination on and collect the PL from a sample for the concurrent PL and XRD measurements discussed in Chapter 6. The optical setup is designed to fit inside a Rigaku SmartLab X-ray diffractometer.

detector face would have been in a true Bragg-Brentano geometry over the course of the conducted experiments. However, given the large distance between the detector and the sample (∼0.3 m) as compared to the dimensions of the detector face (∼0.05 m) it is not expected that the geometry of the setup had a significant effect on the measurement results.

3.4.2 Estimation of Perovskite Bromide Content

The PL emission energy of a mixed-halide perovskite material is influenced by its halide content [17, 43, 65]. Similarly, the lattice spacings within a mixed-halide perovskite material – which influence the 2θ position of measured XRD peaks – are also dependent on the halide content of the perovskite [17, 65, 66, 197]. Thus, assuming that the chemical composition of a given perovskite is determined by the ratio of the halide ions in the material, an estimate of the halide ratio in the perovskite can be made from measurements of either the emission energy or the 2θ position of a known XRD peak and the comparison of such data with those for perovskites with known compositions. In essence, there exists a formula that allows conversion of a PL emission energy into an estimate of the halide content of the emitting perovskite – shown below to be Equation 3.12 – and there exists another formula for converting XRD peak position into an estimate of the halide content of the reflecting perovskite – shown below to be Equation 3.16. Such formulae allow the conversion of horizontal axes (axes of abscissa) for both PL and XRD data such that they are provided in terms of an estimate of the halide content of the investigated mixed-halide perovskite, allowing the optoelectronic and structural properties of the perovskite to be compared. This section details how these conversion formulae were created for use in Chapter 6.

From here on, ABX_3 perovskites are referred to for which B is lead, X is a mixture of iodide and bromide ions, and A is arbitrary but fixed: $APb(Br_xI_{(1-x)})_3$. This particular perovskite composition is most relevant for this thesis, although it is noted that the analysis presented in this section could be applied to other perovskites with different compositions.

3.4.2.1 Estimation Process Based on PL Measurements

In order to create a conversion formula between the PL emission energy of a mixed-halide perovskite and its bromide content, PL measurements must first be made of

similar perovskites with known compositions. PL measurements of $APb(Br_xI_{(1-x)})_3$ perovskite films with known, differing bromide contents, x, allow for an estimate of the PL emission energy, E, to be made across the bromide compositional range. Typically the PL peak emission energy is found to follow a quadratic behavior (referred to as band bowing) as a function of x [17, 43, 65]:

$$E = ax^2 + bx + c \tag{3.11}$$

where a, b and c are parameters determined from the fit of x to the experimentally derived values of E.

Equation 3.11 can be inverted by finding the correct polynomial root, resulting in:

$$x = \frac{-b + \sqrt{b^2 + 4a(E - c)}}{2a} \tag{3.12}$$

Thus, the bromide content, x, of a perovskite can be directly related to PL photon emission energy, E, by inserting E into Equation 3.12, once a, b and c have been determined from measurements of known perovskite compositions.

3.4.2.2 Estimation Process Based on XRD Measurements

In order to create a conversion formula between the 2θ position of a given XRD peak recorded from a perovskite and its bromide content, XRD measurements must first be made of similar perovskites with known compositions. XRD measurements of $APb(Br_xI_{(1-x)})_3$ perovskite films with known, differing bromide contents, x, allow for an estimate of the 2θ position of a given XRD peak to be made across the bromide compositional range. As shown in Section 3.3.1, the 2θ position of an XRD peak is related to the distance between the lattice planes that coherently reflected the XRD signal through Bragg's Law [197]:

$$2d \sin\theta = \lambda \tag{3.13}$$

where d is the distance between the lattice planes that generate the XRD peak, and λ is the wavelength of the incident X-rays.

For a cubic crystal system, the distance between a given set of lattice planes, d, is related to the lattice spacing of the material, a, by the following relationship [197]:

$$d = \frac{a}{\sqrt{h^2 + k^2 + l^2}} \tag{3.14}$$

where h, k and l are the Miller indices of the given set of lattice planes. Via Equations 3.13 and 3.14, it is possible to calculate the lattice spacing, a, of a perovskite from the measured 2θ position of an XRD peak with known h, k and l. Accordingly, this calculation can be performed for a set of perovskites spanning a range of bromide ratios, x, to investigate the relation between bromide content and the resulting perovskite lattice spacing, a. Vegard's law – an empirical law – states that a linear relationship should be found between x and a, i.e. $a = \alpha x + \beta$ [199]. This relationship is usually observed in mixed-halide perovskites, and experimental measurements can determine the value of the fitting constants α and β.

Combining Equations 3.13 and 3.14 leads to the following equation for a:

$$a = \frac{\lambda\sqrt{h^2 + k^2 + l^2}}{2\sin\theta} \tag{3.15}$$

Utilising the linear fit between x and a allows for the derivation of the following equation:

$$x = \frac{\lambda\sqrt{h^2 + k^2 + l^2}}{2\alpha\sin\theta} - \frac{\beta}{\alpha} \tag{3.16}$$

Thus, the bromide content, x, of a perovskite can be estimated by measuring the 2θ position of an XRD peak with known h, k and l indices via an X-ray beam of known wavelength, λ, and inserting the appropriate values into Equation 3.16, given that α and β have been determined from measurements of known perovskite compositions.

3.4.2.3 Estimates for MA- and FACs-Based Perovskites

PL data presented in Figure 3.3 was measured by R. D. J. Oliver, Department of Physics, University of Oxford.

In Chapter 6, estimates of the bromide content of perovskite regions within $MAPb(Br_{0.5}I_{0.5})_3$ and $FA_{0.83}Cs_{0.17}Pb(Br_{0.4}I_{0.6})_3$ thin films are made from recorded PL and XRD data, with calculations performed as according to Sections 3.4.2.1 and 3.4.2.2 above.

For $MAPb(Br_{0.5}I_{0.5})_3$, PL spectra reported in the literature – specifically from Refs. [43], [17], and [65] – were used to determine the relationship between bromide content and PL emission energy. XRD patterns reported in the literature – specifically from Refs. [17] and [65] – were used to determine the relationship between bromide content and the 2θ value of the (200) peak.

For $FA_{0.83}Cs_{0.17}Pb(Br_{0.4}I_{0.6})_3$, PL results recorded in-house – see below and Figure 3.3 – were used to determine the relationship between bromide content and PL emission energy. XRD patterns reported in the literature – specifically from Ref. [66] – were used to determined the relationship between bromide content and the 2θ value of the (220) peak.

PL results for $FA_{0.83}Cs_{0.17}Pb(Br_xI_{(1-x)})_3$ perovskites across the entire $x = 0$ to $x = 1$ compositional range (steps of $x = 0.1$) were recorded in-house, as shown in Figure 3.3. PL spectra were recorded by illuminating the thin film samples with light from a 405 nm laser at an intensity of $\sim$100 mW cm^{-2} when placed in an integrating sphere. The PL spectra were recorded using a QEPRO-FL spectrometer.

3.5 Absorption Spectroscopy

The use of absorption spectroscopy was extremely limited in the work presented in this thesis, and so only the basics of the technique will be discussed here. Photons of different wavelengths upon a given material have different probabilities of undergoing a stimulated absorption process, with the probability of absorption dictated by the photon wavelength and the landscape of electronic energy states within the given material. By analysing how the probability of photon absorption depends on the photon wavelength,

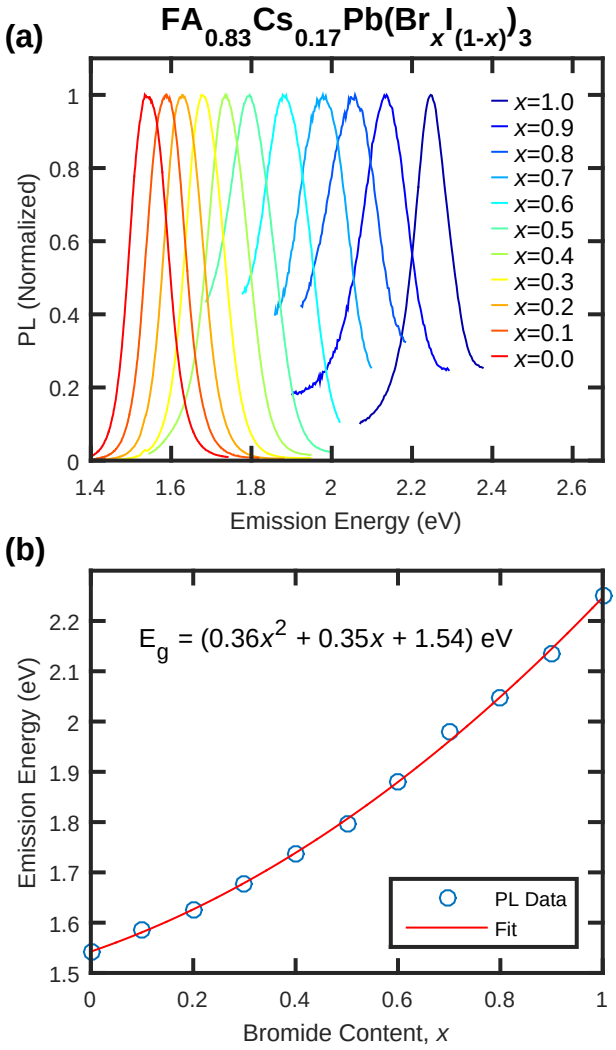

Figure 3.3: PL data measured by R. D. J. Oliver, Department of Physics, University of Oxford. (a) PL spectra showing the high energy, mixed perovskite PL peak from $FA_{0.83}Cs_{0.17}Pb(Br_xI_{(1-x)})_3$ thin films ranging in composition from $x = 1.0$ to $x = 0.0$. The illumination source was at $100\,mW\,cm^{-2}$ intensity and 405 nm wavelength. (b) The centre emission energy of the PL peaks shown in (a) plotted against the bromide content of the perovskite, x. Fitted to this data is a quadratic curve. The PL emission energy exhibits a mild bowing across the compositional range, similar to that previously observed for this perovskite composition [66].

absorption spectroscopy can uncover information about the electronic energy states within the measured material.

Directly measuring the absorption coefficient of a material is difficult, as the excitations in a material generated by the absorption of a photon are often myriad and short lived, and so measuring and accounting for all these excitations is practically impossible. Instead,

the absorption coefficient of a material is deduced from the fact that any light incident on the material that does not transmit through the sample or reflect off it has – to a first approximation – been absorbed. Therefore, the key measurement parameters to determine are the transmittance, T, and the reflectance, R, of the material, which are the fractions of the incident light on the material that are transmitted and reflected, respectively. The absorption coefficient of a material, α, is defined as follows:

$$\alpha(\lambda) = -\frac{1}{d}\log_{10}\left(\frac{T(\lambda)}{1-R(\lambda)}\right) \tag{3.17}$$

where d is the thickness of the measured material, and the absorption coefficient, transmittance, and reflectance of the material are all functions of the wavelength of the incident light, λ. As mentioned above, Equation 3.17 represents a first approximation of the absorption coefficient of a material, and photon scatter and multiple reflection effects must be accounted for in more sophisticated measurements.

In order to calculate the transmittance and reflectance of a sample from the measured transmission and reflection data, reference to the spectrum of incident photons must be made. A simple way of measuring the incident photon flux and accounting for imperfections in the photon coupling of the measurement equipment is to measure the transmitted and reflected signals from samples of known extremely high transmittance and reflectance. Furthermore, background corrections can be applied by measuring samples of known extremely low transmittance and reflectance. Finally, the contribution of the sample substrate can be removed from the transmittance and reflectance spectra by performing similar measurements on a clean substrate. For the work presented in this thesis, these reference measurements were performed on a clean quartz substrate (similar to the substrates used for the perovskite samples) and on a silver mirror. The following equations were then used to estimate the measurement material transmittance and reflectance:

$$T = \frac{t_{\text{sample}} - t_{\text{mirror}}}{t_{\text{substrate}} - t_{\text{mirror}}} \tag{3.18}$$

$$R = \frac{r_{\text{sample}} - r_{\text{substrate}}}{r_{\text{mirror}} - r_{\text{substrate}}} \tag{3.19}$$

where t_{sample}, t_{mirror}, and $t_{\text{substrate}}$ are the transmission spectra measured from the sample, mirror, and quartz substrate, respectively, and r_{sample}, r_{mirror}, and $r_{\text{substrate}}$ are the corresponding reflection spectra measured from the sample, mirror, and quartz substrate, respectively.

3.5.1 AM1.5-Equivalent Intensity

"AM1.5 equivalent intensity" is defined here as the laser intensity at which the same density of charge carriers is photoexcited in a perovskite film as would be under the AM1.5 solar spectrum [200]. This laser intensity is used in Chapter 4 in order to investigate the halide segregation mechanism in $MAPb(Br_{0.5}I_{0.5})_3$ thin films under illumination intensities relevant for commercial solar cells. Due to the sharp absorption onset in the $MAPb(Br_{0.5}I_{0.5})_3$ perovskite films (characterised in Section 4.3) it is expected that only a small number of above-gap photons will pass through the entire film, and thus in this calculation of the AM1.5 equivalent intensity the total absorption of all incident photons with energies higher than the bandgap is assumed. The AM1.5 equivalent intensity is therefore taken to be the same laser intensity at which the flux of incident laser photons matches the flux of above-bandgap photons from the AM1.5 spectrum. The bandgap of the mixed-phase perovskite was determined to be around 665 nm from measurements of the PL and absorption spectra (see Section 4.3), while the iodide-rich phase produced an emissive peak centred on different values depending on the measurement taken, likely due to spot-to-spot variations in the perovskite films. The formed iodide-rich phase PL peak was also observed to red-shift as the perovskite film segregated further, thus making the determination of a bandgap for the iodide-rich perovskite difficult. 745 nm was determined as a suitable representative value. Calculating the effective bandgap of a segregating material is complicated, however it has been reported that the majority of the

perovskite remains near the initial stoichiometric composition throughout the segregation process, with only around 20% of the perovskite converting to the iodide-rich phase [17]. Hence for the calculation of an AM1.5 equivalent intensity an effective bandgap of 680 nm was selected as an 80:20 weighted average of the mixed and iodide-rich perovskite bandgaps. While no single effective bandgap can be completely accurate at all times as the film segregates, the AM1.5 equivalent intensity defined here should generate the same order of magnitude of charge carriers in the perovskite films under laser illumination as the AM1.5 spectrum would. The AM1.5 spectrum represents the power per unit area emitted from the sun at different photon wavelengths, denoted here as AM1.5(λ) [200] and measured in $\mathrm{W\,m^{-2}\,nm^{-1}}$. The number of photons emitted per unit time per unit area in the wavelength range λ to $\lambda + \mathrm{d}\lambda$ is then $\mathrm{AM1.5}(\lambda) \times (\frac{hc}{\lambda})^{-1} \times \mathrm{d}\lambda$, where $\frac{hc}{\lambda}$ is the energy of a photon with a wavelength of λ. Integrating over this expression from $\lambda = 0\,\mathrm{nm}$ to $\lambda = 680\,\mathrm{nm}$ reveals that, under an AM1.5 spectrum for the given scenario, there are 1.19×10^{21} photons per second per meter squared incident on a perovskite material which are above bandgap. The value of 1.19×10^{21} photons per second per meter squared at 400 nm wavelength – the laser wavelength used in Chapter 4 – then corresponds to a laser power of $591\,\mathrm{W\,m^{-2}}$, which is taken as the AM1.5 equivalent power.

3.5.2 Absorption Measurements

The absorption coefficient data presented in Chapter 4 were measured with a Bruker Vertex 80v Fourier-transform infrared spectrometer fitted with the reflection/transmission accessory, a tungsten halogen lamp source, a CaF_2 beamsplitter, and a silicon diode detector. The reference spectra were performed on a Thorlabs UV-protected silver mirror, and on a clean quartz substrate. The thickness of the sample was determined from SEM measurements performed by J. B. Patel at the Department of Physics, University of Oxford – see Section 4.3.

3.6 External Quantum Efficiency Measurements

The external quantum efficiency (EQE) of a solar cell is the ratio of the charge carriers extracted from the cell to the number of photons incident upon the solar cell, and is a function of incident photon wavelength. It is determined by measuring the extracted current from the solar cell as it is illuminated under a known excitation source. In the measurements presented in Chapter 5, Fourier transform photocurrent spectroscopy was utilised to measure the EQE of $MAPb(Br_{0.5}I_{0.5})_3$ solar cells. In Fourier transform photocurrent spectroscopy measurements a Michelson interferometer is used to create an interferogram from an incident light spectrum. To do so, a beamsplitter is used to split the source spectrum along two paths, with one path leading to a fixed mirror and the other leading to a movable mirror. The movable mirror then adds an adjustable amount of path difference between the two beam paths before they are recombined at the beamsplitter. The constructive and deconstructive interference of the different photon wavelengths results in, for a given mirror position, the strengthening and weakening of particular amplitudes of the different photon wavelengths from the initial source spectrum. The dependence of the overall output light intensity as a function of the position of the adjustable mirror generates the interferogram data. By recording the current extracted from the measured solar cell when illuminated with the output light from the interferometer for a large number of mirror positions, it is possible to perform Fourier analysis on the resulting interferogram data to reveal the extracted current from the solar cell when illuminated with a small wavelength interval of the incident source spectrum. Fourier transform photocurrent spectroscopy therefore allows for the rapid measurement of wavelength-dependent data without the complications required of a monochromator-based setup.

The EQEs of the $MAPb(Br_{0.5}I_{0.5})_3$ perovskite solar cells studied in Chapter 5 were measured via a custom built Fourier transform photocurrent spectrometer based on a Bruker Vertex 80v Fourier Transform Interferometer. The devices were illuminated with simulated sunlight with a class AAA Oriel solar simulator. The devices were calibrated to a Newport-calibrated reference silicon solar cell with a known external quantum efficiency. The solar cells were masked with a metal aperture with a defined active area of $0.0625\,cm^2$.

4

Atmospheric Effects and Photon Efficacy in Halide Segregation

Contents

Initially published as Ref. [150].

4.1 Introduction and Background

The experimental work presented in this thesis begins with a fundamental examination of the halide segregation dynamic, and on the basic atmospheric influences on the halide segregation mechanism. As detailed in Section 2.4.5, there is a vast and varied literature discussing the changes observed in the optoelectronic properties of mixed-halide perovskites under different atmospheres [118, 124, 144, 170, 171]. Given the potential of mixed-halide perovskites as a tandem solar cell material, a detailed understanding of both the underlying mechanisms behind these atmosphere-caused changes to perovskite materials and the halide segregation process is desired, with the ultimate aim of suppression or exploitation of these mechanisms under working conditions. Unfortunately, the segregation dynamics reported from PL experiments in the literature are often inconsistent; even among similar perovskite compositions and illumination intensities, the time taken for halide ions to segregate varies between tens of seconds [17, 94, 96] and tens of minutes [66, 93, 176], and the intensity ratio of the initial and final PL peaks varies between roughly 2 to more than 6 [17, 66, 93, 94, 96, 176]. Given the changes in PL intensities that are known to be induced by light and different atmospheres in single-halide perovskites over time [24–32, 201], such discrepancies in the literature on mixed-halide perovskites may therefore potentially be partly caused by the differences in the atmosphere under which perovskites were held, likely alongside other differences such as processing techniques and resulting film crystallinity.

The contribution of atmospheric effects to the contradictions in the literature is determined in Section 4.4.1 by a careful examination of the role of the environmental atmosphere on halide segregation dynamics in $MAPb(Br_{0.5}I_{0.5})_3$ observed through PL experiments. It is found that changes in the PL spectra of mixed-halide perovskites under illumination vary markedly under different atmospheres, with overall trends in

PL amplitudes resembling changes observed in single-halide perovskites, which are however combined with environmentally dependent halide segregation dynamics. It is demonstrated that the influence of atmospheric changes can be mostly suppressed by encapsulation of the perovskite films with a thick (>1 µm) layer of poly(methyl methacrylate) (PMMA), which is a practice adopted whenever possible throughout the experimental work presented in this thesis. Section 4.4.2 details an examination of the role of photogenerated charge-carrier density on the dynamics of halide segregation, where charge carriers recombining through trap-mediated routes are shown to be responsible for halide segregation. The work in Section 4.4.2 allows the creation of an empirical model for the growth of the iodide-rich perovskite PL over time, as a function of various film and illumination parameters. Section 4.4.3 compares the predictions of said empirical model to results in the literature on halide segregation in perovskite films exposed to pulsed illumination, to great success. The empirical model is further utilised to predict that a reduction of the trap-related charge-carrier recombination rate to $\lesssim 10^5\,\mathrm{s}^{-1}$ ($\tau_1 \gtrsim 5\,\mu\mathrm{s}$) would be sufficient in order for halide segregation to be largely suppressed in working perovskite solar cells based on $MAPb(Br_{0.5}I_{0.5})_3$. In Section 4.5 it is proposed that light-induced halide segregation can be understood as a positive feedback system, initiated by electric fields arising from trapped charge carriers and further driven by funnelling of charge carriers into the generated lower-energy iodide rich domains. Finally, Section 4.6 summarises and concludes the results of this chapter.

4.2 Experimental Details

The majority of the data presented in this chapter are steady-state PL data that were collected as described in Section 3.2.1. The TCSPC measurements were collected as described in Section 3.2.2, and the basic absorption measurements presented in Section 4.3 were collected as described in Section 3.5.2.

4.3 Basic Sample Characterisation

4.3.1 Basic PL Measurements

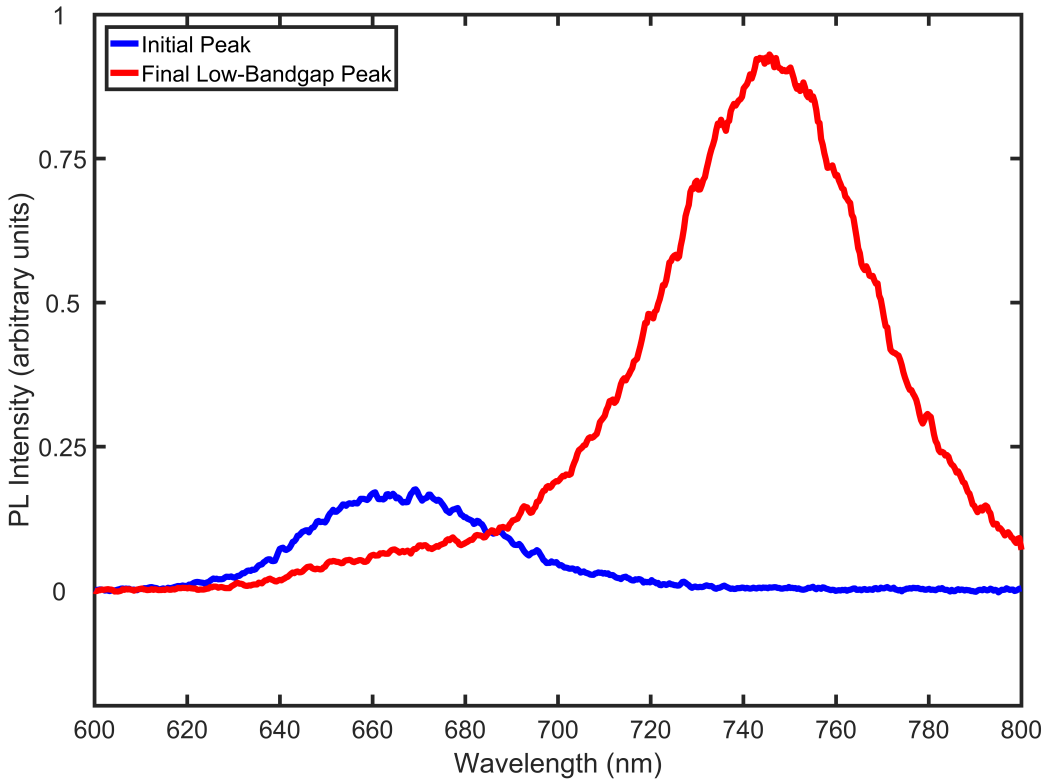

Figure 4.1: PL taken from a PMMA coated $MAPb(Br_{0.5}I_{0.5})_3$ perovskite thin film held under vacuum before (blue) and after (red) 21 seconds of light-soaking under 4.1 kW m^{-2} intensity illumination at 400 nm wavelength.

Figure 4.1 shows the PL emitted from a PMMA coated $MAPb(Br_{0.5}I_{0.5})_3$ perovskite thin film under vacuum before (blue) and after (red) 21 seconds of light-soaking under 4.1 kW m^{-2} intensity illumination at 400 nm wavelength. The emission wavelength of the initial PL peak was determined to be 665 nm and the wavelength of the formed, low-bandgap PL peak varied across spots on the perovskite films, but was generally measured around 745 nm.

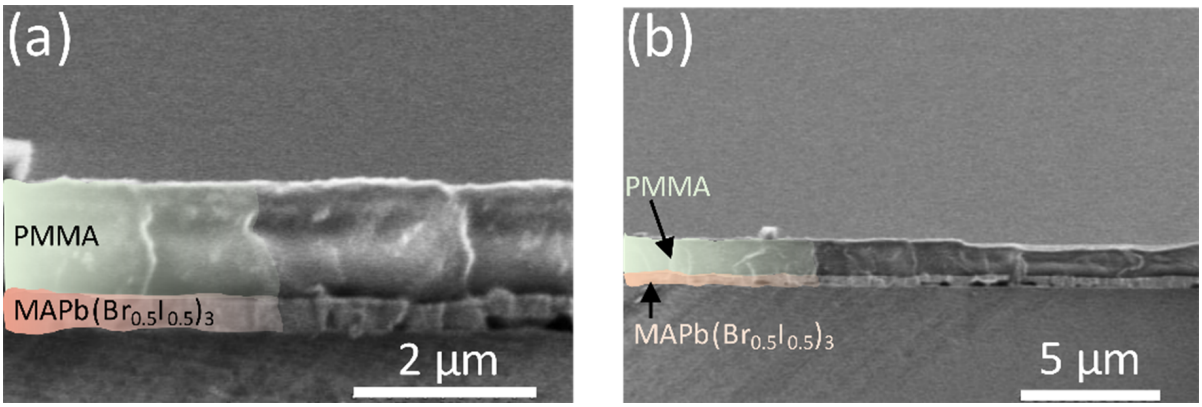

Figure 4.2: Cross-sectional SEM images of the $MAPb(Br_{0.5}I_{0.5})_3$ films with the poly(methyl methacrylate) (PMMA) coating. The same section of film is shown in (a) with a scalebar of 2 µm and in (b) with a scalebar of 5 µm.

4.3.2 Determining Sample Layer Thicknesses

SEM measurements performed by J. B. Patel, Department of Physics, University of Oxford.

The thickness of the $MAPb(Br_{0.5}I_{0.5})_3$ perovskite and poly(methyl methacrylate) (PMMA) layers of the samples was measured from SEM cross-sectional images (see Figure 4.2). The average perovskite layer thickness was found to be 390 nm ± 12% and the average PMMA layer thickness to be 1300 nm ± 6%.

4.3.3 Absorption Spectrum Measurement

An absorption spectrum was obtained from an $MAPb(Br_{0.5}I_{0.5})_3$ film coated with a thick layer of PMMA – see Figure 4.3. The band edge was found to be close to 665 nm, in agreement with the initial PL peak shown in Figure 4.1.

4.4 Main Experimental Results

4.4.1 Atmospheric Effects on Halide Segregation

The main experimental work presented in this chapter begins by establishing how atmospheric conditions influence the changes observed in the PL spectrum of mixed-halide perovskite films during halide segregation and remixing experiments. Assessment

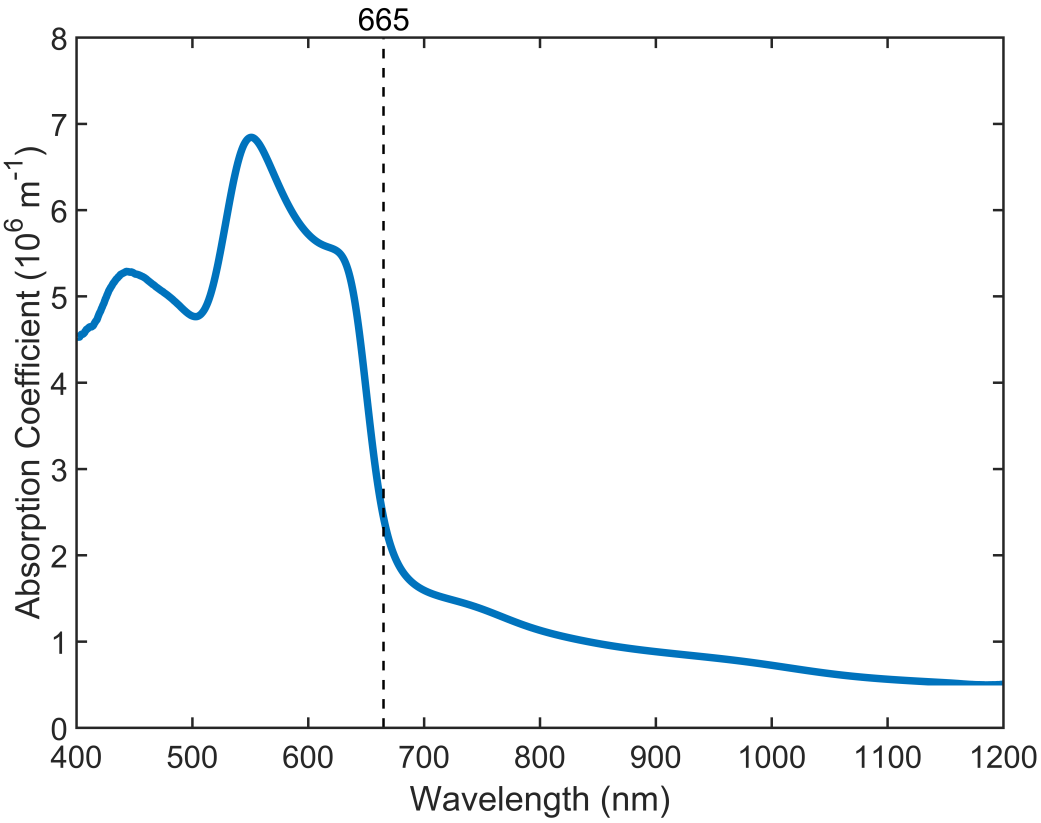

Figure 4.3: Absorption spectrum of an $MAPb(Br_{0.5}I_{0.5})_3$ film coated with a thick layer of PMMA.

of such environmental factors is not only useful for research laboratory studies, but will also give insight into the operation of these wide-bandgap materials under real-world conditions. Figure 4.4 shows that under illumination, the PL spectra of an $MAPb(Br_{0.5}I_{0.5})_3$ perovskite film exhibit a complex fingerprint of both halide segregation and atmospheric effects. Here, the 390 nm thick films were periodically exposed to light under different atmospheric conditions for 8 cycles of induced halide segregation and remixing, where each cycle consisted of 15 seconds of illumination, followed by 30 minutes of darkness. Illumination was conducted by a laser of 400 nm wavelength at an AM1.5 equivalent intensity (591 $W\,m^{-2}$, see Section 3.5.1 for details). Four different atmospheric conditions were explored: vacuum (around 0.2 mbar), air, pressurised nitrogen (around 2 bar), and vacuum with a PMMA top-coating to encapsulate the perovskite films. In

order to probe the full range of segregation and remixing dynamics, the periods of darkness were 120 times as long as the periods of illumination to ensure that the films had sufficient time to recover from the halide segregation. The graphs in Figure 4.4 plot the integrated intensity of two different regions of the perovskite PL spectrum (see Figure 4.1 for examples of the perovskite PL spectra), the range 720 nm-770 nm is plotted in blue and follows the iodide-rich perovskite PL peak, and the range 640 nm-690 nm is plotted in green and follows the mixed-phase PL peak, both scaled such that the initial mixed phase PL measurement is equal to 1. In order to account for spot-to-spot variations in the perovskite, several repeats under each atmospheric condition were performed on different areas of the films. The bold lines in Figure 4.4 show the averaged data from these repeats, and the shaded regions indicate values within one standard deviation of the mean.

Each light/dark cycle for any of the four atmospheric conditions clearly displays an increase in the PL signal of the iodide-rich phase under illumination, indicating that lower bandgap, iodide-rich perovskite regions are forming within the remaining well-mixed phase. The growth rate of low-bandgap signal is heavily dependent on the surrounding atmosphere, with different maximum PL signal intensities reached under the different atmospheres, despite identical illumination conditions used. As the low-bandgap signal was found to have returned to its initial value at the start of every repeat cycle, the 30 minutes of darkness within each cycle is concluded to be sufficient to allow the segregated perovskite to remix. However, under vacuum and under air, the films otherwise clearly do not fully revert to their initial states under darkness, given that the halide segregation dynamics recorded in subsequent cycles progressively differ from those observed in the first cycle. Comparing PL amplitudes from either the iodide-rich or mixed-phase peaks across similar points in each cycle (e.g. the last point of each cycle), it is observed that the long-term changes in the PL intensities displayed in Figure 4.4 are qualitatively similar to

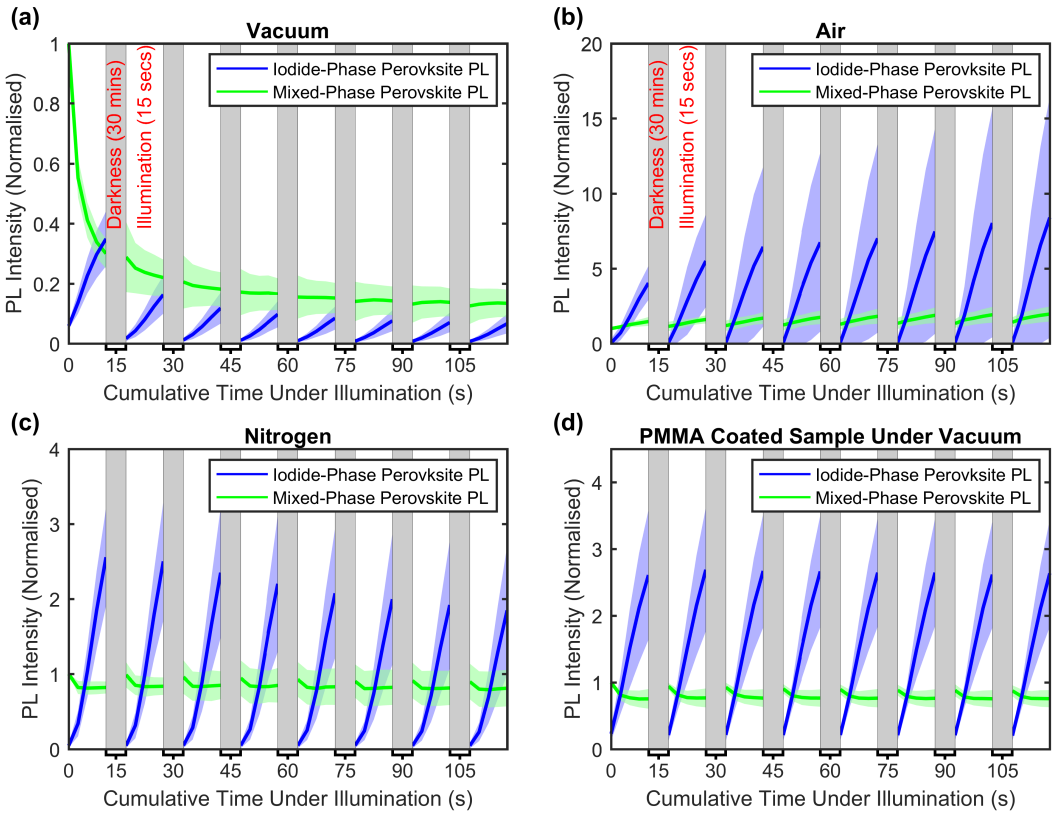

Figure 4.4: Evolution of PL emission monitoring the reversibility of halide segregation when $MAPb(Br_{0.5}I_{0.5})_3$ films are held under 4 different atmospheric conditions, (a) under vacuum (∼0.2 mbar), (b) ambient air, (c) pressurised (2 bar) nitrogen, and (d) film topped with a layer of PMMA and held under vacuum (around 0.2 mbar). To induce repeated segregation and remixing, the films were exposed to 8 illumination cycles, with a single cycle consisting of 15 s of illumination followed by 30 min of darkness. Illumination was achieved with a laser of wavelength 400 nm whose intensity was adjusted to provide excitation equivalent to AM1.5 solar illumination (591 W m^{-2}, see Section 3.5.1). The bold blue lines show the mean integrated intensity of the PL originating from the iodide-rich phase (720 nm to 770 nm) while the bold green lines give the mean integrated intensity of the PL from the mixed-halide (640 nm to 690 nm), both scaled such that the initial mixed-halide PL intensity is set to 1. Bold lines are the calculated mean over several repeats of such runs on fresh areas of perovskite film, and shaded regions indicate the values within one standard deviation of the mean, thus highlighting the extent of spot-to-spot variations.

those reported for single-halide perovskites under comparable conditions. For such single-halide perovskites, the PL has been found to decrease under vacuum [24, 32, 201], increase in air [24–32], and remain fairly constant under nitrogen [24, 27, 31], similar to what is observed here for the average PL signal of $MAPb(Br_{0.5}I_{0.5})_3$ across cycles. Similarly, the large standard deviation observed in the halide segregation dynamics for the mixed-halide samples held under air is reminiscent of the diverse PL changes reported in the literature

for single-halide perovskites under illumination in air [25]. Such variations under air likely result from a combination of slight differences in the atmospheric composition, perovskite film inhomogeneity, the degree the perovskite contacts the atmosphere, and the fact that oxygen and water undergo complex chemical processes with the perovskite [12, 13, 15]. Importantly, when $MAPb(Br_{0.5}I_{0.5})_3$ films are coated with PMMA, the changes observed in the PL spectra under illumination in vacuum are highly repeatable between cycles (Figure 4.4d). Figure 4.5 highlights that a similar PMMA coating also yielded a suppression of atmospheric effects when the sample was held under air or nitrogen, although not as completely as when the sample was held under vacuum.

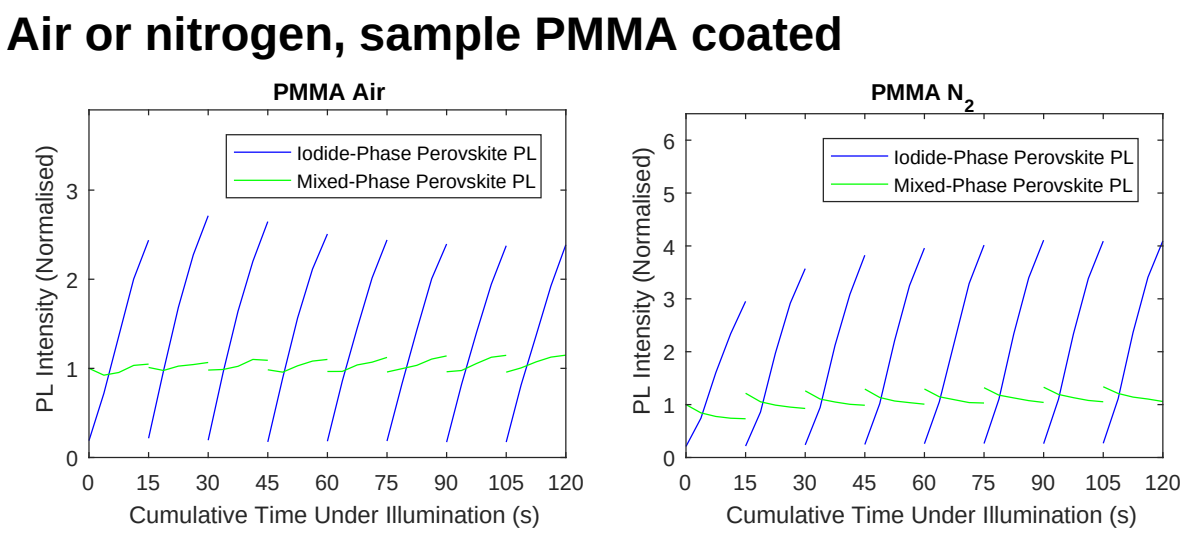

Figure 4.5: PL data highlighting the reversibility of halide segregation when PMMA coated $MAPb(Br_{0.5}I_{0.5})_3$ films are held under either air or pressurised nitrogen (2 bar).

These observations suggest that the proposed photo-induced processes that moderate charge-carrier traps in single-halide perovskites under different atmospheres also occur within mixed-halide perovskites: under vacuum the average PL signal across cycles is reduced as the number of electronic trap states in the perovskite film increases [24, 32], and under air the formation of a superoxide species passivates trap states and increases the average PL signal across cycles [24–26, 28]. Under nitrogen or under vacuum with a PMMA coating protecting the films, on the other hand, neither the photobrightening nor

the photodarkening process may occur [24]. These differences in electronic trap densities or efficacies may affect both the quantum efficiency of PL, and the dynamics of halide segregation, leading to the large atmospheric variation in the curves displayed in Figure 4.4.

The data presented so far also highlight that while halide segregation is reversible under certain atmospheric conditions, under vacuum or air, photo-induced changes occur that cannot be reversed under darkness. This irreversibility is an important issue, as many measurements of halide segregation reported in the literature are not concerned with the remixing process in the dark, but rather record halide segregation over one cycle only [66, 94, 96, 103, 104, 115–117, 122, 176]. However, it is apparent from Figure 4.4 that the atmospheric conditions under which a halide segregation measurement is made will alter the dynamics observed. The difference in observed dynamics will be amplified if the perovskite is assumed to have recovered between measurements and measurements are then taken from the same area of film. Thus comparisons of data in the existing literature must be done with care.

In addition, the findings here elucidate the extent to which halide segregation will be reversible under real-world operating conditions for photovoltaic cells. As Figure 4.4d shows, the atmosphere-induced changes to the perovskite film can be prevented with a thick protective coating of PMMA. In Chapter 5, it is shown that the electrical contacts and charge-carrier transport materials utilised in the architecture of a photovoltaic device can provide a similar protection, and an additional encapsulation will most likely also be present in commercial solar cells. Therefore, halide segregation would most likely be fully reversible in commercial solar cell modules, although still clearly undesirable because of the associated extracted current losses [20, 21, 23]. In order to exclude atmospheric effects and focus on a scenario relevant to photovoltaic (PV) operation, the remaining work in this chapter was performed on PMMA-coated $MAPb(Br_{0.5}I_{0.5})_3$ films held under vacuum.

4.4.2 Photon Efficacy in Halide Segregation

Despite the large volume of literature [17, 20, 21, 23, 92–96, 98, 100, 103, 104, 115–117, 119, 122, 144, 176, 185, 201] on halide segregation in mixed-halide perovskites there is yet to be a definitive explanation of the underlying mechanisms that drive the different halide ions apart in the presence of light. There is evidence that excited charge carriers are responsible [20, 21], but little is known about how these free charge carriers drive halide segregation. Here, in order to probe how the density of charge carriers affects halide segregation, perovskite films were illuminated with a constant number of total photons over different lengths of time, thus changing the generation rate of free charge carriers. Keeping the total incident photon number constant meant, for example, halving the illumination laser intensity if the exposure time was doubled. A subset of the photoexcited charge carriers – those that recombine through electronic trap states – were found to determine the rate of halide segregation. This result provides further insight into the segregation mechanism, and allows the construction of a possible explanation for the observed halide segregation dynamics (Section 4.5).

Figure 4.6 shows how the growth of the PL signal from the iodide-rich perovskite (taken as the spectral integral between 720 nm and 770 nm) depends on the illumination exposure time and thus the photoexcited charge-carrier generation rate. The PL intensity from the iodide-rich phase is normalised such that the initial integrated intensity of the mixed-phase peak (taken as the spectral integral between 640 nm and 690 nm) is set to 1, in order to provide a measure of halide segregation in terms of the relative peak amplitudes, independent of the different illumination powers used. These normalised PL intensities for each exposure time are then plotted against the cumulative number of photons incident per unit volume on the perovskite film. In each case, the low-bandgap PL signal starts at zero intensity (when the perovskite is well mixed) and then increases as the iodide-rich perovskite phase forms. In order to avoid spot-to-spot differences, following illumination

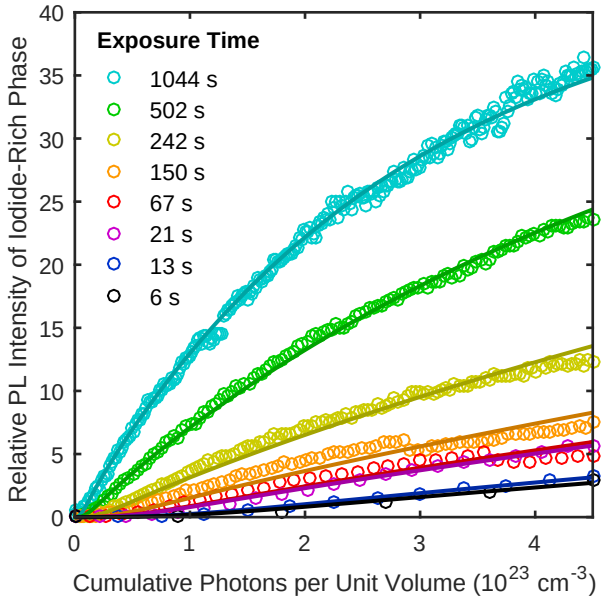

Figure 4.6: The evolution of the PL intensity originating from the low-bandgap iodide-rich phase of $MAPb(Br_{0.5}I_{0.5})_3$ plotted against number of incident photons per unit volume, for different overall exposure times to illumination but constant total incident photons. The hoops represent experimental data points and the solid lines are the fits of Equation 4.1 to the data.

the films were left in the dark so that the halide ions would remix for around 45 minutes before the next exposure-time experiment was performed on exactly the same area of film.

The graphs presented in Figure 4.6 are particularly interesting because they reveal that as the illumination exposure time is increased, an increasing level of halide segregation is encountered even when the same number of cumulative photons have been incident on the film. In other words, if halide segregation only depended on the accumulated number of photoexcited charge carriers generated, then there should be no difference between the experimental runs at points where the same total photon input has been incident, which is clearly not the case. For experiments with longer exposure time, the illumination intensity is lower, photoexciting a smaller charge-carrier density within the perovskite film. Therefore, the efficacy of a charge carrier to induce halide segregation (per unit carrier) appears higher at lower charge-carrier density. These observations can be understood if one considers the changing contributions of various charge-carrier recombination processes in metal halide perovskites as the charge-carrier density is increased [61]. While at

low carrier densities, monomolecular, trap-mediated charge recombination dominates, radiative bimolecular band-to-band recombination becomes increasingly dominant at higher densities (see Section 2.1). Thus the data support the conclusion that excited charge carriers that recombine through trap states mediate halide segregation, as more segregation per photon is observed at longer exposure time, when lower charge-carrier densities lead to a larger proportion of the excited charge carriers being trapped.

Further examination of the segregation dynamics reveal that the overall temporal evolution of the iodide-rich phase signal is extremely similar across all exposure times, i.e. the shapes of the curves are alike, with only the extent reached along the path dictated by the exposure time. In Figures 4.7 and 4.8 it is shown that the traces displayed in Figure 4.6 can be superimposed on each other by a suitably chosen x-axis scaling for each curve. Mathematically this indicates that a single global function will provide an accurate fit to all the experimental runs, with only one local fitting parameter required to scale the x-axis to account for the different exposure times. The following function is found to empirically describe the intensity of the PL originating from the iodide-rich phase in the perovskite, $I_{(\text{I-rich PL})}$, accurately as a function of incident photons per unit volume:

$$I_{(\text{I-rich PL})} = f(gGt) = A\frac{(gGt)^2}{(1+(gGt)^2)}(1-e^{-BgGt}) \tag{4.1}$$

Here G is the generation rate of excited charge-carriers per unit volume measured in $\text{cm}^{-3}\,\text{s}^{-1}$, t is time, A is a dimensionless global fitting parameter that is dependent on the exact method used to define $I_{(\text{I-rich PL})}$ and measured to be 43.6 for the setup utilised in this study (detailed in Section 3.2.1), B is a dimensionless global parameter determined from fits to be 27.5×10^{-3} , and g is the local fitting parameter that represents the scaling of the x-axis, given in centimetres cubed. The values of g fitted to the different exposure time experimental data in Figure 4.6 are given in Table 4.1.

Exposure Time (seconds)	Scaling Factor and Charge-Carrier Efficacy, g (cm^3)
6	5.95×10^{-24}
13	6.74×10^{-24}
21	11.7×10^{-24}
67	12.3×10^{-24}
150	17.3×10^{-24}
242	30.3×10^{-24}
502	66.2×10^{-24}
1044	129×10^{-24}

Table 4.1: The exposure times (at constant overall photon dose) used to collect the data shown in Figure 4.6, with the associated, fitted value of the scaling factor, g, for each exposure time used.

The functional form of Equation 4.1 incorporates two main features that are observed in the data, which are that halide segregation appears to have a delayed onset – as highlighted in Figure 4.8 – with an initially very flat/shallow rise observed in the PL data before the gradient then accelerates, and that the segregation slows and saturates at long exposure times. The delayed onset is captured by the first factor (the fraction) in Equation 4.1, while the latter rise is represented by the second factor which reflects a growth through an exponential asymptote with characteristic rise constant B. The final relative segregation attained is reflected by the expression tending to the value of A at long times. A purely exponential form has previously been used to empirically fit the rise in the PL amplitude of the iodide-rich phase as the perovskite segregates [96] but it was found that this did not adequately capture the initial slow rise of signal especially visible at low exposure times in this study, as highlighted in Figure 4.8.

The fact that the data here can be captured by a single global function indicates that the underlying, intrinsic halide segregation dynamics rely on a single dominating mechanistic pathway, with the local scaling factor, g, providing a measure of the differing degrees of segregation in a unit volume caused per excited charge carrier at different illumination intensities. g can thus be thought of as a charge-carrier efficacy for

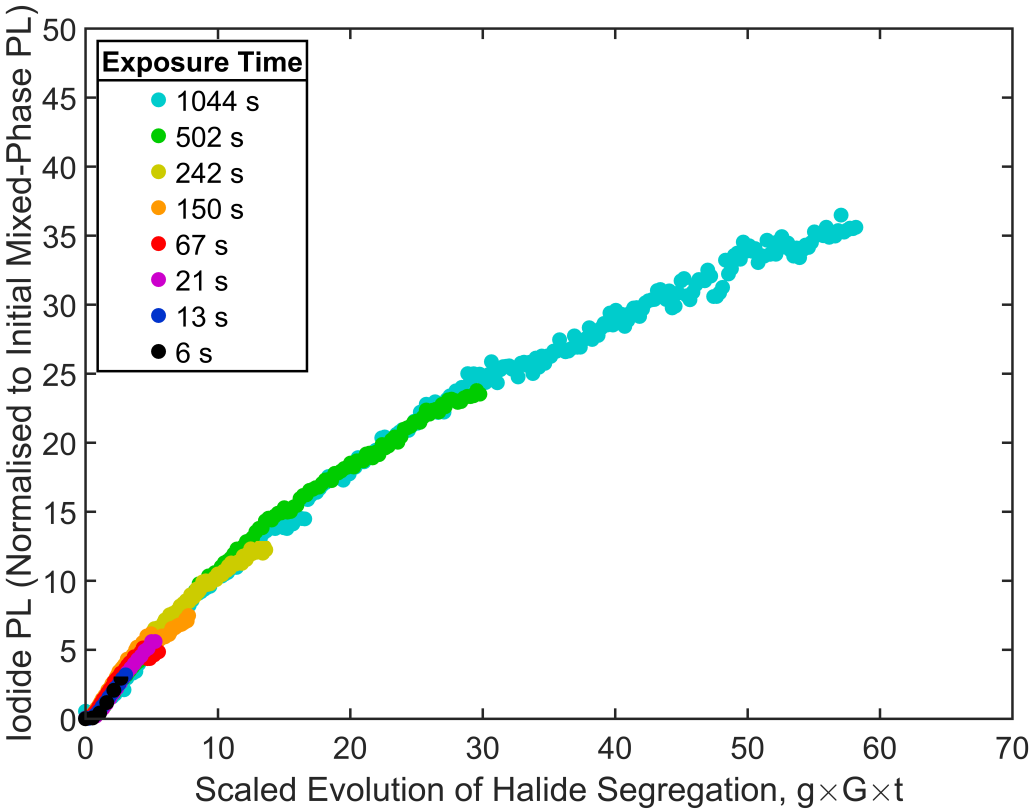

Figure 4.7: The evolution of the integrated iodide-rich perovskite PL signal under different illumination exposure times as a function of the scaling factor, g, times the cumulative number of incident photon number per unit volume, $G \times t$. The scaled cumulative number of incident photon number per unit volume, $g \times G \times t$, is a dimensionless measure of halide segregation. The PL signal is normalised such that the initial mixed phase perovskite PL signal (not shown) is set to 1 for each exposure time. The good overlay suggests that the underlying segregation mechanism remains the same across the charge carrier generation rates explored here.

inducing halide segregation.

4.4.2.1 Determining the Behaviour of g

The behaviour of the parameter g is essential to know if Equation 4.1 is to be used to predict the nature of halide segregation in mixed-halide perovskite materials under given illumination conditions. To recapitulate, the other fitting parameters in Equation 4.1, A and B, are global parameters which define the general behaviour of the iodide-rich PL over time, t, and are not expected to vary according to any reasonable variation in the illumination upon the perovskite material. g, however, is a local fitting parameter,

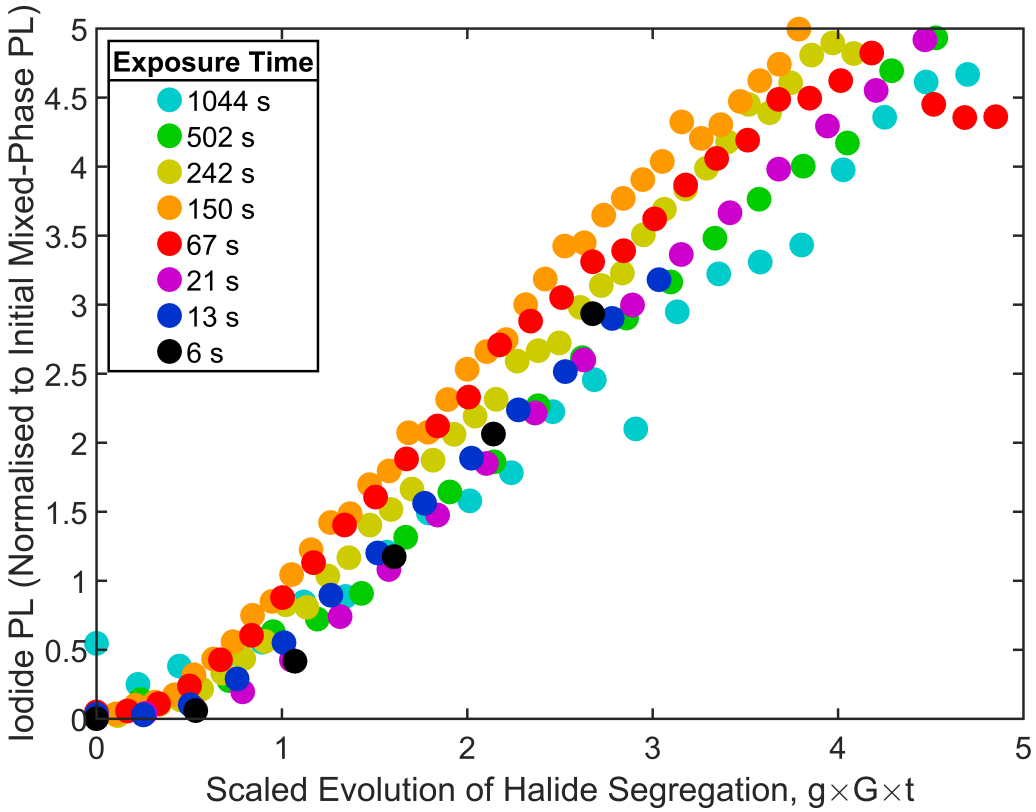

Figure 4.8: Zoomed section of Figure 4.7 to show the non-linear rise of low-bandgap PL at small values of $g \times G \times t$.

and as such represents the dependence of the dynamics of the iodide-rich PL on the experimental conditions. As excited charge carriers, rather than photons, have been shown to be an essential component driving the halide segregation mechanism [20, 21], it is desirable to determine the dependence of g on the fraction of charge carriers that recombine through trap states. The general theory of charge-carrier dynamics is outlined in Section 2.1, and it is found in Section 2.1.1 that for continuous wave illumination, the steady-state charge-carrier dynamics are described by the following expression:

$$k_3 n^3 + k_2 n^2 + k_1 n - G = 0 \tag{4.2}$$

where k_3, k_2 and k_1 are the third-, second-, and first-order decay constants of the perovskite material, respectively, n is the charge-carrier density, and G is the charge-carrier generation rate in the perovskite film. From Equation 4.2 the fraction of charge

carriers that recombine through trap states, $\frac{k_1 n}{G}$, can be numerically evaluated given the values of the three decay constants, and the charge-carrier generation rate, G. The illumination source for the experiments discussed in this chapter was a laser at an emission wavelength of ∼400 nm, well above the bandgap of the $MAPb(Br_{0.5}I_{0.5})_3$ perovskite material (see Figure 4.3). Therefore, it is a valid approximation to assume that all the photons incident on the perovskite were absorbed and generated a charge-carrier pair in the material, which makes it possible to calculate the value of G from the following expression: $G = \frac{P}{AdE}$, where P is the power of the illumination laser (set to different values depending on the exposure time of the experiment), A is the spot size of the illumination laser (measured at 0.0148 mm^2), d is the perovskite film depth (measured via SEM msurements to be 390 nm, see Section 4.3.2), and E is the energy of the incident photons (5×10^{-19} J), all of which are known experimental parameters. A constant form of G assumes a uniform charge-carrier density throughout the perovskite film, which is valid given that the photoexcited charge carriers spread out quickly due to diffusion and photon recycling processes [52]. The value for k_3 is assumed to be similar to other lead-based perovskites [61, 115] at around 1×10^{-28} $cm^6\,s^{-1}$, however it is noted that at the illumination intensities used in the work detailed in this chapter, the amount of Auger recombination within the perovskite films is expected to be negligible. Therefore, in order to calculate the fraction of charge carriers that recombined through trap states within the measured perovskite thin films, k_1 and k_2 must be determined.

In order to extract the first- and second-order rate constants, k_1 and k_2 (see Section 2.1 for a discussion of charge-carrier recombination processes) from the perovskite films used in this chapter, TCSPC measurements were performed on similar PMMA coated $MAPb(Br_{0.5}I_{0.5})_3$ films held under vacuum. The pulsed excitation was provided by a 400 nm wavelength diode laser at 5 MHz repetition rate. In order to monitor changes that might occur as a results of the illumination, e.g. halide segregation, measurements

were made over 320 seconds of illumination, which was separated into three accumulation time windows: 0-100 seconds, 110-210 seconds and 220-320 seconds. The PL was detected at two wavelengths of emitted photons – 660 nm and 740 nm – to examine the mixed and iodide-rich perovskite phases in the perovskite, respectively. Furthermore, three illumination intensities were used to probe different charge-carrier density regimes (1760, 500 and 110 $\mathrm{W\,m^{-2}}$) and three repeats were performed and averaged over for each measurement. The measurements were all made on the same area of perovskite film, with at least 30 minutes left between measurements, and with 45 minutes or more left between measurements at the higher illumination powers. The data from these TCPSC measurements are shown in Figure 4.9.

The fitting of the TCSPC data was complicated by the segregation of the films occurring as the measurements were taken. The formation of low-bandgap, iodide-rich regions of perovskite cause charge carriers to funnel out of the mixed phase and into these forming regions. Charge-carrier funnelling leads to three effects that could influence the results of a TCSPC measurement: 1) The movement of charge carriers between regions creates an extra "decay" mechanism for one region, and a new generation term for the other. 2) As the volume of the iodide-rich perovskite changes, the density of charge carriers within those regions will change. 3) The movement of halide ions will change the microscopic properties of the film, which could in turn alter the values of k_1 though the evolution of trap states, and the measurements of k_2 through the re-absorption of photons and the channeling of charge carriers into iodide-rich regions where confinement effects may enhance k_2. In order to monitor these effects, the three accumulation windows were handled separately, so that any changes in the fitted values of k_1 and k_2 could be observed.

The fitting procedure for the TCSPC traces was performed as outlined in Section 3.2.2.1. The decay trails at the three different illuminations intensities become roughly parallel on a log-lin scale around 100 ns after the pulse arrival, see Figure 4.9, which

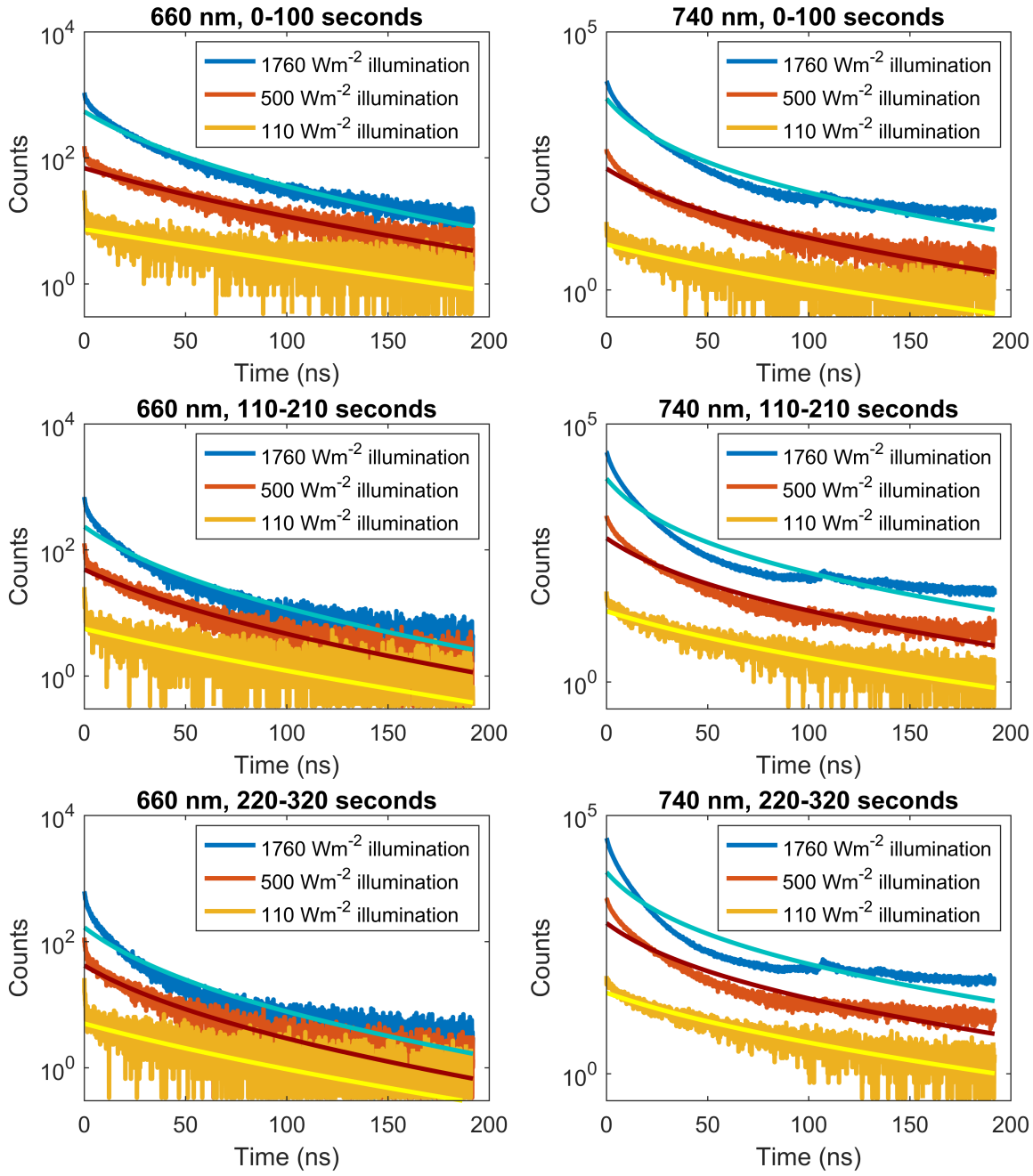

Figure 4.9: Time-resolved PL measured using TCSPC, taken at the mixed phase and iodide-rich perovskite PL peaks. Because the perovskite was segregating as the measurements were performed, three measurement windows of 0-100 s, 110-210 s and 220-320 s were used to observe how the decay curves changed over time. Three experimental repeats were performed for each condition and averaged over to produce these plots, and a trigger frequency of 5 MHz was used. The sample measured was a PMMA coated film under vacuum and the same spot was always illuminated within repeats. Between 30 and 45 minutes was left between each measurement.

indicates that after this time the charge carrier decay is being dominated by monomolecular pathways. Values for k_1 were extracted by fitting a single exponential function, ae^{-bt},

Table 4.2: Extracted values for k_1 from TCSPC measurements.

Wavelength (nm)	Accumulation Window (seconds)	Fitted k_1 (s^{-1})
660	0-100	5.04×10^6
660	110-210	5.57×10^6
660	220-320	5.43×10^6
740	0-100	4.60×10^6
740	110-210	4.84×10^6
740	220-320	4.55×10^6

with fitting parameters a and b to this region and assuming the evolution of the measured counts is well described by Equation 3.2. k_1 was then taken as $\frac{b}{2}$ and the three values for k_1 extracted from the three different excitation fluences were then averaged over.

Table 4.2 presents the extracted values of k_1 from the two collection wavelengths and all three accumulation windows. The values are consistent with each other and similar films in the literature [61], and the average value of $5 \times 10^6\,s^{-1}$ was taken as a representative value for all calculations in this chapter.

Equation 3.6, multiplied by a constant to take into account the imperfect outcoupling of photons emitted from radiative recombination to the measurement apparatus, was then fitted to the acquired TCSPC data (Figure 4.9) to extract values for k_2 and n_0. k_1 was fixed to $5 \times 10^6\,s^{-1}$, the value extracted at low charge-carrier density as previously discussed, and the value for n_0 was fitted to each graph individually because it was impossible to determine how it would develop as the charge carriers funneled into the forming regions of iodide-rich perovskite. k_2 was fitted globally across the three different excitation fluences, but not across the different measurement wavelengths or accumulation windows. The extracted values for k_2 are shown in Table 4.3, and the combined k_1, k_2 fitted functions are shown in Figure 4.9 alongside the TCSPC data.

The fits shown in Figure 4.9 highlight the tendency of the halide segregation mechanism to deviate the decay behaviour away from the expected, "ideal" fitted functions. Correspondingly, the fitted functions appear most accurate at the earliest accumulation window,

Table 4.3: Extracted values for k_2 from TCSPC measurements.

Wavelength (nm)	Accumulation Window (seconds)	Fitted k_2 ($cm^3\,s^{-1}$)
660	0-100	6.38×10^{-10}
660	110-210	6.22×10^{-10}
660	220-320	9.94×10^{-10}
740	0-100	9.28×10^{-10}
740	110-210	8.15×10^{-10}
740	220-320	8.36×10^{-10}

at the 660 nm measurement wavelength, and at the lowest excitation fluence, where the degree of halide segregation is lowest. Due to the variation in the extracted values of k_2, the values of k_2 were not averaged over as was done for the values of k_1, but instead the value of $6 \times 10^{-10}\,cm^3\,s^{-1}$ was taken from the minimally segregated, 660 nm measurement wavelength, 0-100 s accumulation window decay trails. This value is in good agreement with other values reported in the literature for similar perovskite compositions [61].

Now, with k_1 and k_2 determined from measurements, the dependence of g on the fraction of charge carriers that recombine through trap states ($\frac{k_1 n}{G}$) can be determined. To recapitulate, g is a local fitting parameter in Equation 4.1 that is a measure of how much segregation occurs in a perovskite thin film under given illumination conditions. As such, it can be thought of as a measure of the efficacy of a charge carrier to induce segregation. Fitting Equation 4.1 to the data shown in Figure 4.6 gives the values of g for different illumination exposure times, or different illumination intensities. These fitted values of g are detailed in Table 4.4, alongside the corresponding fraction of charge carrier that recombine through trap states calculated from Equation 4.2. Each of these exposure times at overall constant photon dose correspond to different illumination intensities, and therefore correspond to different rates of the charge-carrier recombination processes in the perovskite material. The steady-state fraction of all photoexcited charge carriers that recombine through trap states can be determined from Equation 4.2 utilising the measured values of k_1 and k_2, the assumption of k_3 to be similar to other literature values

at $1 \times 10^{-28}\,\mathrm{cm}^6\,\mathrm{s}^{-1}$, and the values of G which can be calculated for each of the different illumination exposure times. Therefore, the values of g can be correlated with the fraction of charge carriers that recombine through trap states for each of the exposure times used.

Figure 4.10 displays the scaling factor g as a function of the trap-mediated charge-carrier decay fraction. At low fractions of trap-mediated recombination (less than around 95%), Figure 4.10 displays a linear region (highlighted by the inset), possibly suggesting that the underlying halide segregation mechanisms depend linearly on the fraction of charge carriers that recombine through trap states in the perovskite films. This linear increase of g with fraction of trapped charges reflects the increased efficacy of charge carriers for inducing halide segregation at longer exposure times, for which charge-carrier densities are reduced (given the constant overall photon dose). At higher fractions of trap-mediated recombination, there is a sharp onset in g, which is a result of the longer exposure times used in these experimental runs allowing for a greater movement of the halide ions despite the saturation of the fraction of trap-mediated recombination. This conclusion is supported by Figure 4.11, which plots g against experimental exposure time and displays a linear region for the longest three exposure times (corresponding to the three data points within the sharp onset in g in Figure 4.10), suggesting that within this region the halide segregation mechanics become dominated by the time the sample is under illumination.

In summary, Table 4.4 shows the exposure times (at constant overall photon dose) used in the measurement of the PL data shown in Figure 4.6, the resulting charge-carrier generation rate in these measurements, the calculated fraction of charge carriers that recombine through trap states under these generation rates, and the corresponding value of g fitted to the PL data shown in Figure 4.6. The inset to Figure 4.10 highlights that g obeys a linear relationship with the fraction of charge carriers that recombine through trap states, provided that extremely long illumination times are not used.

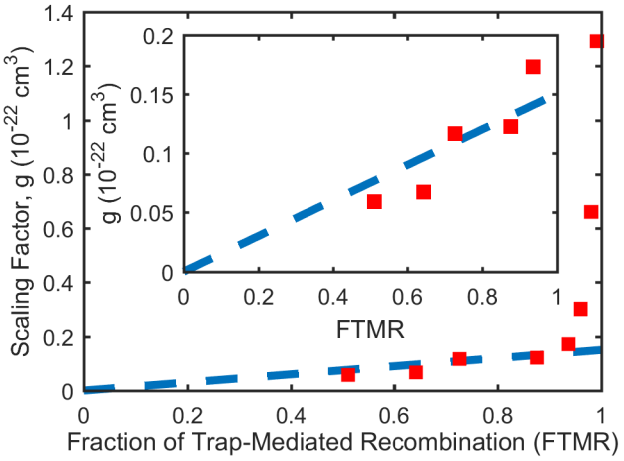

Figure 4.10: The evolution of the fitting parameter g with increasing fraction of trap-mediated recombination, taken from the fits of Equation 4.1 to the data in Figure 4.6. The first five points exhibit a linear relationship, fitted by the dashed blue line with a gradient of $1.5 \times 10^{-23}\,\mathrm{cm}^3$, which is followed by a sharp onset in g. The inset shows a scaled view of the first five data points. The dashed lines are expected to pass through the origin because halide segregation is assumed to be absent when there is no charge-carrier trapping or illumination.

Exposure Time (seconds)	Charge Carrier Generation Rate ($\mathrm{cm}^{-3}\,\mathrm{s}^{-1}$)	Fraction of Charge Carriers that Recombine Through Trap States, $\frac{k_1 n}{G}$	Scaling Factor and Charge-Carrier Efficacy, g (cm^3)
6	7.5×10^{22}	0.51	5.95×10^{-24}
13	3.5×10^{22}	0.64	6.74×10^{-24}
21	2.1×10^{22}	0.73	11.7×10^{-24}
67	6.7×10^{21}	0.88	12.3×10^{-24}
150	3.0×10^{21}	0.94	17.3×10^{-24}
242	1.9×10^{21}	0.96	30.3×10^{-24}
502	9.0×10^{20}	0.98	66.2×10^{-24}
1044	4.3×10^{20}	0.99	129×10^{-24}

Table 4.4: The fraction of charge carriers that recombine through trap states and scaling factors for the different exposure times used to collect the data shown in Figure 4.6.

4.4.3 Halide Segregation Under Other Illumination Conditions

The phenomenological parameterisation of halide segregation through Equation 4.1 is highly useful, as it allows for predictions to be made on the extent of halide segregation under various circumstances. As shown in detail below, such knowledge then grants, for example, an understanding of the recently observed apparent dependence of halide segregation on excitation pulse frequency [185], and an assessment of the degree to which trap-related charge recombination has to be suppressed in order for halide segregation

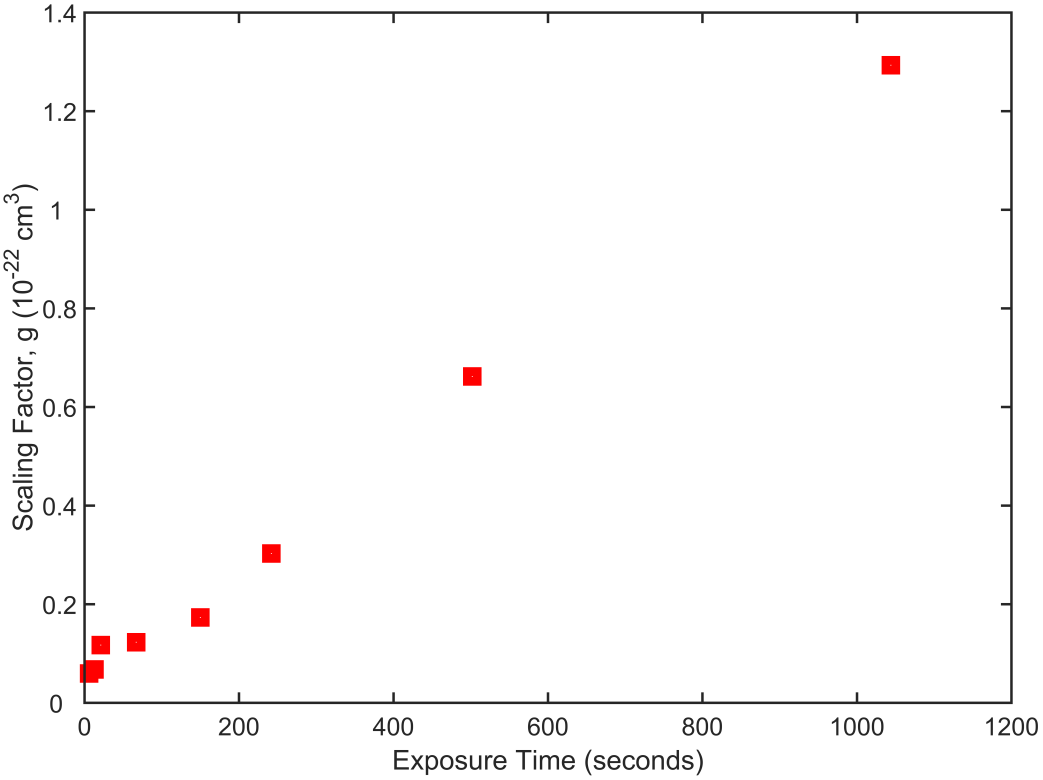

Figure 4.11: The values of the scaling factor, g, extracted from fits of Equation 4.1 to the data shown in Figure 4.6, plotted against the corresponding exposure times of that same data. The seemingly linear trend of the last three data points is attributed to the longer exposure times used in these experimental runs allowing for a greater movement of the halide ions, and thus higher values of g, despite the saturation of the fraction of trap-mediated recombination.

to become insignificant under PV operation conditions. Equation 4.1 depends on four parameters – A, B, G and g – and one variable t, time. A and B both depend on the exact perovskite material excited under illumination, and A further depends on the definition used for the iodide-rich and mixed-phase PL peaks. For the experimental setup and perovskite films used for the work in this chapter, it was determined A and B to have dimensionless values of 43.6 and 27.5×10^{-3} respectively, which is assumed to be similar to the values of A and B for equivalent PL experiments performed on similar perovskite films. The charge-carrier generation rate per unit volume, G, is calculated from knowledge of the illumination source and film thickness, and the charge-carrier efficacy, g, is derived from its fitted, linear dependence on the fraction of charge carriers that recombine via trap

states, as shown in Figure 4.10. The fraction of trap-related charge-carrier recombination can itself be calculated from the illumination and recombination rate parameters (see Section 2.1). Once A, B, G and g are known, Equation 4.1 determines the relative strength of the iodide-rich PL, which is related to the degree of phase segregation the perovskite film has experienced. It is noted that while the form of the empirical function in Equation 4.1 is expected to be inherent to perovskite films that undergo halide segregation, the values of A, B and g may vary with composition (iodide:bromide ratio, and the content of the A- and B-site cations, see Section 2.4.2) and temperature. For the $MAPb(Br_{0.5}I_{0.5})_3$ perovskite under investigation at room temperature here, Figure 4.12 shows the resulting colour plot representing the amount of segregation expected when the fraction of charge carriers undertaking trap-mediated recombination or the number density of cumulative photons incident on the perovskite is varied. The map graphically illustrates how the degree of segregation a perovskite film experiences increases with the number of incident photons and/or fraction of charge carriers that recombine via trap states.

4.4.3.1 Predicting Halide Segregation Under Pulsed Illumination

Interestingly, the findings of this chapter resolve the reasons for an apparent dependence of halide segregation on the pulse repetition frequency of excitation that had recently been observed. Yang *et al.* reported that under pulsed laser illumination at fixed average power, the degree of halide segregation observed in an $MAPb(Br_{0.57}I_{0.43})_3$ perovskite film was dependent on the repetition rate of the laser pulses [185]. They observed that no significant halide segregation occurred below a pulse frequency of 500 Hz over the course of ten minutes, whereas above this repetition rate they found an increasing dominance of an iodide-rich perovskite peak in the PL spectrum with increasing illumination repetition rate, where the average intensity and time of the illumination was always kept constant. Their observations can be explained by the empirical halide segregation model encapsulated by

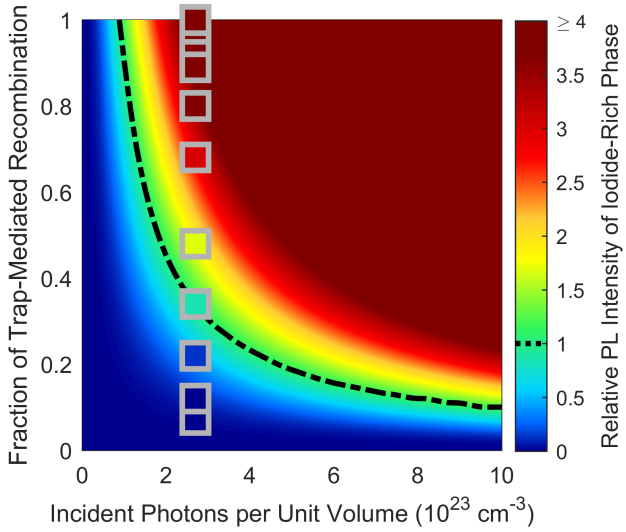

Figure 4.12: Colour map showing the predicted relative PL intensity originating from the iodide-rich phase of $MAPb(Br_{0.5}I_{0.5})_3$ perovskite, as a function of both the fraction of charge carriers recombining through traps, and the number of photons incident on the film per unit volume ($G \times t$). The PL intensity is normalised such that 1 corresponds to the intensity of the mixed-halide PL in the absence of segregation and under similar illumination conditions. The black, dashed line indicates the points at which the PL peak of the iodide-rich phase begins to dominate the spectrum. The gray bordered squares represent halide segregation experiments performed by Yang *et al.* for which the average power of a pulsed illumination source was kept constant, while the repetition rate of the laser pulses was varied [185]. The interior colour of the squares roughly indicate the relative level of iodide-rich perovskite PL observed, which, together with other parameters, was extracted from the work of Yang *et al.*. The good agreement of colours inside the squares with that in their vicinity shows that the variation in repetition rate in these experiments only affects halide segregation because it also changes the fraction of charge carriers recombining through traps.

Equation 4.1, as in order to fix the average power to a constant value while changing the laser pulse repetition rate, Yang *et al.* correspondingly changed the instantaneous excitation pulse intensity, which would have altered the initially injected charge-carrier density in the film. For example, a decreased repetition rate would require a higher pulse fluence (higher instantaneous intensity) to maintain the same fixed average intensity value, which would increase the charge-carrier density injected with each pulse, thus enhancing the radiative band-to-band recombination rate and lowering the fraction of charge carriers that recombine through trap states.

The apparent frequency-dependence observed in the study by Yang *et al.* is therefore an indirect effect, resulting from changes in charge-carrier trapping with injected charge-

carrier density, and a direct link between halide segregation and light modulation frequency is not expected. To prove this point experimentally, a halide segregation experiment was performed during which a PMMA-coated $MAPb(Br_{0.5}I_{0.5})_3$ film under vacuum was exposed to light modulated by a square-wave ("on-off") function of 50% duty cycle and variable frequency, with the recorded PL data presented in Figure 4.13. The average intensity of the modulated illumination was fixed to the AM1.5-equivalent value, $591\,W\,m^{-2}$, see Section 3.5.1. In order to modulate the light and control the separation and the pulse width of the illuminating light pulses, a Stanford Research Systems optical chopper, model SR540, was inserted into the illumination beam line before the sample chamber. A chopper is a component consisting of a rapidly rotating disk with holes that alternatively block and pass the beam, creating a square-wave modulation of the light. The nature of this component means that the instantaneous illumination power of the pulses is constant regardless of the frequency of the chopper. Therefore, unlike in the study by Yang *et al.* [185], the square-wave illumination remains at both constant pulse intensity *and* constant overall intensity as the frequency is changed, i.e. the variation in frequency is accomplished by a mere change in the width of each square-wave pulse. See Figure 4.14 for a comparison sketch of the illumination conditions utilised by Yang *et al.* (Figure 4.14a and 4.14b) and in the experimental work reported here (Figure 4.14c and 4.14d). In contrast to the work of Yang *et al.* where the pulse duration was 10 ns, under the square-wave illumination conditions the charge-carrier generation rate under illumination will be in equilibrium over the pulse duration (which is much longer than the typical charge-carrier recombination life times) and independent of the modulation frequency. As shown in Figure 4.13, no change in the segregation dynamics beyond minor random variations was observed when the frequency was varied over two and a half orders of magnitude from 10 Hz to 3500 Hz, thus proving that the pulse frequency of the illumination alone does not directly affect halide segregation.

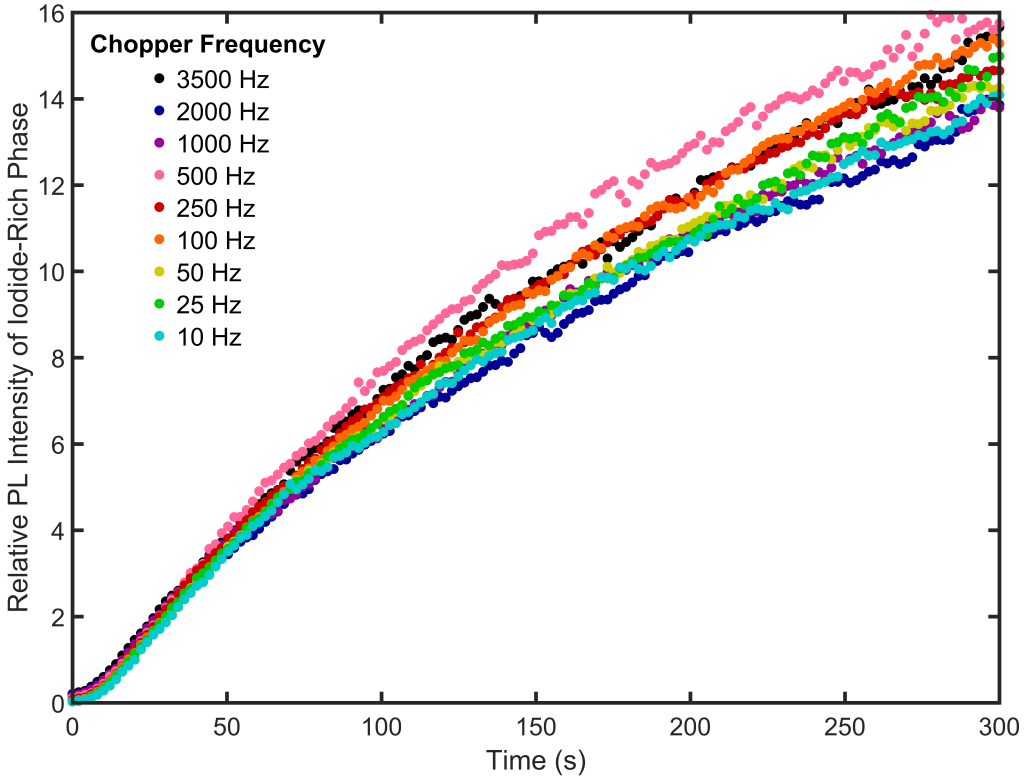

Figure 4.13: The increase in low-bandgap PL (integrated from around 720 nm to 770 nm) when normalised to the initial measurement of the mixed-phase PL peak (integrated from 640 nm to 690 nm) which is attributed to the formation of regions of iodide-rich perovskite from halide segregation under illumination through a chopper at various frequencies. The similar signal growth at all chopper frequencies displayed here shows that illumination pulse frequency has no direct effect on the halide segregation mechanics.

Given the similarity in perovskite composition between the work presented in this chapter ($MAPb(Br_{0.5}I_{0.5})_3$) and that of Yang *et al.* ($MAPb(Br_{0.57}I_{0.43})_3$) [185], it can be shown that the apparent changes in segregation dynamics with pulse repetition rate is fully compatible with the empirical model captured by Equation 4.1. Yang *et al.* used a pulsed laser to illuminated their samples, and so from Section 2.1.2, Equation 2.3 describes the charge-carrier dynamics within the films during the periods of time between the laser pulses. In order for the empirical model based upon Equation 4.1 to predict the levels of halide segregation experienced by the films, the average fraction of charge carriers that recombine through trap states, $\frac{\int k_1 n dt}{n_0}$, must be calculated through numerically

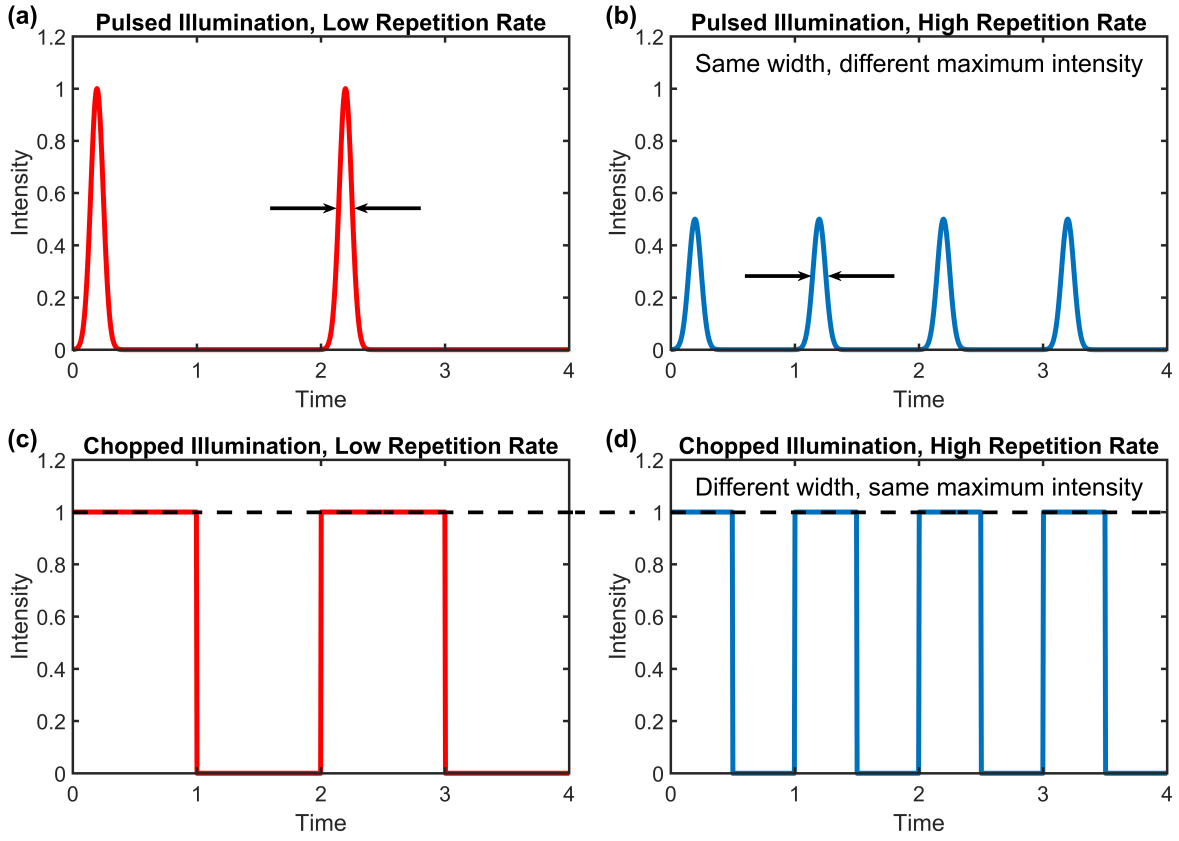

Figure 4.14: Schematic showing two different methods in which to change the repetition rate of incident illumination without changing the average intensity. (a) and (b) show that under pulsed illumination, as in the work of Yang *et al.*, the width of the light pulses remains constant, so the maximum intensity must be reduced to keep the average intensity constant. Lowering the maximum intensity then lowers the density of charge carriers excited by each pulse. (c) and (d) show that under chopped, continuous wave illumination, as in the work presented in this chapter, the pulse width changes with repetition rate, however the illumination intensity remains constant. A constant illumination intensity results in a constant density of photoexcited charge carriers, regardless of the illumination repetition rate.

solving Equation 2.3 for $n(t)$ and evaluating the initial charge-carrier density excited by each laser pulse, n_0. In order for the pulse-averaged, rather than the time-dependent, monomolecular decay fraction to be accurate for the model, the timescales of the electronic decay processes (hundreds of nanoseconds) must be much faster than the migration time of the halide ions (tens of seconds), which is indeed the case here. Yang *et al.* report using a laser intensity of $50\,\mathrm{W\,m^{-2}}$ at a photon wavelength of 532 nm on 300 nm thick samples [185], which, assuming every incident photon generates a charge-carrier pair, allows for

Laser Repetition Rate (Hz), Taken From [185]	n_0 (cm^{-3}), Calculated From [185]	Fraction of Charge Carriers That Recombine Through Trap States, $\frac{\int k_1 n dt}{n_0}$	Predicted Ratio of Final Low-Bandgap PL to Initial PL
100	4.46×10^{18}	0.066	~ 0.02
200	2.23×10^{18}	0.12	~ 0.1
500	8.92×10^{17}	0.22	~ 0.5
1,000	4.46×10^{17}	0.34	1.1
2,000	2.23×10^{17}	0.48	1.8
5,000	8.92×10^{16}	0.68	2.8
10,000	4.46×10^{16}	0.80	3.4
20,000	2.23×10^{16}	0.89	3.8
50,000	8.92×10^{15}	0.95	4.1
100,000	4.46×10^{15}	0.98	4.2
1,000,000	4.46×10^{14}	1.0	4.4

Table 4.5: Various calculated parameters for the different laser repetition rates utilised by Yang *et al.* in their induction of halide segregation in $MAPb(Br_{0.57}I_{0.43})_3$ [185]. n_0 is calculated from the laser power, repetition rate, film thickness and photon energy reported by Yang *et al.* The fraction of charge carriers that recombine through trap states is calculated through numerically solving Equation 2.3 for $n(t)$. The predicted ratio of final low-bandgap PL to initial PL is generated by Equation 4.1, and represents the degree of halide segregation the film undergoes under the corresponding laser repetition rate.

the calculation of n_0 at each repetition rate (see Table 4.5 for calculation results):

$$n_0 = \frac{\text{Laser Intensity}}{\text{Repetition Rate} \times \text{Photon Energy} \times \text{Film Thickness}} \tag{4.3}$$

The calculations of n_0 assume a spatially constant charge-carrier density, a valid assumption given that the charge carriers spread out from diffusion and photon recycling processes on short time scales [52]. k_1 is estimated from the PL transients reported by Yang *et al.* [185] to be $50 \times 10^6\,s^{-1}$, and k_2 and k_3 are taken to be similar to the perovskite films used in this chapter and other perovskite compositions in the literature [61] at $6 \times 10^{-10}\,cm^3\,s^{-1}$ and $1 \times 10^{-28}\,cm^6\,s^{-1}$ respectively, see Section 4.4.2.1. Inserting these rate constants into Equation 2.3 and numerically solving allows for the calculation of $\frac{\int k_1 n dt}{n_0}$ at each repetition rate, see Table 4.5.

In order for the empirical model described by Equation 4.1 to predict the induced level of halide segregation in a perovskite film, three input parameters are required: t, g and

G. t is the time over which the segregation occurred, equal to 600 s in the experiments performed by Yang *et al.* [185]. g is the charge-carrier efficacy, or scaling factor, that measures how effective a given photon is at inducing halide segregation. The empirical dependence between g and the monomolecular decay fraction is shown in Figure 4.10, and using the fit to the linear regime of that figure (the first five data points), an estimated value of g can be extracted for a given fraction of charge carriers that recombine through trap states. This monomolecular decay fraction has been, through the methods discussed above, calculated for every laser repetition rate utilised by Yang *et al.* [185], with the results of these calculations shown in Table 4.5. Finally, G is the generation rate of charge carriers per unit volume, and so can be calculated from dividing the incident laser intensity by the photon energy and film thickness (which again assumes a uniform charge-carrier density is valid [52]). For Yang *et al.* this corresponds to:

$$G = \frac{50\,\mathrm{W\,m^{-2}}}{(3.7 \times 10^{-19}\,\mathrm{J}) \times (3 \times 10^{-7}\,\mathrm{m})} = 4.5 \times 10^{26}\,\mathrm{m^{-3}\,s^{-1}} = 4.5 \times 10^{20}\,\mathrm{cm^{-3}\,s^{-1}} \quad (4.4)$$

Inserting t, g and G into Equation 4.1 generates the expected ratio of final, low-bandgap PL intensity to the initial, mixed-phase PL intensity, which is additionally shown in Table 4.5 for each laser repetition rate.

A direct comparison between the predictions of the empirical model of how much segregation should have been observed versus the amount of segregation actually observed by Yang *et al.* [185] is shown in Figure 4.12. The square data points in Figure 4.12 represent the experiments performed by Yang *et al.*, with the position of the squares calculated from the work carried out in this section, and the interior colour of the squares indicating the *actual* amount of iodide-rich phase PL observed by Yang *et al.*. Thus, if the empirical model determined from Equation 4.1 is capable of predicting the level of induced halide segregation, the interior colour of the squares (corresponding to Yang *et al.*'s observations) should match the colour of their position in the colour map (corresponding to the model's

predictions). The predictions of the model are found to be in excellent agreement with the actual observations, with the data point at 2 kHz predicted and observed to fall where the iodide-rich perovskite emission begins to dominate the PL spectrum.

4.4.3.2 Determination of Phase-Stable Perovskites

From the empirical model of halide segregation detailed above, it is possible to determine the trap-mediated charge-carrier recombination rate for which $MAPb(Br_{0.5}I_{0.5})_3$ perovskite materials would be sufficiently stable against segregation over the course of one day under one sun illumination. Such calculations are valuable as they can serve as guidance to materials design and set an outlook to what must be achieved in order to make perovskite-silicon tandem cells viable. The detrimental effect of halide segregation on PV device performance has recently been reported [20, 21, 23], however, Duong *et al.* also showed experimentally that such effects were less severe for $Rb_{0.05}(Cs_{0.1}MA_{0.15}FA_{0.75})_{0.95}Pb(Br_{0.33}I_{0.67})_3$ (FA = $CH(NH_2)_2^+$) perovskite devices under illumination when the films were operated at maximum power point or short circuit conditions, rather than at open circuit [21]. These observations can be fully understood within the empirical model because charge-carrier extraction – a process inherent in electricity generation – provides a competing process to that of charge-carrier recombination, thus lowering the fraction of charge carriers that are trapped and therefore stabilising the film against halide segregation. To account for such charge-carrier extraction here, a simple approximation is used to integrate an extraction rate into the standard, third-order charge-carrier recombination rate equation, as proposed by Lin *et al.* [175]:

$$\frac{\mathrm{d}n}{\mathrm{d}t} = G - k_1 n - k_2 n^2 - k_3 n^3 - c_{ext} n \tag{4.5}$$

Here n is the charge-carrier density, t is time, G is the generation rate, k_1, k_2 and k_3 are the trap-mediated (monomolecular), band-to-band (bimolecular) and Auger recombination rate constants respectively, and c_{ext} is the charge-carrier extraction rate.

To determine the value of k_1 required to limit halide segregation, the borderline value of g for which $I_{(\text{I-rich PL})}$=1 in Equation 4.1 must first be evaluated, i.e. the proposed condition of stability against halide segregation is that the PL originating from the iodide-rich phase must remain equal or smaller than the initial mixed-phase PL peak intensity. Solving Equation 4.1 for this case, while taking the generation rate, G, under solar illumination (see Section 3.5.1), the time, t, of 12 hours, and the fitting parameters A and B determined above to be 43.6 and 27.5×10^{-3} allows the determination of the value of the scaling factor, g, which will prevent significant segregation under these conditions to be $1.01 \times 10^{-26}\,\text{cm}^3$. Extrapolating the linear fit presented in Figure 4.10 to this value of g then determines that the fraction of charge carriers that recombine through trap states must be lower than about 0.1% for significant segregation to be avoided in $MAPb(Br_{0.5}I_{0.5})_3$ films under solar illumination. Finally, under continuous illumination, Equation 4.5 will be equal to zero, which allows the determination of the required value of k_1 given G, k_2, k_3, c_{ext} and the condition that the fraction of charge carriers that recombine through trap states, $\frac{k_1 n}{G}$, is equal to 0.1%. For this purpose, the calculated value of G under solar illumination is used (see Section 3.5.1), k_2 is assumed to be $6 \times 10^{-10}\,\text{cm}^3\,\text{s}^{-1}$ as determined from the samples used in this study (see Section 4.4.2.1), k_3 is assumed to be $10^{-28}\,\text{cm}^6\,\text{s}^{-1}$ in accordance with similar perovskites [61], and a typical value of c_{ext} is taken to be $10^8\,\text{s}^{-1}$ as suggested by Lin *et al.* [175]. From such considerations, a value for k_1 of $10^5\,\text{s}^{-1}$ is calculated (corresponding to a PL lifetime of $\tau_{\text{PL}}=(2k_1)^{-1}$=5 µs at low excitation fluence) to be just sufficient to prevent the iodide-rich perovskite PL peak from becoming dominant in the PL spectrum of $MAPb(Br_{0.5}I_{0.5})_3$ over the course of a half-day of full solar illumination.

It is noted that values of k_1 near $\sim 10^5\,\text{s}^{-1}$ have been achieved for other perovskites [202], and hence it is not unfeasible that $MAPb(Br_xI_{(1-x)})_3$ could reach these, with further advances in processing and defect passivation. In addition, mixed-halide perovskites

other than $MAPb(Br_xI_{(1-x)})_3$ may be associated with a different set of parameters A, B and g which yield potentially less stringent requirement for lowering trap-related charge-carrier recombination. Section 2.4 highlights that a number of perovskite systems have shown much lower propensity for halide segregation than the corresponding MA-based perovskites. In particular, while $Cs_yFA_{1-y}Pb(Br_xI_{(1-x)})_3$ perovskites have also exhibited clear correlations between trap-mediated recombination rates and propensity for halide segregation [117], $Cs_yFA_{1-y}Pb(Br_xI_{(1-x)})_3$ appears to achieve stability at higher values of k_1 than those predicted to be required for $MAPb(Br_xI_{(1-x)})_3$. Therefore, with both stoichiometric and structural engineering, as well as lowering of defect concentrations, it should be possible to suppress halide segregation sufficiently in functional perovskite solar cells.

4.5 Proposed Halide Segregation Mechanism

Given the results presented in this chapter on the role of electronic trap states in halide segregation, the following description of the underlying halide segregation mechanisms is proposed. Prior to illumination, iodide and bromide ions are entropically well mixed in the perovskite, which therefore has a constant bandgap across all regions of the film. Although the nature of trap states is not yet entirely understood in hybrid perovskite materials [84, 85], reports have suggested that electrons are more likely to be trapped than holes [203, 204], and that these trapped carriers are very long lived (on the order of tens of microseconds) [204, 205]. Initially upon illumination, any trapped electrons will electrostatically attract the photogenerated free holes, reducing the distance between the two and therefore minimising the electric potential in the perovskite film. Additionally, random thermal movements of the halide ions and free charge-carriers may eventually cause small regions of iodide-rich perovskite to form. With a higher valence band [94, 206], these regions act to draw free holes away from the trapped electrons states, creating a degree of

charge separation between the randomly distributed trap states and the iodide-rich regions of perovskite, which thus establishes an electric field in the film. This field increases the degree of halide segregation, which increases the degree of charge separation, thus increasing the strength of the electric field in a feedback loop. Eventually the perovskite film is maximally segregated and limited by back-diffusion of the halide ions due to the large concentration gradient, i.e. the film reaches equilibrium. Without illumination and once the trapped charge-carriers have recombined, the created electric field vanishes, and the halide ions diffuse and remix. This description explains various observed phenomena, including that charge-carriers, [20, 21] electronic trap states and film crystallinity [103, 117, 122] all influence halide segregation, and the initially slow, asymptotic evolution (Figure 4.7) of the iodide-rich perovskite PL intensity reported in this chapter.

4.6 Summary and Conclusion

In summary, the work presented in this chapter has demonstrated that the environmental atmosphere has a profound impact on the halide segregation dynamics in $MAPb(Br_{0.5}I_{0.5})_3$ observed through PL experiments under illumination. In particular, repeated cycles of illumination followed by darkness did not yield identical results when the perovskite was held in air or vacuum, most likely because these environments induce trap passivation or formation, respectively, in accordance to what had previously been reported for single-halide perovskites [24, 26, 28, 30, 32]. On the other hand, halide segregation was found to be mostly reversible under inert nitrogen, or when the film was encapsulated with a PMMA coating. It is concluded that in fully encapsulated photovoltaic devices, halide segregation should therefore be a fully reversible process. The findings of this chapter further highlight a potential source for the discrepancies between different reports of halide segregation in the literature, which may partly derive from experiments having been conducted in a variety of atmospheres.

In addition, the influence of trap states on the rate of halide segregation was explored by monitoring the segregation dynamics for different charge-carrier densities. The formation dynamics of iodide-rich emission from the perovskite film were shown to follow the same functional form, regardless of illumination conditions. It was further established that the efficacy of a photon to induce halide segregation is higher at lower charge-carrier densities, a result attributed to the larger relative fraction of charge carriers being trapped at these low densities. From these observations, an empirical model was established that directly links the amount of halide segregation observed in PL to the fraction of charge carriers recombining through trap-mediated channels, and the photon flux absorbed. Such quantitative analysis allowed a number of conclusions to be drawn on open questions on the mechanism driving halide segregation. For example, it was revealed that if modulated light is used to photoexcite mixed-halide perovskites, the frequency of the modulation alone has no influence on the segregation dynamics. In addition, it is extrapolated that working perovskite solar cells based on $MAPb(Br_{0.5}I_{0.5})_3$ would require a reduction of the trap-related charge-carrier recombination rate to $\lesssim 10^5\,s^{-1}$ ($\tau_{PL} \gtrsim 5\,\mu s$) in order for halide segregation to be sufficiently suppressed. The results in this chapter suggest that light-induced halide segregation is initiated by electric fields arising from trapped charge carriers, and may be further driven by funnelling of charge carriers into the newly formed lower-energy iodide-rich domains. These findings contribute to our understanding of the mysterious underlying mechanics of halide ion movement in perovskites and provide a framework for determining the conditions required for stabilised perovskite devices under working conditions.

5

Electric Fields, Defect Species and Halide Segregation in Mixed-Halide Perovskite Photovoltaic Devices

Contents

Initially published as Ref. [157].

5.1 Introduction and Background

In Chapter 4 it was found that electronic trap states and trapped charge carriers play an important part of the underlying halide segregation mechanism [150]. Additionally, electronic trap states are responsible for the majority of the preventable losses in solar cell performance under typical working conditions, and so understanding and passivating trap states represents one of the greatest challenges for mixed-halide perovskites. This chapter studies the interaction between electric fields, trap states, and ionic motion in mixed-halide perovskite photovoltaic devices, revealing interesting insights about the myriad of different defect species within the perovskite material.

Halide segregation and electronic trap states represent two of the most substantial obstacles for the incorporation of mixed-halide perovskite into stable and efficient tandem solar cells. Particularly important for photovoltaic devices is the interaction of halide ions and trap states with electric fields, since efficient power extraction depends on the combination of external and built-in electric fields within a solar device [48]. Additionally, it has been observed that electric fields can influence the PL from $MAPbI_3$ films through trap state movement [207–210], a process which – similarly to halide segregation – is attributed to the movement of mobile, charged species in the perovskite material. Therefore, in order to fully understand the limiting aspects of mixed-halide perovskite devices under normal working conditions it is necessary to consider the complex interaction between electric fields, different electronic trap states and halide segregation.

In this chapter PL, time correlated single photon counting (TCSPC), and external quantum efficiency (EQE) measurements are performed on full $MAPb(Br_{0.5}I_{0.5})_3$ photovoltaic device stacks under an external bias in order to examine the underlying processes and charge-carrier pathways in segregating mixed-halide perovskite materials. It is noted that while even state-of-the-art $MAPb(Br_{0.5}I_{0.5})_3$ perovskite photovoltaic devices are

relatively inefficient compared to those composed of other mixed-halide perovskites, [65, 66, 167, 211] $MAPb(Br_{0.5}I_{0.5})_3$ still represents an ideal material for studies on halide segregation because it segregates quickly under ∼1 sun illumination intensities, allowing repeated measurements to be made in a reasonable time frame [17]. Section 5.2 gives a brief overview of the experiments performed for this chapter, which are relatively simple in concept. The complexity of the measurements presented in this chapter arises due to the flexibility afforded by the experimental setup – see Section 3.2 – in combining periods of illumination/darkness with periods with or without applied biases across the examined photovoltaic devices. Section 5.3 presents results pertaining to the basic characterisation of the examined photovolatic devices used in the rest of the chapter. Evidence for three species of defects in the perovskite material is discussed in Section 5.4: First, a charged, mobile trap species, proposed to be MA^+ interstitial defects in the perovskite crystal, is observed to detrimentally affect the radiative efficiency of the perovskite material. Second, following the work of the Chapter 4 [150], it is suggested that charge neutral crystal distortions in the perovskite structure trap photoexcited charge carriers and contribute to the halide segregation mechanism. Third, charged, mobile defects, proposed to be halide vacancies and/or interstitials in the perovskite material, are observed to rapidly screen the perovskite layer in the examined photovoltaic devices upon a change in the applied external bias. In Section 5.5 it is found that while halide segregation is detrimental for current extraction from a mixed-halide perovskite solar cell, some current is still extracted from the forming iodide-rich perovskite domains of such a solar cell under illumination. The extraction of current from the low-bandgap domains suggests the existence of percolation pathways between the iodide-rich regions of the perovskite and the charge transport layers in the device stack, which are postulated to be formed at the grain boundaries in the perovskite layer. Section 5.6 presents a Sankey (flow)

diagram to summarise the understanding gained from this chapter – and from Chapter 4 – of the charge-carrier pathways in mixed-halide perovskite devices. Finally, Section 5.7 summarises and concludes the results of this chapter.

5.2 Experimental Details

All steady-state PL and TCSPC data in this chapter were taken as detailed in Section 3.2.1 and 3.2.2, respectively. Illumination was provided by a 400 nm wavelength diode laser (Picoharp, LDH-D-C-405M), at specified illumination intensities and illumination modes (continuous wave or pulsed). Applied voltages were supplied by a Keithley 2450 Sourcemeter, and the same Keithley 2450 Sourcemeter was used for all extracted current measurements. External quantum efficiency (EQE) measurements were performed as detailed in Section 3.6.

5.3 Basic Sample Characterisation

5.3.1 Photovoltaic Device Statistics

The device characterisation data presented in this section was measured by J. B. Patel, Department of Physics, University of Oxford.

The $MAPb(Br_{0.5}I_{0.5})_3$ perovskite solar cells used in this chapter were first characterised under simulated AM1.5, 100 mW cm^{-2} sunlight (1 sun), using an ABET Technologies Sun 2000 and a Keithley 2400 Sourcemeter in ambient conditions. The active area of each device was defined by a mask which exposed a 0.0919 cm^2 active area for testing of both the current voltage characteristics and stabilised power output. The devices were prebiased at 1.4 V for 5 s before initiating the reverse and forward scans. Average and champion device statistics are shown in Table 5.1, where the champion pixel is the one recorded to have the highest stabilised power output (SPO).

Figure 5.1 shows the forward and reverse J-V scans from the champion pixel of the $MAPb(Br_{0.5}I_{0.5})_3$ perovskite solar cells, with the inset showing the SPO (stabilised power output) from this pixel.

Table 5.1: $MAPb(Br_{0.5}I_{0.5})_3$ device statistics for the champion pixel (the one with the highest standardised power output) and the average performance of all 36 pixels made.

	PCE (%)	J_{SC} (mA cm^{-2})	V_{OC} (V)	Fill Factor	SPO (%)
Champion Pixel	5.79	11.90	0.98	0.49	5.32
Average of 36 Pixels	5.64	11.56	1.01	0.48	2.94

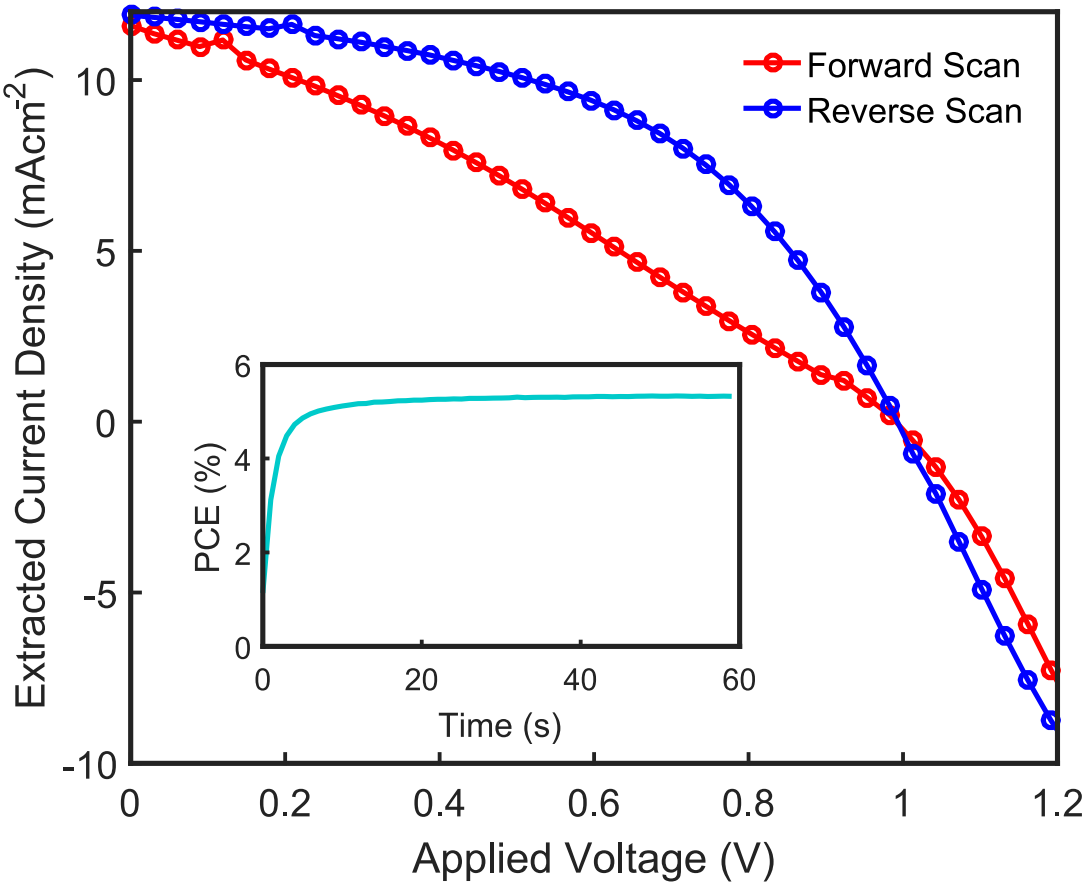

Figure 5.1: The forward and reverse current-voltage scans from the solution processed $MAPb(Br_{0.5}I_{0.5})_3$ device pixel with the highest measured stabilised power output. The stabilised power output for the same device pixel is plotted in the inset.

5.4 Defect Species in $MAPb(Br_{0.5}I_{0.5})_3$

PL and TCSPC measurements are sensitive to both the charge-carrier population in a material and the rules for radiative and nonradiative decay, and so they are powerful tools in uncovering the charge-carrier pathways in mixed-halide perovskites. Figure 5.2a shows a schematic of the basic experimental setup and device layers used for the work presented in this chapter, alongside a set of example PL spectra and a TCSPC trace. Basic device statistics, including current-voltage scans and a stabilised power output graph from the champion pixel, are reported in Section 5.3.1. As shown in the example PL spectra in Figure 5.2a, upon illumination of the device, the PL peak attributed to the mixed-halide perovskite phase (emission around 665 nm) diminished, and a lower energy peak (around 745 nm) was observed to emerge. These changes in the PL spectrum have been well-established by the literature – and the work of Chapter 4 – to result from photoexcited charge carriers funneling from the well-mixed perovskite phase into the lower-bandgap regions of iodide-rich perovskite that form under illumination as halide segregation takes place [17, 176]. The mixed-halide device stack used in this chapter was built upon a glass substrate, with SnO_2 and 2,2',7,7'-Tetrakis[N,N-di(4-methoxyphenyl)amino]-9,9'-spirobifluorene (spiro-OMeTAD) used as the electron and hole transport layers, respectively. Gold and fluorine doped tin oxide (FTO) were used as the top and bottom contact layers, respectively. Applying a voltage between the contact layers allowed an examination of the influence of an electric field on the charge-carrier dynamics within the perovskite layer.

5.4.1 Influence of Charged, Mobile Trap States

Figure 5.2b shows the PL intensity emitted around 745 nm from a fresh $MAPb(Br_{0.5}I_{0.5})_3$ photovoltaic device as an applied voltage across the device was changed multiple times

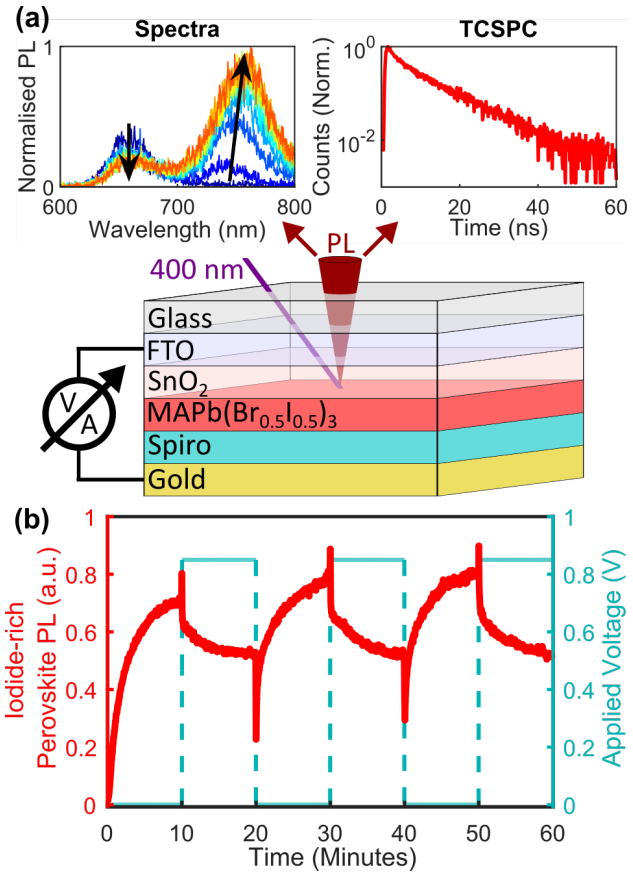

Figure 5.2: Experimental overview and results from PL measurements of an $MAPb(Br_{0.5}I_{0.5})_3$ device held at various applied voltages. (a) Device stack and experimental schematic for PL measurements. Example PL and TCSPC data taken under the same experimental conditions as (b) and Figure 5.5, respectively, are also shown. (b) The behaviour of the low-energy PL (PL spectra integrated from 720 to 770 nm and plotted in red) as a changing voltage (plotted in blue) is applied across a mixed-halide perovskite device under 400 nm, 110 mW cm^{-2}, continuous wave illumination.

between 0 V (short circuit) and 0.85 V. In order to induce halide segregation and to cause the emission of PL, the device stack was illuminated with a continuous wave, 400 nm laser at 110 mW cm^{-2} intensity. Spectral measurements were made every 3 s, and in order to better follow the growth of the iodide-rich regions in the perovskite layer, the corresponding low-energy peak in the PL spectrum was integrated (from 720 to 770 nm) and is plotted in red in Figure 5.2b as a PL intensity. The voltage applied across the device is plotted in cyan in Figure 5.2b, with 0 V being first held across the device for 10 min as the perovskite layer initially segregated, and subsequent 10 min periods of

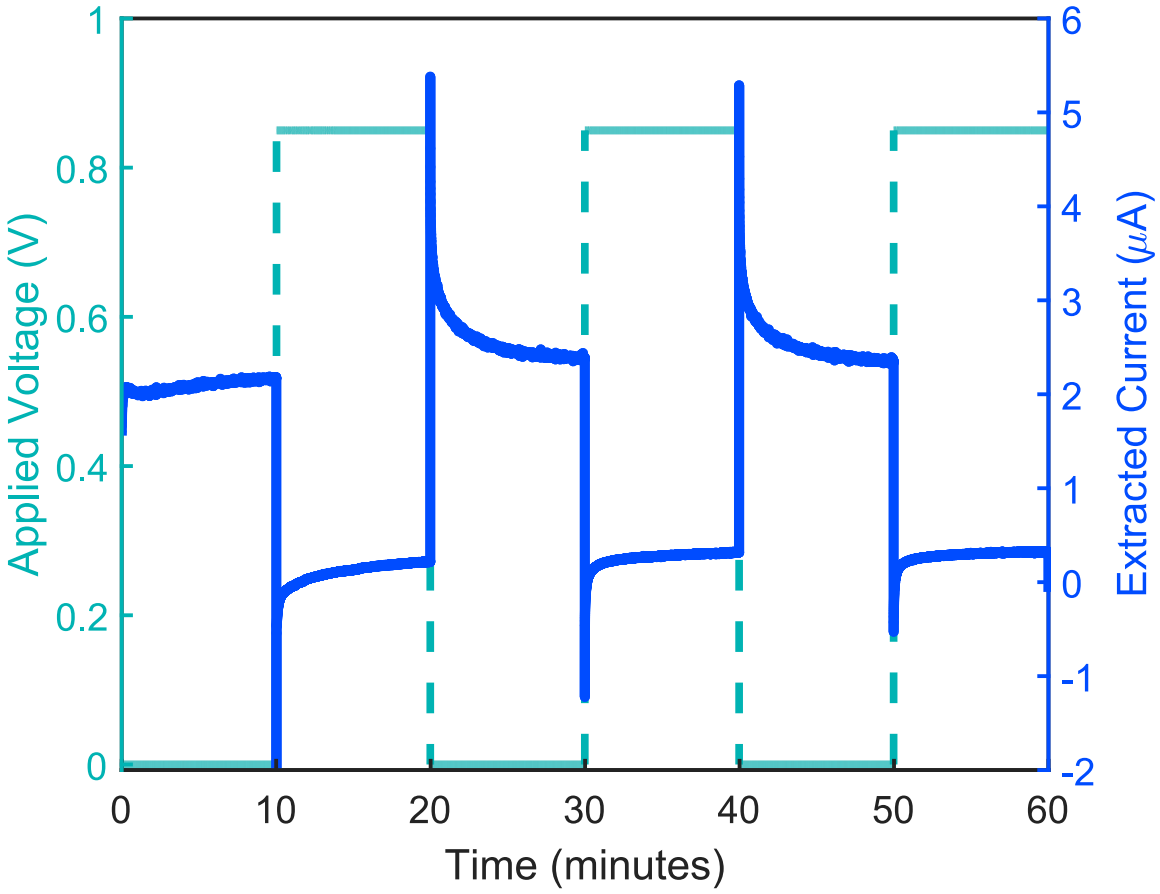

Figure 5.3: The current extracted from an $MAPb(Br_{0.5}I_{0.5})_3$ perovskite device under 400 nm, 110 mW cm^{-2}, continuous wave illumination (plotted in deep blue) as the applied voltage across the device was changed between 0 and 0.85 V every 10 minutes (plotted in turquoise).

applied voltage alternating between 0.85 V and 0 V. The current extracted from the device during this experiment is plotted in Figure 5.3. It is important to note that in n-i-p photovoltaic devices such as the ones used in this chapter, a built-in electric field is generated between the n and p layers, and this field permanently exists across the perovskite layer – see Section 2.2. The external voltage that was applied across the contact layers counteracted this built-in field, allowing control over the total field across the perovskite layer. For example, at 0 V applied bias (i.e. at short circuit) there was no counter-field working against the built-in field and so the voltage across the perovskite layer was relatively high. At an applied bias of 0.85 V the built-in field was

mostly cancelled out by the applied field, resulting in a much lower net field across the perovskite layer. As shown by the current extraction measurements plotted in Figure 5.3, 0.85 V was close to the open circuit voltage of the device, the V_{OC}, as little current was extracted at this applied voltage. As shown in Chapter 4 [150], the combination of a thick encapsulation layer (here a role provided by the spiro-OMeTAD and gold layers) and holding the perovskite device under vacuum (at a pressure of $\sim 10^{-1}$ mbar for this experiment) prevents any significant interaction between the perovskite and the surrounding atmosphere. As a result of this protection, it is noted that no long-term trends attributable to atmospheric influence [24, 32] were observed in data presented either in Figure 5.2b, Figure 5.3, or the rest of the data presented in this chapter.

During the first 10 min under illumination at 0 V applied bias, Figure 5.2b shows a clear rise and plateau of the iodide-rich perovskite PL, which is ascribed to the growth and stabilisation of the iodide-rich domains within the perovskite layer [17]. Thereafter, whenever the applied voltage was increased from 0 to 0.85 V the PL intensity initially spiked sharply upward, before slowly decaying to a lower value. Conversely, when the applied voltage was decreased from 0.85 to 0 V the PL intensity initially spiked sharply downward before slowly rising to a higher value. The sharp spikes follow the behaviour expected of a typical solar cell – see Figure 5.4 for an example of the PL emitted and the current extracted from a solution processed $MAPbI_3$ device under different voltages – as at an applied bias of 0 V (0.85 V), the extracted current was maximal (minimal), and so fewer (more) charge-carriers were available to recombine radiatively, leading to less (more) PL. Figure 5.3 shows that the extracted current from the measured $MAPb(Br_{0.5}I_{0.5})_3$ device was indeed higher and lower at 0 and 0.85 V applied bias, respectively. It is therefore concluded that the spikes in the PL intensity observed in Figure 5.2b were the

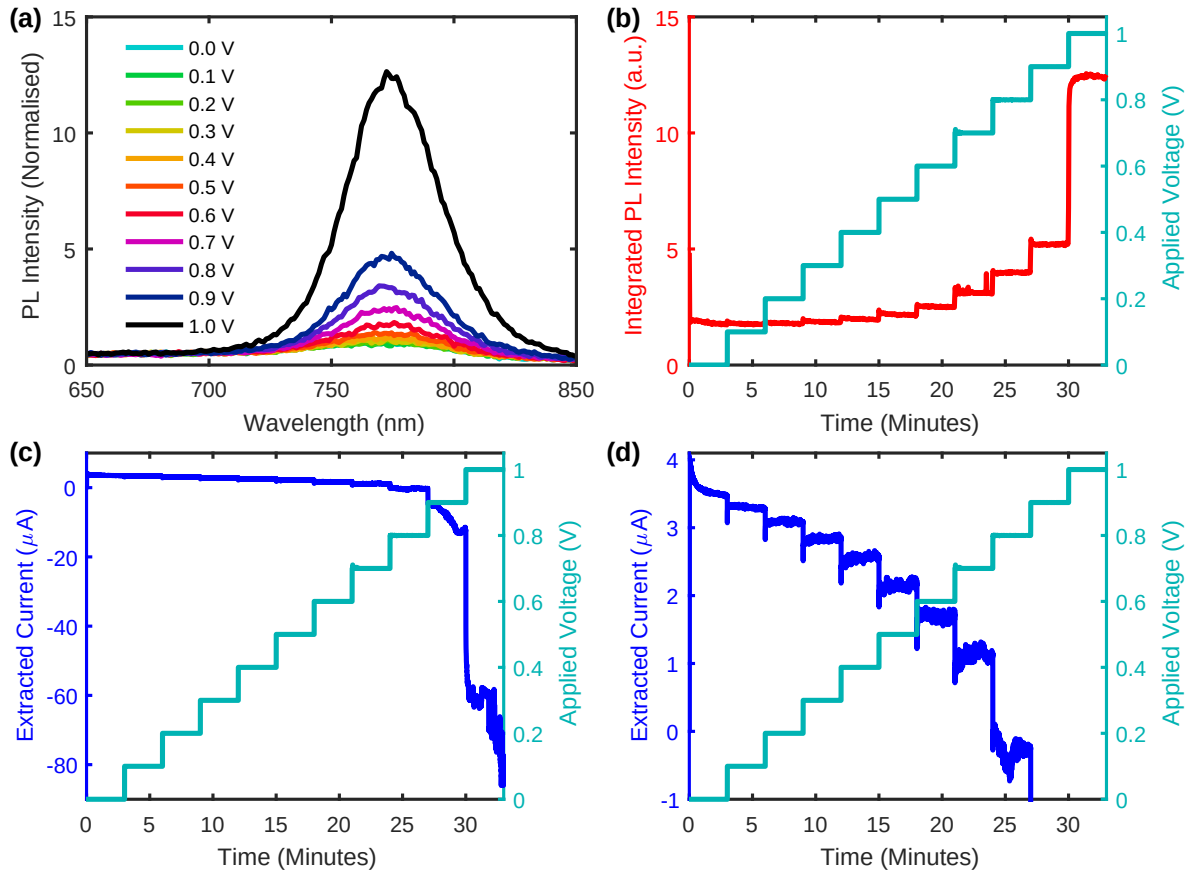

Figure 5.4: (a) Normalised PL spectra from an $MAPbI_3$ device under various applied voltages between 0 and 1 V. At the start of the experiment the voltage held across the device was 0 V, and the applied voltage was raised in 0.1 V steps up to 1 V over the course of 33 min. Each of the 11 voltages was held across the device for approximately 3 min to allow the device to reach equilibrium before the PL spectra were recorded. The illumination was continuous wave, at an intensity of 110 mW cm^{-2}. The spectra have all been globally normalised so that the maximum intensity of the spectrum taken at 0 applied volts is 1. (b) Plotted in red is the integral of the PL spectra (integrated from 700-850 nm) taken from the same $MAPbI_3$ device and during the same experiment as the data in (a). Plotted in light blue is the voltage applied across the $MAPbI_3$ device during the same experiment. (c) Plotted in dark blue is the current extracted from the same $MAPbI_3$ device and during the same experiment as the data in (a). Plotted in light blue is the voltage applied across the $MAPbI_3$ device during the same experiment. (d) The same data as in (c), scaled to show the positive extracted current from the device at voltages below the open-circuit voltage.

result of a higher or lower charge-carrier density within the perovskite layer depending on the level of current extraction present at the applied voltage.

The slower changes in PL intensity following the initial spike at the start of each 10 min period (Figure 5.2b) suggest that the radiative efficiency of the perovskite layer

slowly increased or decreased when held under 0 or 0.85 V applied bias, respectively. These slow changes did not coincide with any significant change in the illumination source (which was held constant), and the extracted current is shown in Figure 5.3 to have reached equilibrium much faster than the PL upon each applied voltage change, ruling out these two alternative explanations. In order for the radiative efficiency to change, it is concluded that the nonradiative recombination pathways (i.e. trap states) increasingly interacted with the photoexcited charge-carrier population as the applied voltage across the device was increased, reducing the emitted PL. It is noted that such behaviour was not found under similar conditions for a solution processed $MAPbI_3$ device (see Figure 5.4), likely due to intrinsic material differences affording different amounts of ion migration between the two materials, and differences in device performance altering how much charge-carrier extraction affected the emitted PL. Correlations between applied voltage and loss of radiative efficiency have previously been reported in $MAPbI_3$ and other metal halide perovskites [207–210, 212].

To further study the influence of electric field on the rate of trap mediated recombination, time-resolved PL measurements (utilising TCSPC) were performed on a perovskite photovoltaic device at various voltages, with the results presented in Figure 5.5. Before each measurement, the same device was subjected to 1 h of illumination with the target voltage applied across the device in order to ensure that any mobile ions within the perovskite layer had reached equilibrium. An additional period of 0.5 h under illumination and bias was applied at the start of the experiment to account for the fact that the mobile ions (particularly the segregating halide ions) would need more time to reach equilibrium when the illumination and bias was applied to the initially fresh device. The illumination source was a 400 nm laser pulsed at 5 MHz and at 1400 mW cm^{-2} intensity,

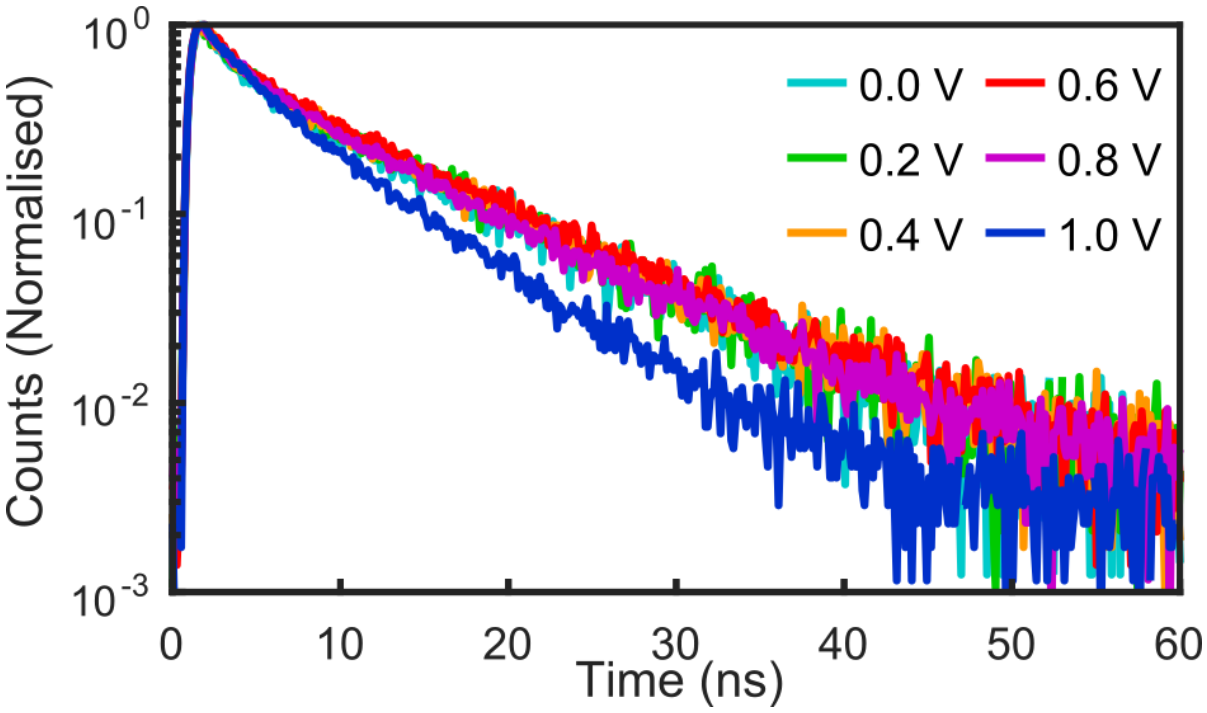

Figure 5.5: TCSPC decay traces measured at the low-energy PL peak (750 nm) of a mixed-halide perovskite device under various applied voltages and under 400 nm, 1400 mW cm^{-2}, 5 MHz pulsed laser illumination. The device was held at each target voltage for at least 1 h before each 120 s TCSPC measurement was taken, and the applied voltages were applied in descending order.

the accumulation time for each trace was 120 s and the measured PL wavelength was at 750 nm, near the centre of the iodide-rich perovskite PL peak.

Figure 5.5 shows that the charge-carrier recombination rate within the iodide-rich regions of the perovskite layer was roughly constant at applied voltages lower than ∼0.8 V, and higher at ∼1.0 V applied bias. In order to ensure that the change in charge-carrier lifetimes was not the result of material degradation over the course of several hours, the set voltages were applied in decreasing value, i.e. with 1.0 V applied first. Figure 5.6 presents near-identical data from a similar experiment in which the set voltages were applied in ascending order, further showing that the changes to the charge-carrier lifetimes were caused by the resulting bias across the perovskite, not material degradation over the course of the experiment. The increase in charge-carrier recombination rate at high applied voltage could be a consequence of an increase in trap-mediated recombination,

radiative recombination, current extraction, or a combination of these factors (Auger recombination is assumed to be negligible at the 1400 mW cm^{-2} illumination intensity used after at most a few nanoseconds into the decay dynamics [61]). It is shown in Section 5.5 that the iodide-rich regions in the segregated perovskite layer do contribute to the current extracted from the mixed-halide perovskite device, however an increase in applied voltage serves to decrease the extracted current, which lengthens the charge-carrier lifetimes – this behaviour is highlighted in Figure 5.7 for an $MAPbI_3$ device. Additionally, it was shown in Figure 5.2b that the rate of radiative recombination (which produces PL) does not increase at high applied voltages, indicating that the shortening of charge-carrier lifetimes at an applied bias of 1.0 V was primarily due to an increase in the rate of trap-mediated recombination in the perovskite layer at high applied voltage. Thus, Figure 5.5 corroborates the evidence in Figure 5.2b that a higher applied voltage increases the rate of trap-mediated charge-carrier recombination in $MAPb(Br_{0.5}I_{0.5})_3$ photovoltaic devices. It is noted that with the setup used in this chapter (detailed in Section 3.2), changes to the radiative efficiency of the devices were more easily resolved through PL measurements than with TCSPC measurements, as also evident from PL and TCSPC measurements of the $MAPbI_3$ device shown in Figures 5.4 and 5.7, respectively.

The timescale and nature of the changes that occur in the PL presented in Figure 5.2b are similar to those that have been observed to occur in the single-halide perovskite $MAPbI_3$ under similar bias conditions [207–210]. Therefore, as has been done in the literature for $MAPbI_3$, the decrease in PL intensity (Figure 5.2b) and charge-carrier lifetime (Figure 5.5) that occurs with an increased applied voltage is attributed to the movement of charged, mobile trap states in the perovskite. Figure 5.2b shows that the radiative efficiency of the perovskite layer is highest at 0 V applied bias, when the total electric field across the perovskite results solely from the built-in field, suggesting that

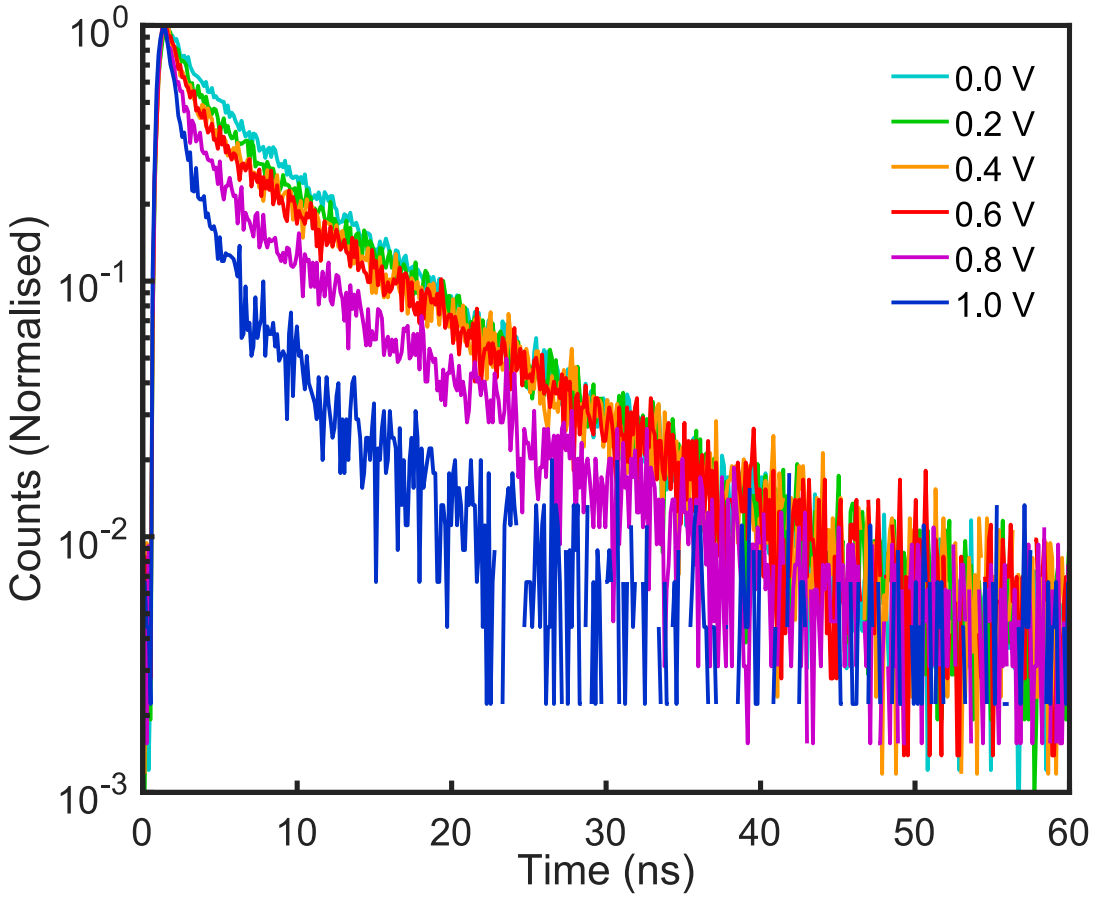

Figure 5.6: TCSPC decay traces measured at the low-energy PL peak (750 nm) of a mixed-halide perovskite device under various applied voltages and under 400 nm, 1400 mW cm^{-2}, 5 MHz pulsed laser illumination. The device was held at each target voltage for 1 hour before each 120 s TCSPC measurement was taken, and the applied voltages were applied in ascending order.

the mobile trap states are forced away from the illumination side of the device – where the density of photoexcited charge-carriers is highest – by the built-in potential field generated by the extraction layers. In n-i-p devices, such as the ones used here, the illuminated volume of the perovskite layer – where the charge-carriers are photogenerated – is near the positively charged, electron extraction layer, which suggests that the mobile trap states carry a positive charge and accumulate near the hole extraction layer at 0 V applied bias. Due to their charge, these proposed trap states will attract and trap electrons, but repel and be largely benign to holes. The quenching of the PL intensity

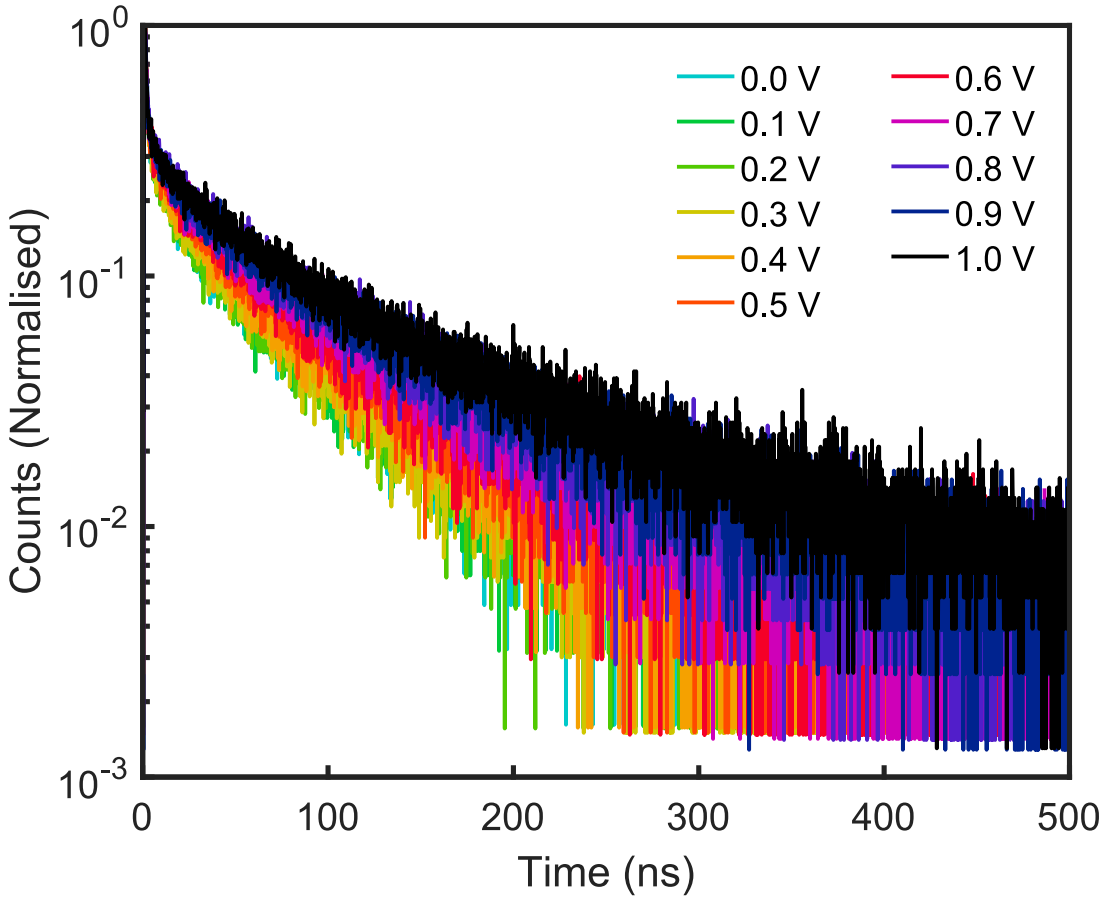

Figure 5.7: TCSPC measurements of an $MAPbI_3$ device under various applied voltages between 0 and 1 V. Each voltage was held across the device for approximately 3.5 min before the corresponding TCSPC measurement was taken, and the voltages were applied in ascending order. The device was constantly held under pulsed illumination at 1 MHz repetition rate and at 320 mW cm^{-2} average intensity throughout the experiment. The PL wavelength measured was 785 nm, and each TCSPC measurement was taken over 30 s of accumulation time. The TCSPC traces have been individually normalised such that the maximum number of counts from each trace is 1.

and lifetime is then explained as follows: at 0 V applied bias, a large voltage is generated across the perovskite layer by the built-in field. This potential forces the positive trap states toward the spiro-OMeTAD side of the device, and collects the electrons into the SnO_2 layer, away from the trap states. Thus at low applied voltage the trap states and the electrons are separated, leading to a limited amount of trap-mediated recombination, and therefore a higher rate of radiative recombination despite the significant current extraction. At an applied bias of 0.85 V, the applied electric field significantly offsets the

built-in electric field, and so the migratory trap states are less appreciably accumulated at the spiro-OMeTAD side of the device and instead diffuse more evenly throughout the perovskite layer, allowing them to interact with and trap the photogenerated electrons. The larger overlap of trap and electron densities at 0.85 V applied bias leads to the observed quenching of PL in Figure 5.2b. Beyond 0.85 V applied bias, the total electric field across the device reduces further and eventually works to collect the trap states at the illumination side of the device, causing an additional increase of the electron-trap density overlap and quenching the PL lifetime as seen in Figure 5.5. It is noted that one possible candidate for these charged trap states could be MA^+ interstitials in the perovskite crystal, since these defects are positively charged, and have previously been observed in $MAPbI_3$ to move on a similar timescale to the dynamics in Figure 5.2b [213].

5.4.2 Dynamic Interaction of Trap States, Electric Fields, and Halide Segregation

It is important to understand how both the mobile trap states discussed above and electric fields will affect the halide segregation dynamics in a mixed-halide perovskite device, as this may provide insight into the underlying segregation mechanism. To study the dynamic ion segregation and remixing processes – as opposed to focusing on the equilibrium state reached by the segregating perovskite as was done in Figures 5.2b and 5.5 – a fresh mixed-halide perovskite device was repeatedly exposed to 1 min intervals of illumination under 110 mW cm^2 (∼1 sun), 400 nm, continuous wave light, followed by 30 min of darkness. The intervals of darkness lasted 30 times longer than the illumination intervals to ensure enough time for the segregated ions to remix [17]. Under darkness no voltage was applied across the device, and under illumination the device was held at various constant biases to vary the total electric field across the perovskite layer. As shown in the top panel of Figure 5.8a, the applied bias was ramped up and down between

0 and 1 V in 0.1 V increments between illumination intervals. The up-down voltage ramp was performed 4 times in order to examine the repeatability of the PL behaviour and to observe any significant long-term changes in the segregation dynamics, of which none were found. As before, the PL spectra were taken every 3 s within the illumination intervals, and the mixed-halide and iodide-rich perovskite PL peaks were integrated over (from 640 to 690 nm and 720 to 770 nm, respectively) to give integrated PL intensities, which are plotted in the bottom and middle panels of Figure 5.8a, respectively.

The middle and bottom panels of Figure 5.8a show that the PL emitted from the perovskite device varied considerably throughout the 88 illumination intervals over the course of the experiment. During each illumination interval, the middle panel of Figure 5.8a shows that the PL signal from the iodide-rich perovskite regions increased from near zero, and the bottom panel of Figure 5.8a shows that the mixed perovskite PL signal decreased. These PL changes are well-reported in the literature to be the result of photoexcited charge carriers funneling from the mixed perovskite phase into the forming regions of iodide-rich perovskite as halide segregation takes place [17, 176]. The variation in PL over the multiple illumination periods resulted from a combination of the movement of charged trap states as observed in Figures 5.2b and 5.5 and – to a lesser extent – the change in extracted current from the device. As shown in Figure 5.2b, the effect of current extraction on the emitted PL from the perovskite layer (the sharp peaks and troughs in PL intensity that occur upon a voltage change) is quickly overwhelmed by the effect of the mobile trap states (the slower, asymptotic behaviour of the PL after a voltage change), suggesting that the radiative efficiency of the perovskite is more heavily dependent on the distribution of the mobile trap states than on the current extraction efficiency. The changes in the emitted PL that occurred over the course of each individual illumination interval are therefore primarily attributed to the effects of

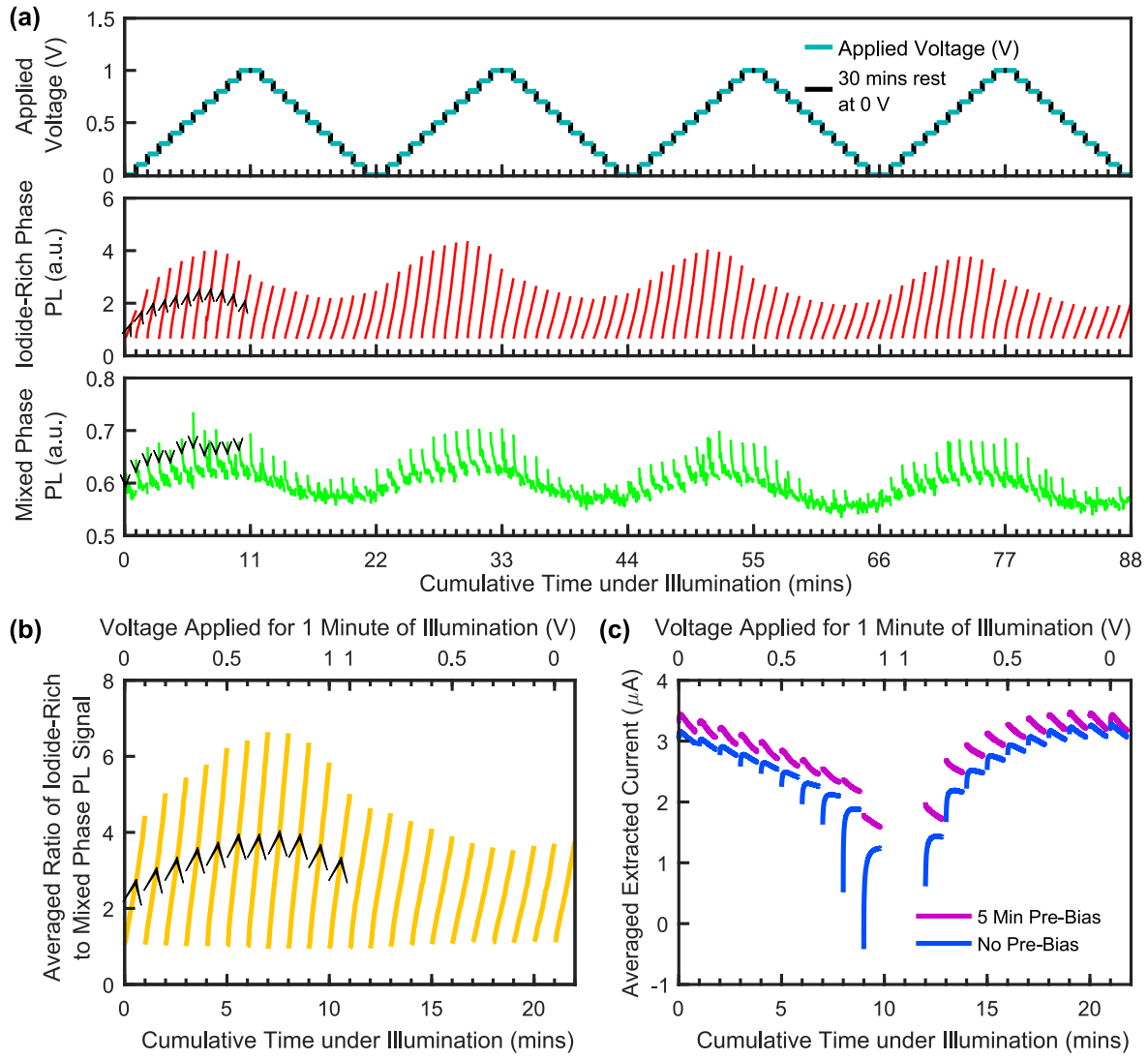

Figure 5.8: PL and extracted current measurements from a mixed-halide perovskite device as an applied voltage across the device was repeatedly ramped up and down between 0 and 1 V. (a) Top panel: The voltages applied across the device and indication of the rest intervals during the experiment. Middle panel: The integrated low energy PL (720-770 nm) from the device under 400 nm, 110 mW cm^{-2}, continuous wave illumination. Arrowheads over the first 11 illumination intervals help to indicate that, over the course of every illumination interval, the low energy PL increased in intensity due to halide segregation effects. Bottom panel: The integrated higher energy PL (640-690 nm) from the device. Arrowheads indicate that, over the course of every illumination interval, the higher energy PL decreased in intensity due to the effects of halide segregation. (b) The ratio of the PL signals from the middle and bottom panels of (a), averaged across the last 3 voltage up-down ramps. Arrowheads indicate that, over the course of every illumination interval, the ratio of the PL signals increased due to halide segregation effects. (c) Averaged behaviour of the extracted current from devices with and without a 5 min prebiasing period before illumination at applied voltage, with the entirety of the corresponding extracted current data presented in Figures 5.12d and 5.11b, respectively.

halide segregation, and the changes that occurred over multiple illumination intervals to the motion of the mobile charged trap states.

Over multiple illumination intervals, the PL signal at a given point in each 1 min interval (for example, the first or last PL measurement) modulated up and down over the course of the experiment. This modulation of PL seen in the middle and bottom panels of Figure 5.8a is attributed to the movement of the mobile trap states toward and away from the illumination side of the perovskite layer according to the applied voltage across the device. Interestingly, this modulation of PL is not quite in phase with the applied voltage ramp, as the largest PL signals were observed when ~0.7 V were applied across the device, 0.3 V before the peak of the applied voltage ramp at 1 V. Additionally, the PL emitted from the perovskite layer is seen in the middle and bottom panels of Figure 5.8a to not only depend on the applied voltage across the device, but also on whether the voltage is ramping up or ramping down, i.e. the PL emitted from the perovskite is not solely dependent on the immediate conditions, but also on the history of the applied electric fields. The dependence on the previous history of the experiment can be thought of as hysteresis in the PL measurements across the voltage up-down ramp. The observed hysteresis suggests that the mobile trap states lag behind the applied voltage, which is expected, given that Figure 5.2b shows the trap states take ~10 min to reach equilibrium, an order of magnitude more than the 1 min illumination intervals used in the multiple voltage ramp experiment. Additionally, the observed hysteresis in the PL in the middle and bottom panels of Figure 5.8a suggests that 30 min under darkness at 0 V applied bias was insufficient to return the mobile trap states to equilibrium. If the trap states reached the same equilibrium between every illumination interval, there would be no way for previous measurements to affect future ones. There are many reports in the literature that ionic diffusion in perovskites is

slower under darkness than in the presence of illumination [17, 214–216], so it is not unreasonable that the trap states were unable to return to their steady-state distribution in the dark. While 30 min under darkness was observed to be enough to remix the halide ions that had segregated under illumination, the dynamics, length scales, and ionic species involved in halide segregation [104, 119, 144] and the observed trap movement are not necessarily expected to be similar, and so different timescales for returning to equilibrium under darkness at 0 V applied bias is not inexplicable.

In order to somewhat disentangle the amount of halide segregation that occurred over the course of each illumination interval from the modulation of the PL intensity that resulted from the movement of the mobile trap states, the plots in Figure 5.8b show the ratio of PL signals from the iodide-rich and the mixed-halide regions of perovskite over the course of an average voltage ramp. The ratio of the two PL signals was averaged over the last three voltage ramps for clarity, with the data from the first voltage ramp excluded from the average to eliminate the effect of the initial state of the device from the periodic trend seen. During halide segregation, the PL signal from the iodide-rich regions of perovskite grows relative to the PL signal from the mixed perovskite phase, and so the ratio of the PL signals in Figure 5.8b represents a measure of the amount of halide segregation in the perovskite layer. While it is acknowledged that a simple ratio of the PL signals is not sufficient to completely cancel out any potential effects of the mobile trap states, Figure 5.8b represents a simple halide segregation measure that is adequate enough for the analysis presented here. The large variation in the relative growth of the iodide-rich perovskite PL peak in Figure 5.8b suggests that the amount of halide segregation that occurred in the perovskite material differed considerably across the different illumination intervals throughout the experiment. To highlight the difference in halide segregation rate across the experiment presented in Figure 5.8, Figures 5.9 and

5.10 present the initial and final PL spectra from particular 60 s illumination intervals. Figure 5.9 shows the first and last normalised PL spectra taken during the illumination period at 0.7 applied volts on the 2nd voltage up-ramp (the 30th illumination period), and Figure 5.10 shows the first and last normalised PL spectra taken during the illumination period at 0.3 applied volts on the 2nd voltage down-ramp (the 41st illumination period). While both Figures 5.9 and 5.10 show the growth of a low-energy PL peak attributed to halide segregation [17], the low-energy peak growth is clearly more prominent in Figure 5.9, indicating that more halide segregation occurred over this illumination period. The measure of halide segregation plotted in Figure 5.8b shows the same hysteresis across the applied voltage ramps as is observed in the PL signals in the middle and bottom panels of Figure 5.8a, suggesting both are influenced by the mobile trap states that lag behind the voltage ramp. Given that the largest amount of halide segregation is observed in Figure 5.8b at ∼0.7 V applied bias on the voltage ramp-up – when the PL is brightest – it is concluded that a lack of interaction between the trap state and the photoexcited charge-carrier densities – which causes high PL emission – correlates with increased amounts of halide segregation. While this conclusion initially appears to contradict the work presented in Chapter 4, further analysis of the defect species present in the $MAPb(Br_{0.5}I_{0.5})_3$ photovoltaic devices allows a congruent picture of trap states and halide segregation to be presented in Section 5.4.4 below.

5.4.3 Screening of Electric Fields by Ion Movement

In order to observe how mobile trap states and halide segregation will affect mixed-halide perovskite solar cells under photovoltaic operation, the blue data plots in Figure 5.8c show the extracted current from the device during the PL experiment discussed above. Due to the high periodicity of the current measurements over the multiple voltage ramps up and down, equivalent points in the last 3 voltage up-down ramps were averaged over

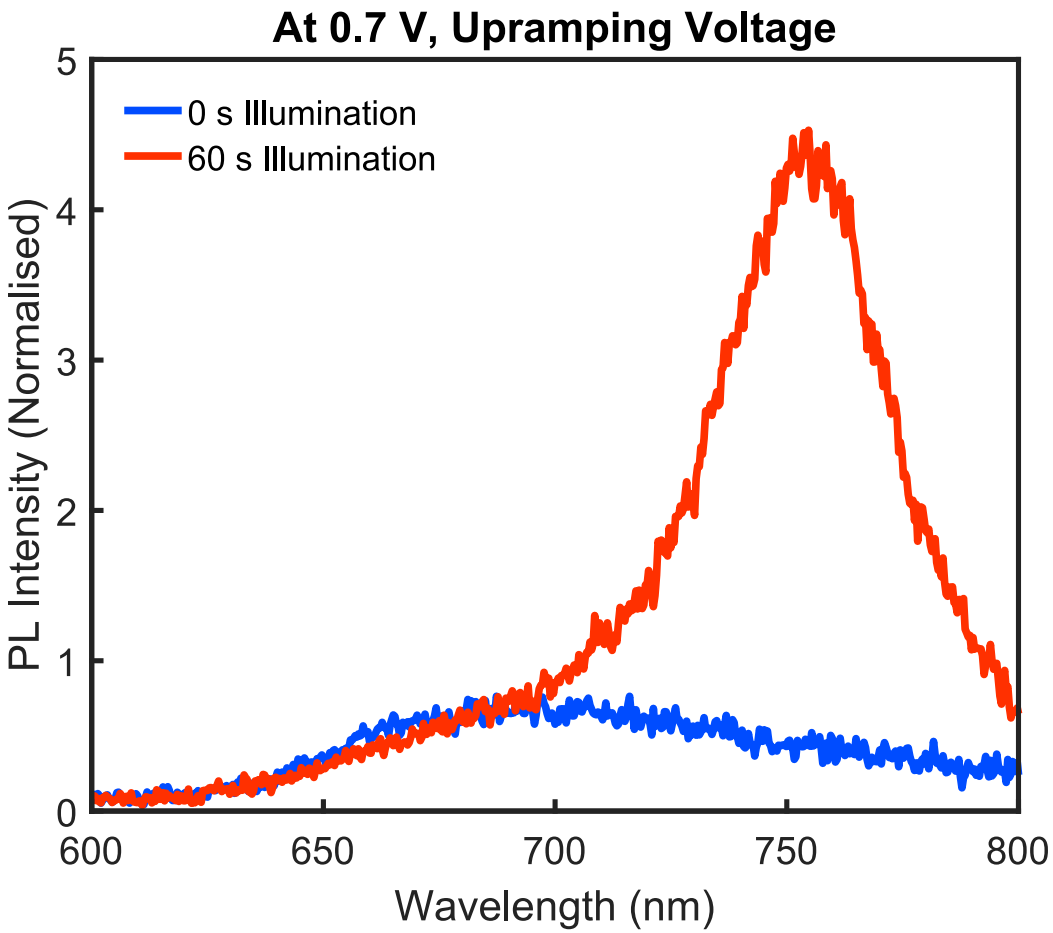

Figure 5.9: Normalised PL spectra from an $MAPb(Br_{0.5}I_{0.5})_3$ device taken at the start and at the end of a 60 s illumination period while 0.7 V was applied across the device. The spectra are both globally normalised such that the maximum signal of the initial spectrum (plotted in blue) is set to 1. The PL spectra were taken on the 2^{nd} voltage up-ramp of the experiment presented in Figure 5.8, and so the illumination period was the 30^{th} out of 88 in the experiment. The spectra are plotted here as an example of the maximum amount of halide segregation that was observed over the course of one illumination period in the experiment shown in Figure 5.8.

to produce the blue plots in Figure 5.8c. The entirety of the extracted current data from this experiment is plotted in Figure 5.11. Because the illumination spot size was different to the device pixel active area, it is difficult to completely accurately calculate the current density from the extracted current. However, for reference, given that the laser spot size used was $\sim 2.1 \times 10^{-4}\,cm^{-2}$ it is expected that 3 µA of extracted current should roughly correspond to a $14\,mA\,cm^{-2}$ current density.

For any given illumination interval, the extracted current plotted in blue in Figure

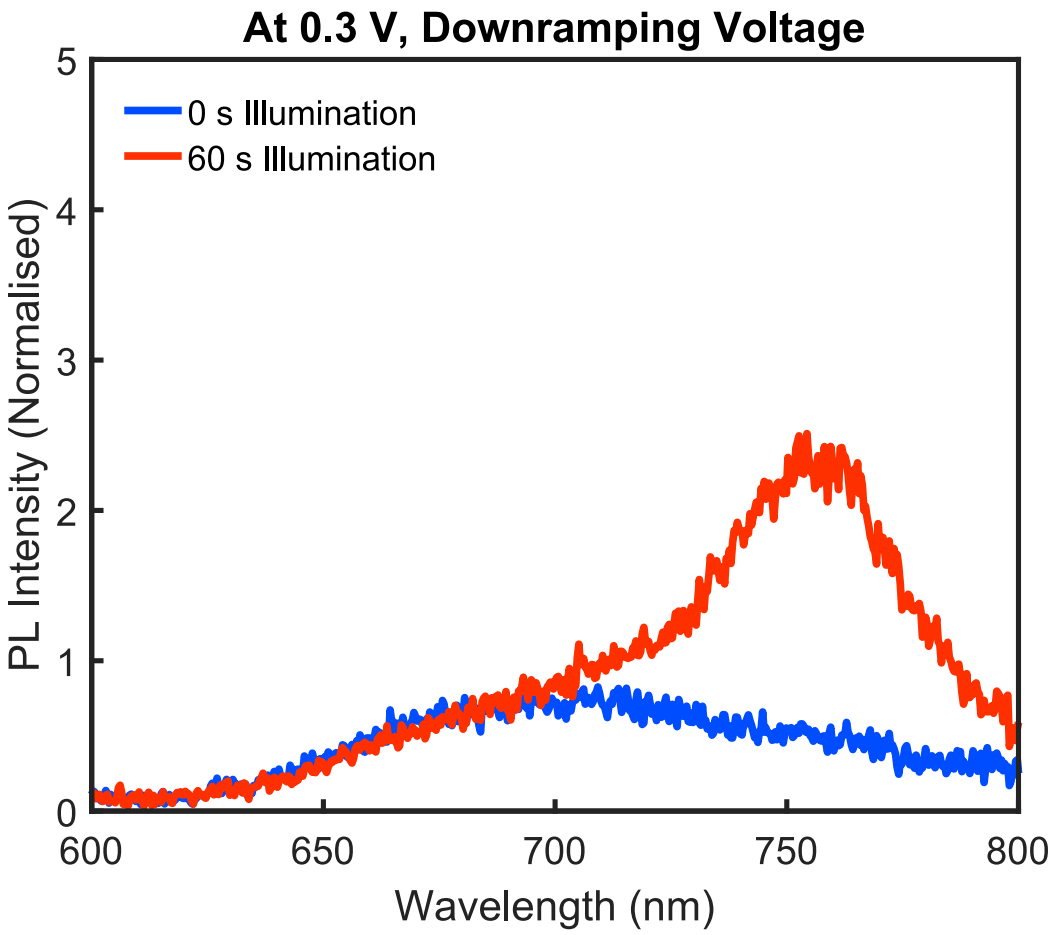

Figure 5.10: Normalised PL spectra from an $MAPb(Br_{0.5}I_{0.5})_3$ device taken at the start and at the end of a 60 s illumination period while 0.3 V was applied across the device. The spectra are both globally normalised such that the maximum signal of the initial spectrum (plotted in blue) is set to 1. The PL spectra were taken on the 2nd voltage down-ramp of the experiment presented in Figure 5.8, and so the illumination period was the 41st out of 88 in the experiment. The spectra are plotted here as an example of the minimum amount of halide segregation that was observed over the course of one illumination period in the experiment shown in Figure 5.8.

5.11b begins with a rapid initial rise. This type of fast current change is indicative of the well-studied phenomenon of current-voltage (J-V) hysteresis observed in metal-halide perovskite devices, where it has been observed that a rapid change in the applied voltage across the device results in a slower response (over the course of seconds) from the extracted current [217–220]. While the combination of a number of factors, including interface effects, is thought to give rise to J-V hysteresis, it has been proposed that a significant part of the mechanism is comprised of slow ionic redistribution upon a rapid

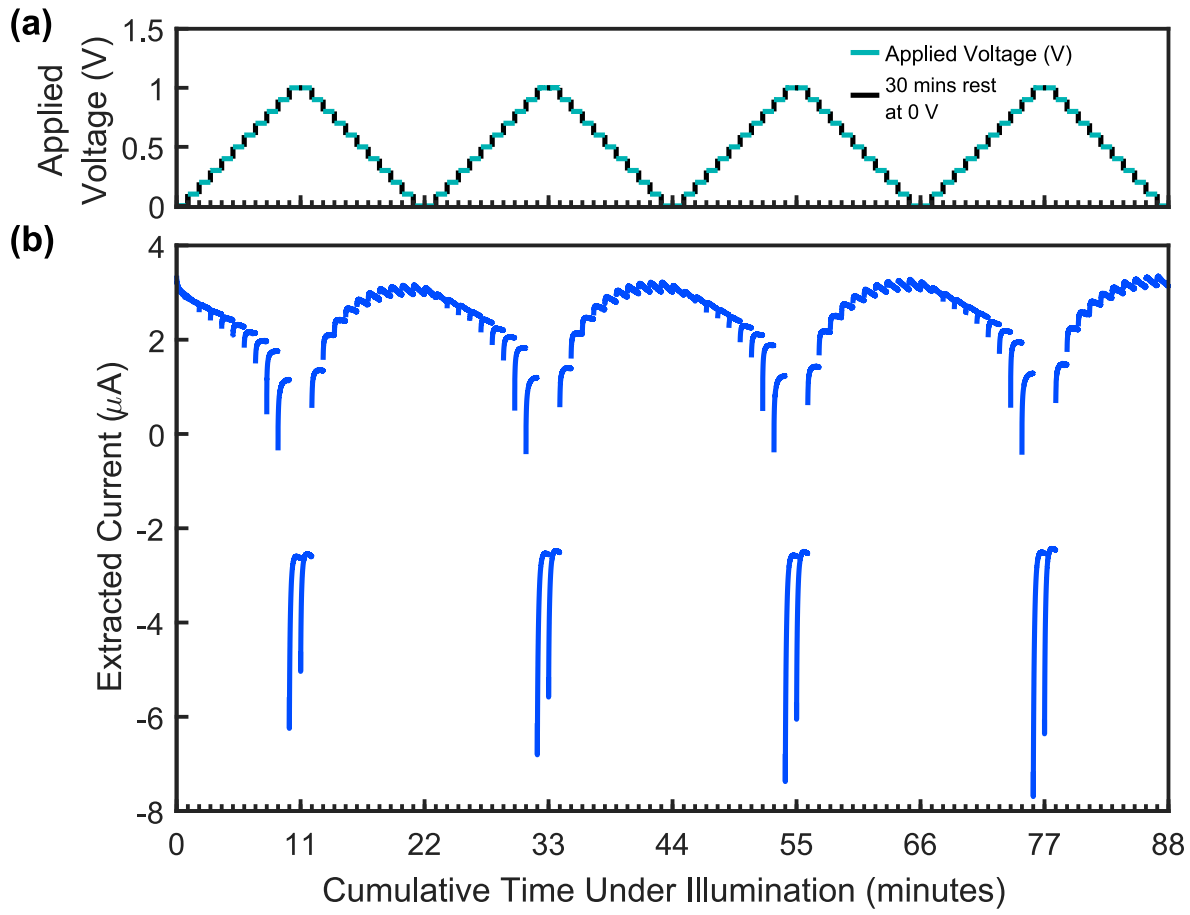

Figure 5.11: (a) Voltages applied across an $MAPb(Br_{0.5}I_{0.5})_3$ device during 1 minute illumination periods (blue) and indications of the 30 minute rest periods under darkness between the illumination periods (black). During the periods of darkness 0 applied volts were held across the device (b) Extracted current from the $MAPb(Br_{0.5}I_{0.5})_3$ device under illumination with the discrete voltage ramp shown in (a) applied. The current data shown in (b) corresponds to the experiment shown and discussed in Figure 5.8, and the blue plots in Figure 5.8c are averages based on the data shown in (b).

change in the applied voltage across the perovskite device [217, 218]. In response to an electric field, mobile ions in the perovskite material set up a screening potential that affects the charge-carrier extraction efficiency from the film and modulates the trap-assisted recombination. A change in the external electric field across the device results in a relatively slower change in the screening potential and the extracted current from the device [221–224]. It is noted that while the consensus is forming that ionic motion plays an important role in *J-V* hysteresis, there are several other possible explanations that have

been put forward [217, 218, 220, 225]. In the case of the voltage ramp experiment that produced the data shown in Figure 5.8, the applied voltage across the device was 0 V in the dark, before being quickly switched to various voltages upon illumination. This rapid change in applied voltage would lead to a slower change (over the course of seconds) in the screening potential within the perovskite layer, resulting in the initial rise in extracted current observed in the blue plots at the start of every illumination interval in Figure 5.11b. The blue plots in Figure 5.11b show that the change in screening potential within the perovskite layer happened on the order of tens of seconds, much faster than the tens of minutes observed in Figure 5.2b required for the migratory trap states to reach equilibrium, which suggests that the screening ions are a different species to the mobile trap states.

5.4.4 Summary of Defect Types

It is worthwhile at this point to briefly summarise the so-far presented findings and discussions about the defect species within the perovskite layer of the measured photovoltaic devices. The data presented so far in this chapter allows three different defect species in the perovskite material to be distinguished, each with different properties. First, Figures 5.2b and 5.5 show that the radiative efficiency of the perovskite depends on the electric field applied across the material, which is indicative of a species of charged, mobile trap state. These trap states were observed to reach their equilibrium distribution on the order of tens of minutes under illumination, but were essentially stationary under darkness (see the discussion surrounding Figure 5.8a in Section 5.4.2). Furthermore, given that the highest emitted PL intensity was observed from the perovskite when the overall electric field was directed away from the illumination side of the device where the density of photoexcited charge carriers is highest, it can be concluded that this species of trap state is positively charged. These defects are proposed to be interstitial MA^+

ions in the perovskite crystal, which have previously been observed in $MAPbI_3$ films to migrate under an applied bias on similar timescales [213].

Second, in Chapter 4 it was observed that the rate of halide segregation in $MAPb(Br_{0.5}I_{0.5})_3$ thin films is positively correlated with the fraction of photoexcited charge carriers that undergo trap-mediated recombination, and it was therefore concluded that some trap states in the perovskite material play an essential role in the halide segregation mechanism [150]. It was suggested in Chapter 4 that photoexcited electrons would be captured by these segregation-responsible trap states, setting up an electric field that would instigate the movement of the halide ions in the perovskite crystal. The responsible trap states therefore are likely to have an intrinsic neutral charge, as a negative charge would produce a low capture cross-section for electrons, and a positive charge would be partly or entirely neutralised by a captured electron, resulting in smaller electric fields within the perovskite and therefore a lower driving force for halide segregation upon illumination. These segregation-responsible trap states are suggested to comprise of crystal lattice distortions located near the grain boundaries in the perovskite material, congruous with the evidence in the literature that these regions are strongly correlated with halide segregation [104, 119, 144].

The interaction of the photoexcited charge-carrier density with both of these two trap states then explains the halide segregation dynamics captured in Figure 5.8b. While the charged, mobile trap states take no direct part in triggering the actual segregation process, they capture a fraction of the photoexcited charge carriers that depends on the applied voltage. This in turn reduces the number of charge carriers that are trapped by the neutral defect states. Since these latter neutral defect states become charged upon charge-carrier capture, they generate the electric fields that induce the segregation of halide ions [150]. Therefore, the charged, mobile trap states (proposed to be MA^+ interstitials)

may suppress halide segregation by reducing the number of charge carriers captured in neutral defect states (proposed to be lattice distortions located at grain boundaries) that directly trigger halide segregation. Thus, it is proposed that by competing with both the radiative recombination pathways and the halide segregation mechanism, the charged, mobile trap states cause the observed correlation between the overall radiative efficiency of the perovskite layer and the relative growth of the iodide-phase perovskite PL peak presented in Figure 5.8b.

Finally, the blue lines in Figure 5.8c and 5.11b show that a third species of defect is responsible for the fast screening of the perovskite material upon a change in the applied voltage. The corresponding defect species must necessarily be charged to induce a screening effect, and they were observed to reach equilibrium on the order of seconds to tens of seconds depending on the magnitude of the change in applied voltage, suggesting a high mobility. These defect states are proposed to be interstitial halide ions and/or halide ion vacancy sites in the perovskite crystal, which are calculated to have the highest mobility and lowest activation energy for transport out of the ionic species in several different MHPs [36, 226, 227], and have gained support in the literature as the cause for *J-V* hysteresis in perovskite photovoltaic devices [217].

5.5 Current Extraction Dynamics

5.5.1 Current Extraction Without Ionic Screening Effects

As real-world solar cells are subjected to both solar illumination and applied voltages, it is important to understand how halide segregation and different biases affect the current extraction from mixed-halide perovskite photovoltaic devices. However, the dynamics of the extracted current plotted in blue in Figure 5.8c and 5.11b are affected by a complicated convolution of both halide segregation and ionic screening effects, making it difficult to

determine the individual effects of each process. In order to observe the extracted current dynamics from a mixed-halide perovskite photovoltaic device without any short-time screening behaviour, a similar voltage ramp experiment to that with results shown in Figure 5.8 and discussed in Section 5.4.2 above was performed on a fresh device with a period of voltage prebiasing across the device applied under darkness. The time under darkness was maintained from the experiment without prebiasing (Figure 5.8) at 30 min, but for the prebias experiment the 30 min under darkness was broken up into 25 min at 0 V applied bias, and 5 min at the applied voltage of the next illumination interval. Otherwise, all other experimental parameters were kept exactly the same between the experiment without a prebias period (Figure 5.8), and the experiment with a prebias period (Figure 5.12). The current extracted from the device under illumination during the prebiasing experiment is plotted in purple in Figure 5.8c where, due to the high periodicity of the measurements, the extracted current at equivalent points in the last 3 up-down voltage ramps are averaged together. The entirety of the extracted current from the measured device under illumination during the prebias experiment is shown in Figure 5.12d, alongside the voltages applied across the device during the experiment (5.12a), and the PL recorded from the device associated with the iodide-rich (5.12b) and well-mixed (5.12c) perovskite phases. The initial fast component of the extracted current dynamics visible in the blue plots is not visible in the purple plots in Figure 5.8c, suggesting that the prebias under darkness allowed the screening ions to redistribute before the illumination interval. Figure 5.13 and 5.14 explicitly show that during the 5 min prebiasing periods under darkness, the extracted current from the device changed as expected according to the variation in the screening potential. The removal of the initial fast component of the extracted current without any significant change to the behaviour of the PL from the perovskite layer (shown in Figure 5.12) further suggests

that the screening ions and migratory trap states are different species. The fact that the extracted current from the prebiased device (purple plots in Figure 5.8c and 5.12d) was higher than the device that was not prebiased (blue plots in Figure 5.8c and 5.11b) even after the tens of seconds required for the ion redistribution is likely a result of device-to-device variations in the device batch.

Without the fast screening dynamic, the purple current extraction curves in Figure 5.8c and Figure 5.12d better show the changes to the current resulting from halide segregation. During every illumination interval the purple curves in Figure 5.8c and Figure 5.12d decrease, clearly indicating that halide segregation reduces the amount of current extracted from the device – as has been observed elsewhere [20, 23]. As halide segregation takes place, the charge carriers within the forming iodide-rich regions of perovskite experience a limited amount of spatial freedom, resulting in high charge-carrier densities and a high rate of radiative recombination [17]. Thus, the observed drop in current across the illumination intervals in Figure 5.8c and Figure 5.12d was likely due to the rising rate of radiative recombination within the iodide-rich regions of perovskite competing against the charge-carrier extraction rate.

5.5.2 External Quantum Efficiency Measurements

As demonstrated in Figure 5.8c and discussed above, halide segregation is detrimental for charge-carrier extraction from mixed-halide perovskite devices, and will therefore hinder potential device performance as reported in Refs. [20, 21, 23]. In order to gain a fuller understanding of the pathways experienced by charge carriers in a segregated device, particularly as to whether funneled charge carriers are completely constrained within the iodide-rich regions of perovskite or whether they can still be extracted, EQE measurements were performed on a fresh mixed-halide perovskite device as the perovskite segregated under illumination of an AM1.5 spectrum. The AM1.5 spectrum was generated

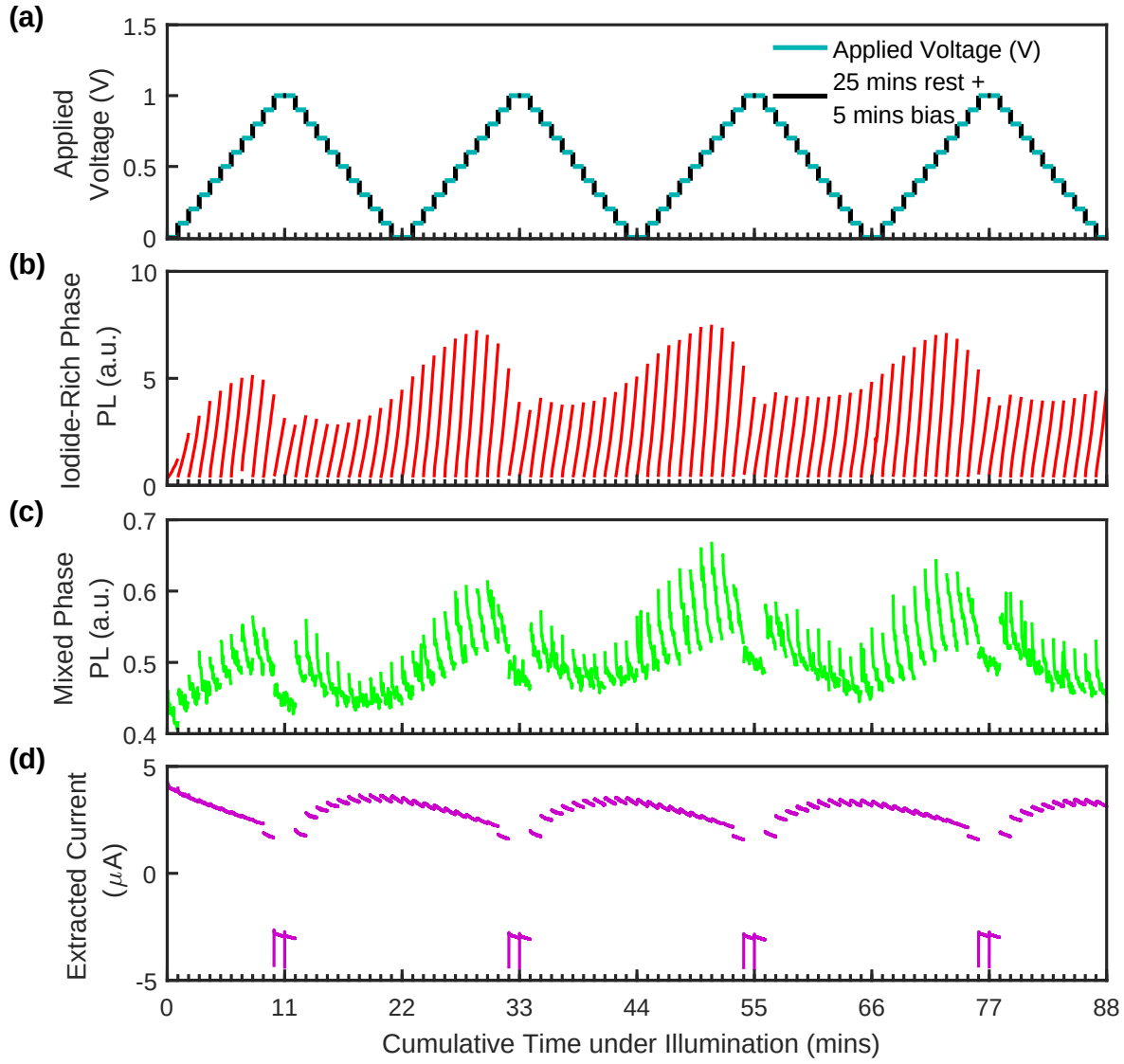

Figure 5.12: (a) Voltages applied across an $MAPb(Br_{0.5}I_{0.5})_3$ device when under illumination (blue) and indications of the 30 min rest periods under darkness (including 5 min of pre-bias) that were applied to the device between 1 min illumination periods (black). (b) The integrated low energy PL (720 nm to 770 nm) from the device under 400 nm, 110 mW cm^{-2}, continuous wave illumination. (c) The integrated higher energy PL (640 nm to 690 nm) from the device under illumination. (d) Extracted current from the $MAPb(Br_{0.5}I_{0.5})_3$ device under illumination with the discrete voltage ramp shown in (a) applied. The purple plots in Figure 5.8c are averages based on the data shown in (d).

by a class AAA Oriel Solar Simulator on a 0.0919 cm^2 pixel size that was covered by a 0.0625 cm^2 aperture, at an integrated power of 0.6 suns (60 mW cm^{-2}), and the device was held under vacuum at 0 V applied bias during the experiment. EQE spectra were

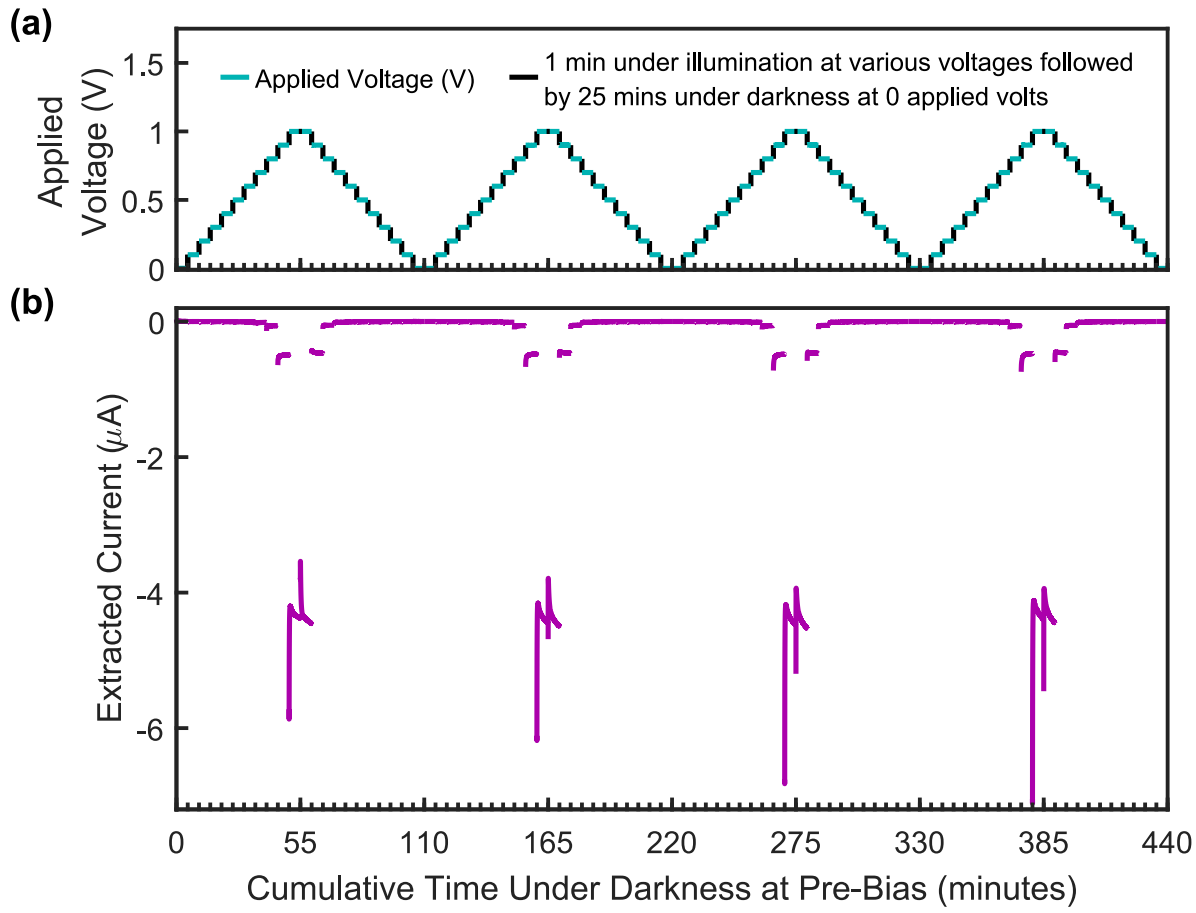

Figure 5.13: (a) Voltages applied across an $MAPb(Br_{0.5}I_{0.5})_3$ device during 5 min pre-biasing periods under darkness (blue) and indications of the 1 min of illumination at various applied voltages followed by the 25 min of darkness at 0 applied volts that were applied to the device between the 5 min pre-biasing periods (black). (b) Extracted current from the $MAPb(Br_{0.5}I_{0.5})_3$ device under darkness with the discrete voltage ramp shown in (a) applied.

taken every 4 s over the course of the 20 min of illumination, with the results plotted in Figure 5.15. Figure 5.15a displays the EQE spectra averaged over 196 s intervals, with an inset showing the extracted current density from the device over the 20 min of illumination. Figure 5.15b shows the fractional component of the extracted current density attributed to the mixed (green) and iodide-rich (red) phases of the perovskite.

The EQE spectra display a sharp onset at 664 nm, which corresponds to the absorption edge of the fully mixed perovskite phase (Figure 5.15a). At longer wavelengths, below the absorption edge, the contribution to the EQE is attributed to the regions of iodide-

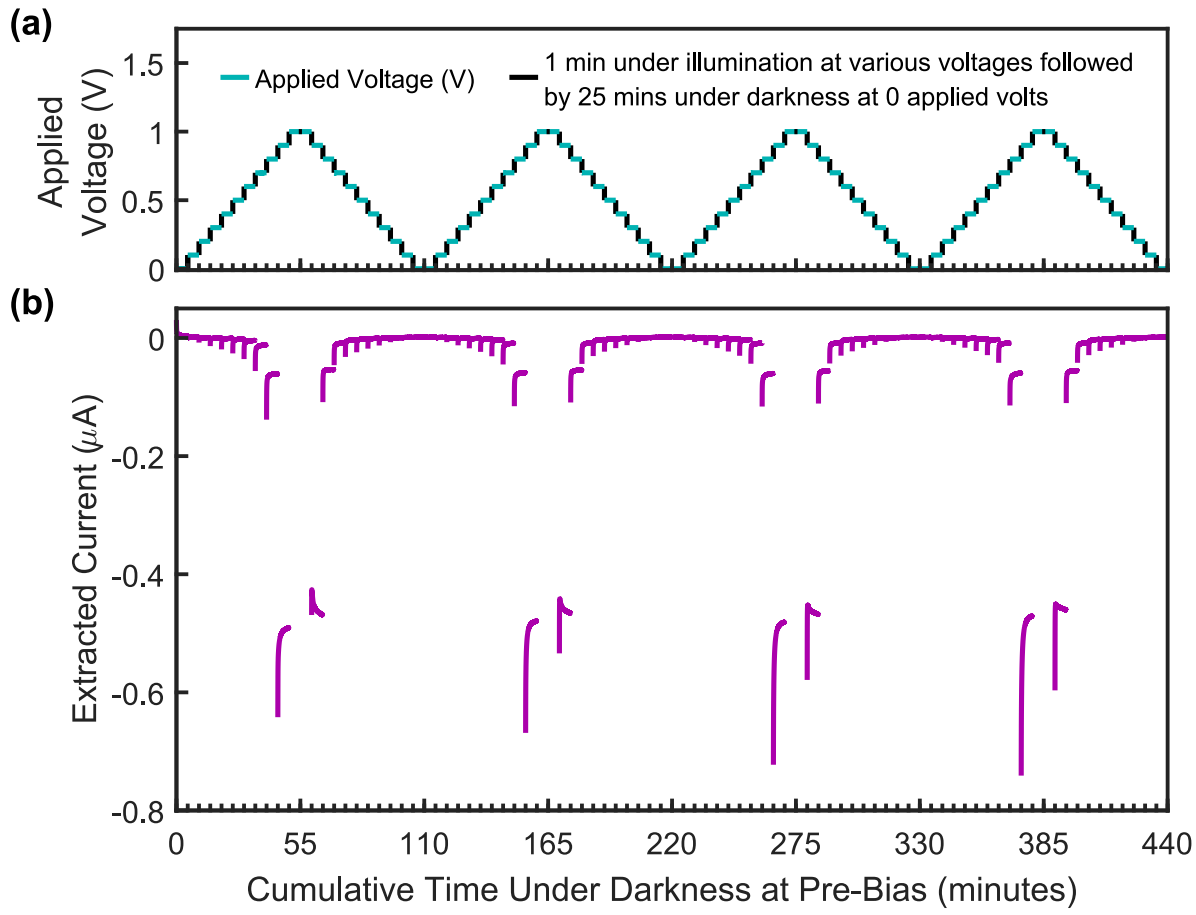

Figure 5.14: (a) Voltages applied across an $MAPb(Br_{0.5}I_{0.5})_3$ device during 5 min pre-biasing periods under darkness (blue) and indications of the 1 min of illumination at various applied voltages followed by the 25 min of darkness at 0 applied volts that were applied to the device between the 5 min pre-biasing periods (black). (b) Zoomed region of Figure 5.13b.

rich perovskite that formed as the material segregated. Over time the EQE below the absorption edge (wavelengths longer than 664 nm) in Figure 5.15a increased, indicating that more light was absorbed and more current was extracted from the forming iodide-rich regions of perovskite as the perovskite segregated. Conversely, there is a dramatic loss in EQE above the absorption edge (wavelengths shorter than 664 nm) over time, attributed to photoexcited charge carriers generated within the mixed phase funneling into the iodide-rich regions of perovskite where the current extraction efficiency was lower. The inset of Figure 5.15a shows that as more charge carriers funneled into these low extraction efficiency regions over time, the overall current density extracted from the device decreased.

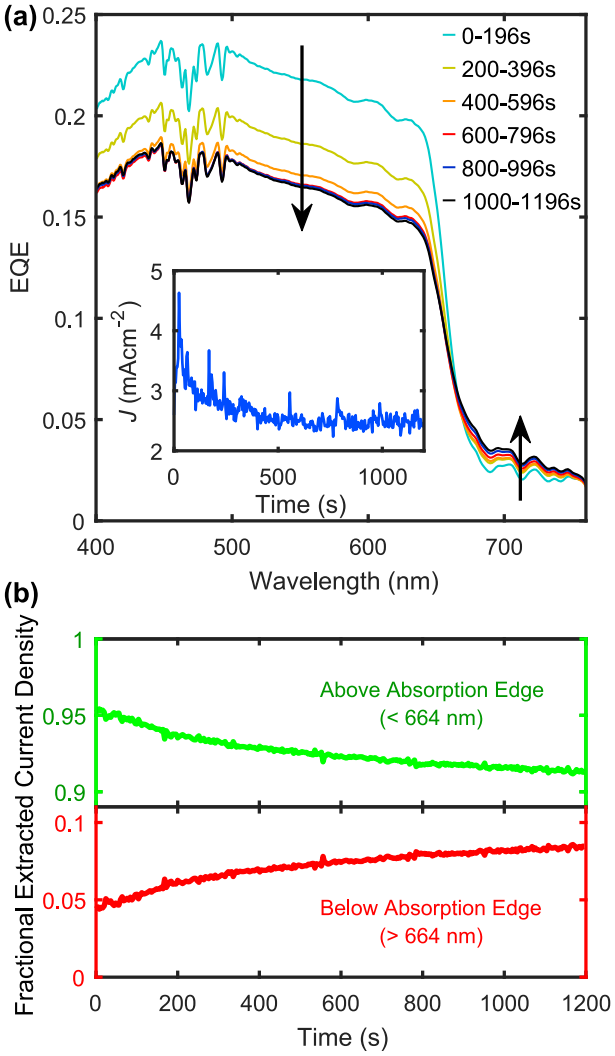

Figure 5.15: (a) Evolution of the EQE spectra from a mixed-halide perovskite device under AM1.5 illumination at 0.6 suns (60 mW cm^{-2}) for 20 min. Spectra were taken every 4 s and averaged over 196 s intervals. The extracted current density is plotted in the inset. The spikes observed between 450 and 500 nm are artefacts resulting from slight fluctuations in the intensity of the solar simulator. (b) Fractions of the extracted current density that originate from above (wavelengths shorter than 664 nm) and below (wavelengths longer than 664 nm) the absorption edge are plotted in green and red, respectively.

The decrease in this short circuit current is similar to previous reports of the detrimental nature of halide segregation on mixed-halide perovskite photovoltaic devices [20, 21, 23].

Plotted in red in Figure 5.15b is the fractional contribution to the extracted current density from the iodide-rich regions of perovskite, which clearly increases as the halide segregation process occurs. Importantly, this contribution to the extracted current

proves that charge carriers can move from the low-bandgap regions of perovskite into the charge-carrier collection layers in the device. This extraction of charge carriers from the low-bandgap regions happens despite the fact that the iodide-rich regions are known to comprise only a small fraction of the volume of the segregated perovskite layer [17, 22], and the energy required to escape these low-bandgap regions into the fully mixed perovskite phase (∼200 meV) is greater than the thermal energy available to the charge carriers at room temperature (∼30 meV). In order to explain how the low-energy charge carriers transferred into the extraction layers it is noted that the iodide-rich regions of perovskite are reported to preferentially form around the grain boundaries in the perovskite material [104, 119, 144]. While the effect of grain boundaries on charge-carrier lifetimes is still under debate [84, 85], charge-carrier transport along perovskite grain boundaries has previously been reported [228–230]. Thus it is proposed that the grain boundaries within the perovskite layer act as percolation pathways for the low-energy charge carriers, acting as a traversable network between the nearby iodide-rich regions of perovskite and the charge-carrier extraction layers. The overall loss of current density extracted from the device (inset of Figure 5.15a) suggests that the transport of the low-energy charge carriers was not as efficient as the transport through the mixed perovskite phase. The low extraction efficiency from the iodide-rich regions of perovskite may result from an increased radiative recombination rate in these regions, or enhanced trap-mediated recombination at the grain boundaries [84, 85] reducing the lifetimes of the excited charge-carriers, as well as more disordered pathways along grain boundaries compared to the bulk.

5.6 Charge-Carrier Pathways in Mixed-Halide Perovskite Photovoltaic Devices

The work reported in this chapter grants good insight into the energy states and pathways experienced by the photoexcited charge carriers in a segregated perovskite device. The

findings are summarised in Figure 5.16: a Sankey diagram that represents the possible pathways from photoabsorption (top of diagram) to recombination event (bottom of diagram) for excited charge carriers. It is stressed that the diagram is only meant to give a qualitative insight into charge-carrier dynamics in a segregating perovskite material as the rate of the various recombination mechanisms will depend heavily on the illumination parameters, exact material properties of the device layers, the degree to which halide segregation has taken place, the applied voltage across the device, and the precise microstructure of the segregated domains. Auger recombination has been ignored as a higher order process that is negligible under typical real-world solar illumination intensities [61]. The mixed and iodide-rich perovskite phases are represented in the diagram as green and red boxes respectively, and recombination events are represented as diamond shaped boxes of various colours.

In a normal photovoltaic device, where the working layer is composed of one phase only, there are three main recombination pathways for the photoexcited charge carriers: trap mediated recombination, radiative recombination, and extraction and recombination via an electrical circuit. In a mixed-halide perovskite device, as the perovskite layer segregates, further pathways open up as the charge carriers are able to transfer between the different perovskite phases. The solid pathways depicted in Figure 5.16 highlight that initially, prior to any segregation, the perovskite layer in the device is composed of one phase (the mixed perovskite phase depicted by the green box) and so recombination occurs in this phase either through trap states, radiatively, or through current extraction. These three recombination pathways persist as the perovskite layer segregates, and the hatched pathways in Figure 5.16 show the additional pathways – involving the iodide-rich regions of perovskite – that open up as halide segregation occurs. The rise in EQE at long wavelengths shown in Figure 5.15a – and absorption measurements in the

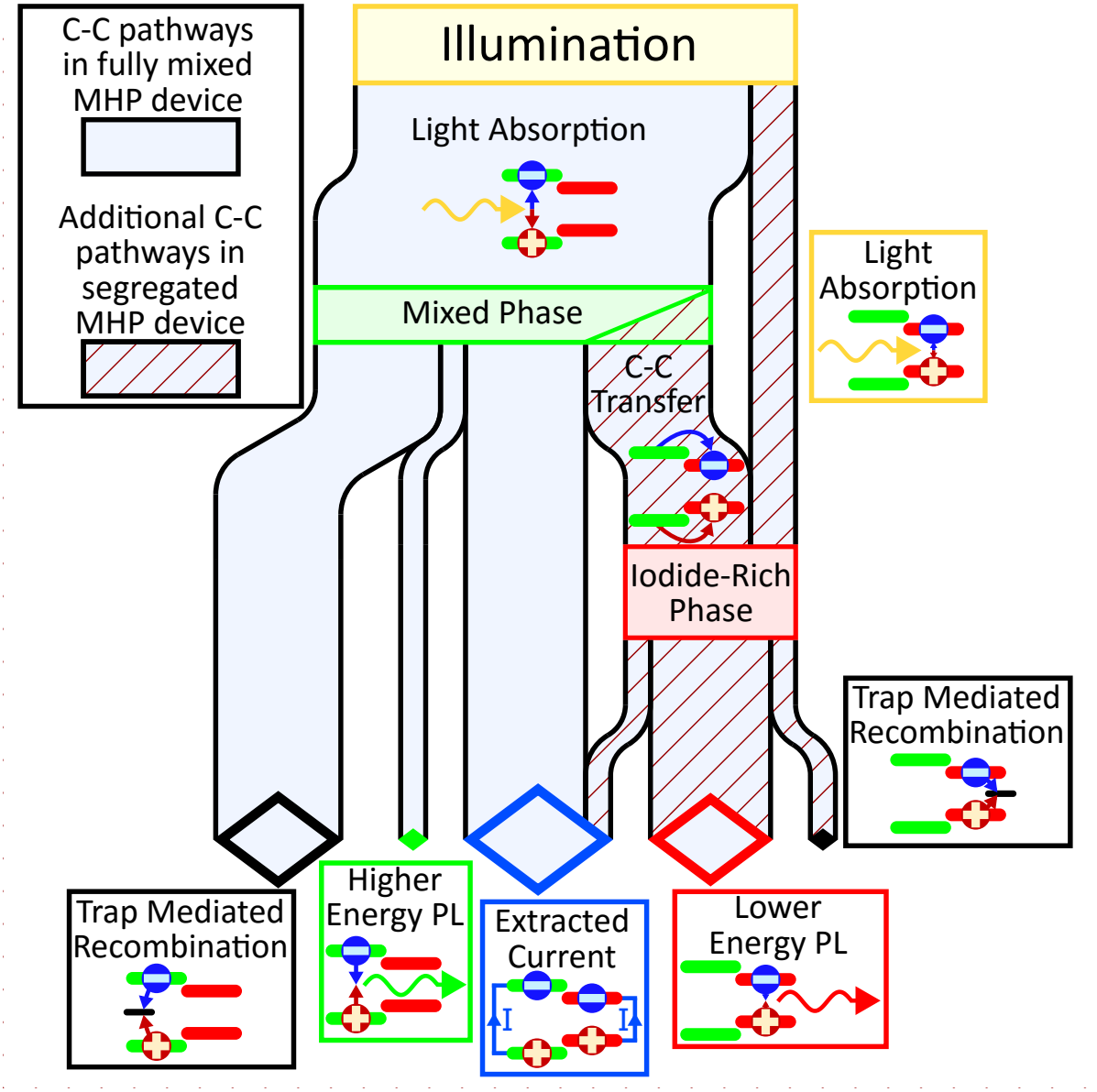

Figure 5.16: Sankey diagram representing the flow of photoexcited charge carriers via various pathways in a fully mixed (solid pathways) and segregated (hatched and solid pathways) mixed-halide perovskite device. Every charge-carrier pathway begins with photoabsorption at the top of the diagram and finishes with a recombination event at the bottom (diamond boxes).

literature [94–96, 167, 170] – prove that a small but not insignificant number of charge carriers are directly photogenerated in the iodide-rich regions of the perovskite, which is reflected in Figure 5.16 as the corresponding pathway into the red iodide-rich phase box. Additionally, the drop in mixed perovskite PL signal intensity indicated in the bottom panel of Figure 5.8a is attributed to a flow of charge carriers from the mixed

perovskite phase into the lower-bandgap regions of perovskite, which is depicted as a pathway between the two phases in Figure 5.16. With regard to the recombination dynamics of the iodide-rich phase, Figure 5.15 shows that some current is extracted from the low-bandgap phase [23, 167], and the middle panel of Figure 5.8a highlights the strength of the radiative efficiency of this phase. Additionally, as discussed in Section 5.4, the changes in the PL intensity presented in Figure 5.2b indicate that a significant amount of trap-mediated recombination occurs within the iodide-rich regions of perovskite, and that the rate of this trap-mediated recombination depends on the electric field applied across the perovskite layer. Figure 5.16 incorporates these recombination pathways as flows out from the iodide-rich perovskite phase, resulting in a complicated final flow diagram from illumination through to recombination. Figure 5.16 represents a good summary of the findings reported in this chapter, and reflects the charge-carrier dynamics within a mixed-halide perovskite device.

5.7 Summary and Conclusion

In this chapter the interactions between halide segregation, electronic trap states, and electric fields in mixed-halide perovskite photovoltaic devices were studied. The results of Section 5.4 suggest the existence of three distinct types of defects within the $MAPb(Br_{0.5}I_{0.5})_3$ perovskite material, each with different properties and effects on the perovskite material. In Section 5.4.1 one species of defect, while essentially stationary under darkness, was observed under illumination to redistribute over the course of tens of minutes upon a change in the bias across the perovskite layer, implying that the defect is charged and somewhat mobile. Additionally, this defect species was observed to heavily reduce the radiative efficiency of the perovskite material. This defect species is proposed to consist of MA^+ interstitials in the perovskite, given similar work in the literature on the movement of MA^+ ions in perovskite materials [213]. Second, given the

work of Section 5.4.2 and following the work of Chapter 4, it is suggested that a second species of defect state is responsible for halide segregation in mixed-halide perovskites [150]. These defect states are posited to cause the observed segregation of halide ions by capturing photogenerated charge carriers and generating electric fields, and it is argued that they must therefore be intrinsically charge neutral when empty. Crystal distortions concentrated at the grain boundaries in the perovskite layer are suggested as a candidate for these charge neutral defect states. Third, in Section 5.4.3, a charged, highly mobile defect was observed to screen the applied voltage across the perovskite layer by redistributing over the course of tens of seconds. Given mobility and activation energy calculations in the literature [36, 226, 227], these defects are suggested to consist of halide vacancies and/or interstitials in the perovskite material.

Additionally, EQE measurements showed that charge carriers can be extracted from the low-bandgap, iodide-rich regions of segregated perovskite into the charge-carrier extraction layers of the device. The grain boundaries within the perovskite material – previously shown to be capable of charge-carrier transport [228–230] – are proposed to provide a percolation network for the low-energy, photoexcited charge-carriers to traverse.

Finally, the findings of this chapter and an understanding of the charge-carrier pathways within a mixed-halide perovskite material are summarised through a qualitative Sankey diagram, which stresses the interconnectivity – and provides a convenient summary – of the multitude of processes reported in mixed-halide perovskites. The findings reported here elucidate the ionic and charge-carrier processes within mixed-halide perovskite materials, particularly the interaction of these processes with electric fields – an essential consideration for working photovoltaic devices.

6

Influence of A-Site Cations on Halide Segregation

Contents

Initially published as Ref. [231].

6.1 Introduction and Background

Having investigated how the optoelectronic properties of mixed-halide perovskites both affect, and are affected by, halide segregation in Chapters 4 and 5, the work of this chapter moves on to study links between halide segregation, the stoichiometry of the

perovskite, and the resulting local variations in perovskite composition. Interestingly, the composition of the A-cation site has been shown in the literature to have a particularly strong effect on the extent to which halide segregation occurs, see Section 2.4.2.1 [18]. $MAPb(Br_xI_{(1-x)})_3$ materials are known to segregate under relatively low photon doses for intermediate iodide-bromide ratios ($0.2 < x < 1$) [17, 18, 95, 96]. In contrast, mixed A-cation $FA_{(1-y)}Cs_yPb(Br_xI_{(1-x)})_3$ perovskites of comparable bromide content x are known to be much more stable and possess a much lower probability for ionic separation within the perovskite structure, with much higher photon doses required to induce halide separation [20, 66, 117] provided the Cs content y remains within the range of ∼10–30% [117]. However, the underlying reasons behind the influence of these factors on the segregation dynamics, and how they may be interconnected, is still largely unclear [18].

Exploration of the causes of halide segregation in mixed-halide perovskites has been further complicated by the separate use of two measurement techniques, photoluminescence (PL) [17, 95, 96, 150] and X-ray diffraction (XRD) [17, 117, 121, 184]. While each technique offers valuable insights, they have mostly been used in isolation, even though each tends to probe different regions and properties of the perovskite. PL techniques reflect the electronic energy levels at sites where charge carriers recombine, meaning they mostly probe the iodide-rich domains formed through the segregation process, since charge carriers will quickly diffuse to such low-energy regions [17, 95, 96, 150]. XRD measurements are more sensitive to the volume average of the crystalline perovskite, and as such give a more comprehensive picture of the compositional variations within the whole material. While PL measurements of mixed-halide perovskites consistently exhibit red-shifted emission following halide segregation, XRD measurements of segregated material tend to vary more substantially, and additionally depend on the perovskite composition [92]. These considerations suggest that an understanding of the halide segregation process would hugely benefit from in situ, combined measurements of changes

in PL and XRD patterns under illumination. Such in situ XRD/PL measurements could grant an understanding of both the underlying ionic movement and the electronic changes that occur during the halide segregation process, elucidating, for example, links between material composition and phase stability.

In this chapter, in situ, combined XRD/PL measurements are implemented to elucidate why MA-cation mixed-halide perovskites exhibit a substantially different propensity towards halide segregation compared with certain mixed formamidinium-caesium (FACs) cation counterparts. Two specific compositions – $MAPb(Br_{0.5}I_{0.5})_3$ and $FA_{0.83}Cs_{0.17}Pb(Br_{0.4}I_{0.6})_3$ – are explored under long-term illumination, and subsequent periods of darkness. While MA-cation mixed-halide perovskites are the prototypical compositions often investigated in halide segregation studies (and in Chapters 4 and 5), [17, 18, 95, 96] the vastly more stable $FA_{0.83}Cs_{0.17}Pb(Br_{0.4}I_{0.6})_3$ [20, 66, 117] is a much more relevant material for high-performance photovoltaic devices [66], especially as the top (sun-facing) absorber layer in perovskite-perovskite tandem solar cells [72, 73, 76]. Selecting perovskite compositions with a roughly even bromide:iodide ratio ensures that the halide segregation process will occur over a reasonable time frame in the experiments [18]. It is noted that differences in the halide compositions and manufacturing processes for the two examined compositions may have had slight influence over the resulting halide segregation dynamics in the perovskite films. However, FACs lead halide perovskites have been observed to possess a much greater stability against halide segregation as compared to MA-based perovskites over a wide range of manufacturing methods and halide contents [18]. Therefore, the A-site cation choice will be the dominant factor in the phase stability of lead mixed-halide perovskites of similar iodide and bromide content.

In this chapter, Section 6.2 briefly outlines the experimental procedures utilised for the work presented here, and Section 6.3 presents basic XRD characterisations of the two investigated perovskite compositions. The main experimental results of this chapter begin

in Section 6.4, with combined XRD/PL measurements presented that allow for a detailed understanding of the halide segregation process in each perovskite material, derived from the observation of both incipient low-bandgap regions in PL measurements, and the analysis of the bulk material gained from XRD measurements. For $MAPb(Br_{0.5}I_{0.5})_3$ it is concluded in Section 6.4.2.1 that halide segregation initiates in minority regions of the perovskite material, rather than throughout the bulk. Such regions must hence be particularly susceptible to ionic re-arrangements, for example, through the existence of fast ionic pathways near grain boundaries [145–149]. It is found that the growth and accumulation of these halide-segregated minority regions gradually reduces the volume of the remaining well-mixed perovskite phase. However, the composition (as inferred from the lattice parameters) of the remnant mixed-halide majority phase itself remains unchanged throughout the halide segregation dynamics. These observations demonstrate that, for $MAPb(Br_{0.5}I_{0.5})_3$, the segregation of halide ions occurs within and spreads from specific locations inside the material. Conversely, it is found in Section 6.4.2.3 that in order for halide segregation to occur in $FA_{0.83}Cs_{0.17}Pb(Br_{0.4}I_{0.6})_3$, large amounts of ionic rearrangement are induced throughout the perovskite in unison, indicating a lack of regions that are particularly susceptible to halide segregation in this material and explaining the typically high photo-stability of FACs A-cation mixed-halide perovskites, [20, 66, 117] for Cs content around 10–30%. It is proposed that for such FACs perovskites, halide segregation may instead be triggered by the initial segregation of the A-site cations, which enriches the bulk perovskite in either FA or Cs, and in turn reduces the stability of the perovskite against halide segregation. Finally, Section 6.5 summarises and concludes the results of this chapter.

6.2 Experimental Details

The setup and use of the equipment used for the concurrent XRD/PL measurements presented in this chapter were conducted as described in Section 3.4.1. Basic XRD measurements (those shown in Figures 6.1, 6.2, 6.5, 6.11, 6.12) were performed as described in Section 3.3.3. All perovskite films investigated in this chapter were over coated with a layer of poly(methyl methacrylate) (PMMA) to provide protection against unwanted interactions between the perovskite and the surrounding air [150].

6.3 Basic Sample Characterisation

6.3.1 Basic XRD Measurements

Figures 6.1 and 6.2 show X-ray diffraction (XRD) patterns recorded from the PMMA-coated $MAPb(Br_{0.5}I_{0.5})_3$ and $FA_{0.83}Cs_{0.17}Pb(Br_{0.4}I_{0.6})_3$ thin film samples discussed in this chapter, prior to any incident illumination. The $MAPb(Br_{0.5}I_{0.5})_3$ films (Figure 6.1) were measured in a Rigaku SmartLab X-ray diffractometer, and the $FA_{0.83}Cs_{0.17}Pb(Br_{0.4}I_{0.6})_3$ film (Figure 6.2) was measured in a PANalytical X'Pert X-ray diffractometer, both as described in Section 3.3.3. Both the $MAPb(Br_{0.5}I_{0.5})_3$ and the $FA_{0.83}Cs_{0.17}Pb(Br_{0.4}I_{0.6})_3$ perovskite were assigned a cubic unit cell in the space group $Pm\bar{3}m$. Texturing effects had a clear influence on the amplitude of the XRD peaks across the two perovskite compositions, which is especially clear in Figure 6.1 by the dominance of the (100) and (200) peaks for the $MAPb(Br_{0.5}I_{0.5})_3$ perovskite.

6.4 Concurrent XRD and PL Measurements

Figure 6.3 presents PL spectra and XRD patterns recorded for $MAPb(Br_{0.5}I_{0.5})_3$ and $FA_{0.83}Cs_{0.17}Pb(Br_{0.4}I_{0.6})_3$ perovskite thin films under illumination, collected in situ utilising a custom-built setup that allows for simultaneous, time-resolved XRD and PL

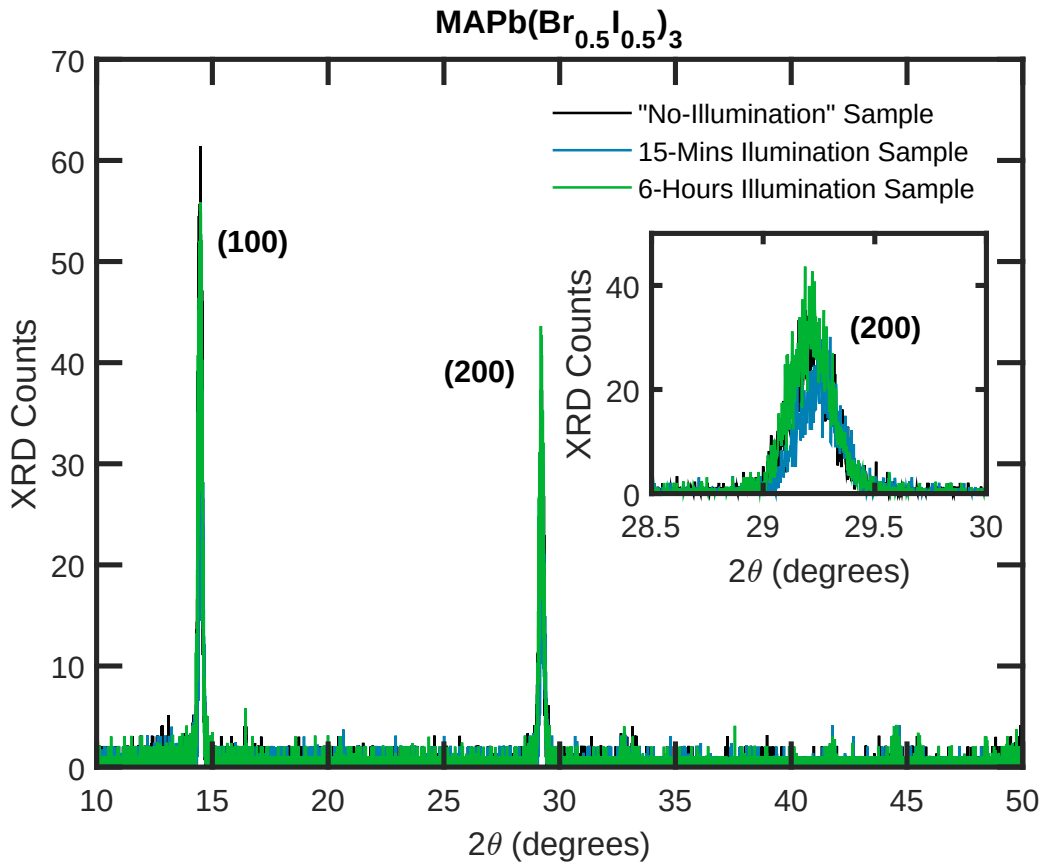

Figure 6.1: XRD patterns taken from three separate $MAPb(Br_{0.5}I_{0.5})_3$ thin films coated with PMMA, with the XRD measurements made prior to any illumination having occurred. The Cu-$K_{\alpha 1}$ line was used as incident radiation. After these XRD measurements, the three films were then used in the no-illumination, 15-minute, and 6-hour illumination experiments discussed in this chapter. The inset shows a zoomed region of the graph highlighting the pseudo-cubic (200) peak of the perovskite XRD pattern, which is the peak used for the analysis discussed below.

measurements. During the measurements, $MAPb(Br_{0.5}I_{0.5})_3$ and $FA_{0.83}Cs_{0.17}Pb(Br_{0.4}I_{0.6})_3$ films were exposed to 15 minutes and 6 hours of illumination, respectively, from a 470 nm wavelength, continuous wave laser. The intensity of illumination was set to 190 mW cm^{-2} for both compositions. This intensity, while somewhat above 1 sun and the level required to induce halide segregation in the $MAPb(Br_{0.5}I_{0.5})_3$ perovskite film, was needed to induce halide segregation in the more stable $FA_{0.83}Cs_{0.17}Pb(Br_{0.4}I_{0.6})_3$ film within a reasonable time frame.

The normalised PL spectra of $MAPb(Br_{0.5}I_{0.5})_3$ and $FA_{0.83}Cs_{0.17}Pb(Br_{0.4}I_{0.6})_3$ thin films develop in a qualitatively similar manner, with the growth and eventual dominance

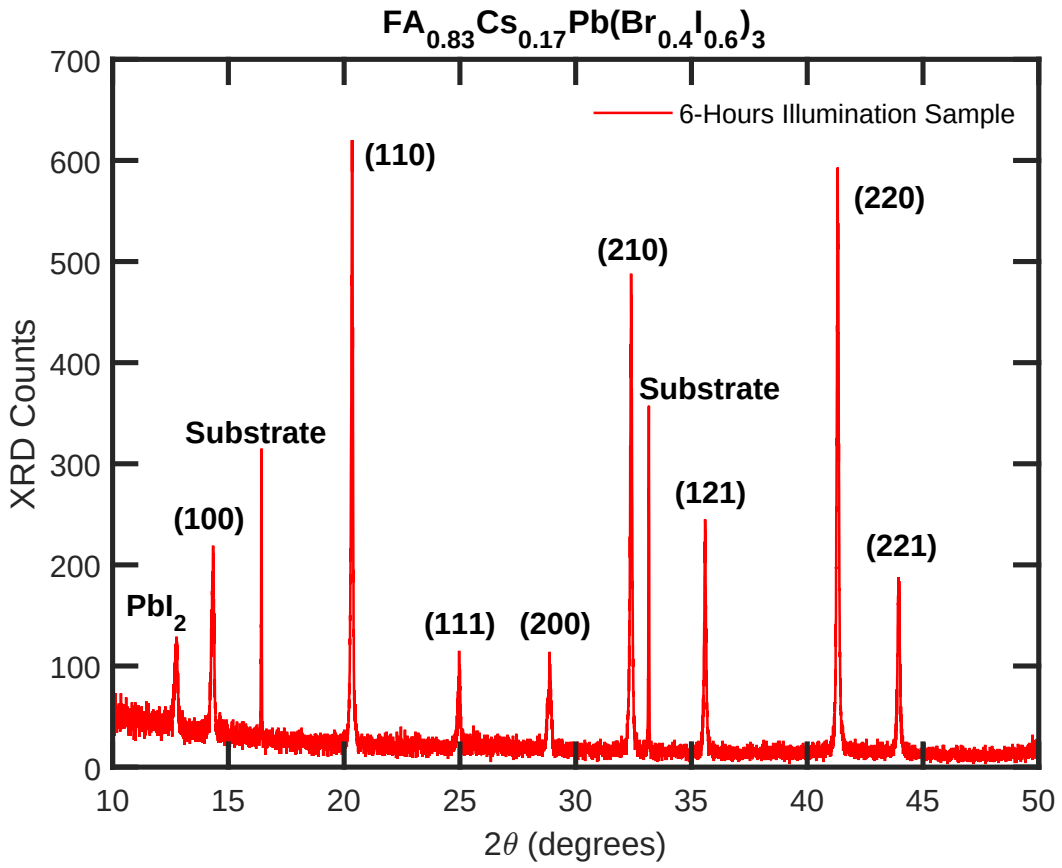

Figure 6.2: XRD pattern taken from an $FA_{0.83}Cs_{0.17}Pb(Br_{0.4}I_{0.6})_3$ thin film coated with PMMA, with the XRD measurements made prior to any illumination having occurred. The Cu-$K_{\alpha 1}$ line was used as incident radiation. After this XRD measurement, the perovskite film was then used in the 6-hour illumination experiment discussed in this chapter. The pseudo-cubic peaks of the perovskite pattern are labelled alongside substrate and other peaks. The (220) perovskite peak was used for the majority of the analysis discussed in this chapter.

of a low-energy PL peak – ascribed to iodide-rich regions – clearly visible in both Figures 6.3a and 6.3b, respectively. However, as expected, the timescales for halide segregation to occur in the two compositions were significantly different, with the PL spectrum of $MAPb(Br_{0.5}I_{0.5})_3$ reaching equilibrium on the order of tens of minutes (Figure 6.3a), while changes still occurred in the PL spectrum of $FA_{0.83}Cs_{0.17}Pb(Br_{0.4}I_{0.6})_3$ after several hours (Figure 6.3b). Despite the large difference in time and photon doses required to induce halide segregation in the two different perovskite thin films, the observed red-shifts of the corresponding PL spectra appear comparable.

In contrast, XRD patterns for $MAPb(Br_{0.5}I_{0.5})_3$ and $FA_{0.83}Cs_{0.17}Pb(Br_{0.4}I_{0.6})_3$ films,

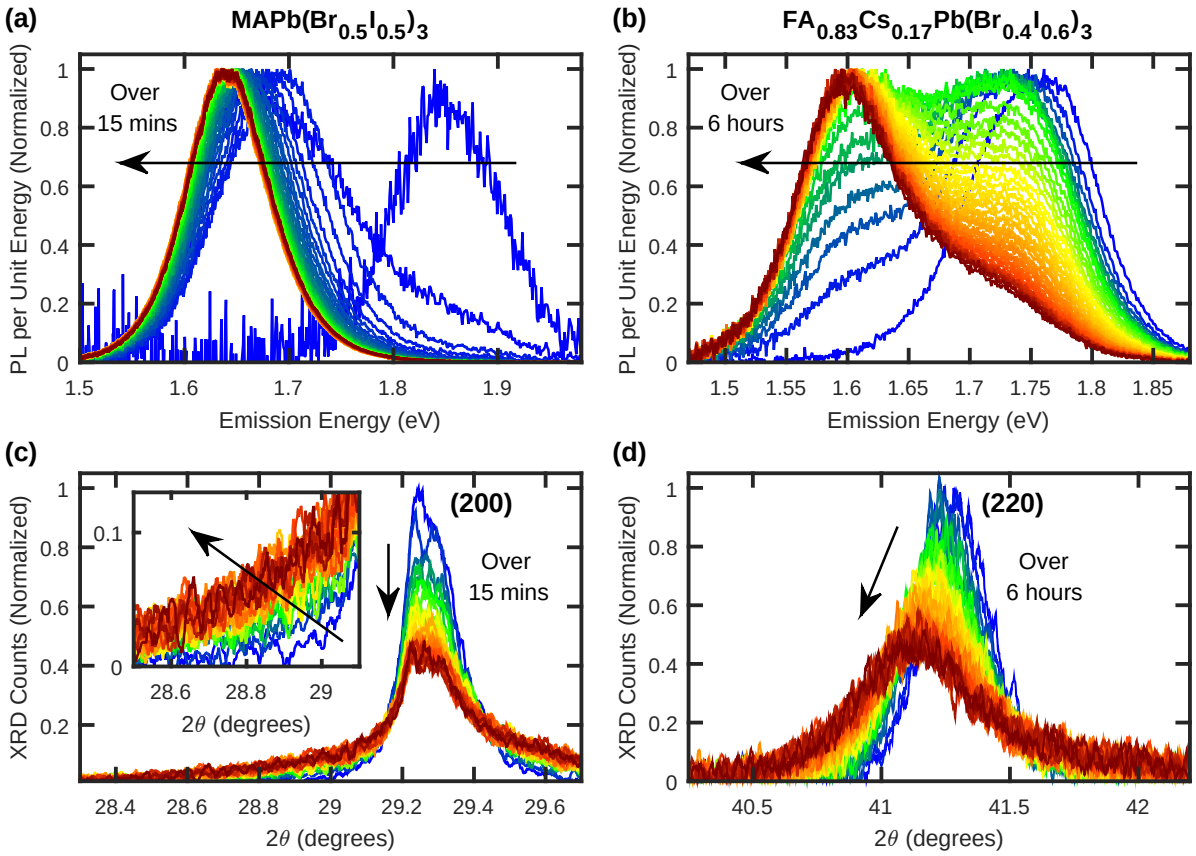

Figure 6.3: (a) Normalised PL spectra for an $MAPb(Br_{0.5}I_{0.5})_3$ thin film coated with PMMA, recorded over 15 minutes of illumination under light of intensity 190 mW cm^{-2}, wavelength 470 nm. (b) Normalised PL spectra for an $FA_{0.83}Cs_{0.17}Pb(Br_{0.4}I_{0.6})_3$ thin film coated with PMMA, recorded over 6 hours of illumination under light of intensity 190 mW cm^{-2}, wavelength 470 nm. Red-shifts in both (a) and (b) are caused by halide segregation. (c) XRD patterns recorded in situ at the same time and on the same $MAPb(Br_{0.5}I_{0.5})_3$ thin film as the data shown in (a). The angle axis is scaled to focus on the region around the cubic (200) peak in the recorded XRD data. The inset shows a zoomed region of the low-angle tail of the (200) peak. (d) XRD patterns recorded in situ at the same time and on the same $FA_{0.83}Cs_{0.17}Pb(Br_{0.4}I_{0.6})_3$ thin film as the data shown in (b). The angle axis is scaled to show the cubic (220) peak in the recorded XRD data. In both (c) and (d) the Cu-$K_{\alpha 1}$ line was used as incident radiation.

recorded in situ at the same time as the PL spectra discussed above and under the same illumination conditions, show markedly different dynamics (Figures 6.3c and 6.3d, respectively). For $MAPb(Br_{0.5}I_{0.5})_3$, Figure 6.3c shows that over the course of 15 minutes of illumination, the (200) diffraction peak in the XRD pattern decreased in amplitude, but remained centred at a fixed 2θ value of around 29.25°. For $FA_{0.83}Cs_{0.17}Pb(Br_{0.4}I_{0.6})_3$, on the other hand, Figure 6.3d illustrates that the (220) diffraction peak shifted to

lower angles and widened significantly during the 6 hours of illumination. In addition, substantial differences can be observed in the tail regions of these peaks, farther away from their centre positions. For $MAPb(Br_{0.5}I_{0.5})_3$, a significant growth of XRD intensity in the high- and low-angle tails of the (200) peak can be observed, as highlighted in the inset to Figure 6.3c for the low-angle tail. For $FA_{0.83}Cs_{0.17}Pb(Br_{0.4}I_{0.6})_3$, such growth in low-angle tail amplitude to the (220) peak is negligible (Figure 6.3d), however, a slight amount of high-angle tail growth is evident, and is highlighted in Figure 6.4 where the data have not been background corrected, have been smoothed, and are plotted on a logarithmic y-axis in order to emphasise the growth of high-angle signal. The specific XRD peaks discussed here were selected based on their prominence in the corresponding XRD pattern (see Figures 6.1 and 6.2), and second-order peaks – the (200) and (220) peaks as opposed to the (100) and (110) peaks – were selected for examination in order to provide a good 2θ resolution. Figures 6.5 and 6.6 show that the behaviour of the (200) and (220) XRD peaks of the $MAPb(Br_{0.5}I_{0.5})_3$ and $FA_{0.83}Cs_{0.17}Pb(Br_{0.4}I_{0.6})_3$ films, respectively, was similar to that observed for additional XRD peaks for these films.

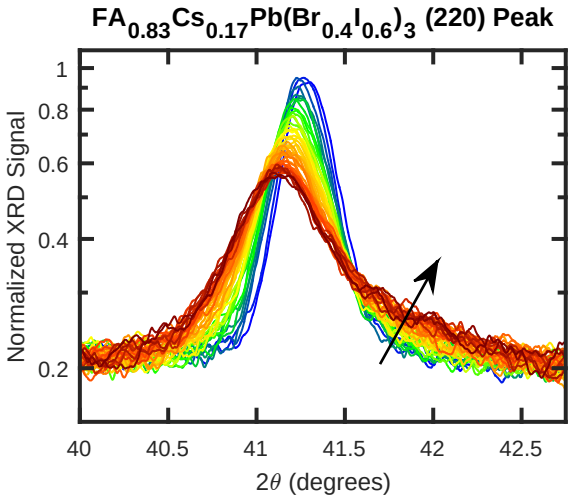

Figure 6.4: Smoothed, normalised XRD patterns displaying the (220) diffraction peak of a PMMA-coated $FA_{0.83}Cs_{0.17}Pb(Br_{0.4}I_{0.6})_3$ perovskite film under 190 mW cm^{-2} intensity illumination over the course of 6 h. The data are plotted on a logarithmic y-axis and are not background corrected in order to emphasise the growth of signal in the high-angle peak tail (∼41.5°–42.75° 2θ). The Cu-$K_{\alpha 1}$ line was used as incident radiation.

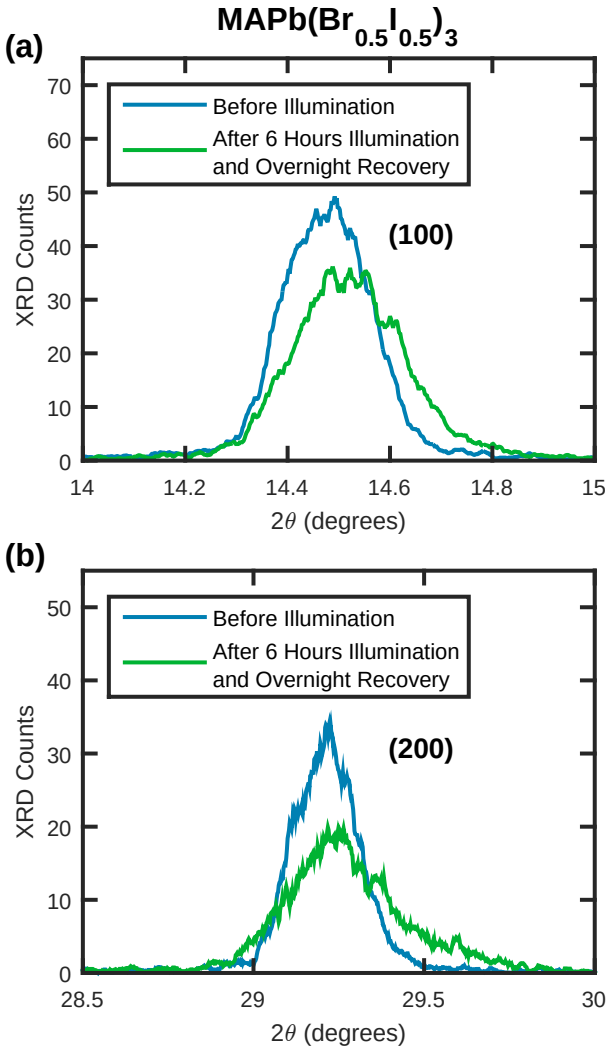

Figure 6.5: (a) and (b) show XRD data of the (100) and (200) XRD peaks, respectively, recorded from an $MAPb(Br_{0.5}I_{0.5})_3$ thin film, with the XRD measurements taken before the film was exposed to any illumination, and after the film was exposed to a 6 h period of 190 mW cm^{-2}, 470 nm wavelength illumination followed by a period of overnight recovery (around 18 h). The XRD patterns in Figure 6.5 were obtained with a Rigaku Smartlab X-ray diffractometer as described in Section 3.3.3. The data shown in blue is the same as that shown in green in Figure 6.1.

6.4.1 Behaviour of XRD Peaks

The observed differences in the evolution of the XRD diffraction patterns for $MAPb(Br_{0.5}I_{0.5})_3$ and $FA_{0.83}Cs_{0.17}Pb(Br_{0.4}I_{0.6})_3$ under illumination suggest that fundamentally different ionic movements accompany and drive halide segregation in these two materials. To explore the causes of such differences further, the changes in XRD

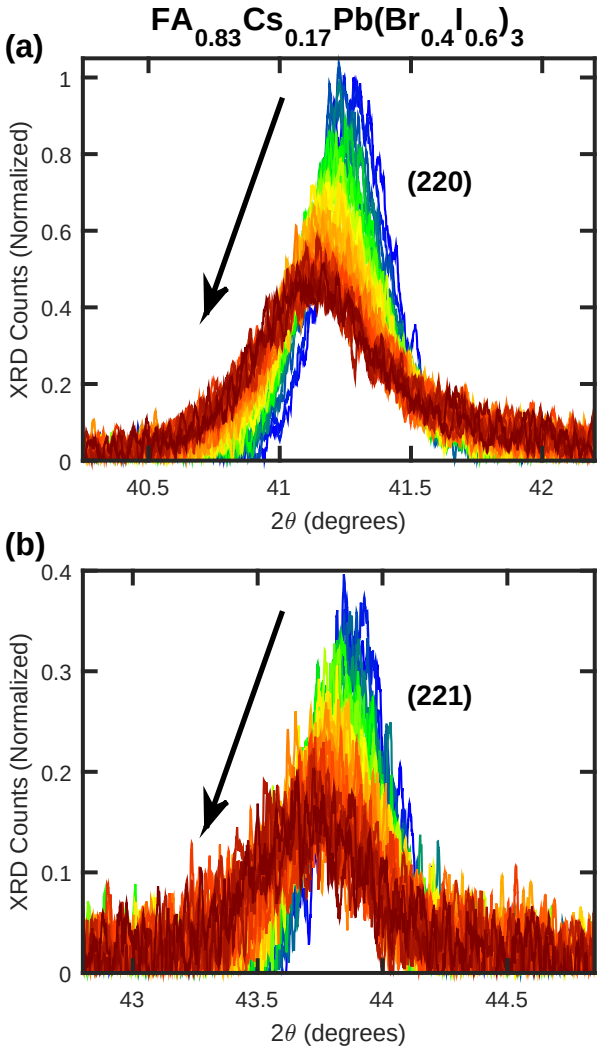

Figure 6.6: (a) and (b) show XRD data of the (220) and (221) XRD peaks, respectively, recorded from an $FA_{0.83}Cs_{0.17}Pb(Br_{0.4}I_{0.6})_3$ thin film, with the XRD measurements taken in situ under 6 h of 190 mW cm^{-2}, 470 nm wavelength illumination. (a) shows identical data of the (220) peak to that shown in Figure 6.3d, but which are repeated here to allow for an easier comparison to the (221) peak data in (b) to be made. The arrows indicate the behaviour of the peaks over the 6 h of illumination.

peak amplitudes, and the peak integrals, can be examined as a function of time under illumination and during the subsequent recovery in the dark. Figures 6.7a and 6.8 present time-resolved XRD peak amplitudes for the (200) diffraction peak of $MAPb(Br_{0.5}I_{0.5})_3$ films and the (220) peak of an $FA_{0.83}Cs_{0.17}Pb(Br_{0.4}I_{0.6})_3$ film, exposed to different periods of 190 mW cm^{-2} intensity illumination and in subsequent darkness. In general, the XRD peak amplitudes of both perovskites decrease under illumination and increase again as

they recover in the periods of post-illumination darkness. However, the $MAPb(Br_{0.5}I_{0.5})_3$ films experienced faster dynamics than the $FA_{0.83}Cs_{0.17}Pb(Br_{0.4}I_{0.6})_3$ film under both illumination and darkness, highlighting the higher susceptibility to ionic movement for $MAPb(Br_{0.5}I_{0.5})_3$. In addition, the initial decrease of XRD peak amplitude under illumination is significantly faster than the subsequent recovery of amplitude under darkness for all perovskite films (highlighted in Figure 6.8), in agreement with previous studies demonstrating that the initial halide segregation proceeds much more rapidly than the subsequent remixing of halide ions under darkness [17]. It was further confirmed that the 18 hours of X-ray exposure themselves did not significantly affect the perovskite material, as an $MAPb(Br_{0.5}I_{0.5})_3$ perovskite thin film was placed in darkness but under X-ray examination for 18 hours, (black plot in Figure 6.7a) which resulted in negligible loss in XRD peak amplitude over the course of the experiment. Figures 6.9 and 6.10 further provide PL spectra and XRD patterns taken before and after the periods of illumination, and after corresponding periods of subsequent darkness, for each of the examined perovskite films.

Interestingly, it is found that unlike the XRD peak amplitudes, the integrals over the same XRD peaks (Figure 6.7b) remain remarkably constant during illumination and subsequent recovery, indicating a lack of film degradation into non-perovskite products during the experiments. The only exception to this observation is when the less-stable $MAPb(Br_{0.5}I_{0.5})_3$ film is illuminated for the prolonged period of 6 hours, during which the integrated XRD signal eventually declines, indicating a small amount of material degradation, and these data are therefore excluded from the following analysis. Any potential emergence of non-perovskite material would be unlikely to produce XRD diffraction signal exclusively within the chosen integral limits used for the respective (200) and (220) peaks of the $MAPb(Br_{0.5}I_{0.5})_3$ and $FA_{0.83}Cs_{0.17}Pb(Br_{0.4}I_{0.6})_3$ films, and so a significant formation of these products would have reduced the overall integral over

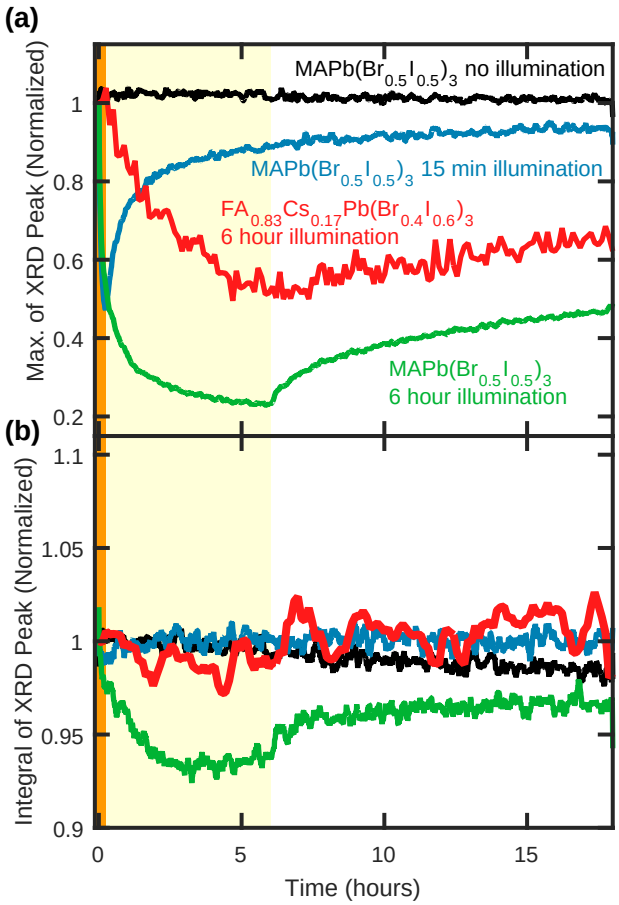

Figure 6.7: The (a) maximum amplitude of and (b) integral over the (200) peak ($MAPb(Br_{0.5}I_{0.5})_3$ thin film samples) and the (220) peak ($FA_{0.83}Cs_{0.17}Pb(Br_{0.4}I_{0.6})_3$ thin film sample) in the XRD patterns of metal halide perovskite films coated with PMMA. The thin film samples were either illuminated for 15 minutes under 190 mW cm^{-2} intensity light of 470 nm wavelength (highlighted by the shaded orange region at early times), illuminated for 6 hours under the same illumination parameters (highlighted by the shaded yellow region), or not illuminated, after which all thin film samples were left in darkness until 18 hours of total experimental time had passed. In (b), the integral was taken from 27.0° to 31.5° 2θ for the (200) diffraction peak of the $MAPb(Br_{0.5}I_{0.5})_3$ perovskite thin films, and from 39.5° to 42.75° 2θ for the (220) peak of the $FA_{0.83}Cs_{0.17}Pb(Br_{0.4}I_{0.6})_3$ thin film. The data plots in (a) are normalised to their initial value, and the data plots in (b) are normalised to an average of the data within the first 2 min of the corresponding experiment.

these XRD peaks, which is not observed. In particular, the generation of two specific non-perovskite degradation products during the periods of illumination can be ruled out. Firstly, little or no material converted from a perovskite crystalline structure into more amorphous material, given that coherent reflection of X-rays may only occur from regions exhibiting a well-ordered structure [197] – see Section 3.3.1. If a significant volume of

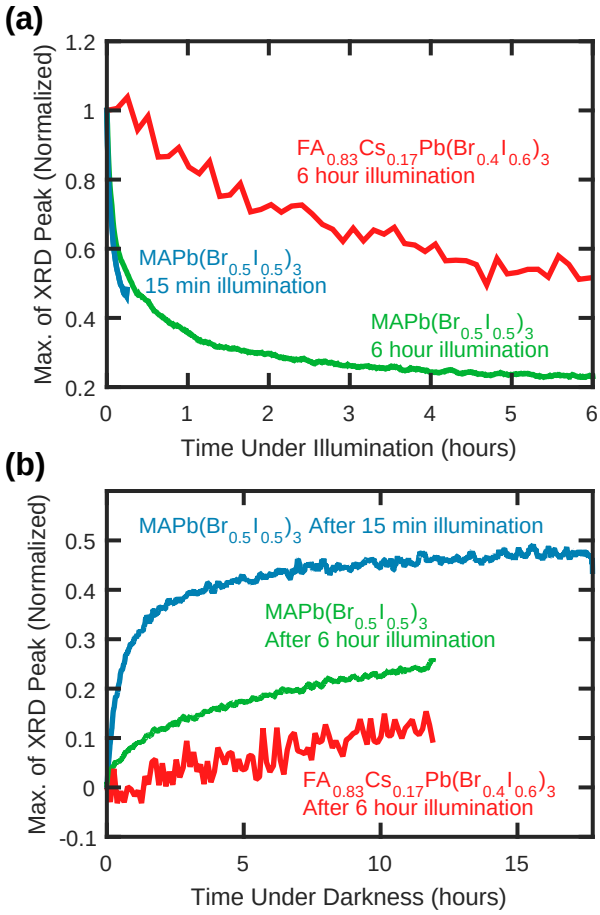

Figure 6.8: The maximum amplitude of the (200) peak ($MAPb(Br_{0.5}I_{0.5})_3$) and the (220) peak ($FA_{0.83}Cs_{0.17}Pb(Br_{0.4}I_{0.6})_3$) in the XRD pattern of metal halide perovskite films coated with PMMA. (a) The behaviour of the XRD peak amplitudes during perovskite film illumination under either 15 min or 6 h of 190 mW cm^{-2} intensity light of 470 nm wavelength. The XRD peak amplitudes are normalised to their initial values before any illumination. (b) The behaviour of the XRD peak amplitudes under darkness, immediately after the corresponding period of perovskite film illumination. The XRD peak amplitudes are normalised to the initial value the XRD peak had before any period of illumination or darkness had commenced, and the axes are shifted so that the plots begin at the origin to allow for an easier comparison of the data.

the perovskite material had converted from an ordered structure into a non-perovskite, random arrangement then a significant decrease in total XRD diffraction signal would be evident in Figure 6.7b. Secondly, little or no perovskite material converted into PbI_2 – or its mixed-halide equivalents – over the course of the experiment. PbI_2 is a very common degradation product for many perovskites, but it contributes insignificant XRD diffraction amplitude in the 2θ regions over which these second-order peaks were integrated [43, 232–234]. Besides, Figures 6.11 and 6.12 confirm that neither of the

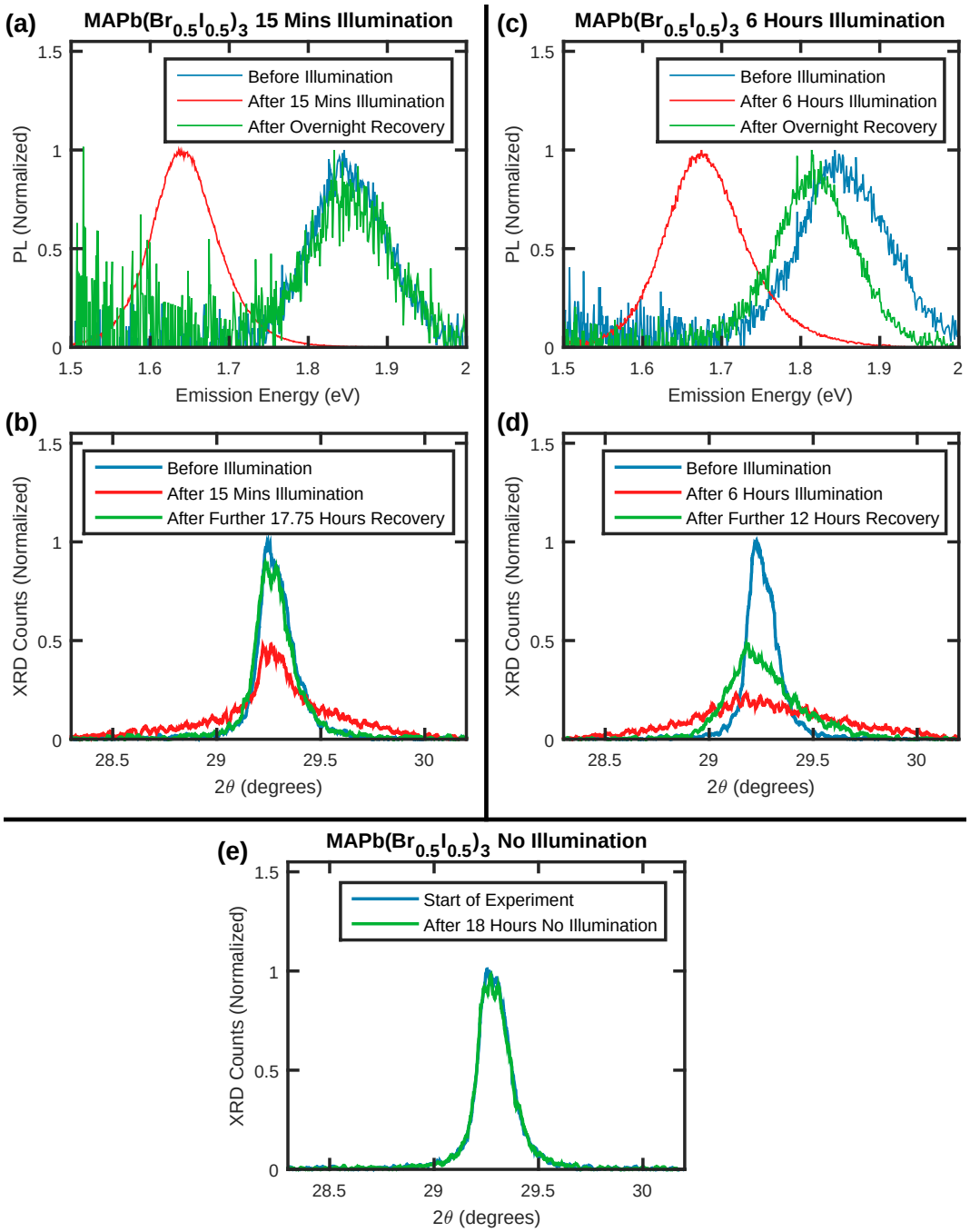

Figure 6.9: (a), (c) PL spectra of $MAPb(Br_{0.5}I_{0.5})_3$ thin films, both coated with PMMA, and recorded before and after 15 min and 6 h, respectively, of 190 mW cm^{-2}, 470 nm wavelength illumination, and after a period of overnight recovery (around 24 h and 18 h, respectively). (b), (d) XRD patterns of the same films, recorded in situ before and after the 15 min and 6 h, respectively, of 190 mW cm^{-2} illumination, and after periods of 17.75 h and 12 h of darkness, respectively, subsequent to the periods of illumination. (e) XRD patterns of an $MAPb(Br_{0.5}I_{0.5})_3$ thin film coated with PMMA, recorded before and after 18 h of darkness in the experimental setup. In (b), (d), and (e) XRD measurements were continuously taken of the films throughout the periods of illumination and the periods of darkness.

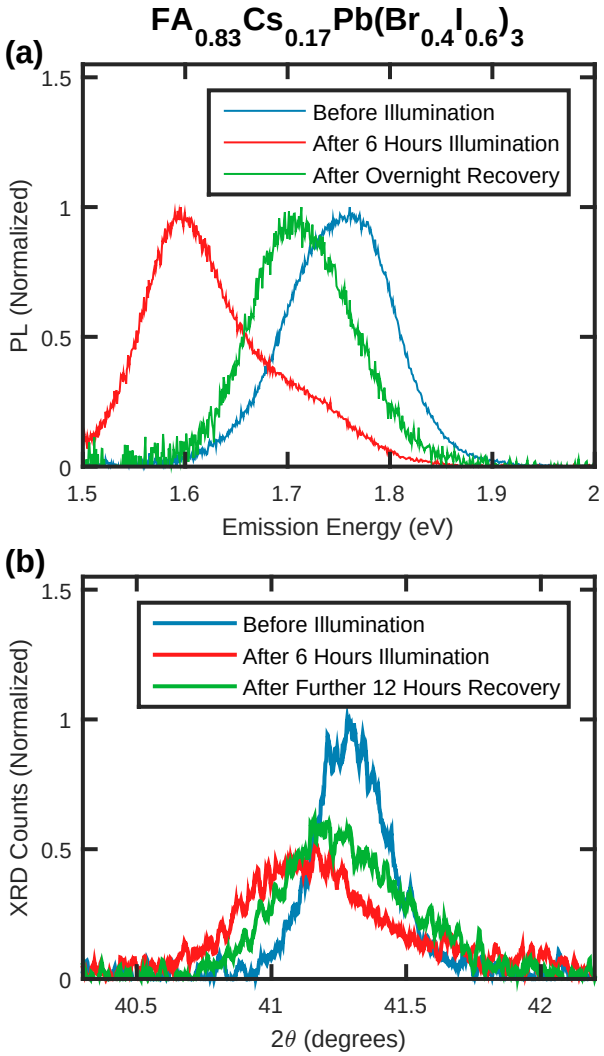

Figure 6.10: (a) PL spectra of an $FA_{0.83}Cs_{0.17}Pb(Br_{0.4}I_{0.6})_3$ thin film coated with PMMA, recorded before and after 6 h of 190 mW cm^{-2}, 470 nm wavelength illumination, and after a period of overnight recovery (around 18 h). (b) XRD patterns of the same film, recorded in situ before and after the 6 h of 190 mW cm^{-2} illumination, and after a period of 12 h of darkness subsequent to the 6 h of illumination. "Before Illumination" (blue) data measurements in (a) and (b) were recorded at approximately the same time, as were the "After 6 Hours Illumination" (red) data measurements. XRD measurements were continuously taken of the film throughout the 6 h of illumination and the further 12 h of darkness.

two perovskites featured a growth in the prominent peak between 12° and 13° 2θ (for Cu-$K_{\alpha 1}$ incident radiation) typically associated with PbI_2 [232, 234, 235] in their recorded XRD pattern as a result of the prolonged illumination.

Given the absence of significant breakdown into non-perovskite structures or amorphous material for both compositions during the conducted experiments, it is concluded

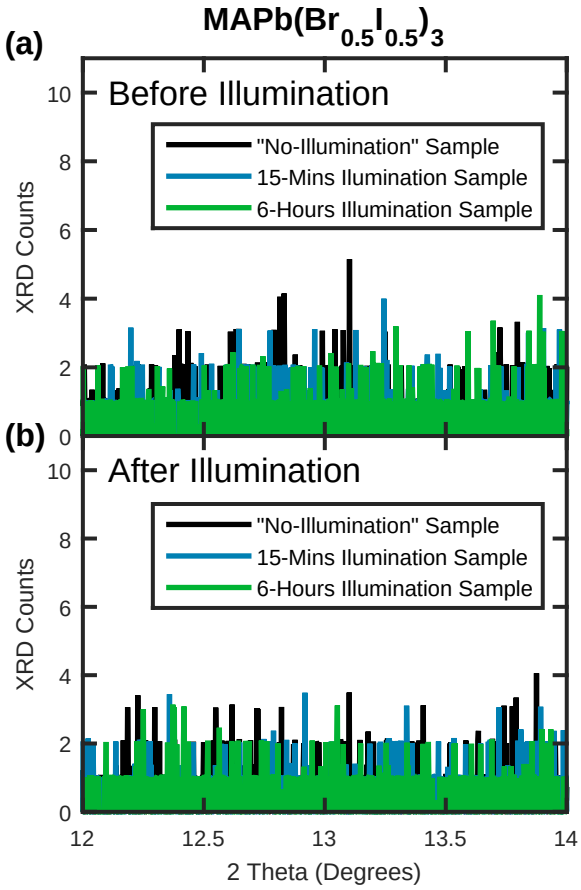

Figure 6.11: XRD patterns of three $MAPb(Br_{0.5}I_{0.5})_3$ thin films coated with PMMA, recorded (a) before and (b) after different lengths of illumination period (all at 190 mW cm^{-2} intensity and 470 nm wavelength) and a period of overnight recovery in the dark. The axes are scaled to show the region of the XRD pattern where peaks pertaining to any PbI_2 or $PbBr_2$ in the perovskite films would be visible. Given the lack of any significant signal in both (a) and (b), it is concluded that there was no significant degradation of perovskite material into either PbI_2 or $PbBr_2$ during the conducted experiments. The XRD data were recorded in a Rigaku SmartLab diffractometer as detailed in Section 3.3.3, and (a) shows a zoomed region of Figure 6.1.

that the changes occurring in the XRD patterns (Figures 6.3c&d) principally result from two effects. Firstly, the red-shifts in the PL emission spectra (Figures 6.3a&b) are indicative of halide segregation and halide ion movement, and it is concluded that such ionic movement is likely primarily responsible for the concomitant changes in the associated XRD patterns (Figures 6.3c&d). Iodide-rich regions of perovskite will generate XRD peak positions at lower values of 2θ than bromide-rich regions, given that these peaks are linked with the lattice spacing of a given structure [17, 43, 65, 197]. The

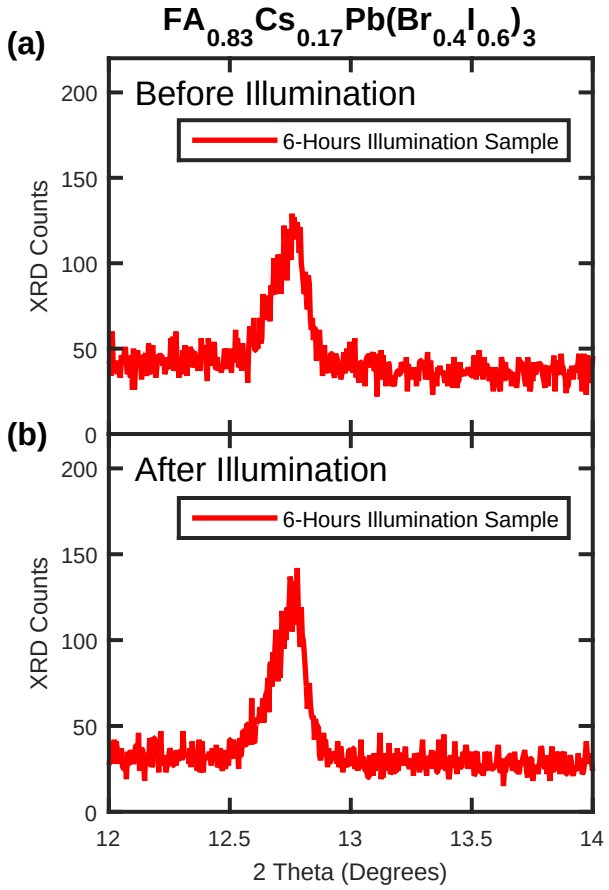

Figure 6.12: XRD patterns of an $FA_{0.83}Cs_{0.17}Pb(Br_{0.4}I_{0.6})_3$ thin film coated with PMMA, recorded (a) before and (b) after 6 h of illumination (at 190 mW cm^{-2} intensity and 470 nm wavelength) and a period of overnight recovery in the dark. The axes are scaled to show the region of the XRD pattern where peaks pertaining to any PbI_2 or $PbBr_2$ in the perovskite films would be visible. The visible signal in this region highlights that there were small amounts of PbI_2 or $PbBr_2$ in the perovskite film. However, given the near-identical signal between (a) and (b), it is concluded that there was no significant degradation of perovskite material into either PbI_2 or $PbBr_2$ over the course of the conducted experiment. The XRD data were recorded in a PANalytical X'Pert diffractometer as detailed in Section 3.3.3, and (a) shows a zoomed region of Figure 6.2.

increased spread of XRD diffraction amplitude across a wide range of 2θ values as illumination progresses (Figures 6.3c&d) may then be primarily explained by a widening of the compositional range present across different perovskite regions. Secondly, as a less significant effect, a breakdown of crystalline volumes into smaller domains may contribute to the broadening of XRD peaks [198], and result in an associated growth in their tails [236, 237], as described in Section 3.3.2. This scenario may apply to the

$MAPb(Br_{0.5}I_{0.5})_3$ film, for which Figure 6.3c indicates a symmetric signal growth in both high- and low-angle tails of the (200) XRD peak, which could to some extent derive from breakdown of crystalline domains. In contrast, Figures 6.3d and 6.4 demonstrate an absence of such symmetric tail growth for $FA_{0.83}Cs_{0.17}Pb(Br_{0.4}I_{0.6})_3$ suggesting domain breakdown to be insignificant here. Additionally, it is noted that a minor extent of XRD peak broadening may result from strain being introduced into the perovskite crystal by halide ion movement and the fracturing of crystalline domains.

6.4.2 Compositional Evolution Analysis

In order for the compositional evolution within the $MAPb(Br_{0.5}I_{0.5})_3$ and $FA_{0.83}Cs_{0.17}Pb(Br_{0.4}I_{0.6})_3$ films to be examined, it is helpful to convert both PL emission energies and XRD 2θ angles to an estimate of the bromide content of the emitting/diffracting perovskite region. Section 3.4.2 provides full details on how these conversions were performed, based on known dependencies of average PL emission and XRD peak positions on bromide content x for a range of corresponding perovskite stoichiometries across the iodide-bromide series. By remapping the PL and XRD measurements displayed in Figure 6.3 onto the same horizontal axis (axis of abscissa), now given in terms of bromide content, it is thus possible to directly correlate the optoelectronic changes with the local compositional changes occurring upon halide segregation. It is noted that because this approach does not capture any potential effects arising from crystal domain fracturing, these bromide content axes should be viewed as estimates, rather than precise measurements. Through this approach, it is possible to elucidate how the associated underlying ionic rearrangement differs between $MAPb(Br_{0.5}I_{0.5})_3$ and $FA_{0.83}Cs_{0.17}Pb(Br_{0.4}I_{0.6})_3$ perovskites films.

6.4.2.1 In-Depth Analysis of $MAPb(Br_{0.5}I_{0.5})_3$

To begin, the analysis is first focused on $MAPb(Br_{0.5}I_{0.5})_3$, for which Figures 6.13a&b present in situ PL and XRD data taken simultaneously over 15 minutes of 190 mW cm^{-2} intensity illumination. Comparison of PL spectra and XRD patterns, now both plotted against an estimated bromide content axis, strikingly highlights how little of the XRD diffraction signal in Figure 6.13b correlates with the bromide content associated with the low-energy PL peak in Figure 6.13a. These observations confirm that iodide-rich regions of perovskite form only a tiny fraction of the total perovskite volume [22], while contributing to the vast majority of the PL emission because charge-carrier diffusion to these regions is highly effective. The XRD spectra displayed in Figure 6.13b also demonstrate that halide segregation results in complex compositional changes, most of which – because of the sensitivity of PL techniques to only the most iodide-rich, lowest bandgap perovskite domains – cannot be detected with PL measurements. The work in this chapter therefore highlights the importance of examining the halide segregation process through techniques that are sensitive to the bulk of the perovskite material, such as XRD measurements.

To confirm that the process of compositional change primarily causes the observed changes to both the PL and XRD data, the temporal evolution of the respective signals around the low-bromide (iodide-rich) region of the PL spectra and XRD patterns is examined. Figure 6.13c presents such time-resolved integrals over the PL and XRD signals presented in Figures 6.13a and 6.13b, between the estimated bromide contents of $x = 0.07$ and $x = 0.16$, as indicated by the shaded red columns. Conversion of both horizontal axes to values of estimated bromide content thus allows a direct comparison to be made between the evolution of PL and XRD data in the same corresponding region. Figure 6.13c clearly illustrates the time-resolved formation of iodide-rich regions within $MAPb(Br_{0.5}I_{0.5})_3$ via both PL and XRD measurements, with the integral of both signal types showing the same rise and plateau over time commonly associated with

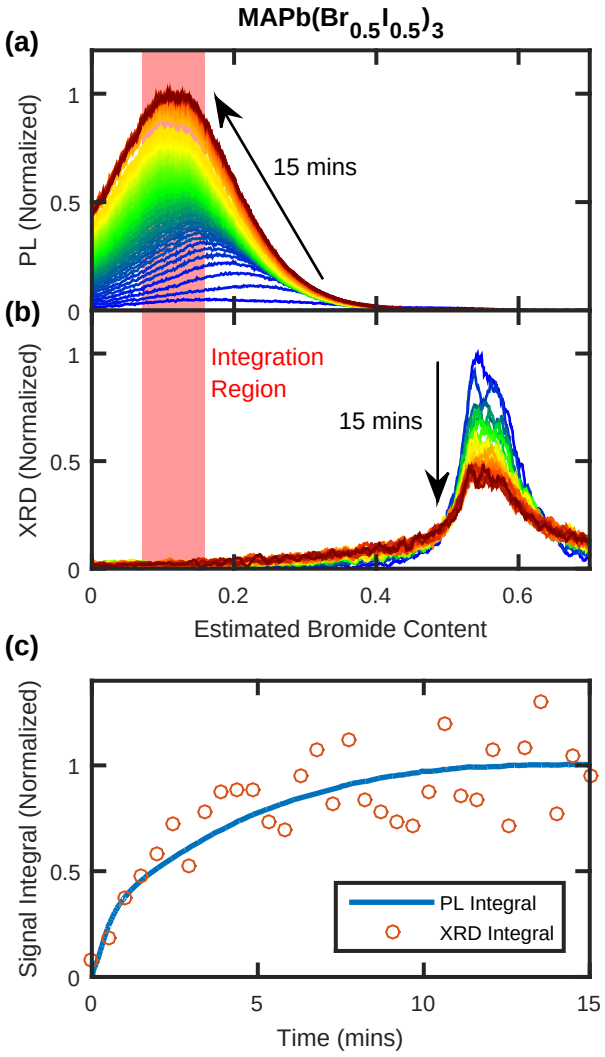

Figure 6.13: (a) PL spectra for an $MAPb(Br_{0.5}I_{0.5})_3$ thin film coated with PMMA, recorded over 15 minutes of 190 mW cm^{-2}, 470 nm wavelength illumination. Spectra are plotted against the estimated bromide content of the emitting perovskite, which was determined from the dependence of the perovskite bandgap on halide composition reported in the literature, as described in Section 3.4.2. (b) XRD patterns for the same $MAPb(Br_{0.5}I_{0.5})_3$ thin film as in (a), recorded in situ over the same 15 minute period of 190 mW cm^{-2} illumination, also plotted against the estimated bromide content of the reflecting perovskite determined from literature reports (see Section 3.4.2). (c) The blue line plots the integral over the PL spectra in (a), and the orange circles plot the integral over the XRD patterns in (b), both taken over the bromide-content interval indicated by the shaded red region in (a) and (b), which centres around the bromide composition matching the final position of the PL peak.

PL measurements of halide segregation in the literature [96, 150] and as observed in Chapter 4. Figure 6.13c therefore confirms that the rise in low-angle XRD tail and low-energy PL signals predominantly results from halide ion rearrangement, with any potential breakdown of crystalline domains being a secondary effect.

6.4.2.2 Halide Ion Dynamics in MAPb($Br_{0.5}I_{0.5}$)$_3$

The above analysis of the changes occurring within the MAPb($Br_{0.5}I_{0.5}$)$_3$ perovskite allows for the halide ion dynamics within the perovskite under illumination to be elucidated. The growth of the low- and high-angle tails surrounding the main XRD (200) peak (evident in Figure 6.13b) is ascribed to the build-up of iodide- and bromide-enriched material as the halide segregation process proceeds. Interestingly, the evolution of the core (200) diffraction peak over time can be explained by the accumulated effect of continuous ionic movements that are initially restricted to specific regions of the MAPb($Br_{0.5}I_{0.5}$)$_3$ perovskite, before these specific regions increase in number due to crystalline domain breakdown and grow in volume, thereby spreading throughout the bulk perovskite material. It is proposed that during any given time interval, a sub-fraction of the bulk material converts into iodide-rich and bromide-rich material, with the nature of the remaining bulk perovskite phase remaining unchanged. As time progresses, such changes become visible in Figure 6.13b as a rise in the high- and low-angle tails of the (200) peak, and a significant decrease of the (200) peak itself, while the overall 2θ position of the (200) peak remains constant. If instead, significant, concurrent ionic rearrangements occurred in large volumes of the perovskite simultaneously, this would be recorded as a shift or change in shape of the main (200) XRD peak, neither of which are strongly apparent in Figure 6.13b. It is therefore concluded that halide segregation in MAPb($Br_{0.5}I_{0.5}$)$_3$ is initiated in specific volumes of the perovskite, with the remaining bulk remaining compositionally stable, as indicated by the unchanged 2θ central position of the XRD peak. Under continued illumination, the regions in which such segregation occurs gradually grow to consume much of the overall volume.

For the halide segregation pathways proposed for MAPb($Br_{0.5}I_{0.5}$)$_3$, the associated ionic movement will be relatively facile, as only the volumes of perovskite most prone to halide segregation will initially participate. Therefore, such segregation pathways help

to explain the relative ease by which MA-cation mixed-halide perovskites are observed to initiate halide segregation. It is proposed that ionic movement might commence in regions such as grain boundaries that may offer enhanced ion mobilities [145–149], which could facilitate the segregation of halide ions in certain, small regions of the perovskite material with initially minor effects on the bulk material. The evolution of the XRD pattern under illumination of $MAPb(Br_{0.5}I_{0.5})_3$ further demonstrates that these specific regions gradually grow, eventually engulfing most of the material. Such growth of halide-segregated material could result from an extension of these domains away from grain boundaries and into the bulk, as charge-carrier funneling and lattice distortion progresses with time under illumination. However, it is suggested that an alternative process, deriving from the fracturing of crystalline domains under illumination may also be in operation. Figure 6.14 presents an analysis of the width of the (200) peak from XRD patterns recorded from an $MAPb(Br_{0.5}I_{0.5})_3$ perovskite thin film over 6 h of illumination at 190 mW cm^{-2} intensity and 470 nm wavelength – see Figures 6.9c&d for PL spectra and XRD patterns recorded from this $MAPb(Br_{0.5}I_{0.5})_3$ film. As explained in Section 3.3.2, the full width at half maximum (FWHM) of an XRD peak can be related, in accordance with various assumptions, to an estimate of the crystallite size within the measured material. Figure 6.14b presents estimates of the crystalline domain size within the $MAPb(Br_{0.5}I_{0.5})_3$ film over the course of the 6 h of illumination, calculated using Equation 3.10, and the FWHM estimates (made both directly from the data and from Lorentzian fits to the data) shown in Figure 6.14a. A clear widening of the (200) XRD peak over the course of the experiment is shown in Figure 6.14a, and Figure 6.14b shows that the crystallite size estimate correspondingly decreases during the period of illumination. Figure 6.14 shows that the observed increase in the full width at half maximum of the (200) peak is commensurate with a significant contraction in crystalline domain size under illumination, if ionic redistribution is neglected. Therefore, halide

segregation in $MAPb(Br_{0.5}I_{0.5})_3$ may partly progress through the gradual fracturing of crystalline domains under illumination, which increases the volume of grain boundaries, generating more regions where halide segregation may easily occur. This proposed picture of the halide segregation mechanism in certain mixed-halide perovskites is congruent with literature reports of halide segregation often being associated with perovskite regions surrounding grain boundaries in the material [104, 119, 144].

6.4.2.3 In-Depth Analysis of $FA_{0.83}Cs_{0.17}Pb(Br_{0.4}I_{0.6})_3$

The halide segregation mechanism for the much more compositionally-stable $FA_{0.83}Cs_{0.17}Pb(Br_{0.4}I_{0.6})_3$ perovskite is now examined, and it is found to be markedly different from that described above for $MAPb(Br_{0.5}I_{0.5})_3$. As already discussed above, the evolution of XRD patterns of $FA_{0.83}Cs_{0.17}Pb(Br_{0.4}I_{0.6})_3$ under illumination, as shown in Figure 6.3d, highlights a different underlying type of ionic motion. Here, the actual (220) diffraction peak of $FA_{0.83}Cs_{0.17}Pb(Br_{0.4}I_{0.6})_3$ perovskite is found to shift and widen over 6 hours of illumination, with a tail appearing at higher angles. Such pronounced changes to the core diffraction peak suggest that large amounts of ionic rearrangement occur throughout the perovskite volume, with a significant change to the average composition of the majority phase. To examine such changes to the bulk of the material, the shifts in the main (220) diffraction peak are therefore compared with those in the PL emission peak associated with only the initially well-mixed, bulk phase of the $FA_{0.83}Cs_{0.17}Pb(Br_{0.4}I_{0.6})_3$, as shown in Figure 6.15a and Figure 6.15b for the first 6 hours of 190 mW cm^{-2} intensity illumination. In order to obtain the PL spectral component associated with only the bulk phase, the low-energy PL peak deriving from the iodide-rich minority phase was captured with a Gaussian fit and removed from the PL spectra. A direct comparison of the PL emission peaks and XRD patterns of the bulk perovskite phase (Figures 6.15a&b), plotted against a common axis of bromide content, shows clear parallel dynamics. Both

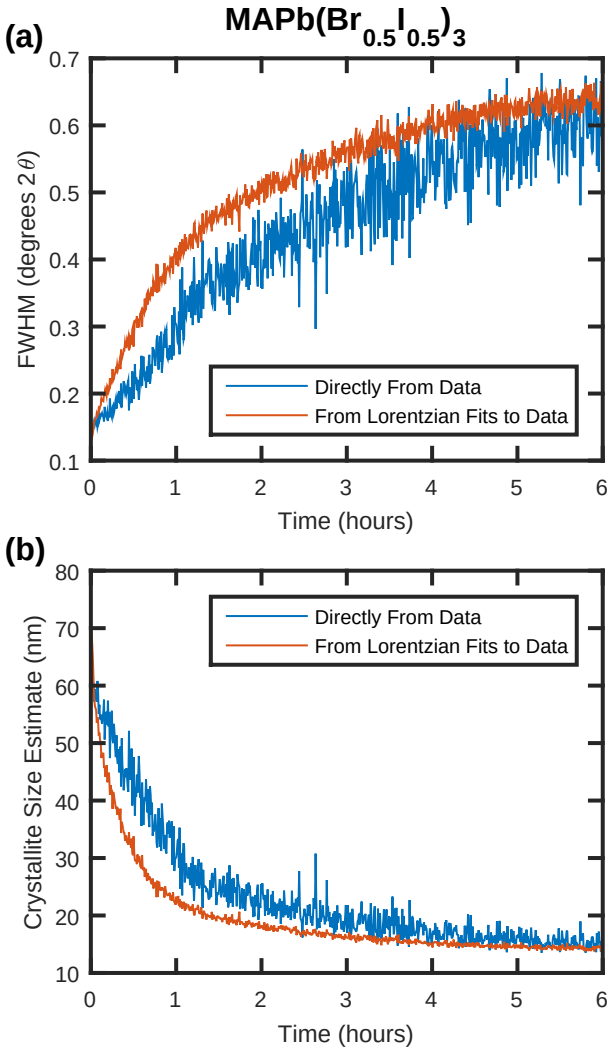

Figure 6.14: (a) The full width at half maximum (FWHM) of the (200) peak in XRD patterns recorded from an $MAPb(Br_{0.5}I_{0.5})_3$ perovskite thin film over 6 h of illumination at 190 mW cm^{-2} intensity and 470 nm wavelength. Plotted in blue is the FWHM estimated directly from the data, and in orange is the FWHM taken from Lorentzian fits to the XRD data. (b) Mean size of the crystalline domains within the $MAPb(Br_{0.5}I_{0.5})_3$ perovskite thin film, estimated using the Scherrer equation [198] – see Section 3.3.2 – and the XRD peak widths shown in (a). It is noted that due to other effects such as compositional inhomogeneities, the crystallite size estimates presented in (b) should only be considered as estimates to the lower bound of the crystalline domain sizes within the $MAPb(Br_{0.5}I_{0.5})_3$ film.

PL and XRD peaks of the bulk perovskite phase shift to lower bromide content and broaden significantly with illumination time. In Figure 6.15c, the peak position of the PL spectra displayed in Figure 6.15a is compared with that of the (220) XRD peak in Figure 6.15b, in terms of bromide content at which the maximum signal occurs, highlighting the similarity in timescales of the changes to the PL spectra and XRD

patterns. Overall, these observations suggest that for $FA_{0.83}Cs_{0.17}Pb(Br_{0.4}I_{0.6})_3$, prolonged illumination primarily affects the optoelectronic properties and the ionic distribution across the whole bulk material, rather than just within a minority phase exhibiting high ion mobility, as for $MAPb(Br_{0.5}I_{0.5})_3$.

To understand the reasons for the observed shift of the (220) XRD diffraction peak of $FA_{0.83}Cs_{0.17}Pb(Br_{0.4}I_{0.6})_3$ under prolonged illumination, the possibilities of ionic rearrangements and of the introduction of lattice strain [193] are considered, which could shift crystal plane spacings. Interestingly, when the XRD signal is evaluated across its full spread, it is found that the *mean* bromide content value (as opposed to just the peak position) is largely unchanged with illumination time, see Figure 6.16 for a comparison of XRD peak and mean values over illumination time. This observation essentially results from the shift of the XRD peak maximum to lower 2θ angles (lower bromide contents) being largely counter-balanced by a growth of XRD signal in the high-angle (high-bromide) tail of the (220) peak (see Figures 6.3d and 6.4). As a result, the mean 2θ position of the XRD (220) peak shifts only by a tiny amount, 0.07°, over the 6-hour illumination period, which would correspond to only a ∼0.2% increase in the average lattice parameter of the perovskite, but could also be explained through several other effects, such as changes in XRD reflectivity for regions of different composition, crystallinity effects, or – while it was concluded in Section 6.4.1 that there was no significant degradation of the perovskite material into non-perovskite structures – minor losses of perovskite structure could have contributed to the minor shift of overall XRD signal. Given the small scale of the overall shift in XRD signal, it is concluded that the evolution in the shape of the XRD (220) peak of $FA_{0.83}Cs_{0.17}Pb(Br_{0.4}I_{0.6})_3$ is primarily caused by ionic rearrangement in the perovskite crystal, rather than large-scale lattice strain or other effects.

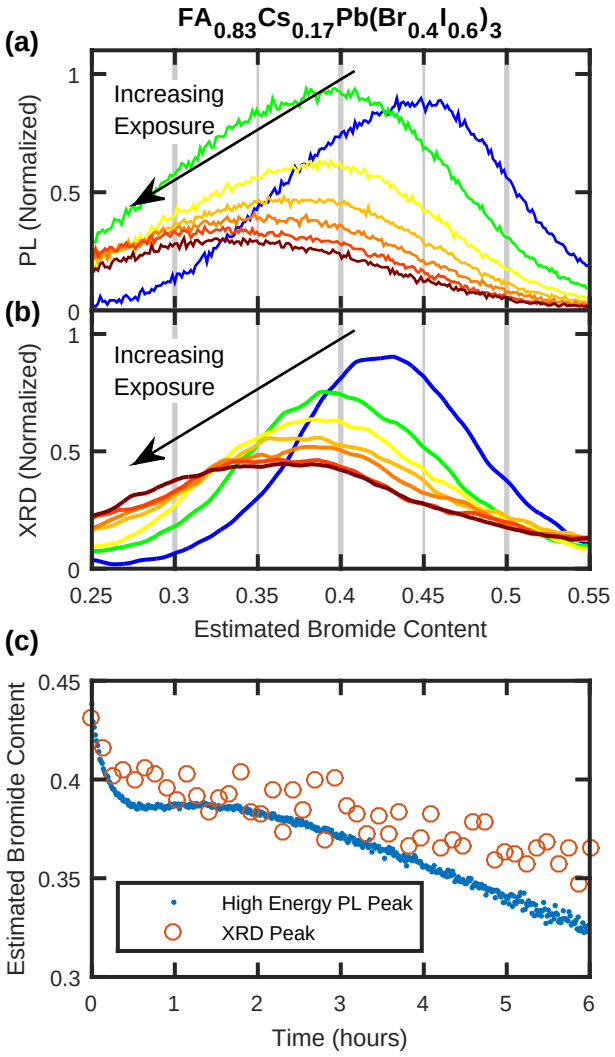

Figure 6.15: (a) PL spectra showing the mixed-phase perovskite emission from an $FA_{0.83}Cs_{0.17}Pb(Br_{0.4}I_{0.6})_3$ thin film coated with a PMMA layer, recorded over 6 hours under light of intensity 190 mW cm^{-2}, wavelength 470 nm. The spectra are plotted on a compositional axis determined from PL measurements, as described in Section 3.4.2. The low-energy, iodide-rich PL peak has been captured by a Gaussian fit and removed from the PL spectra. (b) XRD patterns recorded in situ at the same time and on the same $FA_{0.83}Cs_{0.17}Pb(Br_{0.4}I_{0.6})_3$ film as the data shown in (a). The patterns are plotted on an estimated bromide compositional axis determined from data in literature reports, which may be subjected to errors pertaining to A-site cation movement, as described in Section 3.4.2. Figure 6.16 presents the behaviour of the maximum and mean values of the XRD signal, which shift and remain relatively constant over time, respectively. The differently coloured data plots shown in (a) and (b) were taken at 1-hour intervals, and similarly coloured plots in (a) and (b) correspond to measurements made at approximately the same time. (c) The blue dots plot the peak position of the PL signal shown in (a), and the orange circles plot the peak position of the XRD signal shown in (b), both over 6 hours of illumination.

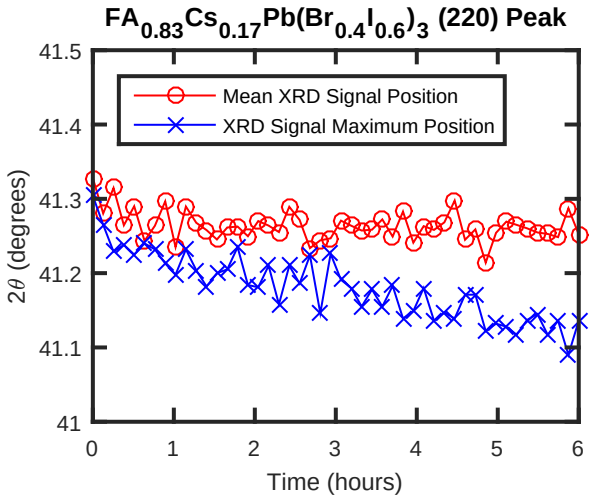

Figure 6.16: The mean position (red) and the position of the maximum signal (blue) of the (220) diffraction peak of a PMMA-coated $FA_{0.83}Cs_{0.17}Pb(Br_{0.4}I_{0.6})_3$ perovskite film under 190 mW cm^{-2} intensity illumination over the course of 6 h – see Figures 6.3d and 6.4 for XRD data of this peak.

6.4.2.4 Ion Dynamics in $FA_{0.83}Cs_{0.17}Pb(Br_{0.4}I_{0.6})_3$

To elucidate the specific ionic rearrangement occurring in $FA_{0.83}Cs_{0.17}Pb(Br_{0.4}I_{0.6})_3$ under illumination, the reasons for the growth of signal in the high-angle (high-bromide) tail of the (220) XRD peak – evident in Figure 6.3d and highlighted in Figure 6.4 – are first analysed. This increase of XRD diffraction amplitude in the range ~41.5°–42.75° 2θ corresponds to the formation of perovskite material with a range of pseudo-cubic lattice parameters between 5.98 and 6.15 Å. Given the variation of ionic radii in the participating FA, Cs, Br, and I ions, it is of course possible for perovskite regions to be generated with a range of different compositions, yet similar average lattice spacings and hence similar XRD patterns. Given the ionic radii of the constituent elements of the $FA_{0.83}Cs_{0.17}Pb(Br_{0.4}I_{0.6})_3$ perovskite, the emerging phase must be bromide-rich, caesium-rich, or enriched in both bromide and caesium. Considering single-cation perovskites, the 5.98–6.15 Å range of lattice parameters approximately corresponds to perovskite materials such as $FAPb(Br_xI_{(1-x)})_3$ for $0.5 \leq x \leq 1.0$ [43, 238] and $CsPb(Br_xI_{(1-x)})_3$ for $0 \leq x \leq 0.4$ [116]. Therefore, the range of perovskite compositions that could generate the 2θ signal

observed at the highest angles – ∼42.75° – runs from $FAPbBr_3$ to $CsPb(Br_{0.4}I_{0.6})_3$. The bandgap values reported in the literature for both $FAPbBr_3$ and $CsPb(Br_{0.4}I_{0.6})_3$ perovskites – approximately 2.3 eV [43, 238] and 1.9 eV [116], respectively – are larger than that of the $FA_{0.83}Cs_{0.17}Pb(Br_{0.4}I_{0.6})_3$ perovskite material used in this study, which has an initial PL peak position of ∼1.76 eV, as shown in Figure 6.3b. Additionally, the bandgap of FA/Cs-based perovskites is observed to vary monotonically with Cs content [66], and similarly the bandgap of Br/I-based perovskites is observed to vary monotonically with bromide content [17, 65, 66, 116]. Due to the monotonic effect of composition on the bandgap in these particular perovskite systems, the formation of either a higher-bandgap $FAPbBr_3$-rich phase or a higher-bandgap $CsPb(Br_{0.4}I_{0.6})_3$-rich phase – or, in principle, a phase enriched with a blend of these compositions – would likely enrich the remaining, majority-volume phase with an ionic composition that would result in a lower-bandgap material. Photoexcited charge carriers would then funnel into the lower energy states of the majority-volume perovskite phase, resulting in red-shifted PL emission. The PL signal associated with the majority-volume $FA_{0.83}Cs_{0.17}Pb(Br_{0.4}I_{0.6})_3$ perovskite phase did in fact red-shift over the course of the experiment, see Figure 6.15a, consistent with the emergence of any of the aforementioned higher-bandgap phases.

In principle, according to the discussion above, the emerging XRD signal observed at ∼42.75° 2θ in Figure 6.4 could be a 0.83 : 0.17 blend of $FAPbBr_3$ and $CsPb(Br_{0.4}I_{0.6})_3$ perovskites – a phase composition of around $FA_{0.83}Cs_{0.17}Pb(Br_{0.9}I_{0.1})_3$. The formation of a minority-volume $FA_{0.83}Cs_{0.17}Pb(Br_{0.9}I_{0.1})_3$ phase from the $FA_{0.83}Cs_{0.17}Pb(Br_{0.4}I_{0.6})_3$ material would require no A-site cation movement, only halide movement, and represents a strong contender for the XRD signal observed at ∼42.75° 2θ. However there are reasons to doubt $FA_{0.83}Cs_{0.17}Pb(Br_{0.9}I_{0.1})_3$ as a candidate for the emerging XRD signal shown in Figure 6.4. Due to the preferential binding of lead to bromide as compared to iodide [125, 174], it would be unexpected – but would in principle match the XRD data in Figure

6.3d – for the bromide ions in the perovskite material to separate out – forming the high-angle XRD tail – and leave the bulk perovskite enriched in iodide – which would consequently shift to lower 2θ angles. Due to the different strengths of the lead-halide bonds, it would instead be considered more likely for the iodide ions to separate out, leaving a bromide-enriched majority-volume phase – which has been observed previously [17] – or for both iodide-rich and bromide-rich phases to separate out from the mixed perovskite – which was observed for the $MAPb(Br_{0.5}I_{0.5})_3$ thin film in Figure 6.3c. As a result, it is proposed that the more likely explanation for the growth the high-angle XRD tail shown in Figure 6.4 involves the movement of A-site cations – a similar conclusion to that reached in the work of Lin *et al.* on related perovskite materials [193] – although the possibility of a mechanism based purely on halide ion movement is acknowledged.

Therefore, it is suggested that the increase of high-angle XRD diffraction amplitude for $FA_{0.83}Cs_{0.17}Pb(Br_{0.4}I_{0.6})_3$ under illumination may partially derive from the initial de-mixing of A-site cations in the perovskite material. Interestingly, it has previously been shown [117] that $FA_{(1-y)}Cs_yPb(Br_{0.4}I_{0.6})_3$ films only exhibit a stable phase space substantially free from halide segregation for caesium contents y approximately between 0.1 and 0.3. Similarly, $FAPb(Br_xI_{(1-x)})_3$ (y=0) [17, 115] and $CsPb(Br_xI_{(1-x)})_3$ (y=1) [116] perovskites have been found to be highly susceptible to halide segregation. Rehman *et al.* [117] have attributed such effects to a lowering of material crystallinity (as derived from charge-carrier lifetimes and XRD peak widths) outside the range $0.1 < y < 0.3$, which in turn reduces the stability of the perovskite against halide segregation, as expected from the strong correlation between crystallinity and photostability reported in the literature [18, 103] – see Section 2.4.3.1. Therefore, it is proposed that for $FA_{0.83}Cs_{0.17}Pb(Br_{0.4}I_{0.6})_3$, illumination could first result in the formation of a minority FA- or Cs-enriched phase, and the FA- or Cs-depletion of the majority-volume phase, as a result of A-site cation separation. The composition of the majority-volume phase of the perovskite would be

shifted from the maximally stable caesium composition of $y \sim 0.2$, which in turn would reduce the overall stability of the material against halide segregation, hastening the formation of iodide-rich domains that lead to the ultimately observed low-energy PL emission. As such, halide segregation in the FACs A-cation mixed-halide perovskite would therefore proceed via a two-step process initiated by A-cation segregation that ultimately enables halide segregation. This multi-step process appears to be applicable to the whole bulk of the material – rather than to specific volumes of the perovskite – and to present a larger hurdle against halide segregation than that operational in an equivalent MA-based perovskite.

6.5 Summary and Conclusion

In conclusion, by comparing simultaneous, in situ PL and XRD measurements, differences in the halide segregation mechanism between $MAPb(Br_{0.5}I_{0.5})_3$ and $FA_{0.83}Cs_{0.17}Pb(Br_{0.4}I_{0.6})_3$ perovskites have been elucidated. Overall, the different structural and optoelectronic changes observed following illumination of the two types of mixed-halide perovskite explain some of the strong variations in phase stability for different mixed-halide perovskites reported in the literature [18]. For $MAPb(Br_{0.5}I_{0.5})_3$, it is concluded that the presence of fast ionic pathways initially results in facile halide segregation in specific, sub-volumes of material under illumination, with the remaining volume of bulk phase maintaining its original mixed-halide composition. Such specific, halide-segregated volumes ultimately grow at the expense of the well-mixed bulk phase as halide segregation proceeds, for example by expanding away from grain boundaries further into the bulk, or by the fracturing of crystalline domains which enlarges the interface areas with crystalline imperfections. In contrast, $FA_{0.83}Cs_{0.17}Pb(Br_{0.4}I_{0.6})_3$ exhibits large, concurrent changes occurring across the whole bulk material, but only after a much longer illumination period of comparable intensity. In particular, the change in shape

and peak position of the main (220) XRD diffraction peak of $FA_{0.83}Cs_{0.17}Pb(Br_{0.4}I_{0.6})_3$ indicate concurrent ionic rearrangement throughout the whole of the perovskite volume, i.e. unlike in the $MAPb(Br_{0.5}I_{0.5})_3$ perovskite, there appear to be few fast ionic pathways that facilitate halide segregation in localised regions. The lack of such fast ionic pathways in $FA_{0.83}Cs_{0.17}Pb(Br_{0.4}I_{0.6})_3$ means that any phase segregation must instead occur across the whole of the more resistant bulk perovskite material, raising hurdles to these effects. Such absence of ionic pathways is likely caused by the $FA_{0.83}Cs_{0.17}Pb(Br_{0.4}I_{0.6})_3$ material possessing superior crystallinity properties over the $MAPb(Br_{0.5}I_{0.5})_3$ perovskite. For materials such as $FA_{0.83}Cs_{0.17}Pb(Br_{0.4}I_{0.6})_3$, their mixed A-cation nature, while allowing for high crystallinity that suppresses halide segregation in the first instance, may ultimately still be their Achilles' heel, given that A-cation segregation may subsequently trigger halide segregation in turn. For such materials, further stabilisation against halide segregation may thus result if processing protocols can be developed that further stabilise A-cation mixing. In addition, it is noted that other factors may also contribute to the different timescales required to induce halide segregation in $MAPb(Br_{0.5}I_{0.5})_3$ and $FA_{0.83}Cs_{0.17}Pb(Br_{0.4}I_{0.6})_3$ thin films, such as trap state density [150] – see the work of Chapter 4. However, it is concluded that the ionic pathways available in a perovskite material are a key indicator of stability against halide segregation. The results presented in this chapter therefore also highlight the importance of bulk-sensitive measurements in determining the susceptibility of a mixed-halide perovskite to halide segregation, and indicate that ionic mobilities, grain boundaries, and crystallinity are key areas of research if completely phase-stable materials are to be manufactured for photovoltaic applications.

7

Conclusion

This thesis has dealt almost exclusively with the problem of halide segregation in mixed-halide perovskite materials under illumination, and a broad understanding of the underlying dependencies, effects, and corresponding charge-carrier and ionic behaviours related to this problem has been found. An understanding of this phase-instability problem is essential for the manufacture of stable, long-lived perovskite photovoltaic devices, and in particular for perovskite-perovskite [72–76] and perovskite-silicon [8, 9, 66] tandem solar cells, which often utilise halide contents particularly susceptible to these segregation effects.

Chapter 4 began with an exploration of the impact of different atmospheres on the halide segregation dynamics in $MAPb(Br_{0.5}I_{0.5})_3$ thin films [150]. The photoluminescence from the perovskite was found to be strongly influenced by the atmospheric environment, and that encapsulation of perovskite films with a layer of poly(methyl methacrylate) allowed for the halide segregation dynamics to be made fully reversible and repeatable. A coating of poly(methyl methacrylate) was applied to all thin film samples investigated in this thesis, where possible, as a result of this finding. Next, through photoluminescence measurements at different illumination intensities but at fixed total incident photon count, an empirical model was established that directly links the amount of halide segregation

observed in the photoluminescence to the fraction of charge carriers recombining through trap-mediated channels, and the photon flux absorbed. From such quantitative analysis the effect of pulsed illumination on the halide segregation dynamics was predicted and shown to match well with results in the literature [185]. Finally, it was extrapolated from the empirical model that working $MAPb(Br_{0.5}I_{0.5})_3$ perovskite solar cells would require a reduction of the trap-related charge carrier recombination rate to $\lesssim 10^5\,s^{-1}$ in order for halide segregation to be sufficiently suppressed.

Chapter 5 utilised photoluminescence techniques to study trap states and halide segregation in full mixed-halide $MAPb(Br_{0.5}I_{0.5})_3$ photovoltaic devices [157]. Through this study, three distinct defect species were identified in the perovskite material: First, a charged, mobile defect was observed to trap charge-carriers in the perovskite, affecting the radiatitve efficiency of the material. Due to the relatively slow speed of the changes attributed to these defects, it was proposed that these defects are MA^+ interstitials. Second, continuing the work of Chapter 4, it was concluded that a charge neutral defect species is responsible for halide segregation. These charge neutral defects were proposed to consist of crystal distortions in the perovskite material, possibly primarily located at grain boundaries. Finally, a charged, mobile defect was found to screen the perovskite from external electric fields over relatively short timescales. Due to the speed of the screening effect, these defects were proposed to be halide vacancies and/or interstitials, which are expected to be the most mobile species in a perovskite material [36]. Additionally, external quantum efficiency measurements showed that photoexcited charge carriers can be extracted from the iodide-rich low-bandgap regions of the phase-segregated perovskite formed under illumination, suggesting the existence of charge-carrier percolation pathways through grain boundaries where phase-segregation may occur. A Sankey flow diagram was presented to summarise the findings of Chapters 4 and 5 on the charge-carrier pathways in mixed-halide perovskite materials.

With the relation between charge-carrier dynamics and halide segregation investigated in Chapters 4 and 5, Chapter 6 granted a broader perspective of the halide segregation mechanism by investigating the role of stoichiometry, and the compositional inhomogeneities that are induced in a perovskite material as a result of halide segregation [231]. This study utilised a home-built experimental setup, allowing combined, in situ photoluminescence and X-ray diffraction measurements to be taken. Such measurements were used to elucidate the compositional and optoelectronic changes associated with halide segregation in $MAPb(Br_{0.5}I_{0.5})_3$ and $FA_{0.83}Cs_{0.17}Pb(Br_{0.4}I_{0.6})_3$ films. Low-barrier ionic pathways were found in $MAPb(Br_{0.5}I_{0.5})_3$, which allow for the rearrangement of halide ions in localised volumes of perovskite without significant compositional changes to the bulk material. In contrast, $FA_{0.83}Cs_{0.17}Pb(Br_{0.4}I_{0.6})_3$ was found to lack such low-barrier ionic pathways, and as such is consequently much more stable against halide segregation. However, under prolonged illumination, $FA_{0.83}Cs_{0.17}Pb(Br_{0.4}I_{0.6})_3$ was found to exhibit considerable ionic rearrangement throughout the bulk material, which may be triggered by an initial de-mixing of A-site cations, altering the composition of the bulk perovskite and reducing its stability against halide segregation.

As a whole, this thesis presents a comprehensive picture of the halide segregation phenomenon. The driving force for the halide ion movement is generated by the separation of excited charge carriers. In particular, under illumination crystal distortions at grain boundaries generate charge neutral trap states that are able to capture and localise excited electrons. Excited holes are localised within nascent iodide-rich domains away from the grain boundaries, a process which, in conjunction with the trapped electrons, generates an electric potential landscape within the grain. Due to the differing mobilities of the halide ion species within the perovskite, the ions are affected differently by the electric fields and separate. In perovskite materials dense with grain boundaries, halide ions around these boundaries are able to move more freely and rapidly, resulting in a growing region

of segregated material around the grain boundaries, and shrinking regions of well-mixed material in the grain centres. In more crystalline perovskite materials, halide ion movement is more difficult, and so the segregation process takes place over much longer timescales, but throughout the perovskite material simultaneously. Charge carriers funnel into the formed regions of low-bandgap material, which then radiate more efficiently and increase the recombination rate within the material. Some charge carriers that do not recombine can be extracted through percolation pathways which exist along and around the grain boundaries and the surrounding low-bandgap material. Under darkness, the driving force for segregation is removed, and entropic factors ensure the halide ions eventually re-mix.

As an outlook to future work, the results of this thesis reveal many important insights into the halide segregation mechanism, and highlight key areas, and key questions, for further study. Chapters 4 and 5 showed that charge-carrier dynamics and trap states have an important role in the segregation mechanism, and while crystal defects at grain boundaries were suggested to contribute to the halide segregation mechanism, further investigations into the identity of, and the mechanisms by which, any trap states may contribute to halide segregation would be highly beneficial. Additionally, charge-carrier transport layers are integral to the performance of photovoltaic devices, and so investigating the role of trap states introduced at the perovskite interfaces in full device stacks on the halide segregation mechanism is highly relevant for operational perovskite solar cells. The empirical model of halide segregation formulated in Chapter 4 paves the way for a more complete model that accounts for several effects, such as temperature and the competition between halide segregation and entropic remixing dynamics, that were not within the scope of the original investigation. Chapter 6 highlighted grain boundaries and halide ion pathways to be integral to halide segregation, and further work could build upon this thesis by investigating the effect of reducing halide ion mobility along grain boundaries, either through the judicious choice of additives or other means, on the halide

segregation mechanism. Again, charge-carrier transport layers could influence the halide segregation mechanism by introducing halide ion pathways at the perovskite interface, an important area of investigation for full perovskite solar cells. Finally, there exist many varieties of perovskite that lay beyond the scope of this thesis, and so investigating the compositional stability of such materials as 2D perovskites and double perovskites would constitute very interesting further work.

Overall, the work of this thesis highlights that grain boundaries and trap states are key factors in the halide segregation dynamic, which helps to explain why improved crystallinity [20, 103, 117, 122, 125] and trap state passivation [123, 151, 152, 167–169] improve the phase-stability of perovskite materials. The results presented here suggest a route to phase-stable perovskite solar cells through the further investigation of these key factors, and this work makes great strides towards a complete understanding of the intriguing phenomenon of halide segregation.

References

[1] Pachauri, R. K.; Allen, M. R.; Barros, V. R.; Broome, J.; Cramer, W.; Christ, R.; Church, J. A.; Clarke, L.; Dahe, Q.; Dasgupta, P. *et al. Climate Change 2014: Synthesis Report. Contribution of Working Groups I, II and III to the Fifth Assessment Report of the Intergovernmental Panel on Climate Change*. Ipcc, 2014.

[2] Ripple, W.; Wolf, C.; Newsome, T.; Barnard, P.; Moomaw, W. and Grandcolas, P. 'World Scientists' Warning of a Climate Emergency'. *BioScience*, 2019.

[3] Pirani, S. *Burning Up: A Global History of Fossil Fuel Consumption*. Pluto Press, 2018.

[4] Correa-Baena, J.-P.; Abate, A.; Saliba, M.; Tress, W.; Jacobsson, T. J.; Grätzel, M. and Hagfeldt, A. 'The Rapid Evolution of Highly Efficient Perovskite Solar Cells'. *Energy Environ. Sci.*, 2017, **10**, 710–727.

[5] Jena, A. K.; Kulkarni, A. and Miyasaka, T. 'Halide Perovskite Photovoltaics: Background, Status, and Future Prospects'. *Chem. Rev.*, 2019, **119**, 3036–3103.

[6] Snaith, H. J. 'Present Status and Future Prospects of Perovskite Photovoltaics'. *Nat. Mater.*, 2018, **17**, 372.

[7] The National Renewable Energy Laboratory. *Best Research-Cell Efficiencies*. [Online; accessed 16-February-2021]. 2020. https://www.nrel.gov/pv/assets/pdfs/best-research-cell-efficiencies.20200104.pdf.

[8] Bush, K. A.; Palmstrom, A. F.; Zhengshan, J. Y.; Boccard, M.; Cheacharoen, R.; Mailoa, J. P.; McMeekin, D. P.; Hoye, R. L.; Bailie, C. D.; Leijtens, T. *et al.* '23.6%-Efficient Monolithic Perovskite/Silicon Tandem Solar Cells with Improved Stability'. *Nat. Energy*, 2017, **2**, 17009.

[9] Duong, T.; Wu, Y.; Shen, H.; Peng, J.; Fu, X.; Jacobs, D.; Wang, E.-C.; Kho, T. C.; Fong, K. C.; Stocks, M. *et al.* 'Rubidium Multication Perovskite with Optimized Bandgap for Perovskite-Silicon Tandem with over 26% Efficiency'. *Adv. Energy Mater.*, 2017, **7**, 1700228.

[10] Werner, J.; Niesen, B. and Ballif, C. 'Perovskite/Silicon Tandem Solar Cells: Marriage of Convenience or True Love Story? – An Overview'. *Adv. Mater. Interfaces*, 2018, **5**, 1700731.

[11] Godding, J. S. W.; Ramadan, A. J.; Lin, Y.-H.; Schutt, K.; Snaith, H. J. and Wenger, B. 'Oxidative Passivation of Metal Halide Perovskites'. *Joule*, 2019, **3**, 2716–2731.

[12] Aristidou, N.; Sanchez-Molina, I.; Chotchuangchutchaval, T.; Brown, M.; Martinez, L.; Rath, T. and Haque, S. A. 'The Role of Oxygen in the Degradation of Methylammonium Lead Trihalide Perovskite Photoactive Layers'. *Angew. Chem. Int. Ed.*, 2015, **54**, 8208–8212.

[13] Aristidou, N.; Eames, C.; Sanchez-Molina, I.; Bu, X.; Kosco, J.; Islam, M. S. and Haque, S. A. 'Fast Oxygen Diffusion and Iodide Defects Mediate Oxygen-Induced Degradation of Perovskite Solar Cells'. *Nat. Commun.*, 2017, **8**, 15218.

[14] Huang, J.; Tan, S.; Lund, P. D. and Zhou, H. 'Impact of H_2O on Organic–Inorganic Hybrid Perovskite Solar Cells'. *Energy Environ. Sci.*, 2017, **10**, 2284–2311.

[15] Yang, J.; Siempelkamp, B. D.; Liu, D. and Kelly, T. L. 'Investigation of $CH_3NH_3PbI_3$ Degradation Rates and Mechanisms in Controlled Humidity Environments Using In Situ Techniques'. *ACS Nano*, 2015, **9**, 1955–1963.

[16] Tong, C.-J.; Geng, W.; Tang, Z.-K.; Yam, C.-Y.; Fan, X.-L.; Liu, J.; Lau, W.-M. and Liu, L.-M. 'Uncovering the Veil of the Degradation in Perovskite $CH_3NH_3PbI_3$ upon Humidity Exposure: a First-Principles Study'. *J. Phys. Chem. Lett.*, 2015, **6**, 3289–3295.

[17] Hoke, E. T.; Slotcavage, D. J.; Dohner, E. R.; Bowring, A. R.; Karunadasa, H. I. and McGehee, M. D. 'Reversible Photo-Induced Trap Formation in Mixed-Halide Hybrid Perovskites for Photovoltaics'. *Chem. Sci.*, 2015, **6**, 613–617.

[18] Knight, A. and Herz, L. M. 'Preventing Phase Segregation in Mixed-Halide Perovskites: A Perspective'. *Energy Environ. Sci.*, 2020, **13**, 2024–2046.

[19] Brennan, M. C.; Ruth, A.; Kamat, P. V. and Kuno, M. 'Photoinduced Anion Segregation in Mixed Halide Perovskites'. *Trends Chem.*, 2020, **2**, 282–301.

[20] Braly, I. L.; Stoddard, R. J.; Rajagopal, A.; Uhl, A. R.; Katahara, J. K.; Jen, A. K.-Y. and Hillhouse, H. W. 'Current-Induced Phase Segregation in Mixed Halide Hybrid Perovskites and its Impact on Two-Terminal Tandem Solar Cell Design'. *ACS Energy Lett.*, 2017, **2**, 1841–1847.

[21] Duong, T.; Mulmudi, H. K.; Wu, Y.; Fu, X.; Shen, H.; Peng, J.; Wu, N.; Nguyen, H. T.; Macdonald, D.; Lockrey, M. *et al.* 'Light and Electrically Induced Phase Segregation and Its Impact on the Stability of Quadruple Cation High Bandgap Perovskite Solar Cells'. *ACS Appl. Mater. Interfaces*, 2017, **9**, 26859–26866.

[22] Mahesh, S.; Ball, J. M.; Oliver, R. D.; McMeekin, D. P.; Nayak, P.; Johnston, M. B. and Snaith, H. 'Revealing the Origin of Voltage Loss in Mixed-Halide Perovskite Solar Cells'. *Energy Environ. Sci.*, 2020, **13**, 258–267.

[23] Samu, G. F.; Janáky, C. and Kamat, P. V. 'A Victim of Halide Ion Segregation. How Light Soaking Affects Solar Cell Performance of Mixed Halide Lead Perovskites'. *ACS Energy Lett.*, 2017, **2**, 1860–1861.

[24] Brenes, R.; Eames, C.; Bulović, V.; Islam, M. S. and Stranks, S. D. 'The Impact of Atmosphere on the Local Luminescence Properties of Metal Halide Perovskite Grains'. *Adv. Mater.*, 2018, **30**, 1706208.

[25] Tian, Y.; Peter, M.; Unger, E.; Abdellah, M.; Zheng, K.; Pullerits, T.; Yartsev, A.; Sundström, V. and Scheblykin, I. G. 'Mechanistic Insights into Perovskite Photoluminescence Enhancement: Light Curing with Oxygen can Boost Yield Thousandfold'. *Phys. Chem. Chem. Phys.*, 2015, **17**, 24978–24987.

[26] Feng, X.; Su, H.; Wu, Y.; Wu, H.; Xie, J.; Liu, X.; Fan, J.; Dai, J. and He, Z. 'Photon-Generated Carriers Excite Superoxide Species Inducing Long-Term Photoluminescence Enhancement of $MAPbI_3$ Perovskite Single Crystals'. *J. Mater. Chem. A*, 2017, **5**, 12048–12053.

[27] Galisteo-López, J. F.; Anaya, M; Calvo, M. and Míguez, H. 'Environmental Effects on the Photophysics of Organic–Inorganic Halide Perovskites'. *J. Phys. Chem. Lett.*, 2015, **6**, 2200–2205.

[28] Brenes, R.; Guo, D.; Osherov, A.; Noel, N. K.; Eames, C.; Hutter, E. M.; Pathak, S. K.; Niroui, F.; Friend, R. H.; Islam, M. S. *et al.* 'Metal Halide Perovskite Polycrystalline Films Exhibiting Properties of Single Crystals'. *Joule*, 2017, **1**, 155–167.

[29] Quitsch, W.-A.; deQuilettes, D. W.; Pfingsten, O.; Schmitz, A.; Ognjanovic, S. M.; Jariwala, S.; Koch, S.; Winterer, M.; Ginger, D. S. and Bacher, G. 'The Role of Excitation Energy in Photobrightening and Photodegradation of Halide Perovskite Thin Films'. *J. Phys. Chem. Lett.*, 2018, **9**, 2062–2069.

[30] Kheraj, V.; Simonds, B. J.; Toshniwal, A.; Misra, S.; Peroncik, P.; Zhang, C; Vardeny, Z. and Scarpulla, M. A. 'Using Photoluminescence to Monitor the Optoelectronic Properties of Methylammonium Lead Halide Perovskites in Light and Dark over Periods of Days'. *J. Lumin.*, 2018, **194**, 353–358.

[31] Fang, H.-H.; Adjokatse, S.; Wei, H.; Yang, J.; Blake, G. R.; Huang, J.; Even, J. and Loi, M. A. 'Ultrahigh Sensitivity of Methylammonium Lead Tribromide Perovskite Single Crystals to Environmental Gases'. *Sci. Adv.*, 2016, **2**, e1600534.

[32] Motti, S. G.; Gandini, M.; Barker, A. J.; Ball, J. M.; Srimath Kandada, A. R. and Petrozza, A. 'Photoinduced Emissive Trap States in Lead Halide Perovskite Semiconductors'. *ACS Energy Lett.*, 2016, **1**, 726–730.

[33] Wojciechowski, K.; Forgács, D. and Rivera, T. 'Industrial Opportunities and Challenges for Perovskite Photovoltaic Technology'. *Sol. RRL*, 2019, **3**, 1900144.

[34] Van Le, Q.; Jang, H. W. and Kim, S. Y. 'Recent Advances Toward High-Efficiency Halide Perovskite Light-Emitting Diodes: Review and Perspective'. *Small Methods*, 2018, **2**, 1700419.

[35] Quan, L. N.; Arquer, F. P. García de; Sabatini, R. P. and Sargent, E. H. 'Perovskites for Light Emission'. *Adv. Mater.*, 2018, **30**, 1801996.

[36] Eames, C.; Frost, J. M.; Barnes, P. R.; O'regan, B. C.; Walsh, A. and Islam, M. S. 'Ionic Transport in Hybrid Lead Iodide Perovskite Solar Cells'. *Nat. Commun.*, 2015, **6**, 7497.

[37] Ball, J. M.; Lee, M. M.; Hey, A. and Snaith, H. J. 'Low-Temperature Processed Meso-Superstructured to Thin-Film Perovskite Solar Cells'. *Energy Environ. Sci.*, 2013, **6**, 1739–1743.

[38] You, J.; Hong, Z.; Yang, Y.; Chen, Q.; Cai, M.; Song, T.-B.; Chen, C.-C.; Lu, S.; Liu, Y.; Zhou, H. *et al.* 'Low-Temperature Solution-Processed Perovskite Solar Cells with High Efficiency and Flexibility'. *ACS Nano*, 2014, **8**, 1674–1680.

[39] Nie, W.; Blancon, J.-C.; Neukirch, A. J.; Appavoo, K.; Tsai, H.; Chhowalla, M.; Alam, M. A.; Sfeir, M. Y.; Katan, C.; Even, J. *et al.* 'Light-Activated Photocurrent Degradation and Self-Healing in Perovskite Solar Cells'. *Nat. Commun.*, 2016, **7**, 1–9.

[40] Zhao, Y.; Wei, J.; Li, H.; Yan, Y.; Zhou, W.; Yu, D. and Zhao, Q. 'A Polymer Scaffold for Self-Healing Perovskite Solar Cells'. *Nat. Commun.*, 2016, **7**, 1–9.

[41] Ceratti, D. R.; Rakita, Y.; Cremonesi, L.; Tenne, R.; Kalchenko, V.; Elbaum, M.; Oron, D.; Potenza, M. A. C.; Hodes, G. and Cahen, D. 'Self-Healing Inside $APbBr_3$ Halide Perovskite Crystals'. *Adv. Mater.*, 2018, **30**, 1706273.

[42] Rakita, Y.; Lubomirsky, I. and Cahen, D. 'When Defects Become 'Dynamic': Halide Perovskites: A New Window on Materials?' *Mater. Horizons*, 2019, **6**, 1297–1305.

[43] Jacobsson, T. J.; Correa-Baena, J.-P.; Pazoki, M.; Saliba, M.; Schenk, K.; Grätzel, M. and Hagfeldt, A. 'Exploration of the Compositional Space for Mixed Lead Halogen Perovskites for High Efficiency Solar Cells'. *Energy Enviro. Sci.*, 2016, **9**, 1706–1724.

[44] Grancini, G.; Roldán-Carmona, C; Zimmermann, I.; Mosconi, E; Lee, X; Martineau, D; Narbey, S; Oswald, F.; De Angelis, F; Graetzel, M. *et al.* 'One-Year Stable Perovskite Solar Cells by 2D/3D Interface Engineering'. *Nat. Commun.*, 2017, **8**, 1–8.

[45] Poorkazem, K. and Kelly, T. L. 'Compositional Engineering to Improve the Stability of Lead Halide Perovskites: A Comparative Study of Cationic and Anionic Dopants'. *ACS Applied Energy Materials*, 2017, **1**, 181–190.

[46] Uddin, A.; Upama, M. B.; Yi, H. and Duan, L. 'Encapsulation of Organic and Perovskite Solar Cells: A Review'. *Coatings*, 2019, **9**, 65.

[47] Wang, R.; Mujahid, M.; Duan, Y.; Wang, Z.-K.; Xue, J. and Yang, Y. 'A Review of Perovskites Solar Cell Stability'. *Adv. Funct. Mater.*, 2019, **29**, 1808843.

[48] Nelson, J. *The Physics of Solar Cells*. Imperial College Press, 2003.

[49] Einstein, A. 'Zur Quantentheorie der Strahlung'. *Phys. Z.*, 1917, **18**, 121–128.

[50] Shockley, W. and Read Jr, W. 'Statistics of the Recombinations of Holes and Electrons'. *Phys. Rev.*, 1952, **87**, 835.

[51] Hall, R. N. 'Electron-Hole Recombination in Germanium'. *Phys. Rev.*, 1952, **87**, 387.

[52] Crothers, T. W.; Milot, R. L.; Patel, J. B.; Parrott, E. S.; Schlipf, J.; Müller-Buschbaum, P.; Johnston, M. B. and Herz, L. M. 'Photon Reabsorption Masks Intrinsic Bimolecular Charge-Carrier Recombination in $CH_3NH_3PbI_3$ Perovskite'. *Nano Lett.*, 2017, **17**, 5782–5789.

[53] Baikie, T.; Fang, Y.; Kadro, J. M.; Schreyer, M.; Wei, F.; Mhaisalkar, S. G.; Graetzel, M. and White, T. J. 'Synthesis and Crystal Chemistry of the Hybrid Perovskite $(CH_3NH_3)PbI_3$ for Solid-State Sensitised Solar Cell Applications'. *J. Mater. Chem. A*, 2013, **1**, 5628–5641.

[54] Green, M. A.; Ho-Baillie, A. and Snaith, H. J. 'The Emergence of Perovskite Solar Cells'. *Nat. Photonics*, 2014, **8**, 506–514.

[55] Leijtens, T.; Eperon, G. E.; Noel, N. K.; Habisreutinger, S. N.; Petrozza, A. and Snaith, H. J. 'Stability of Metal Halide Perovskite Solar Cells'. *Adv. Energy Mater.*, 2015, **5**, 1500963.

[56] Chen, Y.; Sun, Y.; Peng, J.; Tang, J.; Zheng, K. and Liang, Z. '2D Ruddlesden–Popper Perovskites for Optoelectronics'. *Adv. Mater.*, 2018, **30**, 1703487.

[57] Zhou, C.; Lin, H.; He, Q.; Xu, L.; Worku, M.; Chaaban, M.; Lee, S.; Shi, X.; Du, M.-H. and Ma, B. 'Low Dimensional Metal Halide Perovskites and Hybrids'. *Mater. Sci. Eng. R Rep.*, 2019, **137**, 38–65.

[58] Wang, B.; Xiao, X. and Chen, T. 'Perovskite Photovoltaics: A High-Efficiency Newcomer to the Solar Cell Family'. *Nanoscale*, 2014, **6**, 12287–12297.

[59] Konstantakou, M. and Stergiopoulos, T. 'A Critical Review on Tin Halide Perovskite Solar Cells'. *J. Mater. Chem. A*, 2017, **5**, 11518–11549.

[60] Zarick, H. F.; Soetan, N.; Erwin, W. R. and Bardhan, R. 'Mixed Halide Hybrid Perovskites: A Paradigm Shift in Photovoltaics'. *J. Mater. Chem. A*, 2018, **6**, 5507–5537.

[61] Johnston, M. B. and Herz, L. M. 'Hybrid Perovskites for Photovoltaics: Charge-Carrier Recombination, Diffusion, and Radiative Efficiencies'. *Acc. Chem. Res.*, 2015, **49**, 146–154.

[62] Walsh, A. 'Principles of Chemical Bonding and Band Gap Engineering in Hybrid Organic–Inorganic Halide Perovskites'. *J. Phys. Chem. C*, 2015, **119**, 5755–5760.

[63] Hao, F.; Stoumpos, C. C.; Chang, R. P. and Kanatzidis, M. G. 'Anomalous Band Gap Behavior in Mixed Sn and Pb Perovskites Enables Broadening of Absorption Spectrum in Solar Cells'. *J. Am. Chem. Soc.*, 2014, **136**, 8094–8099.

[64] Parrott, E. S.; Green, T.; Milot, R. L.; Johnston, M. B.; Snaith, H. J. and Herz, L. M. 'Interplay of Structural and Optoelectronic Properties in Formamidinium Mixed Tin–Lead Triiodide Perovskites'. *Adv. Funct. Mater.*, 2018, **28**, 1802803.

[65] Noh, J. H.; Im, S. H.; Heo, J. H.; Mandal, T. N. and Seok, S. I. 'Chemical Management for Colorful, Efficient, and Stable Inorganic–Organic Hybrid Nanostructured Solar Cells'. *Nano Lett.*, 2013, **13**, 1764–1769.

[66] McMeekin, D. P.; Sadoughi, G.; Rehman, W.; Eperon, G. E.; Saliba, M.; Hörantner, M. T.; Haghighirad, A.; Sakai, N.; Korte, L.; Rech, B. *et al.* 'A Mixed-Cation Lead Mixed-Halide Perovskite Absorber for Tandem Solar Cells'. *Science*, 2016, **351**, 151–155.

[67] Qiu, W.; Xiao, Z.; Roh, K.; Noel, N. K.; Shapiro, A.; Heremans, P. and Rand, B. P. 'Mixed Lead–Tin Halide Perovskites for Efficient and Wavelength-Tunable Near-Infrared Light-Emitting Diodes'. *Adv. Mater.*, 2019, **31**, 1806105.

[68] Sadhanala, A.; Ahmad, S.; Zhao, B.; Giesbrecht, N.; Pearce, P. M.; Deschler, F.; Hoye, R. L.; Gödel, K. C.; Bein, T.; Docampo, P. *et al.* 'Blue-Green Color Tunable Solution Processable Organolead Chloride–Bromide Mixed Halide Perovskites for Optoelectronic Applications'. *Nano Lett.*, 2015, **15**, 6095–6101.

[69] Liashenko, T. G.; Cherotchenko, E. D.; Pushkarev, A. P.; Pakštas, V.; Naujokaitis, A.; Khubezhov, S. A.; Polozkov, R. G.; Agapev, K. B.; Zakhidov, A. A.; Shelykh, I. A. *et al.* 'Electronic Structure of $CsPbBr_{3-x}Cl_x$ Perovskites: Synthesis, Experimental Characterization, and DFT Simulations'. *Phys. Chem. Chem. Phys.*, 2019, **21**, 18930–18938.

[70] Protesescu, L.; Yakunin, S.; Bodnarchuk, M. I.; Krieg, F.; Caputo, R.; Hendon, C. H.; Yang, R. X.; Walsh, A. and Kovalenko, M. V. 'Nanocrystals of Cesium Lead Halide Perovskites ($CsPbX_3$, X= Cl, Br, and I): Novel Optoelectronic Materials Showing Bright Emission with Wide Color Gamut'. *Nano Lett.*, 2015, **15**, 3692–3696.

[71] Eperon, G. E.; Hörantner, M. T. and Snaith, H. J. 'Metal Halide Perovskite Tandem and Multiple-Junction Photovoltaics'. *Nat. Rev. Chem.*, 2017, **1**, 1–18.

[72] McMeekin, D. P.; Mahesh, S.; Noel, N. K.; Klug, M. T.; Lim, J.; Warby, J. H.; Ball, J. M.; Herz, L. M.; Johnston, M. B. and Snaith, H. J. 'Solution-Processed All-Perovskite Multi-Junction Solar Cells'. *Joule*, 2019, **3**, 387–401.

[73] Eperon, G. E.; Leijtens, T.; Bush, K. A.; Prasanna, R.; Green, T.; Wang, J. T.-W.; McMeekin, D. P.; Volonakis, G.; Milot, R. L.; May, R. *et al.* 'Perovskite-Perovskite Tandem Photovoltaics with Optimized Band Gaps'. *Science*, 2016, **354**, 861–865.

[74] Rajagopal, A.; Yang, Z.; Jo, S. B.; Braly, I. L.; Liang, P.-W.; Hillhouse, H. W. and Jen, A. K.-Y. 'Highly Efficient Perovskite–Perovskite Tandem Solar Cells Reaching 80% of the Theoretical Limit in Photovoltage'. *Adv. Mater.*, 2017, **29**, 1702140.

[75] Forgács, D.; Gil-Escrig, L.; Pérez-Del-Rey, D.; Momblona, C.; Werner, J.; Niesen, B.; Ballif, C.; Sessolo, M. and Bolink, H. J. 'Efficient Monolithic Perovskite/Perovskite Tandem Solar Cells'. *Adv. Energy Mater.*, 2017, **7**, 1602121.

[76] Lin, R.; Xiao, K.; Qin, Z.; Han, Q.; Zhang, C.; Wei, M.; Saidaminov, M. I.; Gao, Y.; Xu, J.; Xiao, M. *et al.* 'Monolithic All-Perovskite Tandem Solar Cells with 24.8% Efficiency Exploiting Comproportionation to Suppress Sn (II) Oxidation in Precursor Ink'. *Nat. Energy*, 2019, **4**, 864–873.

[77] Hörantner, M. T. and Snaith, H. J. 'Predicting and Optimising the Energy Yield of Perovskite-on-Silicon Tandem Solar Cells Under Real World Conditions'. *Energy Environ. Sci.*, 2017, **10**, 1983–1993.

[78] Li, G.; Rivarola, F. W. R.; Davis, N. J.; Bai, S.; Jellicoe, T. C.; Peña, F. de la; Hou, S.; Ducati, C.; Gao, F.; Friend, R. H. *et al.* 'Highly Efficient Perovskite Nanocrystal Light-Emitting Diodes Enabled by a Universal Crosslinking Method'. *Adv. Mater.*, 2016, **28**, 3528–3534.

[79] Vashishtha, P. and Halpert, J. E. 'Field-Driven Ion Migration and Color Instability in Red-Emitting Mixed Halide Perovskite Nanocrystal Light-Emitting Diodes'. *Chem. Mater.*, 2017, **29**, 5965–5973.

[80] Shynkarenko, Y.; Bodnarchuk, M. I.; Bernasconi, C.; Berezovska, Y.; Verteletskyi, V.; Ochsenbein, S. and Kovalenko, M. V. 'Direct Synthesis of Quaternary Alkylammonium Capped Perovskite Nanocrystals for Efficient Blue and Green Light-Emitting Diodes'. *ACS Energy Lett.*, 2019, **4**, 2703–2711.

[81] Nedelcu, G.; Protesescu, L.; Yakunin, S.; Bodnarchuk, M. I.; Grotevent, M. J. and Kovalenko, M. V. 'Fast Anion-Exchange in Highly Luminescent Nanocrystals of Cesium Lead Halide Perovskites ($CsPbX_3$, X= Cl, Br, I)'. *Nano Lett.*, 2015, **15**, 5635–5640.

[82] Li, G.; Price, M. and Deschler, F. 'Research Update: Challenges for High-Efficiency Hybrid Lead-Halide Perovskite LEDs and the Path Towards Electrically Pumped Lasing'. *APL Mater.*, 2016, **4**, 091507.

[83] Wehrenfennig, C.; Eperon, G. E.; Johnston, M. B.; Snaith, H. J. and Herz, L. M. 'High Charge Carrier Mobilities and Lifetimes in Organolead Trihalide Perovskites'. *Adv. Mater.*, 2014, **26**, 1584–1589.

[84] Stranks, S. D. 'Nonradiative Losses in Metal Halide Perovskites'. *ACS Energy Lett.*, 2017, **2**, 1515–1525.

[85] Ball, J. M. and Petrozza, A. 'Defects in Perovskite-Halides and Their Effects in Solar Cells'. *Nat. Energy*, 2016, **1**, 16149.

[86] Stranks, S. D.; Eperon, G. E.; Grancini, G.; Menelaou, C.; Alcocer, M. J.; Leijtens, T.; Herz, L. M.; Petrozza, A. and Snaith, H. J. 'Electron-Hole Diffusion Lengths Exceeding 1 Micrometer in an Organometal Trihalide Perovskite Absorber'. *Science*, 2013, **342**, 341–344.

[87] Xiao, Z.; Dong, Q.; Bi, C.; Shao, Y.; Yuan, Y. and Huang, J. 'Solvent Annealing of Perovskite-Induced Crystal Growth for Photovoltaic-Device Efficiency Enhancement'. *Adv. Mater.*, 2014, **26**, 6503–6509.

[88] Filip, M. R.; Verdi, C. and Giustino, F. 'GW Band Structures and Carrier Effective Masses of $CH_3NH_3PbI_3$ and Hypothetical Perovskites of the Type $APbI_3$: A= NH_4, PH_4, AsH_4, and SbH_4'. *J. Phys. Chem. C*, 2015, **119**, 25209–25219.

[89] Davies, C. L.; Filip, M. R.; Patel, J. B.; Crothers, T. W.; Verdi, C.; Wright, A. D.; Milot, R. L.; Giustino, F.; Johnston, M. B. and Herz, L. M. 'Bimolecular Recombination in Methylammonium Lead Triiodide Perovskite is an Inverse Absorption Process'. *Nat. Commun.*, 2018, **9**, 1–9.

[90] Filip, M. R. and Giustino, F. '*GW* Quasiparticle Band Gap of the Hybrid Organic-Inorganic Perovskite $CH_3NH_3PbI_3$: Effect of Spin-Orbit Interaction, Semicore Electrons, and Self-Consistency'. *Phys. Rev. B*, 2014, **90**, 245145.

[91] Boyd, C. C.; Cheacharoen, R.; Leijtens, T. and McGehee, M. D. 'Understanding Degradation Mechanisms and Improving Stability of Perovskite Photovoltaics'. *Chem. Rev.*, 2018, **119**, 3418–3451.

[92] Brennan, M. C.; Draguta, S.; Kamat, P. V. and Kuno, M. 'Light-Induced Anion Phase Segregation in Mixed Halide Perovskites'. *ACS Energy Lett.*, 2017, **3**, 204–213.

[93] Yoon, S. J.; Kuno, M. and Kamat, P. V. 'Shift Happens. How Halide Ion Defects Influence Photoinduced Segregation in Mixed Halide Perovskites'. *ACS Energy Lett.*, 2017, **2**, 1507–1514.

[94] Yoon, S. J.; Draguta, S.; Manser, J. S.; Sharia, O.; Schneider, W. F.; Kuno, M. and Kamat, P. V. 'Tracking Iodide and Bromide Ion Segregation in Mixed Halide Lead Perovskites During Photoirradiation'. *ACS Energy Lett.*, 2016, **1**, 290–296.

[95] Barker, A. J.; Sadhanala, A.; Deschler, F.; Gandini, M.; Senanayak, S. P.; Pearce, P. M.; Mosconi, E.; Pearson, A. J.; Wu, Y.; Srimath Kandada, A. R. *et al.* 'Defect-Assisted Photoinduced Halide Segregation in Mixed-Halide Perovskite Thin Films'. *ACS Energy Lett.*, 2017, **2**, 1416–1424.

[96] Draguta, S.; Sharia, O.; Yoon, S. J.; Brennan, M. C.; Morozov, Y. V.; Manser, J. M.; Kamat, P. V.; Schneider, W. F. and Kuno, M. 'Rationalizing the Light-Induced Phase Separation of Mixed Halide Organic–Inorganic Perovskites'. *Nat. Commun.*, 2017, **8**, 200.

[97] Elmelund, T.; Seger, B.; Kuno, M. K. and Kamat, P. V. 'How Interplay between Photo and Thermal Activation Dictates Halide Ion Segregation in Mixed Halide Perovskites'. *ACS Energy Lett.*, 2020, **5**, 56–63.

[98] Brivio, F.; Caetano, C. and Walsh, A. 'Thermodynamic Origin of Photoinstability in the $CH_3NH_3Pb(I_{1-x}Br_x)_3$ Hybrid Halide Perovskite Alloy'. *J. Phys. Chem. Lett.*, 2016, **7**, 1083–1087.

[99] Bush, K. A.; Frohna, K.; Prasanna, R.; Beal, R. E.; Leijtens, T.; Swifter, S. A. and McGehee, M. D. 'Compositional Engineering for Efficient Wide Band Gap Perovskites with Improved Stability to Photoinduced Phase Segregation'. *ACS Energy Lett.*, 2018, **3**, 428–435.

[100] Unger, E.; Kegelmann, L.; Suchan, K; Sörell, D; Korte, L. and Albrecht, S. 'Roadmap and Roadblocks for the Band Gap Tunability of Metal Halide Perovskites'. *J. Mater. Chem. A*, 2017, **5**, 11401–11409.

[101] Nandi, P.; Giri, C.; Swain, D.; Manju, U; Mahanti, S. D. and Topwal, D. 'Temperature Dependent Photoinduced Reversible Phase Separation in Mixed-Halide Perovskite'. *ACS Appl. Energy Mater.*, 2018, **1**, 3807–3814.

[102] Xiao, Z.; Zhao, L.; Tran, N. L.; Lin, Y. L.; Silver, S. H.; Kerner, R. A.; Yao, N.; Kahn, A.; Scholes, G. D. and Rand, B. P. 'Mixed-Halide Perovskites With Stabilized Bandgaps'. *Nano Lett.*, 2017, **17**, 6863–6869.

[103] Hu, M.; Bi, C.; Yuan, Y.; Bai, Y. and Huang, J. 'Stabilized Wide Bandgap $MAPbBr_xI_{3-x}$ Perovskite by Enhanced Grain Size and Improved Crystallinity'. *Adv. Sci.*, 2016, **3**, 1500301.

[104] Bischak, C. G.; Hetherington, C. L.; Wu, H.; Aloni, S.; Ogletree, D. F.; Limmer, D. T. and Ginsberg, N. S. 'Origin of Reversible Photoinduced Phase Separation in Hybrid Perovskites'. *Nano Lett.*, 2017, **17**, 1028–1033.

[105] Suchan, K.; Merdasa, A.; Reherman, C.; Unger, E. and Scheblykin, I. G. 'Complex Evolution of Photoluminescence During Phase Segregation of $MAPb(I_{1-x}Br_x)_3$ mixed halide perovskite'. *J. Lumin.*, 2020, **221**, 117073.

[106] Kojima, A.; Teshima, K.; Shirai, Y. and Miyasaka, T. 'Organometal Halide Perovskites as Visible-Light Sensitizers for Photovoltaic Cells'. *J. Am. Chem. Soc.*, 2009, **131**, 6050–6051.

[107] Kim, H.-S.; Lee, C.-R.; Im, J.-H.; Lee, K.-B.; Moehl, T.; Marchioro, A.; Moon, S.-J.; Humphry-Baker, R.; Yum, J.-H.; Moser, J. E. *et al.* 'Lead Iodide Perovskite Sensitized All-Solid-State Submicron Thin Film Mesoscopic Solar Cell with Efficiency Exceeding 9%'. *Sci. Rep.*, 2012, **2**, 591.

[108] Lee, M. M.; Teuscher, J.; Miyasaka, T.; Murakami, T. N. and Snaith, H. J. 'Efficient Hybrid Solar Cells Based on Meso-Superstructured Organometal Halide Perovskites'. *Science*, 2012, **338**, 643–647.

[109] Snaith, H. J. 'Perovskites: the Emergence of a New Era for Low-Cost, High-Efficiency Solar Cells'. *J. Phys. Chem. Lett.*, 2013, **4**, 3623–3630.

[110] Xing, G.; Mathews, N.; Lim, S. S.; Yantara, N.; Liu, X.; Sabba, D.; Grätzel, M.; Mhaisalkar, S. and Sum, T. C. 'Low-Temperature Solution-Processed Wavelength-Tunable Perovskites for Lasing'. *Nat. Mater.*, 2014, **13**, 476.

[111] Kumawat, N. K.; Dey, A.; Kumar, A.; Gopinathan, S. P.; Narasimhan, K. and Kabra, D. 'Band Gap Tuning of $CH_3NH_3Pb(Br_{1-x}Cl_x)_3$ Hybrid Perovskite for Blue Electroluminescence'. *ACS Appl. Mater. Interfaces*, 2015, **7**, 13119–13124.

[112] Fedeli, P.; Gazza, F.; Calestani, D.; Ferro, P.; Besagni, T.; Zappettini, A.; Calestani, G.; Marchi, E.; Ceroni, P. and Mosca, R. 'Influence of the Synthetic Procedures on the Structural and Optical Properties of Mixed-Halide (Br, I) Perovskite Films'. *J. Phys. Chem. C*, 2015, **119**, 21304–21313.

[113] Bi, C.; Yuan, Y.; Fang, Y. and Huang, J. 'Low-Temperature Fabrication of Efficient Wide-Bandgap Organolead Trihalide Perovskite Solar Cells'. *Adv. Energy Mater.*, 2015, **5**, 1401616.

[114] Shah, A.; Torres, P.; Tscharner, R.; Wyrsch, N. and Keppner, H. 'Photovoltaic Technology: The Case for Thin-Film Solar Cells'. *Science*, 1999, **285**, 692–698.

[115] Rehman, W.; Milot, R. L.; Eperon, G. E.; Wehrenfennig, C.; Boland, J. L.; Snaith, H. J.; Johnston, M. B. and Herz, L. M. 'Charge-Carrier Dynamics and Mobilities in Formamidinium Lead Mixed-Halide Perovskites'. *Adv. Mater.*, 2015, **27**, 7938–7944.

[116] Beal, R. E.; Slotcavage, D. J.; Leijtens, T.; Bowring, A. R.; Belisle, R. A.; Nguyen, W. H.; Burkhard, G. F.; Hoke, E. T. and McGehee, M. D. 'Cesium Lead Halide Perovskites with Improved Stability for Tandem Solar Cells'. *J. Phys. Chem. Lett.*, 2016, **7**, 746–751.

[117] Rehman, W.; McMeekin, D. P.; Patel, J. B.; Milot, R. L.; Johnston, M. B.; Snaith, H. J. and Herz, L. M. 'Photovoltaic Mixed-Cation Lead Mixed-Halide Perovskites: Links Between Crystallinity, Photo-Stability and Electronic Properties'. *Energy Environ. Sci.*, 2017, **10**, 361–369.

[118] Andaji-Garmaroudi, Z.; Abdi-Jalebi, M.; Guo, D.; Macpherson, S.; Sadhanala, A.; Tennyson, E. M.; Ruggeri, E.; Anaya, M.; Galkowski, K.; Shivanna, R. *et al.* 'A Highly Emissive Surface Layer in Mixed-Halide Multication Perovskites'. *Adv. Mater.*, 2019, **31**, 1902374.

[119] Li, W.; Rothmann, M. U.; Liu, A.; Wang, Z.; Zhang, Y.; Pascoe, A. R.; Lu, J.; Jiang, L.; Chen, Y.; Huang, F. *et al.* 'Phase Segregation Enhanced Ion Movement in Efficient Inorganic $CsPbIBr_2$ Solar Cells'. *Adv. Energy Mater.*, 2017, **7**, 1700946.

[120] Bischak, C. G.; Wong, A. B.; Lin, E.; Limmer, D. T.; Yang, P. and Ginsberg, N. S. 'Tunable Polaron Distortions Control the Extent of Halide Demixing in Lead Halide Perovskites'. *J. Phys. Chem. Lett.*, 2018, **9**, 3998–4005.

[121] Sutter-Fella, C. M.; Ngo, Q. P.; Cefarin, N.; Gardner, K. L.; Tamura, N.; Stan, C. V.; Drisdell, W. S.; Javey, A.; Toma, F. M. and Sharp, I. D. 'Cation-Dependent Light-Induced Halide Demixing in Hybrid Organic–Inorganic Perovskites'. *Nano Lett.*, 2018, **18**, 3473–3480.

[122] Zhou, Y.; Jia, Y.-H.; Fang, H.-H.; Loi, M. A.; Xie, F.-Y.; Gong, L.; Qin, M.-C.; Lu, X.-H.; Wong, C.-P. and Zhao, N. 'Composition-Tuned Wide Bandgap Perovskites: From Grain Engineering to Stability and Performance Improvement'. *Adv. Funct. Mater.*, 2018, **28**, 1803130.

[123] Abdi-Jalebi, M.; Andaji-Garmaroudi, Z.; Cacovich, S.; Stavrakas, C.; Philippe, B.; Richter, J. M.; Alsari, M.; Booker, E. P.; Hutter, E. M.; Pearson, A. J. *et al.* 'Maximizing and Stabilizing Luminescence from Halide Perovskites with Potassium Passivation'. *Nature*, 2018, **555**, 497.

[124] Ruf, F.; Rietz, P.; Aygüler, M. F.; Kelz, I.; Docampo, P.; Kalt, H. and Hetterich, M. 'The Bandgap as a Moving Target: Reversible Bandgap Instabilities in Multiple-Cation Mixed-Halide Perovskite Solar Cells'. *ACS Energy Lett.*, 2018, **3**, 2995–3001.

[125] Xie, Y.-M.; Zeng, Z.; Xu, X.; Ma, C.; Ma, Y.; Li, M.; Lee, C.-S. and Tsang, S.-W. 'FA-Assistant Iodide Coordination in Organic–Inorganic Wide-Bandgap Perovskite with Mixed Halides'. *Small*, 2020, **16**, 1907226.

[126] Zhao, B.; Abdi-Jalebi, M.; Tabachnyk, M.; Glass, H.; Kamboj, V. S.; Nie, W.; Pearson, A. J.; Puttisong, Y.; Gödel, K. C.; Beere, H. E. *et al.* 'High Open-Circuit Voltages in Tin-Rich Low-Bandgap Perovskite-Based Planar Heterojunction Photovoltaics'. *Adv. Mater.*, 2017, **29**, 1604744.

[127] Anaya, M.; Correa-Baena, J. P.; Lozano, G.; Saliba, M.; Anguita, P.; Roose, B.; Abate, A.; Steiner, U.; Grätzel, M.; Calvo, M. E. *et al.* 'Optical Analysis of $CH_3NH_3Sn_xPb_{1-x}I_3$ Absorbers: a Roadmap for Perovskite-on-Perovskite Tandem Solar Cells'. *J. Mater. Chem. A*, 2016, **4**, 11214–11221.

[128] Liu, C.; Fan, J.; Li, H.; Zhang, C. and Mai, Y. 'Highly Efficient Perovskite Solar Cells with Substantial Reduction of Lead Content'. *Sci. Rep.*, 2016, **6**, 35705.

[129] Yang, Z.; Rajagopal, A.; Chueh, C.-C.; Jo, S. B.; Liu, B.; Zhao, T. and Jen, A. K.-Y. 'Stable Low-Bandgap Pb–Sn Binary Perovskites for Tandem Solar Cells'. *Adv. Mater.*, 2016, **28**, 8990–8997.

[130] Im, J.; Stoumpos, C. C.; Jin, H.; Freeman, A. J. and Kanatzidis, M. G. 'Antagonism between Spin–Orbit Coupling and Steric Effects Causes Anomalous Band Gap Evolution in the Perovskite Photovoltaic Materials $CH_3NH_3Sn_{1-x}Pb_xI_3$'. *J. Phys. Chem. Lett.*, 2015, **6**, 3503–3509.

[131] Stoumpos, C. C.; Malliakas, C. D. and Kanatzidis, M. G. 'Semiconducting Tin and Lead Iodide Perovskites with Organic Cations: Phase Transitions, High Mobilities, and Near-Infrared Photoluminescent Properties'. *Inorg. Chem.*, 2013, **52**, 9019–9038.

[132] Savill, K. J.; Klug, M. T.; Milot, R. L.; Snaith, H. J. and Herz, L. M. 'Charge-Carrier Cooling and Polarization Memory Loss in Formamidinium Tin Triiodide'. *J. Phys. Chem. Lett.*, 2019, **10**, 6038–6047.

[133] Yang, Z.; Rajagopal, A.; Jo, S. B.; Chueh, C.-C.; Williams, S.; Huang, C.-C.; Katahara, J. K.; Hillhouse, H. W. and Jen, A. K.-Y. 'Stabilized Wide Bandgap Perovskite Solar Cells by Tin Substitution'. *Nano Lett.*, 2016, **16**, 7739–7747.

[134] Li, N.; Zhu, Z.; Li, J.; Jen, A. K.-Y. and Wang, L. 'Inorganic $CsPb_{1-x}Sn_xIBr_2$ for Efficient Wide-Bandgap Perovskite Solar Cells'. *Adv. Energy Mater.*, 2018, **8**, 1800525.

[135] Koh, T. M.; Krishnamoorthy, T.; Yantara, N.; Shi, C.; Leong, W. L.; Boix, P. P.; Grimsdale, A. C.; Mhaisalkar, S. G. and Mathews, N. 'Formamidinium Tin-Based Perovskite with Low E_g for Photovoltaic Applications'. *J. Mater. Chem. A*, 2015, **3**, 14996–15000.

[136] Liao, W.; Zhao, D.; Yu, Y.; Grice, C. R.; Wang, C.; Cimaroli, A. J.; Schulz, P.; Meng, W.; Zhu, K.; Xiong, R.-G. *et al.* 'Lead-Free Inverted Planar Formamidinium Tin Triiodide Perovskite Solar Cells Achieving Power Conversion Efficiencies up to 6.22%'. *Adv. Mater.*, 2016, **28**, 9333–9340.

[137] Lee, S. J.; Shin, S. S.; Kim, Y. C.; Kim, D.; Ahn, T. K.; Noh, J. H.; Seo, J. and Seok, S. I. 'Fabrication of Efficient Formamidinium Tin Iodide Perovskite Solar Cells through SnF_2–Pyrazine Complex'. *J. Am. Chem. Soc.*, 2016, **138**, 3974–3977.

[138] Yokoyama, T.; Cao, D. H.; Stoumpos, C. C.; Song, T.-B.; Sato, Y.; Aramaki, S. and Kanatzidis, M. G. 'Overcoming Short-Circuit in Lead-Free $CH_3NH_3SnI_3$ Perovskite Solar Cells via Kinetically Controlled Gas–Solid Reaction Film Fabrication Process'. *J. Phys. Chem. Lett.*, 2016, **7**, 776–782.

[139] Xing, J.; Zhao, Y.; Askerka, M.; Quan, L. N.; Gong, X.; Zhao, W.; Zhao, J.; Tan, H.; Long, G.; Gao, L. *et al.* 'Color-Stable Highly Luminescent Sky-Blue Perovskite Light-Emitting Diodes'. *Nat. Commun.*, 2018, **9**, 3541.

[140] Yao, E.-P.; Yang, Z.; Meng, L.; Sun, P.; Dong, S.; Yang, Y. and Yang, Y. 'High-Brightness Blue and White LEDs based on Inorganic Perovskite Nanocrystals and their Composites'. *Adv. Mater.*, 2017, **29**, 1606859.

[141] Gangishetty, M. K.; Hou, S.; Quan, Q. and Congreve, D. N. 'Reducing Architecture Limitations for Efficient Blue Perovskite Light-Emitting Diodes'. *Adv. Mater.*, 2018, **30**, 1706226.

[142] Ochsenbein, S. T.; Krieg, F.; Shynkarenko, Y.; Raino, G. and Kovalenko, M. V. 'Engineering Color-Stable Blue Light-Emitting Diodes with Lead-Halide Perovskite Nanocrystals'. *ACS Appl. Mater. Interfaces*, 2019, **11**, 21655–21660.

[143] Wang, K.-H.; Peng, Y.; Ge, J.; Jiang, S.; Zhu, B.-S.; Yao, J.; Yin, Y.-C.; Yang, J.-N.; Zhang, Q. and Yao, H.-B. 'Efficient and Color-Tunable Quasi-2D $CsPbBr_xCl_{3-x}$ Perovskite Blue Light-Emitting Diodes'. *ACS Photonics*, 2018, **6**, 667–676.

[144] Tang, X.; Berg, M. van den; Gu, E.; Horneber, A.; Matt, G. J.; Osvet, A.; Meixner, A. J.; Zhang, D. and Brabec, C. J. 'Local Observation of Phase Segregation in Mixed-Halide Perovskite'. *Nano Lett.*, 2018, **18**, 2172–2178.

[145] Yang, B.; Brown, C. C.; Huang, J.; Collins, L.; Sang, X.; Unocic, R. R.; Jesse, S.; Kalinin, S. V.; Belianinov, A.; Jakowski, J. *et al.* 'Enhancing Ion Migration in Grain Boundaries of Hybrid Organic–Inorganic Perovskites by Chlorine'. *Adv. Funct. Mater.*, 2017, **27**, 1700749.

[146] Shao, Y.; Fang, Y.; Li, T.; Wang, Q.; Dong, Q.; Deng, Y.; Yuan, Y.; Wei, H.; Wang, M.; Gruverman, A. *et al.* 'Grain Boundary Dominated Ion Migration in Polycrystalline Organic–Inorganic Halide Perovskite Films'. *Energy Environ. Sci.*, 2016, **9**, 1752–1759.

[147] Meggiolaro, D.; Mosconi, E. and De Angelis, F. 'Formation of Surface Defects Dominates Ion Migration in Lead-Halide Perovskites'. *ACS Energy Lett.*, 2019, **4**, 779–785.

[148] Khassaf, H.; Yadavalli, S. K.; Zhou, Y.; Padture, N. P. and Kingon, A. I. 'Effect of Grain Boundaries on Charge Transport in Methylammonium Lead Iodide Perovskite Thin Films'. *J. Phys. Chem. C*, 2019, **123**, 5321–5325.

[149] Yun, J. S.; Seidel, J.; Kim, J.; Soufiani, A. M.; Huang, S.; Lau, J.; Jeon, N. J.; Seok, S. I.; Green, M. A. and Ho-Baillie, A. 'Critical Role of Grain Boundaries for Ion Migration in Formamidinium and Methylammonium Lead Halide Perovskite Solar Cells'. *Adv. Energy Mater.*, 2016, **6**, 1600330.

[150] Knight, A. J.; Wright, A. D.; Patel, J. B.; McMeekin, D. P.; Snaith, H. J.; Johnston, M. B. and Herz, L. M. 'Electronic Traps and Phase Segregation in Lead Mixed-Halide Perovskite'. *ACS Energy Lett.*, 2018, **4**, 75–84.

[151] Belisle, R. A.; Bush, K. A.; Bertoluzzi, L.; Gold-Parker, A.; Toney, M. F. and McGehee, M. D. 'Impact of Surfaces on Photoinduced Halide Segregation in Mixed-Halide Perovskites'. *ACS Energy Lett.*, 2018, **3**, 2694–2700.

[152] Wang, Z.; Wang, Y.; Nie, Z.; Ren, Y. and Zeng, H. 'Laser Induced Ion Migration in All-Inorganic Mixed Halide Perovskite Micro-Platelets'. *Nanoscale Advances*, 2019, **1**, 4459–4465.

[153] Wu, B.; Nguyen, H. T.; Ku, Z.; Han, G.; Giovanni, D.; Mathews, N.; Fan, H. J. and Sum, T. C. 'Discerning the Surface and Bulk Recombination Kinetics of Organic–Inorganic Halide Perovskite Single Crystals'. *Adv. Energy Mater.*, 2016, **6**, 1600551.

[154] Mao, W.; Hall, C. R.; Chesman, A. S.; Forsyth, C.; Cheng, Y.-B.; Duffy, N. W.; Smith, T. A. and Bach, U. 'Visualizing Phase Segregation in Mixed-Halide Perovskite Single Crystals'. *Angew. Chem. Int. Edit.*, 2019, **58**, 2893–2898.

[155] Chen, W.; Mao, W.; Bach, U.; Jia, B. and Wen, X. 'Tracking Dynamic Phase Segregation in Mixed-Halide Perovskite Single Crystals under Two-Photon Scanning Laser Illumination'. *Small Methods*, 2019, **3**, 1900273.

[156] Byun, H. R.; Park, D. Y.; Oh, H. M.; Namkoong, G. and Jeong, M. S. 'Light Soaking Phenomena in Organic–Inorganic Mixed Halide Perovskite Single Crystals'. *ACS Photonics*, 2017, **4**, 2813–2820.

[157] Knight, A. J.; Patel, J. B.; Snaith, H. J.; Johnston, M. B. and Herz, L. M. 'Trap States, Electric Fields, and Phase Segregation in Mixed-Halide Perovskite Photovoltaic Devices'. *Adv. Energy Mater.*, 2020, **10**, 1903488.

[158] Gualdrón-Reyes, A. F.; Yoon, S. J.; Barea, E. M.; Agouram, S.; Muñoz-Sanjosé, V.; Meléndez, Á. M.; Niño-Gómez, M. E. and Mora-Seró, I. 'Controlling the Phase Segregation in Mixed Halide Perovskites through Nanocrystal Size'. *ACS Energy Lett.*, 2018, **4**, 54–62.

[159] Wang, X.; Ling, Y.; Lian, X.; Xin, Y.; Dhungana, K. B.; Perez-Orive, F.; Knox, J.; Chen, Z.; Zhou, Y.; Beery, D. *et al.* 'Suppressed Phase Separation of Mixed-Halide Perovskites Confined in Endotaxial Matrices'. *Nat. Commun.*, 2019, **10**, 695.

[160] Wheeler, L. M.; Sanehira, E. M.; Marshall, A. R.; Schulz, P.; Suri, M.; Anderson, N. C.; Christians, J. A.; Nordlund, D.; Sokaras, D.; Kroll, T. *et al.* 'Targeted Ligand-Exchange Chemistry on Cesium Lead Halide Perovskite Quantum Dots for High-Efficiency Photovoltaics'. *J. Am. Chem. Soc.*, 2018, **140**, 10504–10513.

[161] Sanehira, E. M.; Marshall, A. R.; Christians, J. A.; Harvey, S. P.; Ciesielski, P. N.; Wheeler, L. M.; Schulz, P.; Lin, L. Y.; Beard, M. C. and Luther, J. M. 'Enhanced Mobility $CsPbI_3$ Quantum Dot Arrays for Record-Efficiency, High-Voltage Photovoltaic Cells'. *Sci. Adv.*, 2017, **3**, eaao4204.

[162] Swarnkar, A.; Marshall, A. R.; Sanehira, E. M.; Chernomordik, B. D.; Moore, D. T.; Christians, J. A.; Chakrabarti, T. and Luther, J. M. 'Quantum Dot–Induced Phase Stabilization of α-$CsPbI_3$ Perovskite for High-Efficiency Photovoltaics'. *Science*, 2016, **354**, 92–95.

[163] Palazon, F.; Dogan, S.; Marras, S.; Locardi, F.; Nelli, I.; Rastogi, P.; Ferretti, M.; Prato, M.; Krahne, R. and Manna, L. 'From $CsPbBr_3$ Nano-Inks to Sintered $CsPbBr_3$–$CsPb_2Br_5$ Films via Thermal Annealing: Implications on Optoelectronic Properties'. *J. Phys. Chem. C*, 2017, **121**, 11956–11961.

[164] Palazon, F; Di Stasio, F; Lauciello, S; Krahne, R; Prato, M and Manna, L. 'Evolution of $CsPbBr_3$ Nanocrystals Upon Post-Synthesis Annealing Under an Inert Atmosphere'. *J. Mater. Chem. C*, 2016, **4**, 9179–9182.

[165] Motti, S. G.; Krieg, F.; Ramadan, A. J.; Patel, J. B.; Snaith, H. J.; Kovalenko, M. V.; Johnston, M. B. and Herz, L. M. '$CsPbBr_3$ Nanocrystal Films: Deviations from Bulk Vibrational and Optoelectronic Properties'. *Adv. Funct. Mater.*, 2020, **30**, 1909904.

[166] Ruth, A.; Brennan, M. C.; Draguta, S.; Morozov, Y. V.; Zhukovskyi, M.; Janko, B.; Zapol, P. and Kuno, M. 'Vacancy-Mediated Anion Photosegregation Kinetics in Mixed Halide Hybrid Perovskites: Coupled Kinetic Monte Carlo and Optical Measurements'. *ACS Energy Lett.*, 2018, **3**, 2321–2328.

[167] Balakrishna, R. G.; Kobosko, S. M. and Kamat, P. V. 'Mixed Halide Perovskite Solar Cells. Consequence of Iodide Treatment on Phase Segregation Recovery'. *ACS Energy Lett.*, 2018, **3**, 2267–2272.

[168] Zhou, Y.; Wang, F.; Cao, Y.; Wang, J.-P.; Fang, H.-H.; Loi, M. A.; Zhao, N. and Wong, C.-P. 'Benzylamine-Treated Wide-Bandgap Perovskite with High Thermal-Photostability and Photovoltaic Performance'. *Adv. Energy Mater.*, 2017, **7**, 1701048.

[169] Yang, J.-N.; Song, Y.; Yao, J.-S.; Wang, K.-H.; Wang, J.-J.; Zhu, B.-S.; Yao, M.-M.; Rahman, S. U.; Lan, Y.-F.; Fan, F.-J. *et al.* 'Potassium-Bromide Surface Passivation on $CsPbI_{3-x}Br_x$ Nanocrystals for Efficient and Stable Pure Red Perovskite Light Emitting Diodes'. *J. Am. Chem. Soc.*, 2020, **142**, 2956–2967.

[170] Fan, W.; Shi, Y.; Shi, T.; chu, s.; Chen, W.; Ighodalo, K.; Zhao, J.; Li, X. and Xiao, Z. 'Suppression and Reversion of Light-induced Phase Separation in Mixed-halide Perovskites by Oxygen Passivation'. *ACS Energy Lett.*, 2019, **4**, 2052–2058.

[171] Howard, J. M.; Tennyson, E. M.; Barik, S.; Szostak, R.; Waks, E.; Toney, M. F.; Nogueira, A. F.; Neves, B. R. and Leite, M. S. 'Humidity-Induced Photoluminescence Hysteresis in Variable Cs/Br Ratio Hybrid Perovskites'. *J. Phys. Chem. Lett.*, 2018, **9**, 3463–3469.

[172] Song, Z.; Abate, A.; Watthage, S. C.; Liyanage, G. K.; Phillips, A. B.; Steiner, U.; Graetzel, M. and Heben, M. J. 'Perovskite Solar Cell Stability in Humid Air: Partially Reversible Phase Transitions in the PbI_2-CH_3NH_3I-H_2O System'. *Adv. Energy Mater.*, 2016, **6**, 1600846.

[173] Leguy, A. M.; Hu, Y.; Campoy-Quiles, M.; Alonso, M. I.; Weber, O. J.; Azarhoosh, P.; Van Schilfgaarde, M.; Weller, M. T.; Bein, T.; Nelson, J. *et al.* 'Reversible Hydration of $CH_3NH_3PbI_3$ in Films, Single Crystals, and Solar Cells'. *Chem. Mater.*, 2015, **27**, 3397–3407.

[174] Yoon, S. J.; Stamplecoskie, K. G. and Kamat, P. V. 'How Lead Halide Complex Chemistry Dictates the Composition of Mixed Halide Perovskites'. *J. Phys. Chem. Lett.*, 2016, **7**, 1368–1373.

[175] Lin, Q.; Wang, Z.; Snaith, H. J.; Johnston, M. B. and Herz, L. M. 'Hybrid Perovskites: Prospects for Concentrator Solar Cells'. *Adv. Sci.*, 2018, **5**, 1700792.

[176] Slotcavage, D. J.; Karunadasa, H. I. and McGehee, M. D. 'Light-Induced Phase Segregation in Halide-Perovskite Absorbers'. *ACS Energy Lett.*, 2016, **1**, 1199–1205.

[177] Motti, S. G.; Crothers, T.; Yang, R.; Cao, Y.; Li, R.; Johnston, M. B.; Wang, J. and Herz, L. M. 'Heterogeneous Photon Recycling and Charge Diffusion Enhance Charge Transport in Quasi-2D Lead-Halide Perovskite Films'. *Nano letters*, 2019, **19**, 3953–3960.

[178] Patel, J. B.; Wright, A. D.; Lohmann, K. B.; Peng, K.; Xia, C. Q.; Ball, J. M.; Noel, N. K.; Crothers, T. W.; Wong-Leung, J.; Snaith, H. J. *et al.* 'Light Absorption and Recycling in Hybrid Metal Halide Perovskite Photovoltaic Devices'. *Adv. Energy Mater.*, 2020, **10**, 1903653.

[179] Milot, R. L.; Eperon, G. E.; Snaith, H. J.; Johnston, M. B. and Herz, L. M. 'Temperature-Dependent Charge-Carrier Dynamics in $CH_3NH_3PbI_3$ Perovskite Thin Films'. *Adv. Funct. Mater.*, 2015, **25**, 6218–6227.

[180] Wu, K.; Bera, A.; Ma, C.; Du, Y.; Yang, Y.; Li, L. and Wu, T. 'Temperature-Dependent Excitonic Photoluminescence of Hybrid Organometal Halide Perovskite Films'. *Phys. Chem. Chem. Phys.*, 2014, **16**, 22476–22481.

[181] Eperon, G. E.; Stranks, S. D.; Menelaou, C.; Johnston, M. B.; Herz, L. M. and Snaith, H. J. 'Formamidinium Lead Trihalide: a Broadly Tunable Perovskite for Efficient Planar Heterojunction Solar Cells'. *Energy Environ. Sci.*, 2014, **7**, 982–988.

[182] Askar, A. M.; Karmakar, A.; Bernard, G. M.; Ha, M.; Terskikh, V. V.; Wiltshire, B. D.; Patel, S.; Fleet, J.; Shankar, K. and Michaelis, V. K. 'Composition-Tunable Formamidinium Lead Mixed Halide Perovskites via Solvent-Free Mechanochemical Synthesis: Decoding the Pb Environments Using Solid-State NMR Spectroscopy'. *J. Phys. Chem. Lett.*, 2018, **9**, 2671–2677.

[183] Weller, M. T.; Weber, O. J.; Frost, J. M. and Walsh, A. 'Cubic Perovskite Structure of Black Formamidinium Lead Iodide, α-$[HC(NH_2)_2]PbI_3$, at 298 K'. *J. Phys. Chem. Lett.*, 2015, **6**, 3209–3212.

[184] Beal, R. E.; Hagström, N. Z.; Barrier, J.; Gold-Parker, A.; Prasanna, R.; Bush, K. A.; Passarello, D.; Schelhas, L. T.; Brüning, K.; Tassone, C. J. *et al.* 'Structural Origins of Light-Induced Phase Segregation in Organic-Inorganic Halide Perovskite Photovoltaic Materials'. *Matter*, 2020, **2**, 207–219.

[185] Yang, X.; Yan, X.; Wang, W.; Zhu, X.; Li, H.; Ma, W. and Sheng, C. 'Light Induced Metastable Modification of Optical Properties in $CH_3NH_3PbI_{3-x}Br_x$ Perovskite Films: Two-Step Mechanism'. *Org. Electron.*, 2016, **34**, 79–83.

[186] Bai, Y.; Meng, X. and Yang, S. 'Interface Engineering for Highly Efficient and Stable Planar p-i-n Perovskite Solar Cells'. *Adv. Energy Mater.*, 2018, **8**, 1701883.

[187] Zhou, Z.; Pang, S.; Liu, Z.; Xu, H. and Cui, G. 'Interface Engineering for High-Performance Perovskite Hybrid Solar Cells'. *J. Mater. Chem. A*, 2015, **3**, 19205–19217.

[188] Grancini, G. and Nazeeruddin, M. K. 'Dimensional Tailoring of Hybrid Perovskites for Photovoltaics'. *Nat. Rev. Mater.*, 2019, **4**, 4–22.

[189] Lin, Y.; Bai, Y.; Fang, Y.; Wang, Q.; Deng, Y. and Huang, J. 'Suppressed Ion Migration in Low-Dimensional Perovskites'. *ACS Energy Lett.*, 2017, **2**, 1571–1572.

[190] Huang, F.; Dkhissi, Y.; Huang, W.; Xiao, M.; Benesperi, I.; Rubanov, S.; Zhu, Y.; Lin, X.; Jiang, L.; Zhou, Y. *et al.* 'Gas-Assisted Preparation of Lead Iodide Perovskite Films Consisting of a Monolayer of Single Crystalline Grains for High Efficiency Planar Solar Cells'. *Nano Energy*, 2014, **10**, 10–18.

[191] Noel, N. K.; Habisreutinger, S. N.; Wenger, B.; Klug, M. T.; Hörantner, M. T.; Johnston, M. B.; Nicholas, R. J.; Moore, D. T. and Snaith, H. J. 'A Low Viscosity, Low Boiling Point, Clean Solvent System for the Rapid Crystallisation of Highly Specular Perovskite Films'. *Energy Environ. Sci.*, 2017, **10**, 145–152.

[192] Anaraki, E. H.; Kermanpur, A.; Steier, L.; Domanski, K.; Matsui, T.; Tress, W.; Saliba, M.; Abate, A.; Grätzel, M.; Hagfeldt, A. *et al.* 'Highly Efficient and Stable Planar Perovskite Solar Cells by Solution-Processed Tin Oxide'. *Energy Environ. Sci.*, 2016, **9**, 3128–3134.

[193] Lin, Y.-H.; Sakai, N.; Da, P.; Wu, J.; Sansom, H. C.; Ramadan, A. J.; Mahesh, S.; Liu, J.; Oliver, R. D. J.; Lim, J. *et al.* 'A Piperidinium Salt Stabilizes Efficient Metal-Halide Perovskite Solar Cells'. *Science*, 2020, **369**, 96–102.

[194] Andor. *An Introduction to the ICCD Camera*. [Online; accessed 2-February-2021]. https://andor.oxinst.com/learning/view/article/intensified-ccd-cameras.

[195] Princeton Instruments. 'PI-MAX® 4 Camera System'. 10 2019.

[196] Wahl, M. 'Technical Note on Time-Correlated Single Photon Counting'. *PicoQuant GmbH*, 2014.

[197] Simon, S. H. *The Oxford Solid State Basics*. OUP Oxford, 2013.

[198] Scherrer, P. 'Nachrichten von der Gesellschaft der Wissenschaften zu Göttingen'. *Mathematisch-Physikalische Klasse*, 1918, **2**, 98–100.

[199] Vegard, L. 'Die Konstitution der Mischkristalle und die Raumfüllung der Atome'. *Z. Phys.*, 1921, **5**, 17–26.

[200] NREL. *Reference Solar Spectral Irradiance: Air Mass 1.5*. [Online; accessed 3-November-2017]. 2004. https://rredc.nrel.gov/solar/spectra/am1.5/.

[201] Anizelli, H. S.; Fernandes, R. V.; Scarmínio, J.; Silva, P. R. C. da; Duarte, J. L. and Laureto, E. 'Effect of Pressure on the Remixing Process in $CH_3NH_3Pb(I_{1-x}Br_x)_3$ Perovskite Thin Films'. *J. Lumin.*, 2018, **199**, 348–351.

[202] deQuilettes, D. W.; Koch, S.; Burke, S.; Paranji, R. K.; Shropshire, A. J.; Ziffer, M. E. and Ginger, D. S. 'Photoluminescence Lifetimes Exceeding 8 μs and Quantum Yields Exceeding 30% in Hybrid Perovskite Thin Films by Ligand Passivation'. *ACS Energy Lett.*, 2016, **1**, 438–444.

[203] Wetzelaer, G.-J. A.; Scheepers, M.; Sempere, A. M.; Momblona, C.; Ávila, J. and Bolink, H. J. 'Trap-Assisted Non-Radiative Recombination in Organic–Inorganic Perovskite Solar Cells'. *Adv. Mater.*, 2015, **27**, 1837–1841.

[204] Leijtens, T.; Eperon, G. E.; Barker, A. J.; Grancini, G.; Zhang, W.; Ball, J. M.; Kandada, A. R. S.; Snaith, H. J. and Petrozza, A. 'Carrier Trapping and Recombination: the Role of Defect Physics in Enhancing the Open Circuit Voltage of Metal Halide Perovskite Solar Cells'. *Energy Environ. Sci.*, 2016, **9**, 3472–3481.

[205] Stranks, S. D.; Burlakov, V. M.; Leijtens, T.; Ball, J. M.; Goriely, A. and Snaith, H. J. 'Recombination Kinetics in Organic-Inorganic Perovskites: Excitons, Free Charge, and Subgap States'. *Phys. Rev. Appl.*, 2014, **2**, 034007.

[206] Schulz, P.; Edri, E.; Kirmayer, S.; Hodes, G.; Cahen, D. and Kahn, A. 'Interface Energetics in Organo-Metal Halide Perovskite-Based Photovoltaic Cells'. *Energy Environ. Sci.*, 2014, **7**, 1377–1381.

[207] Birkhold, S. T.; Precht, J. T.; Liu, H.; Giridharagopal, R.; Eperon, G. E.; Schmidt-Mende, L.; Li, X. and Ginger, D. S. 'Interplay of Mobile Ions and Injected Carriers Creates Recombination Centers in Metal Halide Perovskites under Bias'. *ACS Energy Lett.*, 2018, **3**, 1279–1286.

[208] Jacobs, D. L.; Scarpulla, M. A.; Wang, C.; Bunes, B. R. and Zang, L. 'Voltage-Induced Transients in Methylammonium Lead Triiodide Probed by Dynamic Photoluminescence Spectroscopy'. *J. Phys. Chem. C*, 2016, **120**, 7893–7902.

[209] Zhang, Y.; Wang, Y.; Xu, Z.-Q.; Liu, J.; Song, J.; Xue, Y.; Wang, Z.; Zheng, J.; Jiang, L.; Zheng, C. *et al.* 'Reversible Structural Swell–Shrink and Recoverable Optical Properties in Hybrid Inorganic–Organic Perovskite'. *ACS Nano*, 2016, **10**, 7031–7038.

[210] Deng, X.; Wen, X.; Lau, C. F. J.; Young, T.; Yun, J.; Green, M. A.; Huang, S. and Ho-Baillie, A. W. Y. 'Electric Field Induced Reversible and Irreversible Photoluminescence Responses in Methylammonium Lead Iodide Perovskite'. *J. Mater. Chem. C*, 2016, **4**, 9060–9068.

[211] Jeon, N. J.; Noh, J. H.; Yang, W. S.; Kim, Y. C.; Ryu, S.; Seo, J. and Seok, S. I. 'Compositional Engineering of Perovskite Materials for High-Performance Solar Cells'. *Nature*, 2015, **517**, 476–480.

[212] Li, C.; Guerrero, A.; Zhong, Y.; Gräser, A.; Luna, C. A. M.; Köhler, J.; Bisquert, J.; Hildner, R. and Huettner, S. 'Real-Time Observation of Iodide Ion Migration in Methylammonium Lead Halide Perovskites'. *Small*, 2017, **13**, 1701711.

[213] Yuan, Y.; Chae, J.; Shao, Y.; Wang, Q.; Xiao, Z.; Centrone, A. and Huang, J. 'Photovoltaic Switching Mechanism in Lateral Structure Hybrid Perovskite Solar Cells'. *Adv. Energy Mater.*, 2015, **5**, 1500615.

[214] Xing, J.; Wang, Q.; Dong, Q.; Yuan, Y.; Fang, Y. and Huang, J. 'Ultrafast Ion Migration in Hybrid Perovskite Polycrystalline Thin Films Under Light and Suppression in Single Crystals'. *Phys. Chem. Chem. Phys.*, 2016, **18**, 30484–30490.

[215] Zhao, Y.-C.; Zhou, W.-K.; Zhou, X.; Liu, K.-H.; Yu, D.-P. and Zhao, Q. 'Quantification of Light-Enhanced Ionic Transport in Lead Iodide Perovskite Thin Films and its Solar Cell Applications'. *Light: Sci. Appl.*, 2017, **6**, e16243.

[216] Kim, G. Y.; Senocrate, A.; Yang, T.-Y.; Gregori, G.; Grätzel, M. and Maier, J. 'Large Tunable Photoeffect on Ion Conduction in Halide Perovskites and Implications for Photodecomposition'. *Nature Mater.*, 2018, **17**, 445.

[217] Li, C.; Guerrero, A.; Zhong, Y. and Huettner, S. 'Origins and Mechanisms of Hysteresis in Organometal Halide Perovskites'. *J. Phys.: Condens. Matt.*, 2017, **29**, 193001.

[218] Song, D. H.; Jang, M. H.; Lee, M. H.; Heo, J. H.; Park, J. K.; Sung, S.-J.; Kim, D.-H.; Hong, K.-H. and Im, S. H. 'A Discussion on the Origin and Solutions of Hysteresis in Perovskite Hybrid Solar Cells'. *J. Phys. D: Appl. Phys.*, 2016, **49**, 473001.

[219] Snaith, H. J.; Abate, A.; Ball, J. M.; Eperon, G. E.; Leijtens, T.; Noel, N. K.; Stranks, S. D.; Wang, J. T.-W.; Wojciechowski, K. and Zhang, W. 'Anomalous Hysteresis in Perovskite Solar Cells'. *J. Phys. Chem. Lett*, 2014, **5**, 1511–1515.

[220] Chen, B.; Yang, M.; Priya, S. and Zhu, K. 'Origin of *J–V Hysteresis in Perovskite Solar Cells*'. *J. Phys. Chem. Lett.*, 2016, **7**, 905–917.

[221] Richardson, G.; O'Kane, S. E.; Niemann, R. G.; Peltola, T. A.; Foster, J. M.; Cameron, P. J. and Walker, A. B. 'Can Slow-Moving Ions Explain Hysteresis in the Current–Voltage Curves of Perovskite Solar Cells?' *Energy Environ. Sci.*, 2016, **9**, 1476–1485.

[222] Zhang, Y.; Liu, M.; Eperon, G. E.; Leijtens, T. C.; McMeekin, D.; Saliba, M.; Zhang, W.; Bastiani, M. de; Petrozza, A.; Herz, L. M. *et al.* 'Charge Selective Contacts, Mobile Ions and Anomalous Hysteresis in Organic–Inorganic Perovskite Solar Cells'. *Mater. Horiz.*, 2015, **2**, 315–322.

[223] Zhang, T.; Chen, H.; Bai, Y.; Xiao, S.; Zhu, L.; Hu, C.; Xue, Q. and Yang, S. 'Understanding the Relationship Between Ion Migration and the Anomalous Hysteresis in High-Efficiency Perovskite Solar Cells: A Fresh Perspective from Halide Substitution'. *Nano Energy*, 2016, **26**, 620–630.

[224] Ravishankar, S.; Almora, O.; Echeverría-Arrondo, C.; Ghahremanirad, E.; Aranda, C.; Guerrero, A.; Fabregat-Santiago, F.; Zaban, A.; Garcia-Belmonte, G. and Bisquert, J. 'Surface Polarization Model for the Dynamic Hysteresis of Perovskite Solar Cells'. *J. Phys. Chem. Lett.*, 2017, **8**, 915–921.

[225] Patel, J. B.; Wong-Leung, J.; Van Reenen, S.; Sakai, N.; Wang, J. T. W.; Parrott, E. S.; Liu, M.; Snaith, H. J.; Herz, L. M. and Johnston, M. B. 'Influence of Interface Morphology on Hysteresis in Vapor-Deposited Perovskite Solar Cells'. *Adv. Electron. Mater.*, 2017, **3**, 1600470.

[226] Azpiroz, J. M.; Mosconi, E.; Bisquert, J. and De Angelis, F. 'Defect Migration in Methylammonium Lead Iodide and its Role in Perovskite Solar Cell Operation'. *Energy Environ. Sci.*, 2015, **8**, 2118–2127.

[227] Haruyama, J.; Sodeyama, K.; Han, L. and Tateyama, Y. 'First-Principles Study of Ion Diffusion in Perovskite Solar Cell Sensitizers'. *J. Am. Chem. Soc.*, 2015, **137**, 10048–10051.

[228] Nguyen, B. P.; Jung, H. R.; Kim, J. and Jo, W. 'Enhanced Carrier Transport over Grain Boundaries in Lead-Free $CH_3NH_3Sn(I_{1-x}Br_x)_3$ ($0 \leq x \leq 1$) Perovskite Solar Cells'. *Nanotechnology*, 2019, **30**, 314005.

[229] Yun, J. S.; Ho-Baillie, A.; Huang, S.; Woo, S. H.; Heo, Y.; Seidel, J.; Huang, F.; Cheng, Y.-B. and Green, M. A. 'Benefit of Grain Boundaries in Organic–Inorganic Halide Planar Perovskite Solar Cells'. *J. Phys. Chem. Lett.*, 2015, **6**, 875–880.

[230] Li, J.-J.; Ma, J.-Y.; Ge, Q.-Q.; Hu, J.-S.; Wang, D. and Wan, L.-J. 'Microscopic Investigation of Grain Boundaries in Organolead Halide Perovskite Solar Cells'. *ACS Appl. Mater. Interfaces*, 2015, **7**, 28518–28523.

[231] Knight, A. J.; Borchert, J.; Oliver, R. D. J.; Patel, J. B.; Radaelli, P. G.; Snaith, H. J.; Johnston, M. B. and Herz, L. M. 'Halide Segregation in Mixed-Halide Perovskites: Influence of A-Site Cations'. *ACS Energy Letters*, 2021, **6**, 799–808.

[232] Habisreutinger, S. N.; Leijtens, T.; Eperon, G. E.; Stranks, S. D.; Nicholas, R. J. and Snaith, H. J. 'Carbon Nanotube/Polymer Composites as a Highly Stable Hole Collection Layer in Perovskite Solar Cells'. *Nano Lett.*, 2014, **14**, 5561–5568.

[233] Dualeh, A.; Tétreault, N.; Moehl, T.; Gao, P.; Nazeeruddin, M. K. and Grätzel, M. 'Effect of Annealing Temperature on Film Morphology of Organic–Inorganic Hybrid Pervoskite Solid-State Solar Cells'. *Adv. Funct. Mater.*, 2014, **24**, 3250–3258.

[234] Gujar, T. P.; Unger, T.; Schönleber, A.; Fried, M.; Panzer, F.; Smaalen, S. van; Köhler, A. and Thelakkat, M. 'The Role of PbI_2 in $CH_3NH_3PbI_3$ Perovskite Stability, Solar Cell Parameters and Device Degradation'. *Phys. Chem. Chem. Phys.*, 2018, **20**, 605–614.

[235] Buin, A.; Comin, R.; Xu, J.; Ip, A. H. and Sargent, E. H. 'Halide-Dependent Electronic Structure of Organolead Perovskite Materials'. *Chem. Mater.*, 2015, **27**, 4405–4412.

[236] De Keijser, T. H.; Langford, J. I.; Mittemeijer, E. J. and Vogels, A. B. P. 'Use of the Voigt Function in a Single-Line Method for the Analysis of X-ray Diffraction Line Broadening'. *J. Appl. Crystallogr.*, 1982, **15**, 308–314.

[237] Nandi, R. K. and Sen Gupta, S. P. 'The Analysis of X-ray Diffraction Profiles From Imperfect Solids by an Application of Convolution Relations'. *J. Appl. Crystallogr.*, 1978, **11**, 6–9.

[238] Slimi, B; Mollar, M; Assaker, I. B.; Kriaa, A; Chtourou, R and Marí, B. 'Synthesis and Characterization of Perovskite $FAPbBr_{3-x}I_x$ Thin Films for Solar Cells'. *Monatsh. Chem.*, 2017, **148**, 835–844.